PROCEEDINGS

Montana Mining and Mineral Symposium 2023
September 27–September 30, 2023

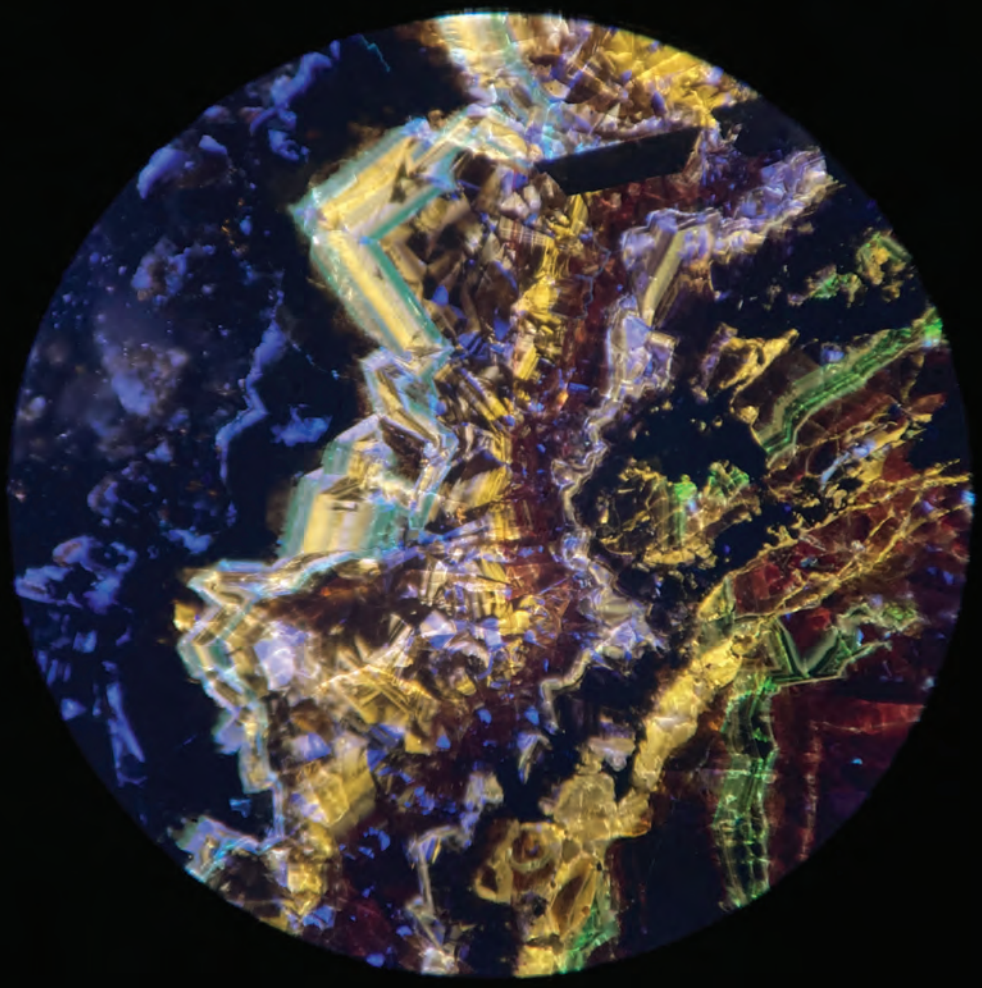

Montana Bureau of Mines and Geology
Special Publication 124

Cover photo: Photomicrograph featuring submillimeter-scale bands of fluorescent sphalerite from the True Fissure Mine, Philipsburg Mining District, Granite County, Montana. Taken under longwave UV (365 nm) light. Field of view = 7 mm. Photo by Celine Beaucamp.

PROCEEDINGS:
MONTANA MINING AND MINERAL SYMPOSIUM 2023

TECHNICAL PAPERS

Special Publication 124

Edited by Adrian Van Rythoven and Susan Barth

Montana Bureau of Mines and Geology, Butte, MT

https://doi.org/10.59691/TTSI4436

Technical Editor: Susan Barth

Scientific Editor: Adrian Van Rythoven

Cartographer: Susan Smith

Peer Reviewers: Richard Berg, George Brimhall, Ryan Davison, Kyle Eastman, Alan English, Christopher Gammons, John LaFave, John R. Ridley, and Adrian Van Rythoven

Symposium Committee: Daniel Brennan, Kyle Eastman, Christopher Gammons, Steven Quane, Amanda Rossi, Kaleb Scarberry, and Adrian Van Rythoven

Research Division Chief: John LaFave

MBMG Director and State Geologist: John Metesh

Cite as: *Van Rythoven, A., and Barth, S., 2024, Proceedings: Montana Mining and Mineral Symposium 2023: Technical papers: Montana Bureau of Mines and Geology Special Publication 124, 94 p.*

UUNO SAHINEN MEDALLION AWARD

The Silver Medallion is given annually by the Montana Bureau of Mines and Geology in memory of Dr. Uuno Sahinen (1906–1982), the first full-time Director and State Geologist of the MBMG (1969–1971).

The award is presented to those who made long-term and significant contributions to the understanding and development of the geologic and groundwater resources of Montana.

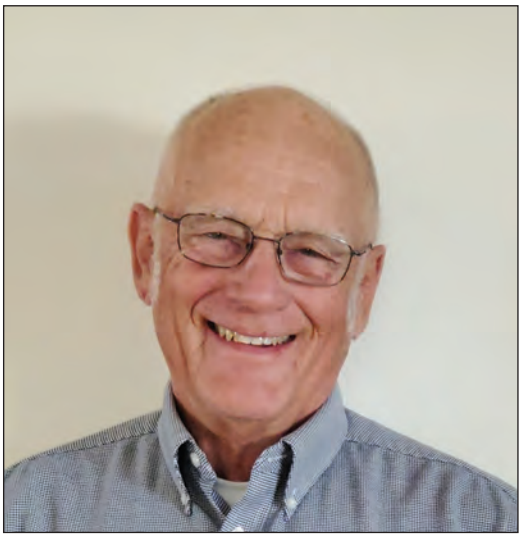

2023 Uuno Sahinen Medallion Awardee: Steve Custer

Steve grew up in Marshfield, Wisconsin. He received a bachelor of science degree in Geology from Lawrence University in Wisconsin (1968). After graduation he served in the U.S. Army from 1969 to 1971. He received a master of science degree from the University of California, Berkeley in 1973. In 1976, Steve received his doctorate from the Geosciences Department at the University of Montana, Missoula. His dissertation was on Saline Seep near Rapelje, Montana.

He went on to teach and conduct research in the Earth Sciences Department at Montana State University, Bozeman (1976–2011) where, for 35 years, he taught courses in geology, mineralogy, petrology, hydrogeology, surface-water resources, snow dynamics and accumulation, and field geology.

Steve advised over twenty undergraduate and graduate students. His hydrogeologic research focused on surface water and snow dynamics. He published many oral presentations with abstracts, 13 refereed journal articles and 19 other written works. In 2000, he was given the Water Legend Award by the Montana branch of the American Water Resources Association for his teaching and research in water resources.

Steve was one of the four “founding fathers” of the Field Hydrogeology Course started by the MBMG in 1985—a course that has been attended by a multitude of students and professionals over the years.

Steve served briefly as acting Director of the Geographic Information and Analysis Center at Montana State University from 1996 to 1997, and as Department Head of Earth Sciences from 1983 to 1991 and from 2007 until his retirement in 2011.

In retirement, he is professor emeritus at the Department of Earth Sciences, Montana State University. He also volunteered as a board member on the Gallatin City–County Board of Health and the Gallatin Local Water Quality District. He chaired the Technical Oversight Committee for the Yellowstone Controlled Ground Water Area in Montana.

2022 Uuno Sahinen Medallion Awardee: Donald Hyndman

Originally from Vancouver, British Columbia (BC), Dr. Donald Hyndman spent seven undergrad and grad college summers, 1955 to 1963, mapping regional geology in the mountains of BC for the Geological Survey of Canada. In the summer of 1957, he worked for a Cominco and Noranda mining joint venture in the Okanagan Valley, at what became the large Brenda Cu-Mo mine. In the summer of 1958, he did exploration work for Yukon Consolidated Gold Corp. He earned his B.A.Sc. (Geological Engineering) from the University of British Columbia in 1959. The Canadian Geological Survey (CGS) funded his doctoral research and he earned his Ph.D. from the University of California, Berkeley in 1964. In 1964 he moved to Missoula, where he could continue both geology research and teaching at the University of Montana.

Dr. Hyndman's teaching at UM included courses in mineralogy, igneous and metamorphic petrology, crystallography, regional tectonics, introductory geology and roadside geology, and in later years, natural hazards. He mentored numerous grad students, many of whom went to work in mineral exploration, especially in Montana and Colorado. His research, and that of many of his students, included studies of the Idaho batholith, the mylonite zone marking the eastern flank of the batholith in the Bitterroots, origin of batholith magmas, alkaline igneous rocks in central Montana, origin of radial dikes and laccoliths in Montana, regional tectonics of the Pacific Northwest, and sundry other aspects of Montana geology. He spent a couple of years as chairperson of the Geology Department, and a sabbatical-leave year as visiting Professor at Stanford University, teaching their required undergrad course in igneous petrology, while writing the second edition of his petrology textbook. Don published two textbooks: *Petrology of Igneous and Metamorphic Rocks* (2 editions) and *Natural Hazards and Disasters* (5 editions and working on the 6th), coauthored with David Hyndman. Don is the co-originator of the Roadside Geology (RG) Series with David Alt. He then coauthored with David Alt seven Roadside Geology books: *Rocks, Ice, and Water; RG Northern Rockies, Montana* (1st ed.); *RG Idaho; RG Washington; RG Oregon; RG Northern California; RG Northern and Central California*; and two with other authors, R*G Hawaii* (with Richard Haslett), and *Roadside Geology of Montana* 2nd ed., with Robert Thomas. He also published more than 100 scientific research papers, most as sole author, as well as several other geological research volumes and geological field guides, some as sole author, others as coauthor with other scientists.

Don Hyndman was the recent recipient of the 2021 High Plains Book Awards in Medicine and Science for *Roadside Geology of Montana* 2nd edition, by Donald W. Hyndman & Robert C. Thomas. He is a Fellow of the Geological Society of America and the American Geophysical Union, and is a Member of the National Academy of Sciences panel on nuclear waste disposal.

TABLE OF CONTENTS

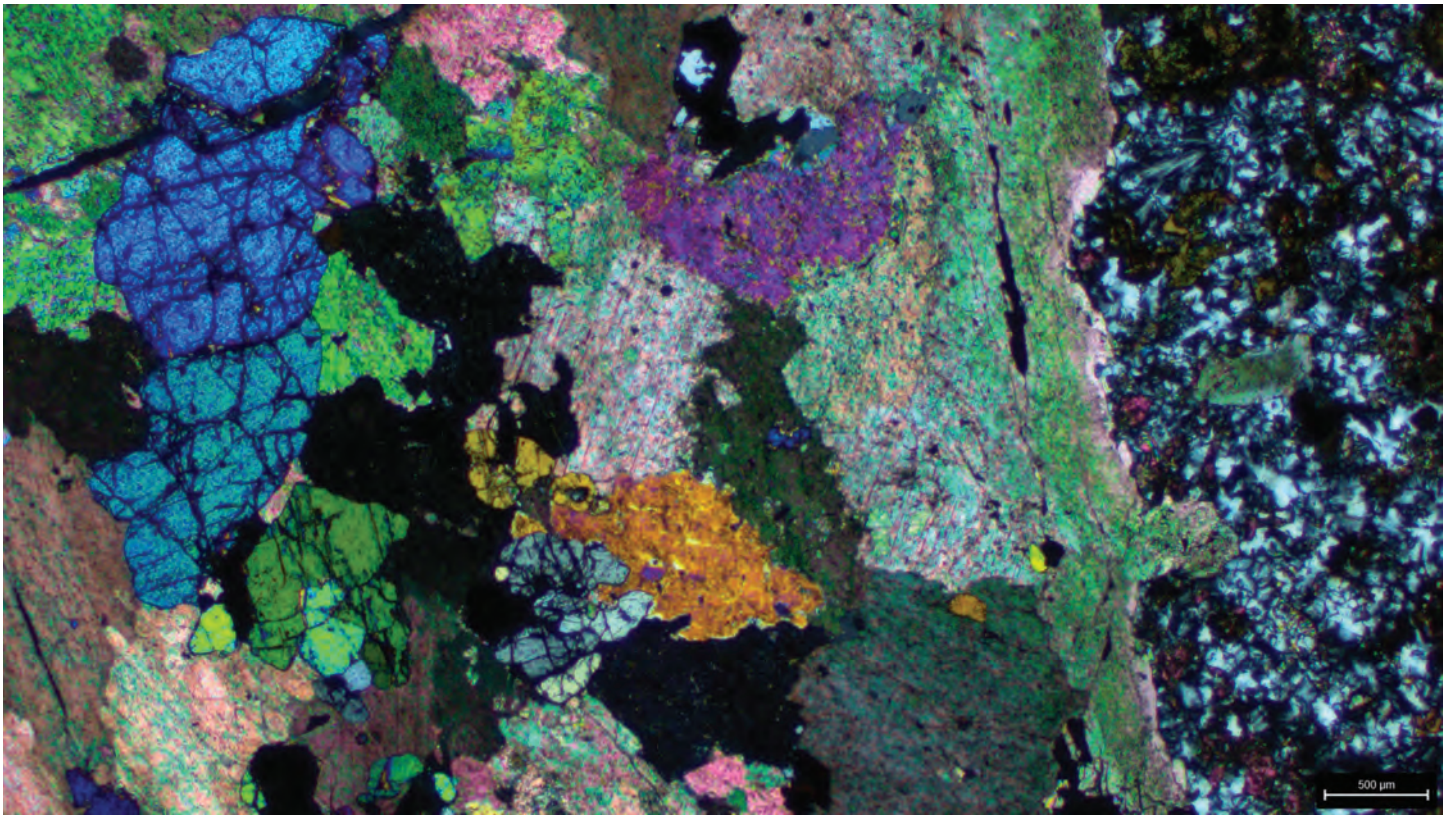

A cross-polarized transmitted light photomicrograph of a carbonatite vein in contact with fenite (far right of photo) from the Sheep Creek Carbonatite, Ravalli County, Montana. Large subhedral high-relief crystals on left of photo are monazite, surrounded by calcite.

Trace Elements in Fluorescent Sphalerite from the Philipsburg Mining District, Granite County, Montana

Celine M. Beaucamp

Earth Science and Engineering Ph.D. Candidate, Montana Technological University, Butte, Montana

cbeaucamp@mtech.edu

The Philipsburg mining district in Granite County, Montana, has been identified as a cordilleran polymetallic Ag-Cu-Zn±Pb lode district associated with a Mo-Cu porphyry of unknown extent (Beaucamp and Gammons, 2022). Some sphalerite samples from the Philipsburg mining district display unusually bright fluorescence under longwave (365 nm) UV light (figs. 1, 2). Generally, brown sphalerite fluoresces red, and green sphalerite fluoresces orange, yellow, blue, purple, or green (fig. 3). Green and red phosphorescence can be observed for a few seconds after the UV light is turned off. Light green (in visible light) sphalerite also shows triboluminescence when scratched with a nail (figs. 4e, 4h).

These fluorescent sphalerite samples, along with low- to non-fluorescent sphalerite samples from Philipsburg, were analyzed with laser ablation inductively-coupled mass spectroscopy (LA-ICP-MS) for trace element content (by Dr. Jay Thompson, USGS-LTRACE laboratory, Geology, Geophysics, and Geochemistry Science Center, Denver, Colo.). Sphalerite is a mineral known to regularly contain trace elements, many of which are listed in USGS' 2022 list of critical minerals, e.g., In, Bi, Ge, and Ga. These analyses were filtered to remove solid inclusions and reflect only lattice-bound substitutions. All the fluorescent samples come from a high-sulfidation state central zone where the low-Fe sphalerite coexists with enargite and tennantite. These fluorescent samples contain variable amounts of Cd, Cu, Ga, In, Hg, Ge, and W. Ga averages 525 ppm (max value of 4,997 ppm), and In averages 114 ppm. Fe is remarkably low (average of ~100 ppm), whereas Cu is high (average of 907 ppm; Beaucamp and others, 2022). Also, up to ~2,000 ppm of W was detected in the sphalerite lattice of four fluorescent samples (average of these four samples:

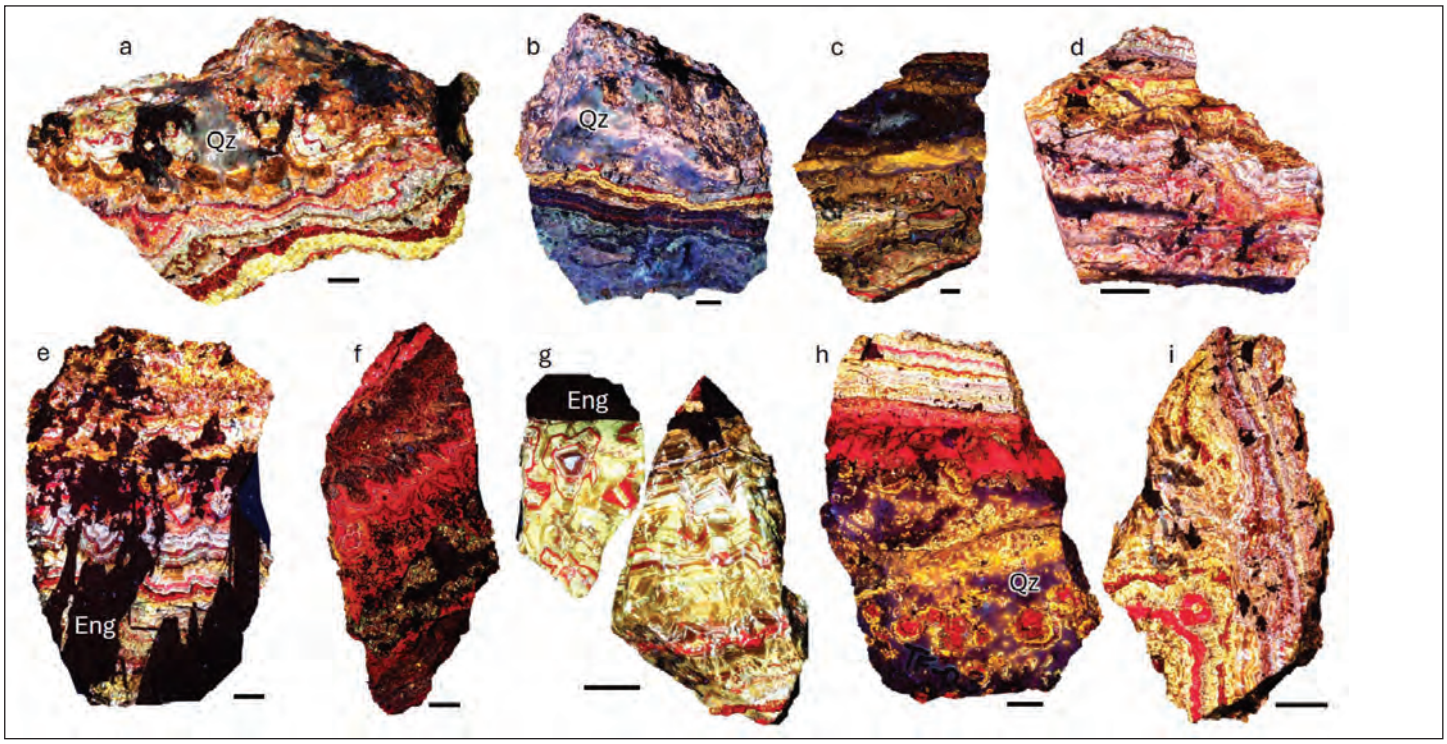

Figure 1. Sphalerite samples from the Philipsburg mining district under long-wave (365 nm) UV light. The scale under each sample is 1 cm. Everything is sphalerite unless noted otherwise: Eng, enargite; Qz, quartz. (a) Algonquin Mine, L. Dudas collection, Sample B15; (b) Algonquin Mine, L. Dudas collection, Sample B3; (c) Scratch Awl CB-SA-06; (d) Scratch Awl CB-SA-18; (e) Scratch Awl CB-SA-03; (f) Scratch Awl CB-SA-31; (g) Scratch Awl CB-SA-22; (h) True Fissure CB-TF-03; (i) Scratch Awl CB-SA-35.

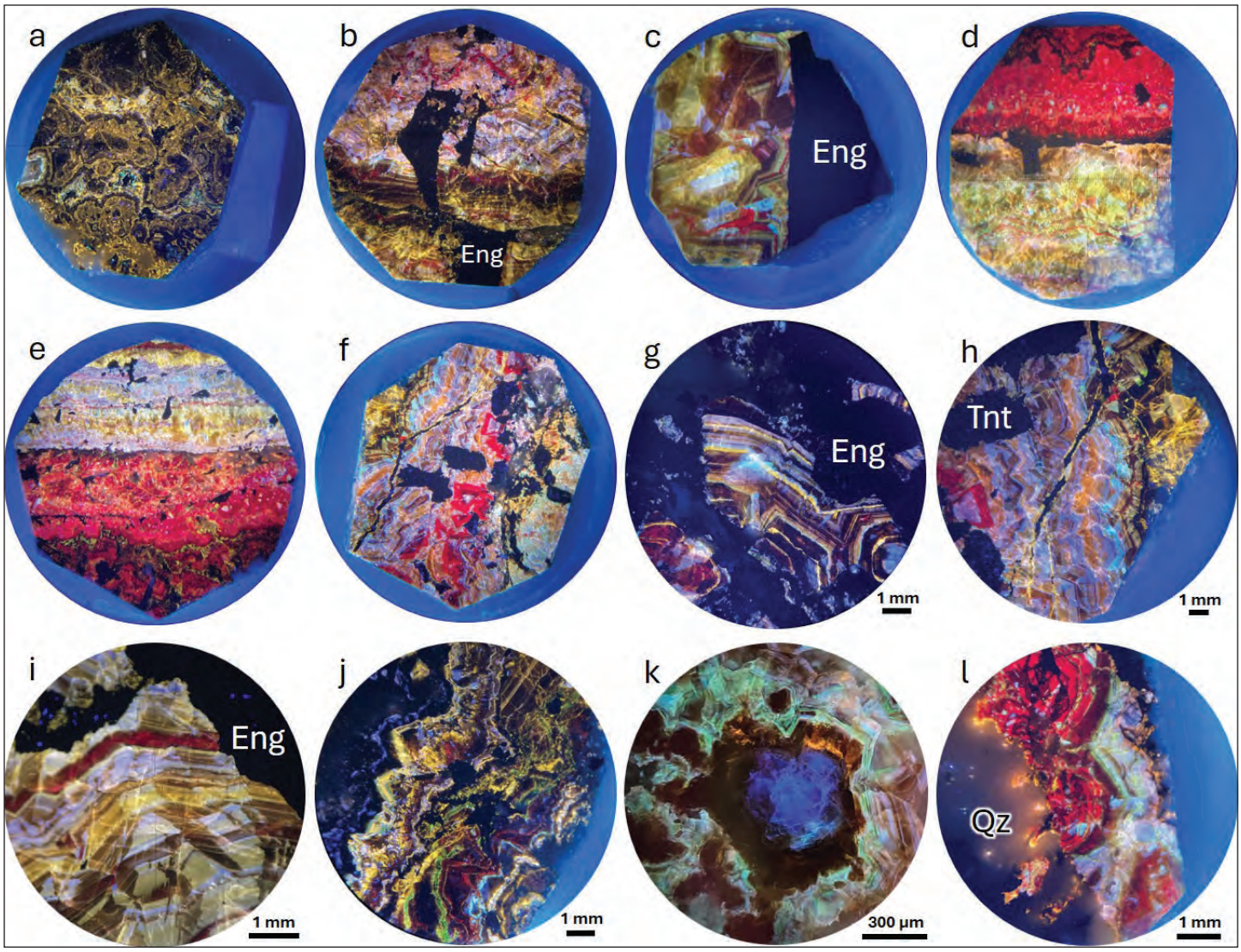

Figure 2. Microscope view of sphalerite sample epoxy mounts from the Philipsburg mining district under long-wave UV light. Everything is sphalerite unless noted otherwise: Eng, enargite; Tnt, tennantite; Ccp, chalcopyrite; Qz, quartz. Samples mounted in epoxy plugs (2.5 cm diameter) and polished. (a) CB-SA-17; (b) CB-SA-18a; (c) CB-SA-22; (d) CB-TF-01b; (e) CB-TF-03b; (f) CB-SA-04; detailed feature under magnification; (g) CB-AL-101; (h) CB-SA-04; (i) CB-SA-10a; (j) CB-TF-102; (k) sample from Trout Mine; (l) CB-AL-104.

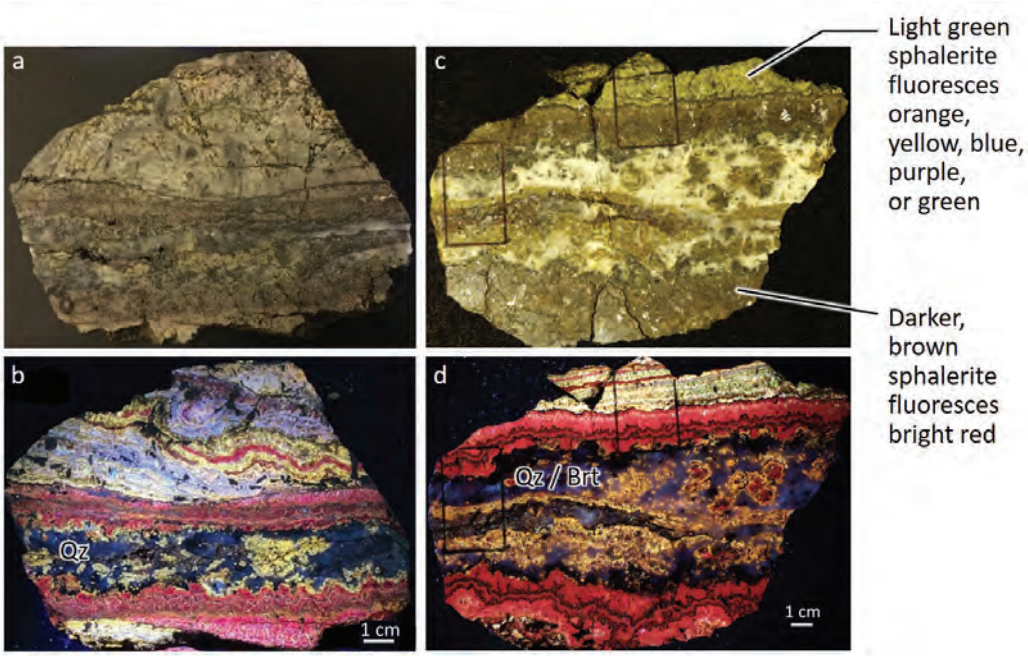

Figure 3. Samples from the Philipsburg mining district showing the two main types of sphalerite, light green and brown, and their respective fluorescence. Everything is sphalerite unless noted otherwise: Qz, quartz; Brt, barite. (a) CB-SA-04 under visible light; (b) CB-SA-04 under long-wave UV light; (c) CB-TF-01 under visible light; (d) CB-TF-01 under long-wave UV light.

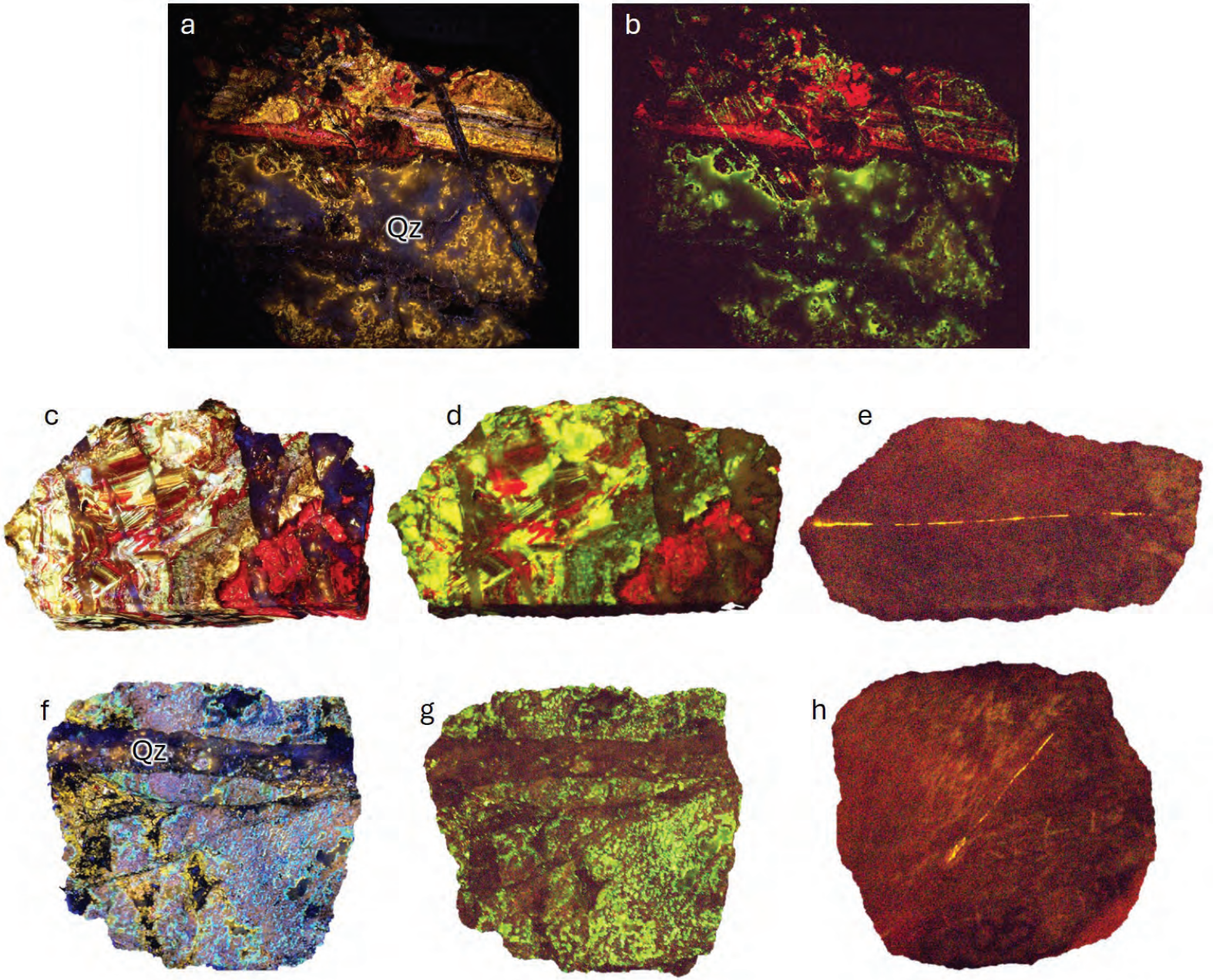

Figure 4. UV-fluorescence, phosphorescence, and triboluminescence of sphalerite samples from the Philipsburg mining district. Everything is sphalerite unless noted otherwise: Qz, quartz. (a) CB-SA-01 under long-wave UV light; (b) Phosphorescence of CB-SA-01 after exposure to long-wave UV light; (c) CB-SA-23 under long-wave UV light; (d) Phosphorescence of CB-SA-23 after exposure to long-wave UV light; (e) Triboluminescence of CB-SA-23 when scratched with a nail; (f) CB-TF-05under long-wave UV light; (g) Phosphorescence of CB-TF-05 after exposure to long-wave UV light; (h) Triboluminescence of CB-TF-05 when scratched with a steel nail.

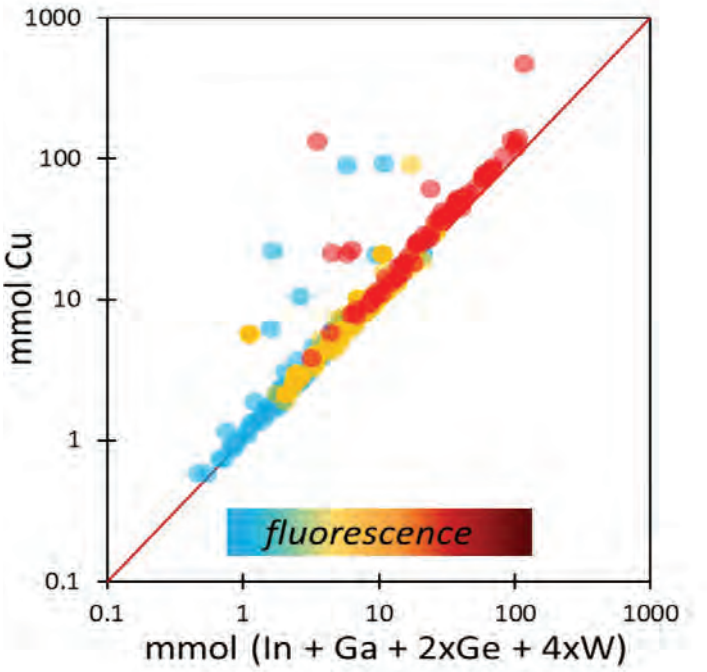

Figure 5. Colors of UV-fluorescence of Philipsburg's sphalerite according to trace elements content.

152 ppm). When separated by fluorescence color, the data reveal samples with the lowest total content (in ppm) of trace elements systematically fluoresce blue and green. Conversely, samples with the highest total content (ppm) fluoresce bright red. Orange and yellow fluorescence are intermediate colors with intermediate content of trace elements.

In comparison, low- to non-fluorescent samples exist in both high- and low-sulfidation state mineral assemblages. The trace elements in these samples are Fe, Mn, Ag, Cd, Cu, As, Pb, Sb, Sn ± Ge, and Hg. Notable values are high Ag (>1,000 ppm) and high Ge (average of 255 ppm). Cu also remains high in these samples (average of 2,280 ppm). Fe is variable, generally low, with an average of ~100 ppm. An exception is the Granite-Bimetallic Mine, which averages ~ 50,000 ppm Fe.

Some elements have the same valence as Zn^{2+} and can substitute directly into the ZnS lattice, including Fe^{2+}, Mn^{2+}, Cd^{2+}, Hg^{2+}, and Pb^{2+}. Other elements require coupled substitution to maintain the overall charge balance: Cu^{+}, Ag^{+}, As^{3+}, Ga^{3+}, In^{3+}, Sb^{3+}, Ge^{4+}, Sn^{4+}, and W^{6+}. The proposed coupled substitutions for fluorescent sphalerite are: $Cu^{+} + (Ga^{3+}, In^{3+}) = 2Zn^{2+}$ and $2Cu^{+} + Ge^{4+} = 3Zn^{2+}$. Because the redox potential to reduce W^{6+} to W^{4+} is high, the tetravalent form of tungsten, such as in tungstenite, is rare (Kazamel and others, 2023). Therefore, for high W samples, the coupled substitution of W and Cu for Zn is proposed as: $4Cu^{+} + W^{6+} = 5Zn^{2+}$, without the need for vacancies. In the low- to non-fluorescent samples, the following coupled substitutions are proposed: $(Cu^{+} + Ag^{+}) + (As^{3+}, Ga^{3+}, In^{3+}, Sb^{3+}) = 2Zn^{2+}$ and $2(Cu^{+} + Ag^{+}) + (Ge^{4+}, Te^{4+}, Sn^{4+}) = 3Zn^{2+}$.

Trace elements in sphalerite have been studied extensively (among many: Cook and others, 2009; Frenzel and others, 2016; Benites and others, 2021), but associated fluorescence is usually not reported. These preliminary results indicate a correlation between fluorescence and the elements Cd, Cu, Ga, In, Hg, Ge, and W in the sphalerite crystal lattice. However, the fundamental mechanisms creating the fluorescence are unclear at this time and should be investigated further.

Acknowledgments

The author would like to thank Dr. Jay Thompson and Heather Lowers from the USGS Denver office for their work supporting this research and her advisor, Dr. Christopher Gammons, from the Geological Engineering Department at Montana Tech.

References

Benites, D., Torró, L., Vallance, J., Laurent, O., Valverde, P.E., Kouzmanov, K., Chelle-Michou, C., and Fontboté, L., 2021, Distribution of indium, germanium, gallium, and other minor and trace elements in polymetallic ores from a porphyry system: The Morococha District, Peru: Ore Geology Review, v. 136, no. 104236, https://doi.org/10.1016/j.oregeorev.2021.104236.

Beaucamp, C., and Gammons, C.H., 2022, New investigations of polymetallic lode deposits of Philipsburg, Granite County, Montana: Montana Bureau of Mines and Geology, Special Publication 123, p. 131–136, https://doi.org/10.59691/YXKU1170.

Beaucamp, C., Thompson, J., Gammons, C.H., Cangelosi, G., and Lund, K., 2022, Fluorescent sphalerite from Montana, USA: Coupled substitutions of Cu, Ga, and W: Proceedings 2022 V.M. Goldschmidt Conference, https://doi.org/10.46427/gold2022.11433.

Cook, N.J., Ciobanu, C.L., Pring, A., Skinner, W., Shimizu, M., Danyushevsky, L., Saini-Eidukat, B., and Melcher, F., 2009, Trace and minor elements in sphalerite: A LA-ICPMS Study: Geochimica et Cosmochimica Acta, v. 73, p. 4761–4791, https://doi.org/10.1016/j.gca.2009.05.045.

Frenzel, M., Hirsch, T., and Gutzmer. J., 2016, Gallium, germanium, indium, and other trace and minor elements in sphalerite as a function of deposit type—A meta-analysis: Ore Geology Review, v. 76, p. 52–78, https://doi.org/10.1016/j.oregeorev.2015.12.017.

Kazamel, B.G., Jamieson, H.E., Leybourne, M.I., Falck, H., and Johannesson, K.H., 2023, Aqueous geochemistry and mineralogy of tungsten with emphasis on mine wastes: Economic Geology, v. 118, no. 3, p.659–674, https://doi.org/ 10.5382/econgeo.4939.

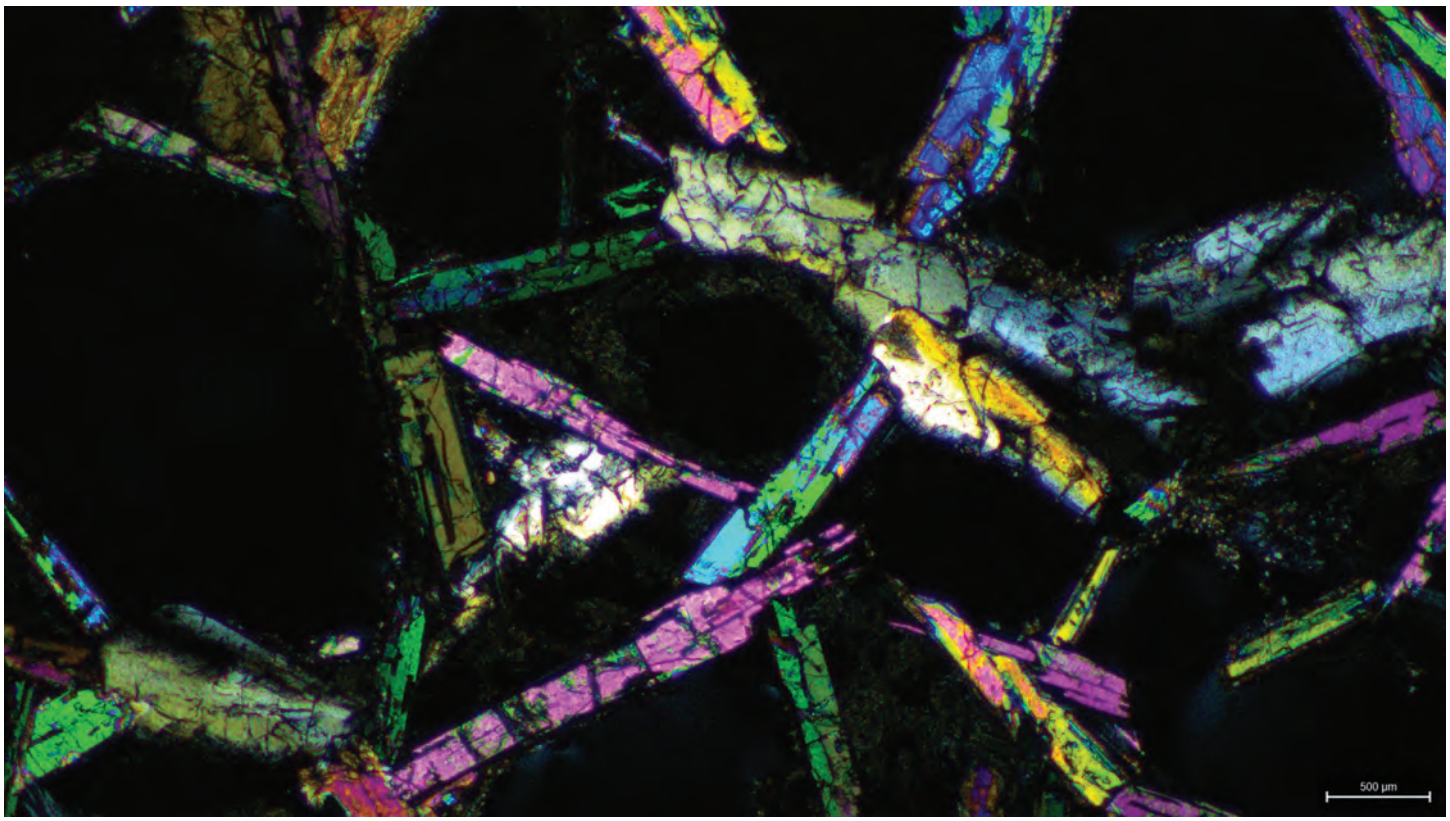

A cross-polarized transmitted light photomicrograph of slag from phosphorite refining, Silver Bow County, Montana. Acicular Ca-Mg-Fe silicate crystals with high birefringence surrounding isotropic vesicles.

Ruby Graphite Project—Early Exploration Results

Gregory J. Bell

Ruby Graphite Holdings LLC and Reflex Advanced Materials Corp., Phoenix, AZ

greg@rubygraphite.com

Located in the Ruby Range mountains in southwestern Montana near Dillon, a natural graphite deposit was mined from 1901 until 1948 by the Crystal Graphite Company (Hum, 1943; Ford, 1954). After producing approximately 2,400 tons (2,200 tonnes) of vein graphite using artisanal mining methods more than 70 years ago (Cameron and Weis, 1960), the location was abandoned and mostly forgotten. Most of the sales occurred during WW I with hand cobbing and sorting; pneumatic tools and a small mill were only in operation during WW II at the end of the last active mining operations. The deposit was first described by Winchell (1911), and origin of the graphite mineralization has been long debated (Perry, 1948; Ford, 1954; Heinrich, 1960; Duke and others, 1990; James, 1990).

Until now, the original deposit and surrounding lands had never been properly explored with modern methods, and had never been drilled. The Ruby Graphite Project was initiated in 2015 to turn this previously discovered deposit into a resource with new value in the current age of electric vehicles. A combination of private and Federal mineral rights totaling 1,865 acres (755 hectares), including 96 lode mining claims, were acquired by Ruby Graphite Holdings LLC. Then, in 2022 under an option agreement, Reflex Advanced Materials Corp. proceeded to fund an exploration program to demonstrate the extent and grade of the Ruby Graphite deposit.

The initial exploration effort concentrated on developing a geological model of the stratigraphy and structure and identifying potential graphite-bearing areas. Detailed geologic mapping was conducted, which included soil sampling for geochemical rare-earth fingerprinting and pH measurement to support lithology and structure mapping (details found in Kerins and Close, 2023). Remote sensing included drone-based photogrammetry and elevation modeling; handheld electromagnetic (EM) survey using a multifrequency, shallow-looking survey tool; and an induced potential (IP) survey to delineate conductivity trends indicative of graphite. Later followup EM surveys included an aerial time-domain EM (TDEM) survey and several lines of horizontal-loop EM (MaxMin) survey.

These survey results indicate several conductive trends that correlate well among the shallow EM survey and progressively deeper MaxMin, IP, and TDEM surveys. Shown in figure 1, these potential graphite-bearing trends within the layered Archean granitic gneiss, schist, and marble are more extensive than what was previously known.

One of the anticipated trends confirmed by the geophysical surveys, labeled the “Saddle Trend” in figure 1, extends from the abandoned Ground Hog mine complex northeasterly toward the original Bird’s Nest mine adits. Note that all the conductivity prospects tend to run subparallel to the interface between marble and granitic rock types and predominantly within the granite.

HQ diameter core drilling from August to October 2023 confirmed the presence of vein and flake graphite at depth. Figure 2 shows locations of the 24 holes drilled from 8 drill pads, with a total length of 11,125 ft (3,391 m). Average depth for these holes was 463 ft (141 m). Drilling was relatively shallow due to the presence of graphite mineralization at surface and in shallow historical workings next to the drill target area.

The holes were generally drilled in a vertical-fan arrangement with inclinations of 45°, 60°, 75°, or 90° from horizontal. All holes were surveyed to determine azimuth and inclination. The acquired data allows for modeling and determination of structural trends. This helps with targeting in future drill programs. Typically, two to three holes were drilled per pad, with five holes near the existing mine workings.

Graphite was encountered in each of the completed holes, ranging from tens of meters of disseminated graphite flake to multiple veins of graphite, with individual veins typically 1 to 5 cm thick in zones up to

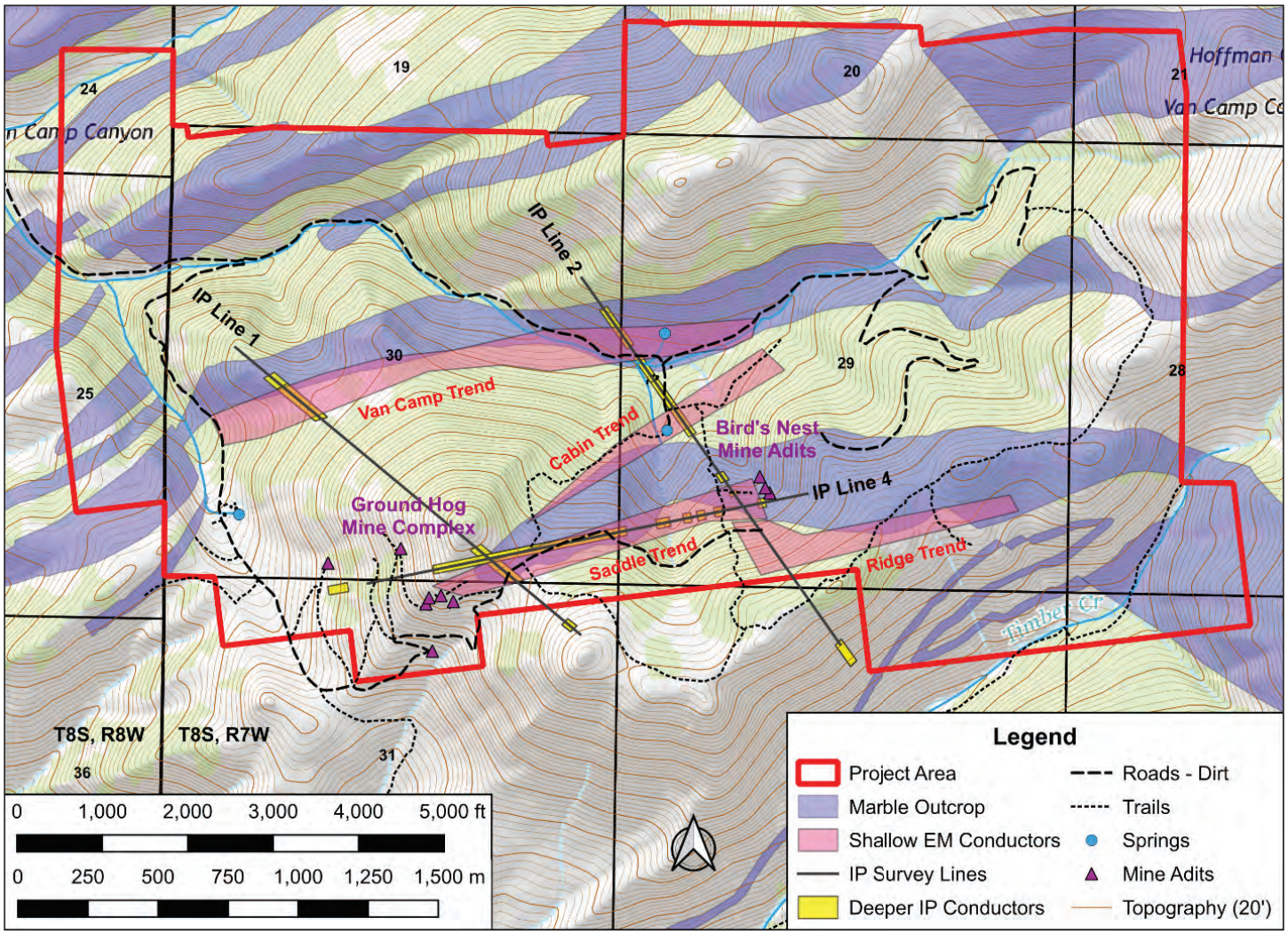

Figure 1. Map of Ruby Graphite project area showing four main conductivity trends as delineated by (1) Shallow EM (in pink), and (2) IP (in yellow) surveys. Note that the conductive trends are approximately aligned with the interface between the marble (in blue) and surrounding granitic rocks (not colored). Location of marble per geologic survey by Okuma (1971). For additional details, see Kerins and Close (2023).

30 cm long (assays pending). All recovered core was descriptively logged and photographed. The ore grade was visually estimated, and it was found that three different forms of graphite were encountered: vein graphite, disseminated flake graphite, and what appears to be a “clotty” form of graphite that replaced biotite and perhaps garnet. Figure 3 shows a photograph of one of the visibly richest core sections encountered, which displays these three graphite forms.

The entire lengths of mineralized intervals have been split with a diamond saw and sampled. Samples will be analyzed for graphitic carbon as the target analyte, and sulfide sulfur for waste-rock disposal purposes. As part of the assaying protocol, multi-element analysis will also be initiated to test the geochemical associations of the graphite mineralization. Also, carbon isotope and related studies are being pursued to better understand the origin and exploration footprint of the mineralization.

This deposit is notable as the U.S. has not produced its own natural graphite for more than 40 years. With the growing demand for natural graphite for use as anodes in lithium-ion batteries, as well as other advanced materials such as graphene and expandable graphite, the mineral is recognized as a critical and strategic resource by the U.S. government (Department of the Interior, 2022).

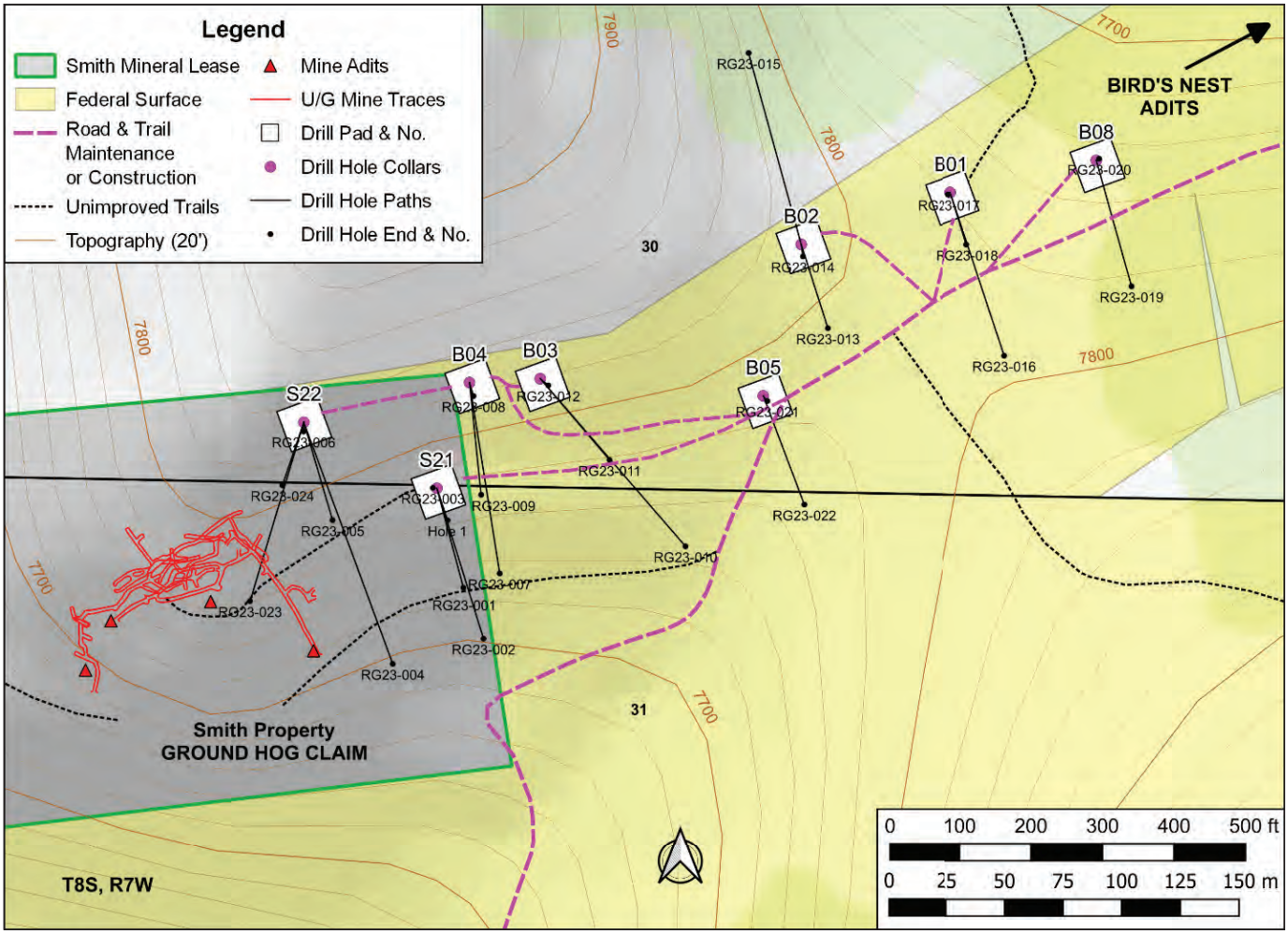

Figure 2. Map of as-built drillhole locations along the Saddle Trend. Note the location of abandoned mine workings on the left (Armstrong and Full, 1950).Two or three holes were drilled from each of 8 pads, with two additional holes drilled near and under the mine workings.

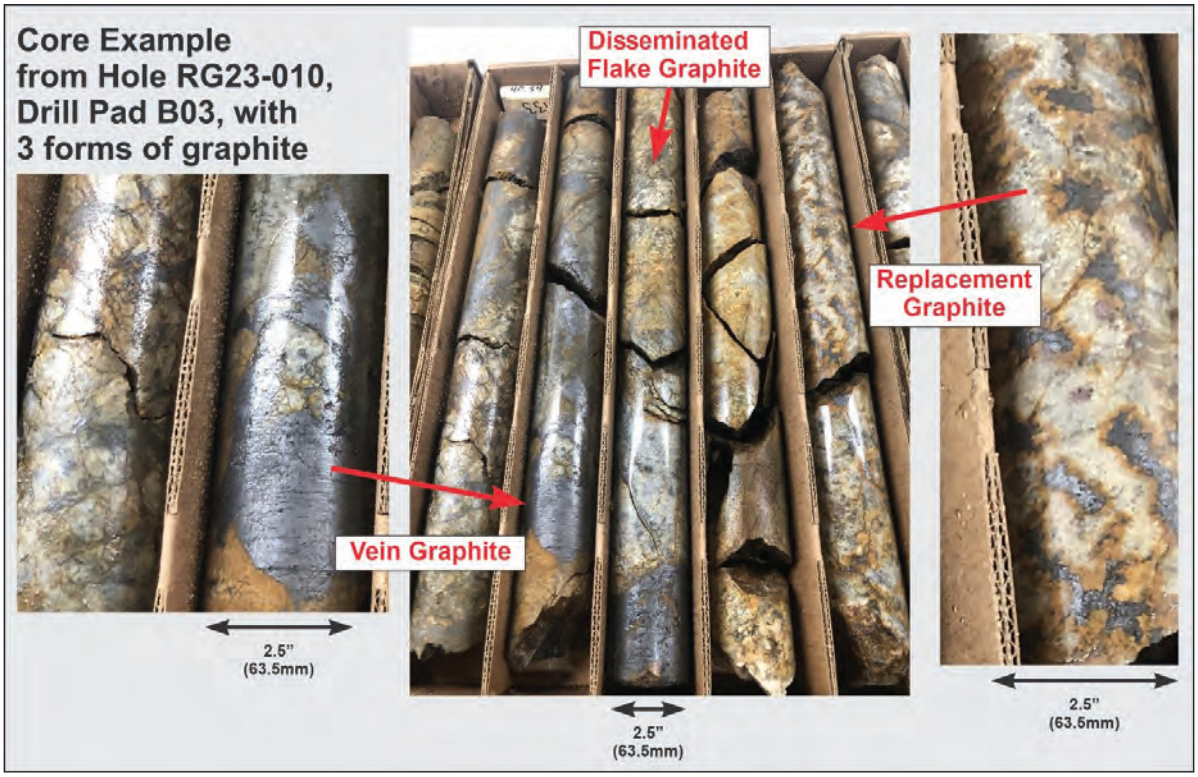

Figure 3. Photographs of a graphite-rich 10-ft-long (3 m) section of core. Note the three forms of graphite encountered in this core run from 133.0 ft (40.54 m) depth of Hole RG23-010: (1) vein graphite; (2) disseminated flake graphite; and (3) replacement graphite. Photo scales approximate.

References

Armstrong, F.C., and Full, R.P., 1950, Geologic maps of Crystal Graphite mine, Beaverhead County, Montana: U.S. Geological Survey Open-File Report 50-26, https://doi.org/10.3133/ofr5026.

Cameron, E.N., and Weis, P.L., 1960, Strategic graphite—A survey, contributions to economic geology: U.S. Geological Survey Bulletin 1082-E, https://doi.org/10.3133/b1082E.

Department of the Interior, Geological Survey, 2022, 2022 Final List of Critical Minerals. Federal Register, v. 87, no. 37, p. 10381–10382,available at https://www.govinfo.gov/content/pkg/FR-2022-02-24/pdf/2022-04027.pdf

Duke, E.F., Galbreath, K.C., and Trusty, K.J., 1990, Fluid inclusion and carbon isotope studies of quartz-graphite veins, Black Hills, South Dakota, and Ruby Range, Montana: Geochimica et Cosmochimica Acta, v. 54, no. 3, p. 683–698, https://doi.org/10.1016/0016-7037(90)90364-Q.

Ford, R.B., 1954, Occurrence and origin of the graphite deposits near Dillon, Montana: Economic Geology, v. 49, p. 31–43, https://doi.org/10.2113/gsecongeo.49.1.31.

Heinrich, E.W., 1960, Pre-Beltian geology of the Cherry Creek and Ruby Mountains areas, southwestern Montana, Part 2—Geology of the Ruby Mountains: Montana Bureau of Mines and Geology Memoir 38, 40 p., 2 sheets.

Hum, C.K., 1943, Geology and occurrence of graphite at the Crystal Graphite mine near Dillon, Montana: Butte, Mont., Montana Technological University, PhD thesis, available at https://digitalcommons.mtech.edu/bach_theses/184

James, H.L., 1990, Precambrian geology and bedded iron deposits of the southwestern Ruby Range, Montana: U.S. Geological Survey Professional Paper 1495, https://doi.org/10.3133/pp1495

Kerins, E., and Close, S., 2023, Ruby graphite project, Beaverhead County, Montana, 2022 technical report: Bozeman, Mont., Ethos Geological, available at https://reflexmaterials.com/wp-content/uploads/2023/03/Ruby-Graphite-2022-Technical-Report_Feb-22-2023.pdf

Okuma, A.F., 1971, Structure of the southwestern Ruby Range near Dillon, Montana: State College, PA, Pennsylvania State University.

Perry, E.S., 1948, Talc, graphite, vermiculite and asbestos deposits in Montana: Montana Bureau of Mines and Geology Memoir 27, available at https://mbmg.mtech.edu/pdf-publications/m_27.pdf

Winchell, A.N., 1911, A theory for the origin of graphite as exemplified in the graphite deposit near Dillon, Montana: Economic Geology, v. 6, p. 218–230, https://doi.org/10.2113/gsecongeo.6.3.218.

An Operative Porphyry Copper Model Based on Thermochemical Evidence of Convective Gaseous Hydrogen Transport and Mega-Stratovolcanic Eruptions Containing Anhydrite

George Brimhall

Clementine Exploration, LLC, Wise River, MT and Berkeley, CA

brimhall@clementinemt.com

Abstract

What do giant porphyry copper deposits (PCD) and cataclysmic mega-strata volcano eruptions like Mt. Pinatubo in the Philippines have in common besides the mineral anhydrite ($CaSO_4$)? Why do mineralized porphyry magmas explosively hydro-fracture and drive long-lived hydrothermal convection cells in the subsurface, while some rare arc magmas instead erupt explosively to form stratovolcanoes with atmospheric impacts? These questions are answered here by invoking hydrogen gas (H_2), rather than oxygen (O_2), to gauge redox processes leading to anhydrite stability over that of titanite ($CaTiSiO_5$). The H_2 geochemical reference frame affords an opportunity to reevaluate oxidation processes from first principles, free of assumptions and precedence. A thermodynamic diagram is developed here for redox equilibria in porphyry copper genesis using H_2 instead of O_2, which is not present. The H_2 vs 1/T Van't Hoff reference frame at water saturation works as a powerful operative geochemical diagram. Confined-flow migration of H_2 by protracted magmatic outgassing during thermal advection causes oxidation by dehydrogenation and reduction in the return flow heating path approaching the pluton. Expulsion of highly oxidized early high-temperature aqueous fluids continue to lose H_2 and oxidize along a cooling path. This path is defined by the Mg-rich ($X_{Fe} = 0.2$), Ti-poor hydrothermal biotite–magnetite–K–feldspar potassic alteration mineral assemblage line. This serves as definitive trajectory of the cooling pathway. The return heating pathway is marked by propylitic alteration, and finally distal diffusion-controlled orbicular actinolite alteration. Two distinct concentric advective circulation cells emerge in the log H_2 vs. 1/T space. The largest advective circulation cell defines sediment-hosted Bingham-type PCD systems that reach both extreme early oxidative states with chalcopyrite, bornite, and digenite (chalcocite) and extreme reductive states with distal actinolite orbicular alteration. In contrast, the batholith-hosted Butte-type PCD cell has a narrow limited early oxidation range that does not extend up to bornite or digenite and instead consists of only of chalcopyrite–pyrite. It also lacks a distal orb ring due to restrictive chemical buffering by the influence of granite wall rocks with red-colored high-Ti ($X_{Fe} = 0.5$) biotite terminating in the advanced argillic assemblage with covellite and chalcocite on the oxidized end. Occurrences of actinolite orbs at Bingham, Escondida, El Hueso, Cajamarca, Morenci, Fortitude, Cananea, and Oyu Tolgoi imply that an actinolite orb ring may be a definitive indicator of large PCD systems. Given the necessity of electron conservation, a large actinolite orb ring portends a large highly oxidized Potassic alteration zone with chalcopyrite, bornite, and digenite. This potential exploration target size indicator supported by H_2 dynamics and redox thermochemistry may help guide discovery of new deep confined PCDs of considerable size. This is being tested at the Clementine prospect in southwest Montana, which has a 3 by 5 km orb ring. Besides realization that H_2 gas plays an important role in magma genesis and ore deposition raises the possibility that it also has a chemo-mechanical impact of H_2 through hydrolytic weakening or embrittlement of silicate rock-forming minerals. If such weakening occurs, the assumed stresses required for over-pressured fluids exsolved from magmas to induce brittle failure and promote explosive hydrofracturing could be dramatically reduced. Similarly, if hydrofracturing in the rigid carapace above volcanic magma chambers was induced at lower stress levels because of H_2-driven hydrolytic weakening, less energy is then required to drive the cataclysmic eruptions of super strata volcanoes. Porphyry copper deposits have been described as "failed" large volcanic eruptions. Conversely, oxidized anhydrite-bearing mega-strata volcanic eruptions containing anhydrite can be considered as once-potential porphyry copper magmas that, upon exsolution of magmatic water, breached the surface explosively rather than becoming a confined mineralized convective system at depth. Confinement in the case of porphyries precludes the escape of H_2

to the atmosphere and instead promotes the downward advective transport of H_2, thus contributing to the formation of an elliptical torus convective system centered on the cooling parental porphyry.

Introduction

In memory of Jim F. Luhr, whose legacy to volcanology, like his music, was made with rare insight, universal kindness, and joy.

Although critical minerals and copper are vital to attaining a carbon neutral society through electrification, decarbonization of heavy industries, transportation, and aviation systems may require molecular hydrogen, which is a powerful, portable, emission-free combustible fuel with a higher energy density (35 watts/g) than lithium (0.2 watts/g). However, the minute molecular size of H_2 (0.27 nm) makes it readily subject to diffusion even through many, but not all, metals and rocks, making conveyance, storage, and petrological interpretation challenging. Such remarkably selective physical behavior raises the question as to where in nature hydrogen transport may have played an as yet unrecognized role of considerable importance. Especially for an abundant element in gaseous form, hydrogen's capability of affecting oxidation and reduction through its migration and electron transfer could have had major consequences on natural systems, and so far has gone largely unrecognized—although speculations infer that oxidation follows hydrogen escape by magmatic outgassing from volcanoes to explain the higher oxidation state of arc magmas compared to other mantle-derived magma types. This assertion, however, remains to date a vague hypothesis and its resolution motivates this study to discover an operational mechanism.

There is a remarkable lack of high-temperature phase equilibria with which to start assessing the roles of H_2 in nature and quantitatively address H_2 outgassing. The paucity of relevant studies involving H_2 is likely due to the historical use of oxygen (O_2) in gauging redox states in nature rather than H_2. Therefore, to advance understanding of H_2 geochemistry beyond inference, chemical thermodynamics is used here to construct new equilibrium phase diagrams where hydrogen is the principal variable of interest. Well-known recurrent potassic and propylitic mineral assemblages in PCD ore deposits of (Meyer and Hemley, 1967; Hemley and others, 1980; Lowell and Guilbert, 1970; Gustafson and Hunt, 1975; Sillitoe, 2010; John and others, 2010) can then serve as recognizable markers defining both the cooling and heating pathways of convective fluid flow. For each mineral assemblage selected by the present author, the stoichiometry of each reaction has been computed defining the reaction coefficient mole numbers for each reactant and product. Once the reaction stoichiometry has been determined, equilibrium thermodynamic calculations have been made using the CHNOSZ thermodynamic code of Dick (2019) to yield the equilibrium constants.

Although hydrogen may have escaped these geological systems *en masse*, in its wake is left a discernible mineralogical architecture in rocks that reveals the role of hydrogen over a wide temperature range from magmatic to hydrothermal conditions. One anhydrite-bearing mineral assemblage that is known to form under highly oxidizing conditions is common to both porphyry copper deposits and certain very large stratovolcanoes including El Chichon, Mexico, where their similarities to PCDs has been noted (Luhr, 2008), including their occurrence with the tectonic metallogenic belt for PCDs known as the Ring of Fire, located along a convergent tectonic plate boundary subduction zone. While their similarities are compelling, including their water and sulfur-rich composition and high oxidation state, one telling difference is that while anhydrite has been shown to be a primary igneous mineral that formed from the crystallizing magma erupted to form volcanic ash, in contrast, in porphyries anhydrite precipitates from early high-temperature hydrothermal solutions. Given these similarities and differences, it is possible then that mega-strata volcanic eruptions with primary igneous anhydrite represent the sudden interruption of porphyry copper deposit development. Rather than develop a subsurface mineralized hydrothermal convective cell driven by the heat dissipation of the cooling porphyritic magma, the evolving magma body and the rigid carapace above the magma chamber failed, exploded, and erupted violently onto the earth's surface and into the stratosphere. This study then explores what role hydrogen gas may have played in both cases; one hidden from human view in space and time and the other, in contrast, leaving a vivid, lived memory of a globally cataclysmic event on the earth's surface. This comparison of an intact subsurface ore deposit potentially contributing vital metals to a technologically greener future versus its dissipation in a giant stratovolcano may provide a useful image for advancing public understanding of the immense physical scale of ore genesis and the unprecedented

societal choices at stake. Social understanding of mineral resources and the necessity of mining in general is necessary now when critical and essential minerals, including copper, must be discovered to meet the accelerating industrial demands of decarbonization. Only though broad acceptance of this need based in some level of scientific understanding will a social license for mining be earned—at least within the United States.

Potential Impact of this Work

Explaining the origin and characteristics of a porphyry copper deposit is difficult at best, even to professional geologists who are not specialists in mining geology or geochemistry. While a lay person may know about the Ring of Fire, volcanoes, and earthquakes related to subduction zones at convergent tectonic plate margins, few have any reference frame for appreciating a description of porphyry ore deposits in terms of their size, crustal depth, multi-stage processes involving both magmas and aqueous fluids, the enormous energy involved, and singular importance as mineral resources of copper and a host of related chemical elements, including sulfur. Without a meaningful reference frame, conveying the origin and importance of porphyry systems to the public can seem impossible. Furthermore, most outcropping PCDs have already been discovered and are being mined; the genetic paradigm is out of date. The pre-mine surface of known PCDs intersected the cylindrical ore-forming column somewhere near its high-sulfide midsection. Today, these outcropping systems are exceedingly rare and what is left are exposures of the low sulfide tops of much deeper PCDs, which may well have an atypical surficial presentation lacking abundant stockworks and a leached capping. In fact, much less is known about the upper reaches of deep PCD systems, requiring that a major revision be made of the prevailing exploration model (Brimhall, 2018. 2021; Brimhall and Fanning, 2019). The aspects of a new PCD exploration model that could be most impactful are those that can be recognized during early stage exploration when a potentially large system could help motivate funding for deep drilling—an imperative that has long been recognized in Montana (Worthington, 2007). Since the zoning patterns of PCDs are concentric, the outermost shells then are likely to be encountered first. Therefore, correct interpretations of these outer hydrothermal rings could be disproportionally important.

Context

The thermochemical research described here involving hydrogen stems from ongoing field-based studies and copper exploration in southwest Montana. First, advancement of the porphyry copper paradigm used in exploration based on detailed geological mapping at the Clementine prospect (Brimhall, 2018, 2021) showed that distal actinolite (Fe–tremolite) alteration with orbicules 1 to 2 cm in diameter forms a ring that surrounds the central vein gossan system and has also been noted at Bingham Canyon, Utah, where it was first recognized (Atkinson and Einaudi, 1978) in drill core. Actinolite orbs have also been noted at seven additional major porphyry copper deposits worldwide, including Escondida, Morenci, and Oyu Tolgoi (Marco Einaudi, written commun.). Hence, a key objective here is to determine if an actinolite orb ring that formed by radial diffusive processes might surround only large, well-mineralized porphyries and hence provide a useful indicator of highly prospective systems in contrast to smaller, less economic occurrences.

How the Presence of H_2 Gas in Porphyries Was Recognized

In the process of advancing the porphyry copper model to include sedimentary wall-rock interactions, Brimhall (2021) developed an isothermal–isobaric phase diagram using log $f CO_2/CH_4$ vs log $f H_2S$ coordinates presented in figure 1 computed for 300°C and 500 bars (50 MPa). Along the righthand side the redox state is shown using the conventional variable log fO_2 computed from the equilibria: $CH_4 + 2O_2 = CO_2 + 2H_2O$, and setting the value of the activity of H_2O at 1.0. In the process of seeking a still more realistic measure of redox state than log fO_2 which has miniscule values, log fH_2 values were computed from the equilibria: $2H_2O = 2H_2 + O_2$. These values are labeled in red just left of the logfO_2 values and are indeed much higher than the log fO_2 values. Notice also that near the bottom of figure 1, where the log fH_2 values are 0 to +1, a number of reduced organic gases also occur, including CH_4, n-decane, n-hexane, and kerogen. Just above these organic gases orbicular actinolite alteration at both Bingham and Clementine occur along the outer edge of the actinolite stability field shown in green, with co-exiting titanite and either magnetite or ilmenite within the biotite stability field shown in purple. Graphite becomes stable at logf_{H2}, just below the values where the orbicular alteration plots.

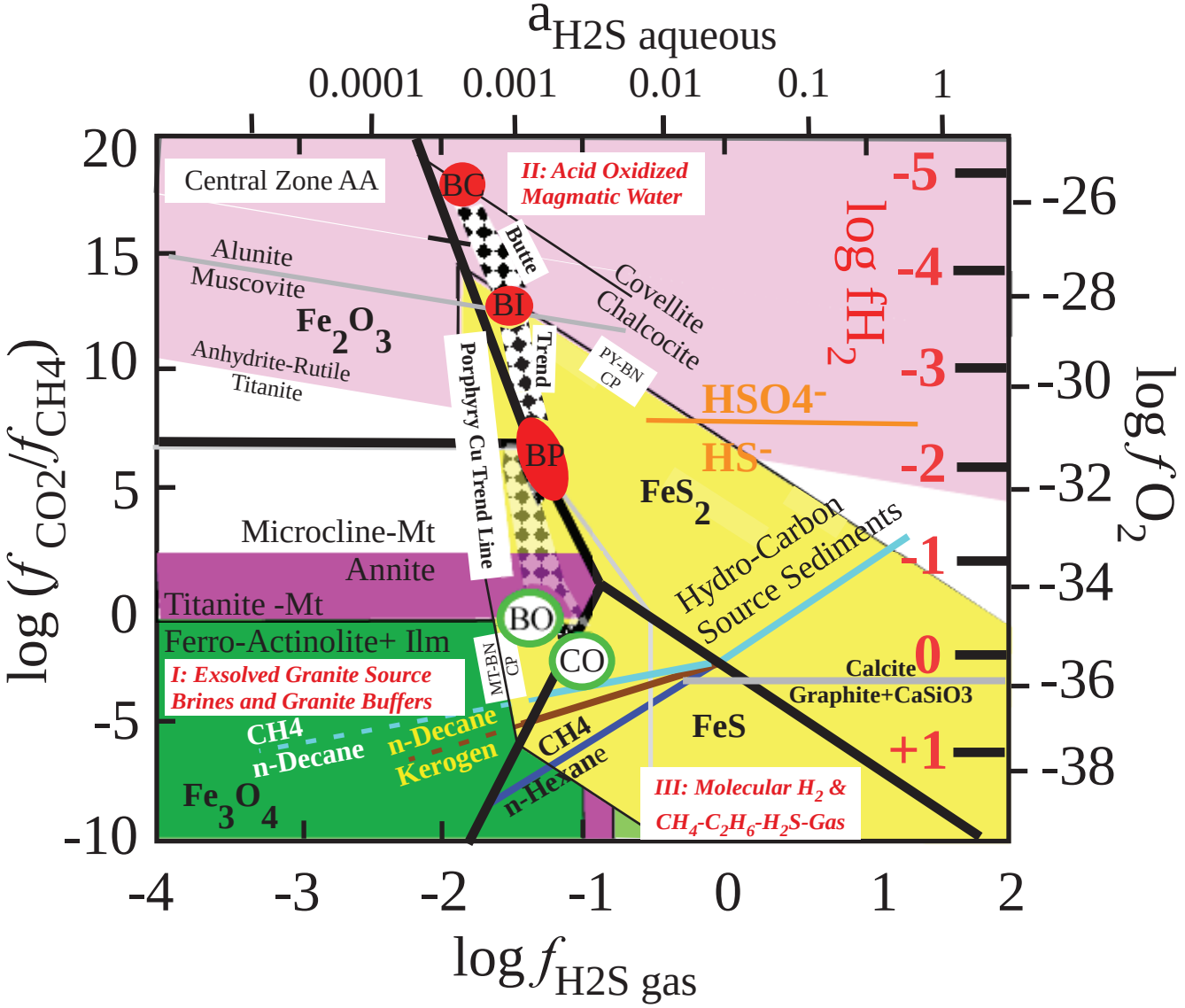

Figure 1. Isobaric (500 bars, 50 MPa) isothermal plot. On the righthand vertical axis logfO_2 is shown in black and corresponding logfH_2 in red, which are far higher values signifying the actual presence of H_2 gas. Color patterns are as follows: dark green represents actinolite (Fe–tremolite); purple represents biotite. Near the top of the figure are oxidizing conditions while the bottom reflects reducing conditions. Pink represents anhydrite. Hydrocarbon source sediments are represented by a brown line (Kerogen/n-Decane), light blue line methane/n-Decane, and dark blue represents methane/n-Hexane equilibria. Porphyry copper deposits shown in stipples define a nearly vertical band in which the Butte pre-Main Stage (BP), Intermediate Zone (BI), and Central Zone (BC) with covellite–chalcocite and advanced argillic alteration (AA) and alunite occur forming the Butte Trend Line shown as a diamond checkerboard pattern. Orbicular actinolite alteration at the Bingham porphyry copper Mine in Utah (BO) and the Clementine Prospect in Montana (CO) are shown as circles with a green rim and fall on the stippled porphyry Copper Trend Line.

Source of the Hydrogen

Unlike oxygen gas, which was absent, hydrogen in contrast was present as a gas phase with a minute molecular size of 0.27 nm, making its diffusion through some of the most permeable surrounding rocks highly likely. A question as to the source of the hydrogen then arises. Two possibilities exist. First, hydrogen may have been derived locally from organics in the surrounding sedimentary wall rock sequence, implied by the stability of methane, kerogen, n-decane, and n-hexane shown in figure 1. However, the fact that the matrix rock between orbicular actinolite orbs has disseminated chalcopyrite, pyrrhotite, and ilmenite, which are absent outside the orb ring, implies that the source of H_2 was from fluids related somehow to the center of the district alteration zonation, vein gossan system, and plutons (Brimhall 2018, 2020, 2021). The source of the fluid in the orbs is in fact proven to be from inside the orb ring and emanating from the center of the district by three facts: (1) the U/Pb SHRIMP date on titanite in the orbs of 70.7 ± 1.3 million yr is within analytical uncertainty of the age of a small altered pluton with titanite age of 72.7 ± 1 Ma (Brimhall and Fanning, 2019). (2) Multi-element geochemistry shows that the enrichment factor hierarchy of

Te> Se> Bi> As> Sb> Ag> Mo> W> Cu> Pb> Zn is the same for the orbs as it is for the vein gossans located at the center of the district, positioned at the apex of a doubly plunging anticline (fig. 2). Finally, orbicular alteration postdates and alters all the lithologies shown in figure 2, proving that orb alteration is epigenetic.

Retrospective Study of Ore-Forming Mineral Assemblages

Rocks in ore deposits are among the most mineralogically complex rocks known on earth. Ores are formed by heat and mass transport processes that, while being part of the array of normal earth processes operative at vastly different scales from plate tectonics down to submicroscopic fluid inclusions, reach extreme enrichment levels rarely attained in nature (Brimhall, 1987). Today, then, we study ores formed millions of years ago *ex post facto*. The causative hydrothermal fluids are now long gone except for microscopic fluid inclusions in quartz and other minerals. Were gases present, they too are largely gone except for their occasional presence in fluid inclusions. If hydrogen is trapped within fluid inclusions, it may have at least partially diffused through minerals selectively and even diffused out of the fluid inclusions altogether. All *post facto* interpretations made today of the geochemistry of ore-forming fluids and gases are based on observations at different scales, including mapped field relationships; observed mineral assemblages and sequences; structures including veins, veinlets, alteration envelopes, alteration zonation, and miarolitic cavities; and fluid inclusion studies. Once the mineral assemblages and their temporal and spatial sequence are known and the physical conditions determined by geothermometry and geobarometry, then chemical thermodynamic calculations provide equilibrium phase diagrams in a coordinate space where each mineral assemblage can be located and used as a signpost to constrain and ultimately reconstruct the geochemical paths taken in nature. Theoretical fluid mechanics provides a second powerful tool to validate conclusions.

Methods for Computing Chemical Phase Equilibria and Thermodynamic Databases

A wealth of interdisciplinary knowledge supports the current understanding of porphyry copper deposit genesis and the mineral-solution equilibria involved. A variety of methods have been employed, including hydrothermal experiment, hydrofluoric acid solution calorimetry, and heat capacity measurements. Studies span biotite (Eugster and Wones, 1962,; Wones and Eugster, 1965), alkali feldspar (Meyer and Hemley, 1967; Thompson and Waldbaum, 1967, 1968), and magnetite (Chou and Eugster, 1977; Eugster and Chou, 1979). This work heralded the birth of experimental geochemistry at Johns Hopkins, UC Berkeley, Harvard, Princeton, and Penn State, among other universities, as well as the Geophysical Lab of the Carnegie Institute, the Geochemistry and Petrology Branch of the USGS, and the U.S. Bureau of Mines program on theoretical metallurgy (Kelly, 1960). Emerging from this voluminous research was an internally consistent thermodynamic database of Gibbs Free energy, Enthalpy, Volume, Entropy, and Heat Capacity functions summarized by the Helgeson Group at UC Berkeley in SUPCRT92 (Johnson and others, 1992) and made accessible for online computing using the program CHNOSZ (Dick, 2019), which runs on the "R" online platform open to all users free of charge. Theoretical thermodynamic calculations herein are made possible by this complex internally consistent database and extensive use of CHNOSZ.

log fO_2 versus log fS_2 Diagrams

Among the first thermodynamic calculations of mineral-solution equilibria, Holland (1959), Meyer and Hemley (1967), Einaudi (1977), Brimhall (1980), and many others devised plots of log $f\mathrm{O}_2$ versus log $f\mathrm{S}_2$ to help explain reaction paths of ore-forming solutions defined by sulfide, oxide, and silicate mineral assemblages and sequences. Hydrogen gas as such was not explored in these studies. Although experiments by Eugster and Wones used nested gold capsules to avoid hydrogen embrittlement of their steel pressure vessels, which surrounded inner capsules of platinum to control $f\mathrm{O}_2$ in experiments on granite mineral-solution equilibria, H_2 was considered as a challenging experimental factor to be controlled in order to define O_2 fugacity rather than as a prime geological variable of interest as it has become in this study.

Oxidation-Reduction Reactions involving H_2 Gas

Two different methods are discussed below that address the phase equilibria of H_2 gas and its geochemistry differently; one method lumps H_2 and $\mathrm{H}_2\mathrm{O}$ together as a combined function so that they are inseparable, and the second method focuses on H_2 by itself by assuming that the $a\mathrm{H}_2\mathrm{O}$ was unity.

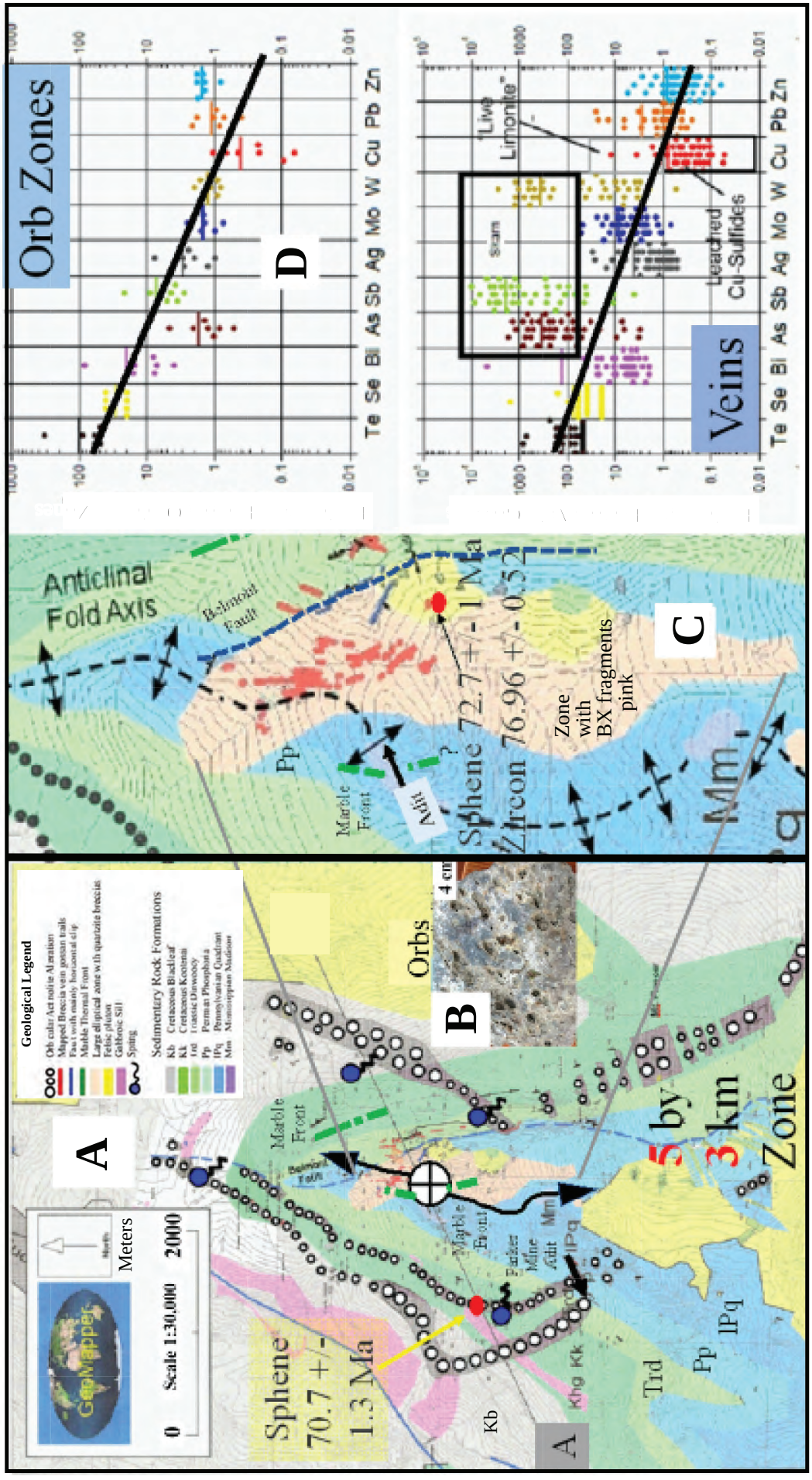

Figure 2. (A) Geological map of the Clementine prospect in southwest Montana, located between the southwest edge of the Boulder Batholith, shown in yellow, and the most northerly pluton of the Pioneer Mountains, the Big Hole River pluton, also in yellow. Springs are shown as blue dots with squiggly black tails and occur within or near orb zones. (B) Photograph of orbicular actinolite alteration shown in A with a stippled pattern. Rocks between the orbs have disseminated chalcopyrite, pyrrhotite, and ilmenite. (C) Enlargement of the map shown in A centered on the large elliptical zone containing barren quartz-rich breccias shown in pink, which is 2.2 km long. This breccia zone is centered on a doubly plunging anticline co-axial with the surrounding actinolite orbicular rings and central zone containing a breccia vein gossan trail system shown in red, with two small plutons in yellow just east of horizontal bedding symbol. The marble front is shown in a thick green line on the east side of the anticline and a green line on the west side where it has been approximately located. It is important to note that the orbicular actinolite bands occur outside of the marble front, implying a lower temperature, yet actinolite growth is related to the early high-temperature Potassic alteration expected at the deposit interior. SHRIMP dates on titanite in the orbs are shown. (D) Enrichment factors for the vein gossan systems below the enrichment factors for the actinolite orbs. Notice that both have the same hierarchy of Te>Se>Bi>As>Sb>Ag>Mo>W>Cu>Pb>Zn. Veins closest to outcropping limestones show the effect of skarns enriched in As, Sb, and W, with individual assays reaching over 2,000 ppm. Cu is leached but in samples with hematic limonite instead of goethite; Cu assays reach 800 ppm. All chemical analyses have been done by ALS Global in Sparks, Nevada using a four-acid rock pulp digestion and ICP-MS analysis for all elements. Crustal abundances used in computing the enrichment factors are from pTable.com

Hydrogen Ratio R_H

Giggenbach (1987) proposed a redox variable called $R_H = \log (fH_2/fH_2O)$ as an alternative expression to $\log fO_2$, asserting that it offered an estimate of the abundance of an actual reaction participant as the fugacities of O_2 in contrast are so low that they indicate essentially no presence of oxygen gas as such. This insightful approach was summarized later by Hedenquist in Einaudi and others (2003). R_H does have the advantage of not having to know the activity or fugacity of H_2O to address H_2 indirectly, but this approach leaves open the question as to the actual value of H_2 fugacity, which is the objective in this work. In the limit when the activity of H_2O equals a value of 1, then $R_H = \log fH_2$, otherwise R_H is a unitless ratio that in some ways is hard to interpret. To the extent that solutes lower the activity of H_2O in solution, R_H may overestimate the actual $\log fH_2$. Hence, a different approach is taken here that develops an explicit value of $\log fH_2$ consistent with the fact that hydrothermal solutions are intrinsically aqueous.

Results

Here, rather than use the R_H, which is rigorous but makes it difficult to separate and extract values of fH_2, it was decided to directly calculate fH_2 by assuming that the aH_2O was 1. While the results are approximate, they may well be sufficiently accurate to form new useful conclusions.

Direct Discernment of Convective Cooling and Heating Paths

Interpreting complex multistage processes demands selection of a definitive analytical coordinate space that faithfully divulges nature's rules. Figures 3A through 3F present the systematic development of a new phase diagram in which $\log fH_2$ is the variable of interest rather than fO_2. The vertical axis is $\log fH_2$ and the horizontal axis is 1/T K absolute temperature relative to absolute zero, with corresponding temperature in degrees Centigrade shown across the top of the diagram. Such a modified Van't Hoff plot showing $\log fH_2$ rather than log K has several powerful advantages useful in geological interpretations. First, in Van't Hoff coordinates many equilibria plot as relatively straight lines with slopes proportional to the value of enthalpy of the reaction and the y-intercept is proportional to entropy (Lewis and Randall, 1961). Second, depending upon the direction of temperature change, some lines represent cooling paths as hot magma-derived fluids undergo cooling toward the left. Similarly, other mineral-solution equilibria represent convective heating paths as temperature increases toward the right approaching a pluton. Assembly of this collection of lines, which are vectors pointing either to the left for cooling or to the right for heating, identifies mineral assemblages in terms of their fluid flow direction. This graphical interpretation in a Van't Hoff plot yields cooling and heating paths directly and thus offers a viable, straightforward alternative to far more complex calculations involved in parametric numerical modeling. Earlier work using Van't Hoff coordinates by Hedenquist (Einaudi and others, 2003) was focused on defining the evolutionary pathways of multistage ore deposits and redox state of magmas, especially demonstrating the continuity of fumaroles and magmatic-hydrothermal fluids using R_H calculated using Program QUILF (Andersen and others, 1993) in relation to geothermal fluids in shallow systems. In contrast, the use of Van't Hoff plots here is fundamentally different. Here, specific recurrent hydrothermal alteration and mineralization mineral assemblages including well-known variable biotite solid solution compositions are studied to ascertain the architecture of deeper convective magmatic–hydrothermal regimes and the role of wall rock buffering. In particular, proximal upflow heating paths and distal downflow cooling and finally heating return paths are revealed.

The stoichiometry of all the chemical reactions described below that involve H_2 gas as a key geochemical variable are determined by computing balanced oxidation and reduction equilibria of iron and hydrogen; sulfide (S^{2-}) and oxidized sulfate states (S^{6+}) and (S^{4+}); carbon dioxide (C^{4+}); and graphite (C^0). For consistency, all reactions are written so as to be exothermic; that is, to have a negative Δ Enthalpy of reaction. In figure 3A the equilibria of hematite (Fe_2O_3) and magnetite ($FeO \bullet Fe_2O_3$) shown by the line 1 provides a useful example in equation 1.

$$3Fe_2O_3 + H_2\,gas \leftrightarrow 2Fe_3O_4 + H_2O. \qquad \text{(eq. 1)}$$

First, the number of moles of iron is balanced with a total of six on both sides. In terms of the valences of iron, the lefthand side of the reaction has a total of 6 ferric ions, while the righthand side has two ferrous ions and four ferric ions, since magnetite contains iron in both valence states and can be expressed as

$FeO*Fe_2O_3$. The overall or net ionic changes are $2Fe^{3+}$ of the $3Fe^{3+}$ in hematite being reduced to $2Fe^{2+}$ in magnetite. This oxidation is balanced by one H_2 or two H molecules becoming oxidized to $2H^+$ in water.

In terms of electron conservation, the hematite–magnetite reaction is the sum of two half-cell equilibria:

$$2Fe^{3+} + 2e^- \leftrightarrow 2Fe^{2+} \quad \text{(eq. 2)}$$

$$H_2 \leftrightarrow 2H^+ + 2e^- \quad \text{(eq. 3)}$$

The equilibrium constant is given in equation 4.

$$K_{HM\text{-}MT} = a\,H_2O / fH_2 \text{gas or } \log K_{HM\text{-}MT} = \log aH_2O - \log fH_2 \quad \text{(eq. 4)}$$

By setting the aH_2O to 1, then $\log aH_2O$ becomes 0, and $\log fH_2$ is equal to $-\log K_{HM\text{-}MT}$.

H_2 Fugacity as the Principal Geochemical Variable Assuming the Activity of H_2O Equals One in Hydrothermal Fluids

Here, rather than compute R_H, an explicit expression is calculated that yields an expression of hydrogen fugacity by assuming that the *activity* of water is 1. Rather than use R_H here, we set the activity of water to unity in all the calculations of hydrothermal equilibria that follow. While this is clearly is an assumption, it is evident from the presence of ubiquitous fluid inclusions in vein quartz and other minerals that porphyry copper hydrothermal systems are wet and water-saturated. Within the constraints of the assumption that the activity of H_2O equaled 1, then setting $aH_20 = 1$ reduces the number of variables, thus making it possible to calculate the log fH_2 as the principal variable of interest within the water-rich compositions. While the values of log fH_2 calculated in this fashion are approximate, they are sufficiently accurate to reveal the essential topology of the phase equilibria involved. It is unlikely that the activities of water in nature vary enough from a value of 1 that the essential topology of figures 3A through 3F would be dramatically different.

Redox Buffer Assemblages

Figure 3A shows four of the major redox buffer equilibria commonly used in geochemistry and petrology as lines 1, 2, 3, and 4. Of these the fayalite–magnetite–quartz line 3 (FMQ) is fundamental to characterizing the variation in redox states of certain magmatic systems, including parental magmas for porphyry copper deposits and tectonic arc magmas as well. Together all these equilibria span six orders of magnitude of log fugacity H_2. What is different from the values shown here, extending from -4 to +2, is that these values are far higher than the log fO_2 values commonly used in petrology, which range from -11 to -30 (Eugster and Wones, 1962). Hydrogen gas is an actual gas phase present while oxygen is not. The fact that H_2 is present is evident on the right of figure 3A on the axis where the values of fH_2 are labeled in bars. Of the 500 bars total confining pressure, up to 100 bars are due to the presence of hydrogen, proving that H_2 represents up to one-fifth of the total pressure, especially in the lower parts of figure 3A, which is the reducing end of the spectrum. In contrast, the top of figure 3A is the oxidizing end.

Effect of Water Activity Less than Unity on the Equilibrium Lines Plotted

Notice that the equilibria for lines 1, 2, 3, and 4 all involve water (H_2O). The thermodynamic calculations shown here and throughout the rest of this paper set the aH_2O to 1.0. By stipulating that the aH_2O is 1.0, fH_2 can be computed, as one algebraic unknown has been eliminated from the equilibrium constant expression. The impact of water activities departing from 1.0 are contoured in figure 3A for the hematite–magnetite

Figure 3 (opposite page). (A) Isobaric (500 bars, 50 MPa) polythermal Van't Hoff plot with horizontal axis 1/T K absolute temperature relative to absolute zero with corresponding temperature in degrees Centigrade shown across the top of the diagram. Vertical Y-axis is log fugacity H2(gas) rather than log K in standard Van't Hoff plots. This figure shows the stepwise construction of this new phase diagram. (A) Four conventional redox buffers are plotted in terms of log*f*H2. (B) The redox space is subdivided into two distinct parts: an upper oxidizing region colored pin,k where anhydrite occurs, and a lower reduced region colored brown where titanite occurs. The boundary is near the transition from reduced sulfur in the form of HS- to oxidized sulfur occurring as HSO4-. (C) Shows a spectrum of well-known magma types with increasing oxidation state from MORBs, to arc magmas, to ore-forming porphyritic magmas and primary anhydrite-bearing strata volcano volcanics, including Pinatubo, which plot inside the blue box that represents magmatically derived water, which becomes the ore-forming hydrothermal fluids. (D) Shows the distinct types of biotite that become progressively more magnesian (less iron-rich) with increased oxidation. Miarolitic cavities are shown diagrammatically as a group of small circles along line 17. While these represent localized saturation with magmatic water, they do not indicate escape of that water as a free ore-form-

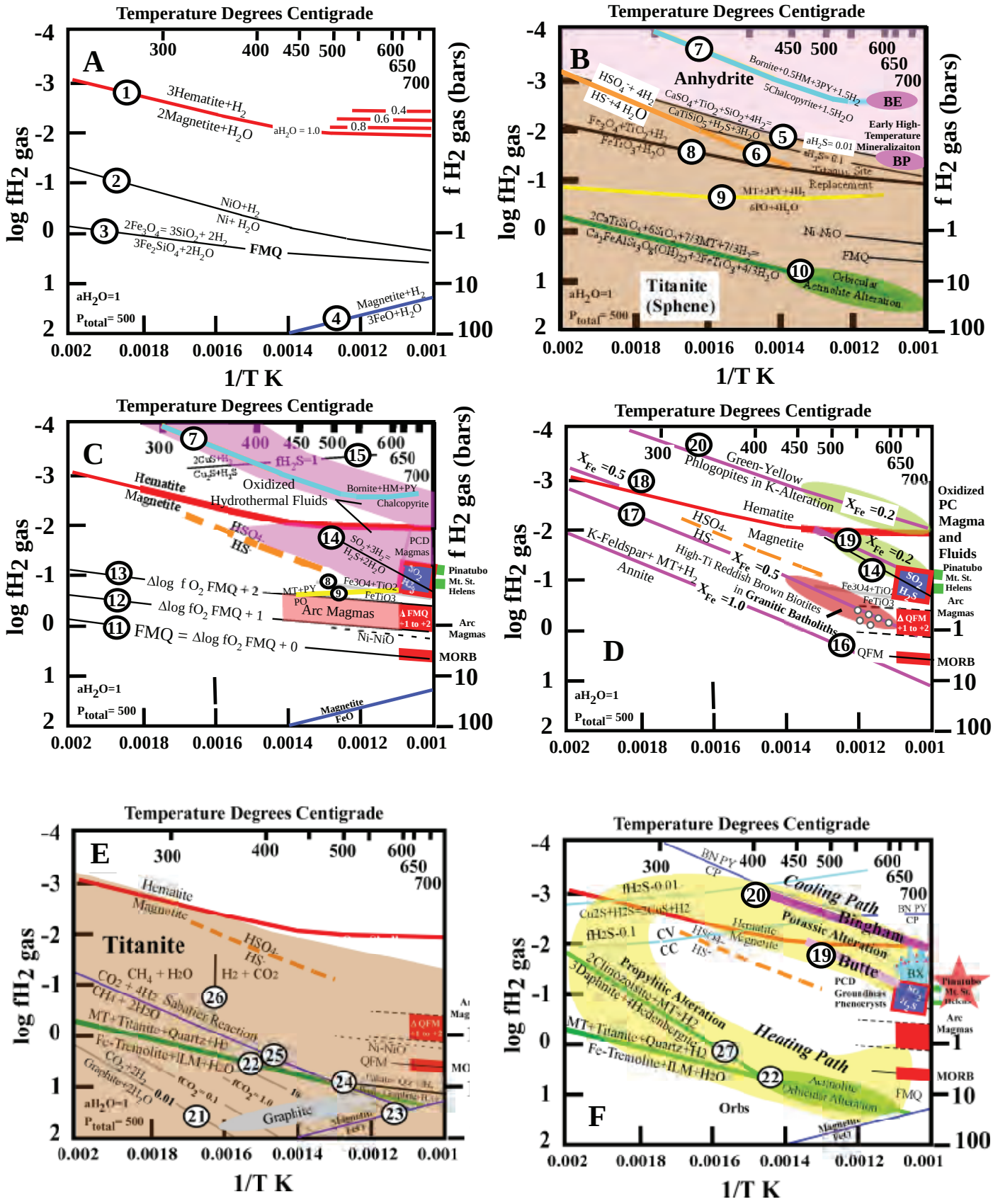

ing phase. (E) Shows as a green line the distal orbicular actinolite–titanite alteration discovered at Bingham, Utah and mapped at the Clementine prospect in Montana in relation to even more reduced mineral assemblages with graphite as at the Ruby graphite deposit in Montana. The thermodynamic properties of Fe–tremolite are used for actinolite as both are Fe-rich amphiboles, as none are available in the SUPCRT database for actinolite. (F) Shows the full repeating convective cycle of fluids in yellow starting with outgassed fluids from a porphyry magma through 3 stages: (1) magmatic H2 release by oxidative dehydrogenation, (2) sulfide mineralization during cooling once fluids leave the thermal influence of the crystallizing magma and densify, (3) heating as the return flow fluids approach the pluton and become buoyant, and finally (4) distal propylitic alteration occurs with actinolite forming.

equilibria line 1. Lines for water activities of 0.8, 0.6, and 0.4 are shown. The effect of water activities departing from a value of 1.0 on the other reactions in this study are of identical magnitude since the stoichiometric coefficients of H_2 and H_2O are the same but of opposite sign with two exceptions. First, in a few reactions in later sections that involve H_2S as a variable besides H_2 and H_2O, departure of the computed lines may vary differently depending on the magnitudes of the stoichiometric coefficients of H_2, H_2O, and H_2S. Second, and far more importantly, all reactions with biotite contain hydrogen, so that H_2O does not appear in the equilibria. Hence, the lines drawn for reactions with biotite (figs. 3C, 3D) do not vary with H_2O activity. Given the fact that hydrothermal fluids are mostly water, the deviations from unity in nature should be well within the width of this band even for brines with large total dissolved solids (TDS). Furthermore, the lines shown will deviate in the same direction so that the lines shown all move together. Therefore, the departure of aH_2O from unity should not change the general topology of the phase diagram calculated in this study as shown in figures 3A through 3F.

Sources of the Mineral-Solution-Gas Equilibria Used

Lines 1, 2, 3, 4, and 16 all involve equilibria containing H_2 investigated earlier by Eugster and Wones (1962) where hydrogen gas was used to (1) control and buffer the desired oxygen fugacity inside platinum capsules where the experimental charge was located and (2) eliminate hydrogen embrittlement of the steel high-pressure vessel by encapsulating the platinum capsule within a gold capsule through which H_2 diffusion was impossible. This innovative nested capsule method of Eugster and Wones was focused on determination of the compositional variation of biotite solid solutions under different oxygen fugacities, as log fO_2 was considered the primary measure of redox in rocks and has been widely used ever since. Here the focus has changed from log fO_2 to log fH_2. Lines 5 through 28, with the one exception of line 16, are all developed for this study with a focus on H_2 as the primary variable of scientific interest rather than a necessary experimental parameter to control O_2 and protect equipment, as in the Eugster and Wones study (1962).

While earlier investigators could have chosen to use H_2 rather O_2 to express redox states, there are three reasons why this was not the case and why the preference for O_2 has persisted for 60 yr. First, log fO_2 has long been the choice of geochemists to express redox state in ore deposits (Holland, 1959; Meyer and Hemley, 1967). Second, the ease of use of the Buddington and Lindsey (1964) geothermometer provides both temperature and calculated equilibrium O_2 fugacity independent of having to know the activity of water. Petrologists have retained this convention focusing on log fO_2 since no assumption about the activity of water is necessary to derive a value for log fO_2. Third, use of O_2 to express redox states, although recognized as rarely being physically present petrologically, has become a convention.

Sulfide Mineralization and Related Alteration Reactions: Magmatic Water Redox State

Figure 3B adds sulfur to the system, and line 5 represents anhydrite–rutile–quartz–titanite (sphene) assemblage, which subdivides the entire space into the upper pink oxidizing region where anhydrite is present, and the lower reducing region (brown) where titanite is present. The boundary between the anhydrite and titanite domains in this figure is closely related to line 6, representing the iso-fugacity line of HS^- and HSO_4^- separating sulfur in reduced form (-2) below the line and oxidized value (+6) above the line. This sulfide to sulfate line is also discernible in rare cases in volcanic rocks that have primary igneous anhydrite, which is central to the arguments made herein (fig. 3C, labeled Pinatubo in green).

The temperature range of early high-temperature sulfide mineralization in porphyry copper deposits is known from fluid inclusion homogenization upon heating using a heating–freezing microscope stage and from a variety of mineral geothermometers. The pre-Main Stage at Butte formed between 550° and 650° C. (Brimhall, 1973, 1977; Roberts, 1973). Line 7 is the equilibria of copper ore minerals chalcopyrite and bornite—another major recognizable feature in ore deposits. Point “BP” represents the early high-temperature sulfide mineral assemblage at Butte, Montana, which lacks bornite but has a chalcopyrite–pyrite–magnetite–hematite assemblage (Brimhall, 1977) and is responsible for widespread biotitization of hornblende (Brimall and others, 1985). Point “BE” represents the early high-temperature sulfide mineral assemblage at Bingham, Utah, where bornite is included in the early sulfide high-temperature ore mineral assemblage (Einaudi and others, 2003).

Anhydrite and titanite have a central importance in interpreting early high-temperature hydrothermal processes and constraining the composition of fluids from which sulfides formed. Anhydrite represents oxidized fluids with sulfur in its highest valence +6 state and is ubiquitous in early high-temperature sulfide ores. Titanite is present in many igneous rocks as a common accessory mineral and can be radiometrically dated using U/Pb methods. It has in addition two more important features. Titanite has also been shown to form as a hydrothermal mineral within distal actinolite orbicular alteration (Brimhall, 2018, 2021; Brimhall and Fanning, 2019) and can be radiometrically dated, thus providing two possible age dates: one for magmatic crystallization and another for related hydrothermal activity. Finally, when primary titanite in an igneous rock becomes altered under early stage hydrothermal processes, the titanium combines with iron to form complex secondary mineral assemblages that can be used to constrain the chemical composition of the fluid precisely, as shown by line 8 representing the titanite site replacement equilibria with magnetite, rutile, and ilmenite (Roberts, 1973, 1975). Notice the proximity of line 8 to line 6 for the HS^-/HSO_4^-boundary. Line 9 represents the pyrite–magnetite–pyrrhotite boundary. Below this line, pyrrhotite is present rather than pyrite. In contrast, the orbicular actinolite assemblage shown by line 10 contains pyrrhotite, chalcopyrite, and ilmenite formed under very reducing conditions with a high fugacity of H_2.

fO_2 Redox Buffers, Arc Magma Reference Frame, and Oxidized Ore-Forming Fluids

In order to ease the transition from using fO_2 to fH_2, the common petrological redox buffer quartz–fayalite–magnetite (QFM) is recalculated in terms of H_2 assuming the $aH_2O = 1$ (shown in fig. 3C). QFM is shown as line 11 and Ni-NiO is dashed. Hematite–magnetite is shown as a heavy solid red line. Several key magma types of importance in igneous petrology and ore genesis are shown in order to anchor this new figure with respect to a broad understanding of magma genesis in relation to plate tectonic regimes where porphyry copper deposits form, often nearby to arc-related strata-volcanoes. This association is at the heart of the "Systems" approach to exploration, which includes the full chain of metal enrichment processes involved from source to final ore deposit. The start of this chain is metallogenic fertility of the region where magmas form by partial melting within the mantle wedge above subduction zones. Line 11 represents FMQ ($\Delta \log fO_2 = 0$). On the righthand side of figure 3C is a small red box labeled MORB (mid-ocean ridge basalt) formed at spreading centers in ocean basins. In comparison, on continental margins where subduction occurs, these sea floor slabs move away from the spreading ridges where MORBs form and descend into the mantle, including the MORB basalts and the entire sedimentary sequence deposited over time on top of them. Oxidation of downgoing slab complex (MORB slabs and overlying sediments) occurs by several mechanisms. Metamorphic devolatilization of (H_2O, H_2, CH_4, and H_2S) from subducted slabs and their sedimentary cover rocks generates aqueous fluids that ascend upwards into the mantle wedge, inducing the partial melting that produces arc magmas by lowering the melting temperature. These volcanic arc magmas have oxygen fugacities some 10 to 1,000 times higher than magmas generated at mid-ocean ridges since oxidized sedimentary rocks are subducted along with the MORBs (Ague and others, 2022) and slab-derived devolatilization fluids are oxidized by subducted metasedimentary rocks. Another cause of oxidation (Bruce Marsh, written commun.) takes place in the oceanic crust as it moves away from the ridge axis and is highly altered by ongoing hydrothermal convection with sea water that is sulfate-rich—changing the initial $^{87}Sr/^{86}Sr$ ratio from 0.7025 at the ridge to 0.7035 or more by the time it becomes subducted. Arc magmas may come directly from this altered oceanic crust.

These subduction-related "arc" magmas, which are the parental plutons for porphyry copper deposits (Richards, 2015), are generally described as having a redox value of delta log fO_2 of +1 to +2 relative to the FMQ buffer. Lines 12 and 13 show these delta logfO_2 values re-calculated into logfH_2 values defining a pink box labeled "arc magmas." While such magmas have crystalized by 700°C, this box is bounded by the extrapolated mineral equilibria lines involved. Line 14 represents the iso-fugacity boundary of H_2S and SO_2. Notice a small blue box outlined by red-labeled SO_2/H_2S located immediately above line 8 for the titanite replacement assemblage (magnetite–rutile–ilmenite) of Roberts (1973). This box is interpreted here to represent the composition of ore-forming magmas and their exsolved magmatic water, which have been oxidized relative to arc magmas by continued hydrogen outgassing to the extreme levels required for ore genesis. Notice that this box plots near the anhydrite/titanite boundary and within the anhydrite stability

field and is positioned right above the magnetite–rutile–ilmenite line 8. This fluid composition is critically important as it is the starting point for early high-temperature mineralization and alteration in porphyry copper deposits.

The upwards oxidative sequence of the red boxes on the righthand edge of figure 3C is key to understanding the origin of highly evolved ore-forming magmas, which starts with MORB basalts, their subduction and oxidation, partial melting of hanging wall mantle—which creates oxidized arc magmas and their continued oxidation to form ore-forming magmas—all with continued hydrogen outgassing called oxidative dehydrogenation.

Since this blue box outlined in red is a key composition of hydrothermal fluids exsolved from ore-forming magmas in porphyry copper genesis, its hydrogen fugacity is important to understand. Notice that the log fH_2 value is -1.0, which implies an H_2 partial pressure of about 0.1 bars out of a total pressure for this calculation of 500 bars. While this shows that H_2 is not a major component of the total confining pressure, H_2 is indeed an important minor component and is present as a gas, unlike O_2 with a fugacity of 10^{-29} at 700°C.

Role of H_2 Bubbles in Oxidation and Reduction

In addition to outgassing from magmas causing oxidation of the remaining melt, H_2, which has low solubility in water, becomes free to physically migrate *en masse*. Such migration is not by diffusion, but rather as tiny bubbles transported by advecting water escaping from magma once fluid saturation occurs. Transport of H_2 bubbles in the fluid phase occurs when the rate of fluid advection overcomes the buoyancy of the individual bubbles (Bruce Marsh, written commun.). This is the case with tiny bubbles. Figure 3C thus helps confirm and, more importantly, quantify the assertion that H_2 outgasses from magmas and causes their oxidation.

Certain dramatic volcanic eruptions in recent years help visualize this oxidation by H_2 diffusion and ore genesis in general, which is normally hidden at depth from human observation. On the righthand side of the blue box in figure 3C are two short, thick, green line segments representing the log fH_2 values computed for two major and now famous volcanic eruptions that contained anhydrite in their pumice: Mt. Pinatubo in the Philippines in 1991 and Mt. St. Helens in the U.S. in 1980. Anhydrite is actually not very common in volcanic eruptions, so the occurrence of anhydrite is viewed in igneous petrology as being very significant and is indicative of rare, highly oxidized, volatile-rich magmas. The published data for delta log fO_2 from Rutherford (1993) for both these eruptions have been recalculated here to logH_2 values as shown using the equilibria $H_2O = H_2 + ½\ O_2$, setting $aH_2O = 1.0$. Anhydrite occurring as a microphenocryst in volcanic rocks has been well-documented and interpreted in two seminal research studies published by Luhr (2008) and Luhr and others (1984). Both eruptions were responsible for the massive injection of oxidized (SO_2) sulfur into the stratosphere, which lingered for years, and may represent the composition of magmatic intrusives equivalent to supergiant porphyry copper deposits (Chiaradia and Caricchi, 2022). In that respect, porphyry magmas have, from a volcanological perspective, been referred to as “failed” megavolcanic eruptions by Chiaradia and Caricchi (2022) based upon Monte Carlo modeling of the role played by magma injection rates into the upper crust on the formation of porphyry copper deposits with different copper endowments. Their mass balance calculations suggest that supergiant porphyry copper deposits (>10 million tonnes copper) require magma volumes (up to >2500 km^3) and magma injection rates (>0.001 km^3/yr) typical of large volcanic eruptions from rift, hotspot, and subduction-related settings. However, not all supergiant volcanic eruptions are sulfate-rich. Yellowstone, for example, is not, but this fact may reflect its mantle hotspot origin. Because large volcanic eruptions would destroy magmatic-hydrothermal systems or prevent their formation, the largest porphyry copper deposits can be considered as failed large eruptions, and this may be one of the causes of their rarity. Both mega-eruptions and porphyry copper ore deposits are enormous, oxidized sulfur anomalies in the crust driven by comparably energetic magmatic and related hydrogeochemical systems. As figure 3C shows, they both have a similar highly oxidized character, well above normal Arc magmas. The volcanic systems erupt, explode, disperse, and dominate the earth’s atmosphere on a planetary scale while the porphyry copper magmas explode, hydro-fracture, and convect water at depth on a localized scale that concentrates metals to enrichment factors in excess of 100 times crustal abundances (Brimhall, 1987). For humans living on the earth’s surface, visualization of these anhydrite-bearing eruptions can help convey the massive power released in the subsurface when a por-

phyry copper deposit forms. In comparison, MORB lavas plot along line 11 and are far less oxidized and erupt slowly from cracks—as witnessed in Iceland today, usually without explosions, as the magma is less silica-rich, and hence far less viscous.

Possible Geochemical Basis for Rare Cataclysmic Megavolcanic Stratovolcano Eruptions Containing Anhydrite and Porphyry Copper Ore Deposits: Is Hydrogen the Missing Link?

On a comparative basis, the Mt. Pinatubo stratovolcano is the second-largest eruption of the 20th century. The ash plume height reached more than 40 km high and ejected more than 10 km^3 of magma, classifying it as an Ultra-Plinian eruption style. The world's largest eruption of the 20th century occurred in 1912 at Novarupta on the Alaska Peninsula, which is also part of the Pacific Ring of Fire where porphyry copper deposits form at depth. An estimated 15 km^3 of magma was explosively erupted equivalent to 230 yr of eruption at Kilauea (Hawaii) or about 30 times the volume erupted by Mt. St. Helens in Washington. What aspect of these unusually energetic geochemical systems makes them *both* so explosive? A speculative answer is proposed here—one that at least may explain why so much volcanic ash exploded and why hydrofracturing is so well developed in porphyry systems. With the previous focus on oxygen as the measure of redox state, no explanation is evident for these mega- eruptions in the published literature. However, here by translating the redox metric into a hydrogen frame of reference, a possible answer, or at least a new factor to consider, emerges. One unique aspect of hydrogen stems from its minute molecular size and well-known tendency to weaken structures in contact with it for forming hydrides or weakening mineral strength. It is suggested there is a possible chemical–mechanical effect of abundant hydrogen (Griggs, 1967). Hydrogen gas may have played a major role in the multistage fracturing characteristic of porphyry copper deposits and perhaps also in certain volcanic mega-eruptions. Conventionally, overpressured aqueous fluids are invoked to explain fracture development with release of magmatic water that expands and does pressure-volume work, causing brittle rock failure at depths where such expansion is accommodated. The accepted hypothesized mechanism is that the partial molal volume of water in the aqueous phase is far greater than within the silicate melt and causes the proposed expansion. Here a mechanism that may enhance this volumetric expansion is proposed when hydrogen is present, as shown in figure 3C, and thus may augment the explosiveness of porphyry melts. Hydrogen, as recognized herein, may dramatically enable the hydrofracturing process through hydrolytic weakening of quartz and other minerals (Griggs, 1967; Rovetta and others, 1989; and Strauch and others, 2023) or embrittlement so that the stress levels required to cause brittle failure induced by water expansion are dramatically lowered. Hydrolytic weakening and embrittlement of rocks by hydrogen could then significantly enlarge the volume of a hydrofractured rock mass, enhancing convective flow and related alteration and mineralization in porphyries and affecting rock fragmentation at depth necessary for volcanic eruption.

Biotite Mineral Chemistry and Redox

Stemming from the blue box in figure 3C are broad zones shown in pink that represent the composition of oxidized hydrothermal fluids in equilibrium with the oxidized magmas as they cool. Notice that the pink zones are displaced to the right along the hematite–magnetite boundary and follow the bornite–chalcopyrite line shown in blue line 7. At low values of H_2, this zone passes from the chalcocite field into that of covellite at line 15, typical of the advanced argillic assemblage at temperatures below 400°C.

Figure 3D shows the location of biotite-bearing granitic rock assemblages, which are well known as geochemical sensors of fluid composition (Brimhall and Crerar, 1987; John and others, 2010). Biotite equilibria are used to establish the purple zones in figure 3C. Since most hydrothermal biotite occurs in solid solution containing iron, magnesium, and other elements, we show these phases as their Fe-end member and then illustrate how incorporation of magnesium changes the phase relations using ideal site mixing in annite–phlogopite solid solutions (Brimhall and Crerar, 1987; Ague and Brimhall, 1987, 1988). Ideal site mixing provides a useful substitution where the activity of the annite $KFe_3AlSi_3O_{10}(OH)_2$ component in biotite solid solution equals X_{Fe}^3.

Line 16 is for pure ferrous Fe biotite annite in equilibrium with magnetite and K-feldspar denoted as $X_{Fe} = 1.0$. Line 17 represents the measured average biotite composition in granitic batholiths with a X_{Fe} of 0.5 (Ague and Brimhall, 1987, 1988a,b). These igneous biotite crystals are distinctly reddish brown under the petrographic microscope and have elevated TiO_2

contents up to 4.5 wt.%, responsible for the brownish color. Networks of tiny acicular rutile grains are often observed exsolved into the basal 001 plane of these micas, illustrating the intrinsic instability of such high-Ti biotite. A gray zone is shown surrounding line 17, representing the lowest oxidation state of typical granitic batholiths. These rocks then serve as regional-scale redox buffers as within the Butte Granite, thus keeping early high-temperature fluids from becoming more reduced and forming actinolite orbs.

Line 17 is displaced to the right to line 18, where it crosses the hematite–magnetite boundary. Lines 17 and 18 are typical of primary igneous biotite formed within thousands of plutons that occur within batholiths like the Sierra Nevada or the Boulder Batholith as part of the Pacific Ring of Fire formed along a convergent tectonic plate boundary. Saturation with magmatic water and fluid escape ,which quenches the melt, is very rare, yielding a porphyritic texture. In contrast, the norm is slow cooling, which causes an equigranular texture. Miarolitic cavities are shown diagrammatically in Figure 3D as a group of small circles on line 17. While these represent localized saturation with magmatic water, they do not coalesce, nor do they indicate escape of that water as a free ore-forming phase. Hence, in general, plutons with miarolitic cavities do not constitute ore-forming magmas, which instead yield magmatic water *en masse* once hydrofracturing initiates. In comparison, many hydrothermal biotite crystals formed from such ore-forming fluids are pale greenish to yellow in thin section and have far less titanium than igneous biotite. Hydrothermal biotite occurs along lines 19 and 20, labeled $X_{Fe} = 0.2$. Notice that these lines are also displaced to the right across the hematite–magnetite boundary.

Reduced H_2-Rich Mineral Assemblages: Orbicular Actinolite Alteration and Occurrences of Graphite

Figure 3E shows in brown the expanse of the titanite stability field formed under reducing, high fH_2 conditions, contrasting sharply with the stability field of anhydrite shown in pink in figure 3B. Line 21 shows the graphite–CO_2 boundary for an fCO_2 of 0.01. This line migrates to the right as the fCO_2 increases. Note that line 22 demarking the equilibria of the actinolite (calculated here using Fe–tremolite, its thermodynamic properties) orbicular alteration is in the vicinity of the graphite–CO_2 equilibria shown in gray when the fCO_2 has a value of 10 bars, which is similar to the fH_2 at a temperature of approximately 450° to 550°C. This association of graphite with actinolite calcite orbs was vividly borne out in the field when Neil Griffis of the USGS made a discerning discovery of graphite near the type section of actinolite orbs on Parker Creek (fig. 2). The Sabatier Reaction (line 25) predicts that at such elevated temperatures, CO_2 and H_2 would be the dominant species. The rock sample analyzed by ALS Global showed 13% total carbon using infrared spectroscopy (IR), and after HCl leaching, showed over 2% graphitic carbon remaining, detected by IR spectroscopy and confirmed by optical mineralogy in polished thin section.

This association of graphite with amphibole-bearing assemblages is also consistent with the fact that the Ruby Mine flake graphite deposits southeast of the Dillon (Bell, this volume) have amphibolite wall rocks nearby (James, 1990) as well as marbles. If the source of fluids that caused graphite to form came from magmas then figure 3E implies that the fluids were very reducing and had a very high fH_2, perhaps similar to those shown as MORBs in the red box on the FMQ line on the y-axis, or other mantle-derived highly reduced mafic magmas. Serpentinized ultramafic rocks are known to have a redox state even lower near magnetite–FeO shown as line 23, directly below line 24 representing hydrothermal reduction of calcite by H_2 in the presence of quartz. Salotti and others (1971) proposed an abiotic mechanism for the formation of graphite with the carbon being supplied from the carbon in preexisting carbonate minerals. The carbon is released by direct methanation through a reaction with elemental hydrogen. The subsequent pyrolysis of methane releases elemental carbon (Salati and others, 1971). Similarly, Galvez and others (2013) concluded that graphite may form by carbonate reduction during subduction and Rumble and others (1986) presented evidence of hydrothermal graphite genesis.

Sabatier Reaction and H_2 and CO_2 in Porphyry Copper Ore-Forming Fluids

Line 25 in figure 3E demarks the position of the well-known Sabatier reaction, shown here for an iso-fugacity of CO_2 and CH_4 and an activity of H_2O equal to 1. The value of the equilibrium constant for this reaction changes sign at about 350°C. Above 350°C to the right of the vertical line 26, the favored species are H_2 and CO_2. Fluid inclusions in the early high-temperature stage of porphyry copper deposits

often have CO_2. However, H_2 to date has not been noted. Mavrogenes and Bodnar (1994) showed experimentally that H_2 readily diffuses through quartz, which is the most common host for fluid inclusions, and concluded that "hydrogen will diffuse out of inclusions if the inclusion-bearing sample is exposed to conditions significantly different from those in the inclusions." The rapid diffusion of H_2 into fluid inclusions in quartz was consistent with the diffusion rate constants measured by Kats and others (1962). From this work it is clear that H_2 will diffuse through many rocks whenever an H_2 concentration gradient exists. Therefore, it is not surprising that while the thermochemical results presented here prove a substantial H_2 concentration in ore-forming fluids, H_2 has not been recognized as a common constituent in fluid inclusions as it is probably a largely fugitive species. The only lasting evidence of the migration of H_2 in porphyry copper deposits is then likely to be the recurrent mineral assemblage supported by theoretical chemical phase equilibria from which fluid composition is computed. The mixture of molecular hydrogen and carbon dioxide, which is favored by the Sabatier reaction above about 350°C, together constitutes a powerful agent for reduction.

Cycling of H_2 by Convection in Butte and Bingham Type Systems: Cooling and Heating Paths

Finally, shown as a yellow arc in figure 3F, are the cooling and heating portions of the convective cycling of H_2 proposed here for two distinct types of PCD deposits: Butte (line 19) and a more oxidized system at Bingham (line 20) shown as BP and BE, respectively, in figure 3B. These heating paths *point upwards to the left.* For Butte, the initial hydrothermal fluid escapes from the blue box along line 14 (figs. 3C, 3D), which is similar to the redox state of oxidized Pinatubo arc magmas with anhydrite. As H_2 on the righthand side of line 14 escapes from porphyry copper magmas as minute bubbles carried in early high-temperature fluids, Le Chatelier's principle drives the reaction to the right, creating more SO_2. Biotitic breccias formed explosively on the tops of Butte porphyry dikes are shown in the light blue zone labeled "BX." At Butte, the only early sulfides to form are chalcopyrite and pyrite without bornite. With cooling, the path along line 19 intersects the magnetite–hematite line. At lower temperatures around 300°C, chalcocite and covellite form where the early stage buffer with magnetite–K–feldspar–biotite is destroyed by sericitic and advanced argillic alteration. In contrast, at Bingham, which formed along a higher oxidation state (line 20), the early stage sulfides are chalcopyrite, pyrite, and bornite, formed along line 7 as shown in figure 3B.

The heating paths shown in Figure 3F are shown in green *pointing downward to the right* and consist of the equilibria of propylitic alteration line 27 and the actinolite orbicule assemblages shown as line 22. It is known that convective hydrothermal cells develop at the top of ore-forming magmas driven by the temperature gradients between the hot but cooling plutons and the surrounding wall rocks (Norton and Knight, 1977). The shape of the convective systems are elliptical toroids. This means that the cooling paths shown in figure 3F connect with the return heating paths as a convective loop shown in gray.

Timing and Duration of Hydrogen Gas Release from Magma

While bubble accumulation and magmatic vapor transport (MVP) has been modeled by Parmigiani and others (2016, 2017) and Gruzdeva and others (2024), the volatile species considered are H_2O, CO_2, S, Cl, F, Li, B, and noble gases but not H_2 in particular. While all these gas species are important in ore genesis, it has been shown here that H_2 has an unequaled influence on oxidation and reduction. Nevertheless, modeling by Parmigiani and others (2016, 2017) and Gruzdeva and others (2024) show that ore formation from hydrous magmas may involve distinct phases of volatile release. From Gruzdeva and others (2024): "Magma convection at early melt-dominated states leads to homogenization, which delays fluid release and promotes a rapid evolution toward a mush state. Subsequent onset of magmatic volatile release can be near-explosive with a tube-flow outburst event that could result in the formation of hydrothermal breccias and vein stockworks or trigger eruptions. This event can be followed by sustained fluid release at moderate rates by volatile flushing caused by magma convection."

Volcanic Eruptions Containing Anhydrite and their Parallel with Porphyry Copper Deposit Magmas

Luhr (2008) summarized global volcanic eruptions containing primary igneous anhydrite extending as far back as 1948 and provides a detailed description of microphenocrysts of anhydrite coexisting with pyrrhotite and titanite in fresh pumices in the 1982 eruption of El Chichon, Mexico, as well as in the far larger

eruption at Mt. Pinatubo in 1992 in the Philippines, which is a mega-strata volcanic eruption. Coexisting anhydrite and titanite is consistent with the highly oxidized state implied in figure 3B, line 5, and figure 3D for Mt. Pinatubo, shown as green lines. Luhr (2008) cites anhydrite crystallizing from the melt during the final stages of crystallization prior to eruption, noting glass inclusions within anhydrite crystals as the strongest evidence in favor of direct crystallization of anhydrite from the melt. The high content of water, incompatible trace elements, high K_2O, high sulfur as SO_3, presence of titanite and high calculated log fO_2 far in excess of Ni-NiO, and porphyritic texture show a similarity with porphyry copper magmas and points out also that El Chichon is within the regional PCD metallogenic belt in Mexico. The water- and gas-saturated condition and calculated depth of 9 km are also similar to PCDs including Butte, Montana. Most revealing is the "excess gas release" phenomena of 5–8 million tonnes of SO_2 released to the stratosphere by the El Chichon eruption and larger excess gas release of ~18 million tonnes of SO_2 for the significantly larger eruption of Mt. Pinatubo.

Fluid Circulation Cell

In figure 4 an ideal advective circulation cell with an elliptical torus shape is shown surrounding a central pluton. Potassic alteration occurs within and slightly outside of the pluton. Anhydrite, shown in pink, occurs within the potassic alteration zone. At Butte, Montana, where the ore body occurs within the Butte Granite wall rock, a zone of biotitized hornblende demarks the Potassic zone, which dies out upwards where the granite contains unaltered titanite and hornblende in fresh granite. Stockworks and biotite crackle veinlets also die out upwards. In Bingham-type systems, the potassic zone is surrounded by an actinolite–titanite–calcite ring shown as green dots surrounded by a propylitic zone, shown in solid green. The distal actinolite orbs are shown as green dots that form an annular shell surrounding the convective system, thus appearing like a bullseye target in plan view. This distal ring of orbicular actinolite is easily recognized in the field and is mappable even under dense tree canopy as it is intensely silicified and resists soil-forming processes. This orb ring is absent from batholith-hosted systems like Butte as the granitic rock buffer precludes the redox state from descending low enough to form actinolite orbs.

An Operative Porphyry Copper Model

The tube flow outburst followed by sustained fluid (including H2 gas) release in combination with the thermochemical mineral assemblage analysis provided here can together be assembled into an operative porphyry copper model. A thermodynamic diagram is developed here for redox equilibria in porphyry copper genesis presented in figure 5. The H_2 vs 1/T Van't Hoff reference frame at water saturation works as an operative geochemical diagram because confined-flow migration of H_2 by magmatic outgassing and thermal advection causes oxidation by dehydrogenation and reduction in the regions where H_2 concentrates along

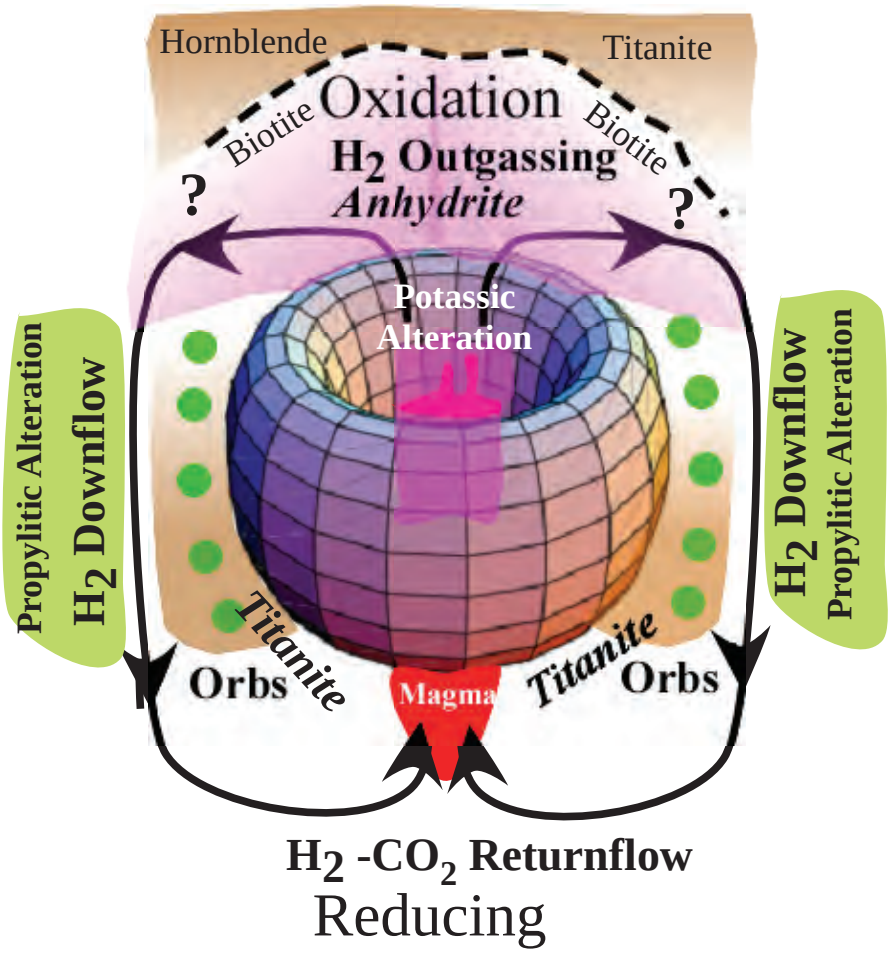

Figure 4. Elliptical torus fluid flow geometry around a cooling pluton for porphyry copper deposits. Actinolite orbicular alteration is shown diagrammatically in cross-section as distal green dots inside of the rocks containing titanite, shown in brown. In the central upper part of the system, titanite is not stable and anhydrite occurs instead, shown in pink. On the very top of the early high-temperature system titanite is again stable in granitic wall rocks above a zone of biotitized hornblende.

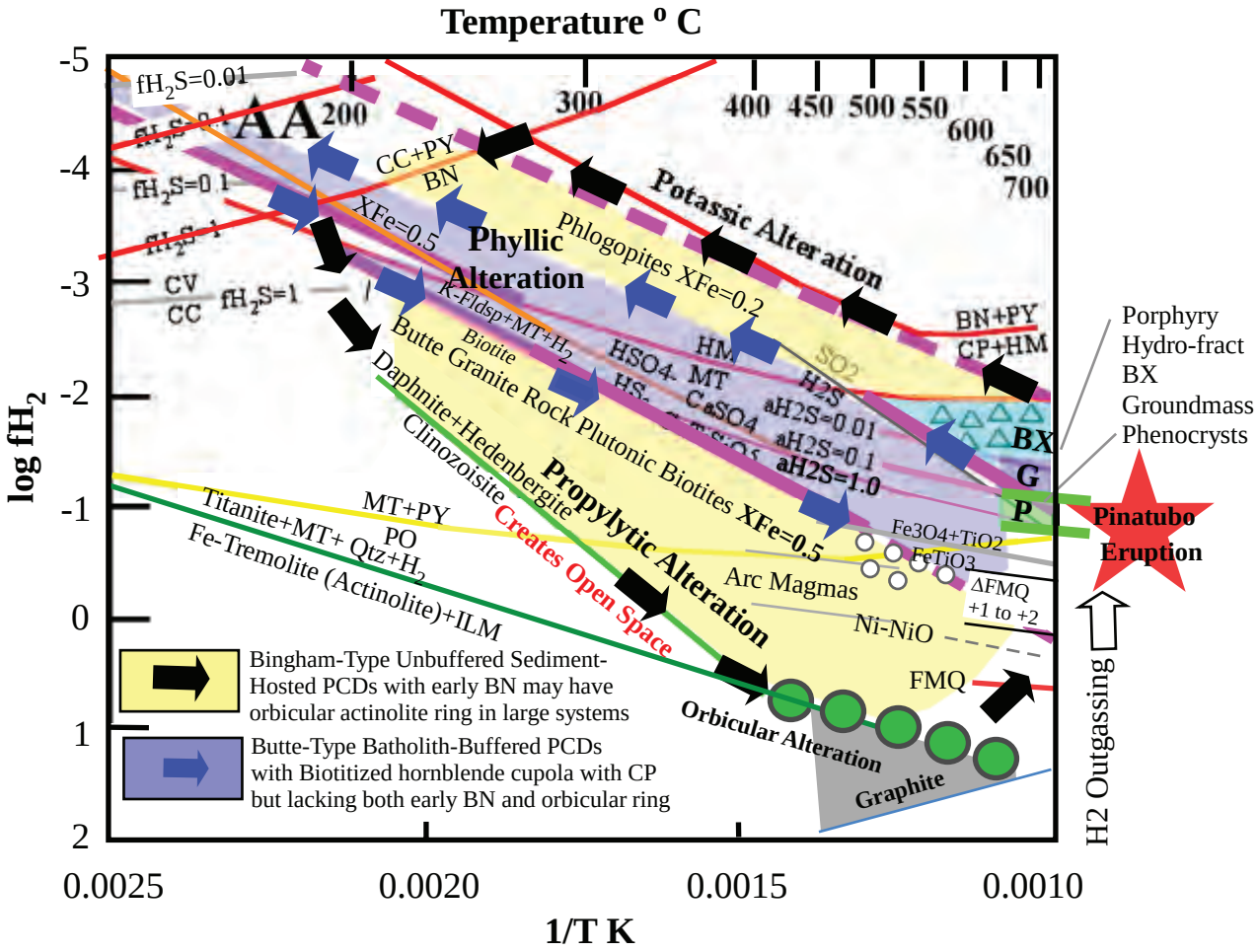

Figure 5. An operative porphyry copper model is shown. Two concentric advective circulation cells are shown with arrows. Confined-flow hydrogen bubble migration by magma outgassing and thermal advection causes oxidation where dehydrogenation occurs and reduction along the return flow heating path approaching the pluton where hydrogen accumulates. The larger cell shown with black arrows defines Bingham-type systems, which attain both extremely high early oxidative states with chalcopyrite, bornite, and digenite and extreme reductive states with propylitic and finally orbicular actinolite alteration. In contrast, the smaller batholith-hosted Butte-type porphyry Cu cell, shown with blue arrows, has a narrow limited early oxidation range that consists only of chalcopyrite–pyrite. It also lacks a distal orb ring due to restrictive chemical buffering by the Butte granite wall rocks with high-Ti (XFe = 0.5) biotite. This cell extends up to the advanced argillic assemblage with covellite and chalcocite by cooling while the heating path causes propylitic alteration with epidote as the upper shell above biotitized hornblende. Conventionally, water saturation in magmas creating overpressured fluids is invoked to explain fracture development by violent release of magmatic fluids that expand and cause explosive brittle rock failure. Here I assert that hydrogen diffusion may dramatically enhance the fracturing process through hydrolytic weakening of quartz and other silicate minerals. Hydrolytic weakening by H_2 may also explain why the few springs on the Clementine prospect all occur only within or very near orb alteration zones. Finally, H_2 diffusion may also cause hydrolytic weakening of the carapace that confines deep porphyry systems. Hydrogen may be a part of vapor saturation at great depth of 7 to 9 km, noted by Jim Luhr for the El Chichon and Mt Pinatubo volcanoes, which both had primary igneous anhydrite and released tens of millions of tons of SO_2. As the threshold required for overpressure fracturing is lowered, a cataclysmic strata-volcanic eruption containing anhydrite may occur as a destructive alternative fate of a deep porphyry copper deposit (shown as a large red star).

the return flow heating path approaching the pluton. Two concentric advective circulation cells emerge in the log H_2 vs. 1/T space. The largest advective circulation cell, shown as black arrows surrounding a yellow zone, defines sediment-hosted Bingham-type PCD systems that reach both extreme early oxidative states with chalcopyrite, bornite, and digenite (chalcocite) and extreme reductive states with distal actinolite orbicular alteration. Expulsion of highly oxidized early high-temperature aqueous fluids continue to lose H_2 and oxidize along a cooling path defined by the Mg-rich (X_{Fe}= 0.2), Ti-poor hydrothermal biotite–magnetite–K–feldspar Potassic alteration mineral assemblage line, which serves as definitive trajectory of the cooling pathway. The return heating pathway is demarked by propylitic alteration and distal actinolite orbicular alteration. In contrast, the batholith-hosted Butte-type PCD cell, shown as blue arrows surrounding a gray area, has a narrow limited early oxidation range that does not extend up to bornite or digenite and consists only of chalcopyrite–pyrite. It also lacks a distal orb ring due to restrictive chemical buffering

by the influence of granite wall rocks with red high-Ti (X_{Fe}= 0.5) biotite terminating in the advanced argillic assemblage, with covellite and chalcocite on the oxidized end where intense sericitic and advanced argillic alteration destroys the granite buffer. Occurrences of actinolite orbs at Bingham, Escondida, El Hueso, Cajamarca, Morenci, Fortitude, Cananea, and Oyu Tolgoi imply that an actinolite orb ring may be a definitive indicator of large PCD systems. Given the necessity of electron conservation, a large actinolite orb ring portends a large highly oxidized potassic alteration zone with chalcopyrite, bornite, and digenite. This exploration target size indicator supported by H_2 dynamics and redox thermochemistry may provide focus and help guide discovery of new deep confined PCDs of considerable size and is being tested at the Clementine prospect in southwest Montana, which has a 3 by 5 km orb ring.

Proposal of a Target Size Indicator (TSI)

Knowing now that H_2 was in fact present in early high-temperature processes, impacts of this conclusion may have broad potentially useful implications. The distal diffusion-controlled orbicular actinolite (Fe–tremolite)–titanite–ilmenite calcite assemblages reflect the advective return of H_2 gas to edges of the magmatic–hydrothermal convection cell. Multielement geochemistry shows that the same hydrothermal fluid was responsible for veins as well as orbs as part of an upright barrel-shaped elliptical torus convection system. Thus, the *oxidative* processes within the central part of a district forming early high-temperature Potassic alteration and related early high-temperature sulfide mineralization must be balanced by the *reductive* processes occurring in the surrounding distal actinolite–titanite–ilmenite alteration zones. If correct, then the inferred district-scale H_2 and electrochemical linkage has important implications for early stage exploration strategies. The physical dimensions in plan view of the reduced actinolite orb ring may be forced by H_2 mass balance and electrochemistry on a convective scale to be at least roughly proportional to the size of the coaxial central zone of oxidized copper sulfide veining. Hence, a potential exploration target size indicator supported by thermochemistry emerges from this use of the hydrogen geochemical perspective.

Conclusions

The H_2 geochemical reference frame adopted here works because it is the migration of H_2 by magmatic outgassing that causes oxidation and reduction in the regions where it concentrates. By specifying water activity at unity to discover results that are *approximately* correct, several important outstanding questions involving magmatic processes and ore genesis are resolved and a vivid volcanic frame of reference is offered to describe the processes involved.

First, while earlier studies using the FMQ fO_2 redox buffer have speculated that H_2 degassing may have elevated the oxidation state of subduction-related arc magmas to $\Delta\log fO_2$ FMQ of + 1 to 2, here formulation of this buffer in terms of fH_2 instead of fO_2 quantifies this assertion that shows that H_2 mobility is indeed the major factor in magma oxidation. This process, here referred to an oxidative dehydrogenation, is the operational mechanism that has been missing. These oxidized arc magmas have a redox state typical of equigranular plutons forming batholiths but lacking mineralization. Igneous biotite crystals reflect this redox state with reddish brown color in thin section and high TiO_2 contents around 4 percent.

Second, ore-forming porphyritic magmas that exsolve water and outgas H_2 *en masse* experience extreme oxidation attending early high-temperature potassic wall-rock alteration with titanite destruction and anhydrite formation. Mg-rich hydrothermal phlogopitic alteration in the biotite–magnetite–K–feldspar equilibria define reaction paths parallel to the HS^-/HSO_4^- boundary but directly over the iso-fugacity boundary of H_2S and SO_2. Such oxidized biotite crystals have lost their TiO_2 content and are yellow to greenish in color.

Third, continued H_2 outgassing causes continued oxidation of HS^- to $HSO4^-$, which serves as an effective H_2 pump where if structural confinement limits H_2 escape, it continues to create hydrothermal fluids rich in H_2 that advect downward along the sides of the ore-forming hydrothermal barrel-shaped elliptical torus convection cell centered on the parental porphyry pluton.

Fourth, at the high H_2 fugacity caused by H_2 pumping, actinolite (Fe–tremolite)–titanite–ilmenite assemblages form reflecting the advective return of H_2 gas to distal edges of the magmatic–hydrothermal convection cell.

Fifth, H_2 movement by district-scale advection requires conservation of electrons as well as hydrogen mass. Thus, the *oxidative* processes within the central part of a district forming early high-temperature

Potassic alteration and sulfide mineralization must be balanced by the *reductive* processes occurring in the surrounding distal edge zones. If correct, then the inferred district-scale H_2 and electrochemical linkage has important implications for early stage exploration strategies. The dimensions in plan view of the actinolite orb ring are likely forced by electrochemistry on a convective scale to be proportional to the size of the coaxial central zone of copper sulfide mineralization within the Potassic alteration zone. Hence, a potential exploration target size indicator supported by thermochemistry emerges from this use of the hydrogen geochemical perspective.

Finally, since earning a social license for mining deep ore bodies is based in part on the public's understanding of ore genesis, a vivid example of the hydrogen recycling model proposed here is provided by the eruption of Mt. Pinatubo in the Philippines in 1991, which contained phenocryst anhydrite and a magma similar to the highly oxidized melts in porphyry copper deposits. Envisioning how a rare energetic megastrata volcanic eruption containing anhydrite may represent a once-potential porphyry copper deposit that was not confined at depth but instead exploded and erupted cataclysmically may provide a useful public outreach model as it offers tangible evidence of the size of these systems and the energy levels involved.

Acknowledgments

Kaleb Scarberry is thanked for organizing the scientific program. Chris Gammons and Kyle Eastman provided insightful reviews of this manuscript. The late Jim Luhr is recognized for inspirational insights in volcanism, mastery of petrological methods that revealed the importance of anhydrite in volcanic rocks, and for shared excitement and engaging friendship. Jeff Dick is acknowledged for his CHNOSZ computational package and mineralogical thermodynamic database that make all the thermodynamic calculations presented here possible. Jay Ague and Bruce Marsh are thanked for numerous enlightening discussions of geological processes. Bill Atkinson and Marco Einaudi, who recognized and logged the first actinolite orbs at Bingham, are thanked for their gracious help to the author after he recognized similar orbs in Montana. Neil Griffis (USGS) is heartily thanked for his discerning discovery of graphite near the type section of actinolite orbs on Parker Creek. The author thanks all of his colleagues in Clementine Exploration LLC for their abiding interest and support, including Mary Jane Brimhall, Doug Fuerstenau, Ray Morley, Daniel Kunz, Ed Rogers, Bruce Marsh, Abel Vanegas, Chris Lewis, and Tim Teague. Brian Collins kindly provided the mathematical name of elliptical torus used to describe the convective field in three dimensions. The fieldwork that supports this project starting in 2011 was augmented by the support of neighbors in Wise River and Butte, including Dean Stodden, Jim Freestone, Ryan Brown, Don Heffington, Jim Holland, and John Lundborg in shuttling vehicles in support of mapping and helping recover from inevitable vehicle breakdowns. Finally, Erik Torgeson, Licette Hammer, and Jim Freestone of the USFS made environmental regulatory compliance tractable through sharing their considerable expertise and engagement with us in ongoing fieldwork.

References

Ague, J.J., and Brimhall, G.H., 1987, Granites of the batholiths of California: Products of local assimilation and regional-scale crustal contamination: Geology, v. 15, p. 63–66, https://doi.org/10.1130/0091-7613(1987)15<63:GOTBOC>2.0.CO;2

Ague, J.J., and Brimhall, G.H., 1988a, Regional variations in bulk chemistry, mineralogy, and the compositions of mafic and accessory minerals in the batholiths of California: Geological Society of America Bulletin, v. 100, p. 891–911.

Ague, J.J. and Brimhall, G.H., 1988b, Magmatic arc asymmetry and distribution of anomalous plutonic belts in the batholiths of California: Effects of assimilation, crustal thickness, and depth of crystallization:, Geological Society of America Bulletin, v. 100, p. 912–927.

Ague, J., Tassara, S., Holycross, M., Li, J., Cottrell, E., Schwarzenbach, E., Fassoulas, C., and John, T., 2022, Slab-derived devolatilization fluids oxidized by subducted metasedimentary rocks: Nature Geoscience, v. 15, p. 320–326.

Andersen, D.J., Lindsley, D.H., and Davidson, P.M, 1993, QUILF: A Pascal program to assess equilibria among Fe-Mg-Mn-Ti oxides, pyroxenes, olivine, and quartz: Computers and Geosciences, v. 19, no. 9, p. 1333–1350, https://doi.org/10.1016/0098-3004(93)90033-2.

Atkinson, W., and Einaudi, M.T., 1978, Skarn formation and mineralization in the contact aureole at Carr Fork, Bingham, Utah: Economic Geology, v.

75, p. 1326–1365, https://doi.org/10.2113/gsecongeo.73.7.1326.

Brimhall, G.H. Jr., 1973, Mineralogy, texture, and chemistry of early wall rock alteration in the deep underground mines and Continental area, *in* Miller, R.N., ed., Guidebook for the Butte field meeting of the Society of Economic Geologists: Society of Economic Geologists Guidebook, Anaconda Company, Butte, Montana, p. H1–H5.

Brimhall, G.H., 1977, Early fracture-controlled disseminated mineralization at Butte, Montana: Economic Geology, v. 72, p. 37–59, https://doi.org/10.2113/gsecongeo.72.1.37.

Brimhall, G.H, 1979, Lithologic determination of mass transfer mechanisms of multiple stage porphyry copper mineralization at Butte, Montana: Vein formation by hypogene leaching and enrichment of potassium-silicate protore: Economic Geology, v. 74, p. 556–589, https://doi.org/10.2113/gsecongeo.74.3.556.

Brimhall, G.H., 1980, Deep hypogene oxidation of porphyry copper potassium-silicate protores: A theoretical evaluation of the copper remobilization hypothesis: Economic Geology, v. 75, p. 384–409, https://doi.org/10.2113/gsecongeo.75.3.384.

Brimhall, G.H., 1987, Preliminary fractionation patterns of ore metals through Earth history: Chemical Geology, v. 64, p. 1–16.

Brimhall, G.H., 2018, Orbicular alteration at the porphyry copper prospect of southwest Montana: Defining the edges of advective flow in the porphyry copper paradigm: Montana Bureau of Mines and Geology Special Publication 120, p. 71–84.

Brimhall, G., 2021, Deep sediment-hosted porphyry copper deposits with critical mineral potential and the geochemical relationship of orbicular actinolite alteration to district zoning and oxidation by carbonate dissolution CO2 release: Montana Bureau of Mines and Geology, Special Publication 123, p. 27–58, https://doi.org/10.59691/YXKU1170.

Brimhall, G.H., and Crerar, D.A., 1987, Ore fluids: Magmatic to supergene, *in* Thermodynamic modeling of geological materials: Minerals, fluids and melts, I. Carmichael and H. Eugster, eds.: Mineralogical Society of America Reviews in Mineralogy, v. 17, ch. 10, p. 235–321.

Brimhall, G.H, and Fanning, M., 2020, Supporting the transition to deep porphyry copper exploration: SHRIMP U/Pb radiometric dating of titanite (CaTiSiO5) in the distal and superjacent orbicular alteration zone of the Clementine prospect, southwest Montana: Montana Bureau of Mines and Geology Special Publication 121, p. 117–132.

Brimhall, G.H., Agee, C., and Stoffregen, R., 1985, Hydrothermal conversion of hornblende to biotite: Canadian Mineralogist, v. 23, no. 3, p. 369–379.

Chiaradia, M., and Caricchi, L., 2022, Supergiant porphyry copper deposits are failed large eruptions: Communications Earth & Environment v. 3, no. 107.

Chou, I., and Eugster, H., 1977, Solubility of magnetite in supercritical chlorides solutions: American Journal of Science, v. 277, p. 1296–1314.

Einaudi, M.T., 1977, Environment of ore deposition at Cerro de Pasco, Peru: Economic Geology, v. 72, p. 893–924, https://doi.org/10.2113/gsecongeo.72.6.893.

Einaudi, M.T., Hedenquist, J., and Inan, E., 2003, Sulfidation state of fluids in active and extinct hydrothermal systems, Giggenbach Volume, Simmons, S.F., ed.: Society of Economic Geologists and Geochemical Society Special Publication 10, p. 285–313, https://doi.org/10.5382/SP.10.15.

Eugster, H., and Wones, D., 1962, Stability relations of the ferruginous biotite, annite: Journal of Petrology, v. 3, p. 81–125, https://doi.org/10.1093/petrology/3.1.82.

Eugster, H., and Chou, I., 1979, A model for the deposition of Cornwall-type magnetite deposits: Economic Geology, v. 763–774.

Galvez, M., Beyssac, O., Martinez, I., Benzerara, K., Chaduteau, C., Malvoisin, B., and Malavieille, J., 2013, Graphite formation by carbonate reduction during subduction: Nature Geoscience, v. 6, June, https://doi.org/10.1038/NGEO1827.

Giggenbach, W.F., 1987, Redox processes governing the chemistry of fumarolic gas discharges from White Island, New Zealand: Applied Geochemistry, v. 2, p. 143–161, https://doi.org/10.1016/0883-2927(87)90030-8.

Griggs, D., 1967, Hydrolytic weakening of quartz and other silicates: Geophysical Journal of the Royal

Astronomical Society, v. 14, p. 19–31, https://doi.org/10.1111/j.1365-246X.1967.tb06218.x.

Gruzdeva, Y., Weis, P., and Andersen, C., 2024, Timing of volatile degassing from hydrous upper-crustal magma reservoirs with implications for porphyry copper deposits: Journal of Geophysical Research: Solid Earth, 129, e2023JB028433, https://doi.org/10.1029/2023JB028433.

Gustafson, L.B., and Hunt, J.P., 1975, The porphyry copper deposit at El Salvador, Chile: Economic Geology, v. 70, p. 857–912.

Hemley, J.J., Montoya, J.W., Marinenko, J.W., and Luce, R.W., 1980, Equilibria in the system Al2 O3 -SiO2 -H2 O and some general implications for alteration/mineralization processes: Economic Geology, v. 75, p. 210–228, https://doi.org/10.2113/gsecongeo.75.2.210.

Holland, H.D., 1959, Stability relations among the oxides, sulfides, sulfates and carbonates of ore and gangue metals, Part 1 of Some applications of thermochemical data to problems of ore deposits: Economic Geology, v. 54, p. 184–233, https://doi.org/10.2113/gsecongeo.54.2.184.

James, H.L., 1990, Precambrian geology and bedded iron deposits of the southwestern Ruby Range, Montana: U.S. Geological Survey Professional Paper 1495, 39 p., https://doi.org/10.3133/pp1495.

John, D.A., Ayuso, R.A., Barton, M.D., Blakely, R.J., Bodnar, R.J., Dilles, J.H., Gray, F., Graybeal, F.T., Mars, J.C., McPhee, D.K., Seal, R.R., Taylor, R.D., and Vikre, P.G., 2010, Porphyry copper deposit model, ch. B, *in* Mineral deposit models for resource assessment: U.S. Geological Survey Scientific Investigations Report 2010–5070–B, 169 p. 56.

Johnson, J., Oelkers, E., and Helgeson, H., 1992, SUPCRT92: A software package for calculating the standard molal thermodynamic properties of minerals, gases, aqueous species, and reactions from 1 to 5000 bar and 0 to 1000°C: Computers and Geoscience, v. 18, no. 7, p. 899–947, https://doi.org/10.1016/0098-3004(92)90029-Q.

Kats, A., Haven, Y., and Stevels, J., 1962, Hydroxyl groups in alpha quartz: Physics and Chemistry of Glasses, v. 3, p. 69–75.

Lewis, G., and Randall, 1961, Thermodynamics, revised by Pitzer, K., and Brewer, L.: McGraw Hill, p. 173–175.

Lowell, J.D., and Guilbert, J., 1970, Lateral and vertical alteration-mineralization zoning in porphyry ore deposits: Economic Geology, v. 65, p. 373–408, https://doi.org/10.2113/gsecongeo.65.4.373.

Luhr, J., 2008, Primary igneous anhydrite: Progress since its recognition in the 1982 El Chichón trachyandesite: Journal of Volcanology and Geothermal Research, v. 175, p. 394–407, https://doi.org/10.1016/j.jvolgeores.2008.02.016.

Luhr, J., Carmichael, I., and Varekamp, J., 1984, The 1982 eruptions of El Chichón Volcano, Chiapas, Mexico: Mineralogy and petrology of the anhydrite bearing pumices: Journal of Volcanology and Geothermal Research, v. 23, p. 69–108, https://doi.org/10.1016/0377-0273(84)90057-X.

Mavrogenes, J., and Bodnar, R., 1994, Hydrogen movement into and out of fluid inclusions in quartz: Experimental evidence and geologic implications: Geochimica et Cosmochimica Acta, v. 58, no. 1, p. 141–148.

Meyer, C., and Hemley, J.J., 1967, Wall rock alteration, *in* Barnes, H.L., ed., Geochemistry of hydrothermal ore deposits: New York, Holt, Rinehart, and Winston, p. 166–232.

Norton, D., and Knight, J., 1977, Transport phenomena in hydrothermal systems: American Journal of Science, v. 277, p. 937–981, https://doi.org/10.2475/ajs.277.8.937.

Parmigiani, A., Faroughi, S., Huber, C., Bachmann, O., and Su, Y., 2016, Bubble accumulation and its role in the evolution of magma reservoirs in the upper crust: Nature, v. 532, no. 7600, p. 492, https://doi.org/ 10.1038/nature17401.

Parmigiani, A., Degruyter, W., Leclaire, S., Huber, C., and Bachmann, O., 2017, The mechanics of shallow magma reservoir outgassing: Geochemistry, Geophysics, Geosystems, v. 18, no. 8, p. 2887–2905, https://doi.org/10.1002/2017GC006912.

Richards, J., 2015, The oxidation state, and sulfur and Cu contents of arc magmas: Implications for metallogeny: Lithos, v. 233, p. 27–45, https://doi.org/10.1016/j.lithos.2014.12.011.

Roberts, S.A., 1973, Pervasive early alteration in the Butte district, Montana, *in* Miller, R.N., ed.,

Guidebook for the Butte field meeting of the Society of Economic Geologists: Society of Economic Geologists Guidebook, Anaconda Company, Butte, Montana, p. HH1–HH8.

Roberts, S.A., 1975, Early hydrothermal alteration and mineralization in the Butte district, Montana: Harvard University, Ph.D. dissertation, 157 p.

Rovetta, M., Blacic, J., Hervig, R., and Holloway, J., 1989, An experimental study of hydroxyl in quartz using infrared spectroscopy and ion microprobe techniques: Journal of Geophysical Research, v. 94, no. B5, p. 5840–5850, https://doi.org/10.1029/JB094iB05p05840.

Rumble, D., Duke, E., and Hoering, T., 1986, Hydrothermal graphite in New Hampshire: Evidence of carbon mobility during regional metamorphism: Geology, v. 14, no. 6, p. 452–455, https://doi.org/10.1130/0091-7613(1986)14<452:HGINHE>2.0.CO;2

Rutherford, M., 1993, Experimental petrology applied to volcanic processes: EOS, Transactions, American Geophysical Union, v. 74, no. 5, p. 49–55, https://doi.org/10.1029/93EO00142

Salotti, C.A., Heinrich, E.W., and Giardini, A.A., 1971, Abiotic carbon and the formation of graphite deposits: Economic Geology, v. 56, p. 929–932.

Sillitoe, R., 2010, Porphyry copper systems: Economic Geology, v. 105, no. 1, p. 3–41, https://doi.org/10.2113/gsecongeo.105.1.3.

Strauch, B., Pilz, P., Hierold, J., and Zimmer, M., 2023, Experimental simulations of hydrogen migration through potential storage rocks: International Journal of Hydrogen Energy, v. 48, p. 25808–25820, https://doi.org/10.1016/j.ijhydene.2023.03.115.

Worthington, J.E., 2007, Porphyry and other molybdenum deposits of Idaho and Montana: Idaho Geological Survey Technical Report 07-3, 22 p.

Wones, D. R. and Eugster, H. P., 1965, Stability of Biotitie: Experiment, Theory, and Applications: American Mineralogisit, v. 50, p. 1228-1272.

Petrography of a Box of High-Grade, Gold–Telluride Drill Core from the Golden Sunlight Mine

Christopher H. Gammons and Jasmine Singh

Montana Technological University, Department of Geological Engineering, Butte, MT

cgammons@mtech.edu

Introduction

The Golden Sunlight Mine (GSM), located 50 km east of Butte (fig. 1), produced over 3.6 M oz of gold in its 36-yr history (Gammons and others, 2020). The GSM belongs to a class of telluride-rich, epithermal precious metal deposits that includes Porgera and Ladolam, New Guinea (Richards and Kerrich, 1993; Müller and others, 2002); Emperor, Fiji (Ahmad and others, 1987); and Cripple Creek, Colorado (Thompson and others, 1985). The geology and mineralization at GSM were described in detail by previous workers (Porter and Ripley, 1985; Foster and Childs, 1993; DeWitt and others, 1996; Spry and others, 1996, 1997; Spry and Thieben, 2000; Oyer and others, 2014; Gammons and others, 2020). Most of the gold came from the Mineral Hill Breccia Pipe (MHBP), a west-plunging, cylindrical body of brecciated latite porphyry and sedimentary rocks of the Belt Supergroup. Despite its impressive total production, the overall grade of gold in the deposit was low, approximately 0.054 oz/short ton (1.7 mg/kg; Spry and others, 1997).

After mining operations at the GSM shut down in 2019, a box of unusually high-grade drill core was donated to Montana Technological University (MTU) for educational and research purposes. This hole was drilled through the center of the MHBP, at a depth below the base of the final open pit. Preliminary

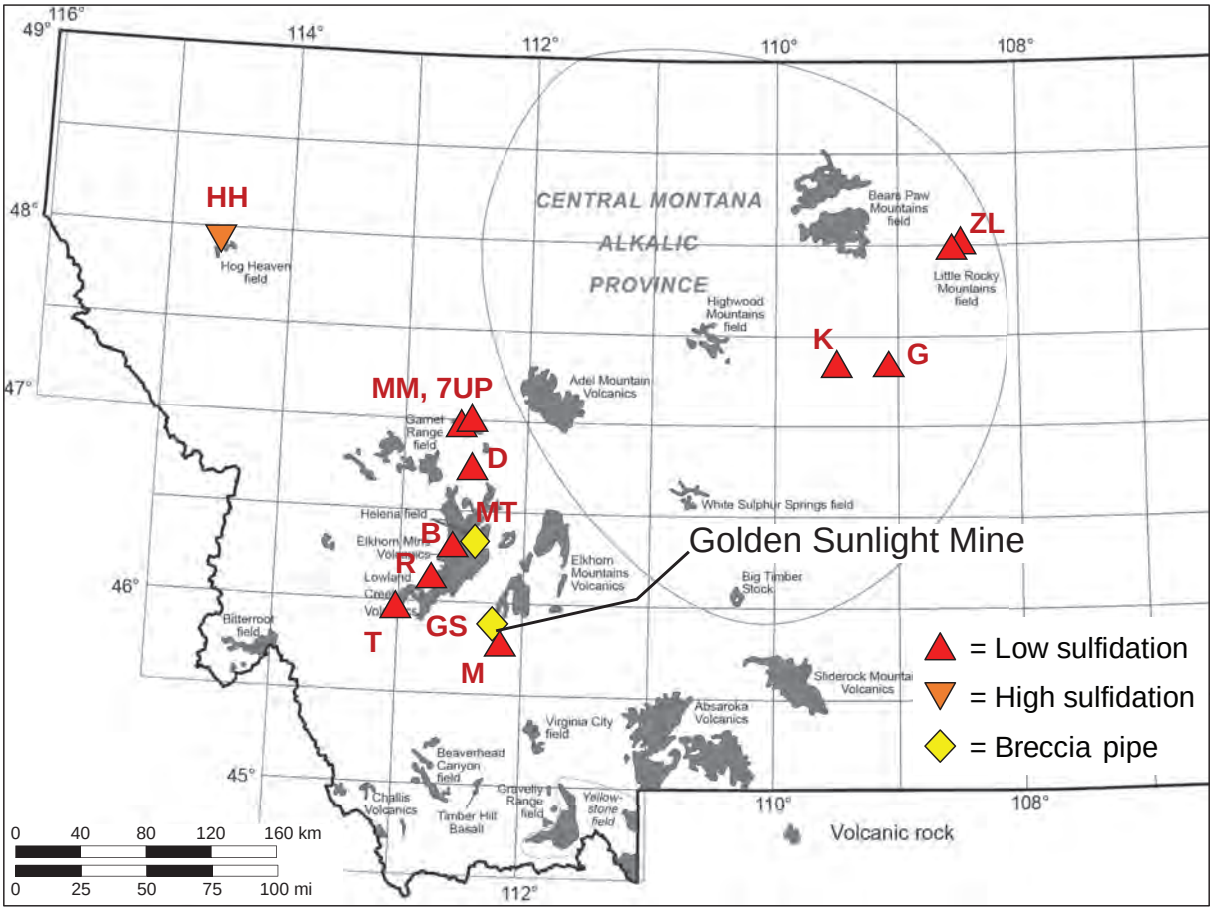

Figure 1. Location of the Golden Sunlight mine (GS) and other epithermal gold-silver deposits of Montana, with volcanic rocks of Cretaceous or younger age shown in gray. Other deposits: B, Basin; D, Drumlummon; G, Geis; HH, Hog Heaven; K, Kendall; M, Mayflower; MM, McDonald Meadows; MT, Montana Tunnels; R. Ruby (Oro Fino); T, Tuxedo; ZL, Zortman–Landusky. Diagram modified from Gammons and others (2022).

examination of the core by students using a portable X-ray fluorescence spectrometer confirmed the high gold grades, with roughly half of the 62 spot analyses exceeding 1000 mg/kg Au (fig. 2). The purpose of the current study, which began as an undergraduate research project for the second author, was to examine the mineralogy of the core using reflected light microscopy and scanning electron microscopy. In addition to documenting the unusual ore mineral textures, several minerals were found that were not previously described from the GSM deposits.

Methods

Portable X-ray fluorescence (pXRF) measurements were made with a Niton XL3t GOLDD+ instrument in "Test-All Geo" mode, with 50-second scans (15 seconds for the Main and Heavy element filters, and 10 seconds for the Low and Light filters). Photographs were taken of the core sections, both dry and wet. To obtain samples for detailed work, two pieces of gold-rich core were sliced horizontally with a water saw, roughly 1 cm below the split face. The back piece was used to create a set of six polished epoxy-mounted plugs (1-in round) while the top piece was returned to the core box. The samples were polished using a Buehler automated polisher and examined in reflected light using a Leica polarizing microscope and digital camera with LAS imaging software. Two samples were selected for additional study using the scanning-electron microscope (SEM) at MTU. This unit is a Tescan MIRA3–TIMA GMU field emission scanning electron microscope equipped with two EDAX element electron dispersive spectroscopy (EDS) detectors. The SEM was operated in back-scatter electron (BSE) and EDS modes for imaging and chemical analysis, respectively.

Results

Mineralogy and Textures

A list of the minerals found in this study is included in table 1. Pyrite is ubiquitous, being overall about 10 to 80% of the core by volume. The main gangue minerals are quartz, barite, and adularia (hydrothermal K-feldspar), although trace amounts of celestite and monazite were also found. The monazite is intergrown with pyrite, and is believed to be hydrothermal. Ore minerals, mainly Bi-Cu-Au tellurides and sulfides, are abundant, and occur as rounded inclusions in pyrite, or as irregular patches replacing pyrite and the gangue minerals (fig. 3). Of this list, calaverite, tetradymite, and native gold are by far the most common, with

Table 1. List of minerals found in this study.

Ore Minerals	Ideal Formula	Gangue Minerals	Ideal Formula
Pyrite	FeS_2	Quartz	SiO_2
Gold	Au	Barite	$BaSO_4$
Calaverite	$AuTe_2$	Celestite	$SrSO_4$
Tetradymite	Bi_2Te_2S	Adularia	$KAlSi_3O_8$
Wittichenite	Cu_3BiS_3	Monazite	$(REE)PO_4$
Hodrušite	$Cu_8Bi_{12}S_{22}$		
Goldfieldite	$Cu_{10}Te_4S_{13}$		
Tennantite	$Cu_{10}(Fe,Zn)_2As_4S_{13}$		
Chalcopyrite	$CuFeS_2$		
Mawsonite	$Cu_6Fe_2SnS_8$		

Figure 2. Photographs of the high-grade core (2.5-in diameter) from Golden Sunlight. Stickers show the locations of pXRF analyses and are color-coded to gold concentration (green <10 ppm, orange 10 to 1,000 ppm, pink >1000 ppm).

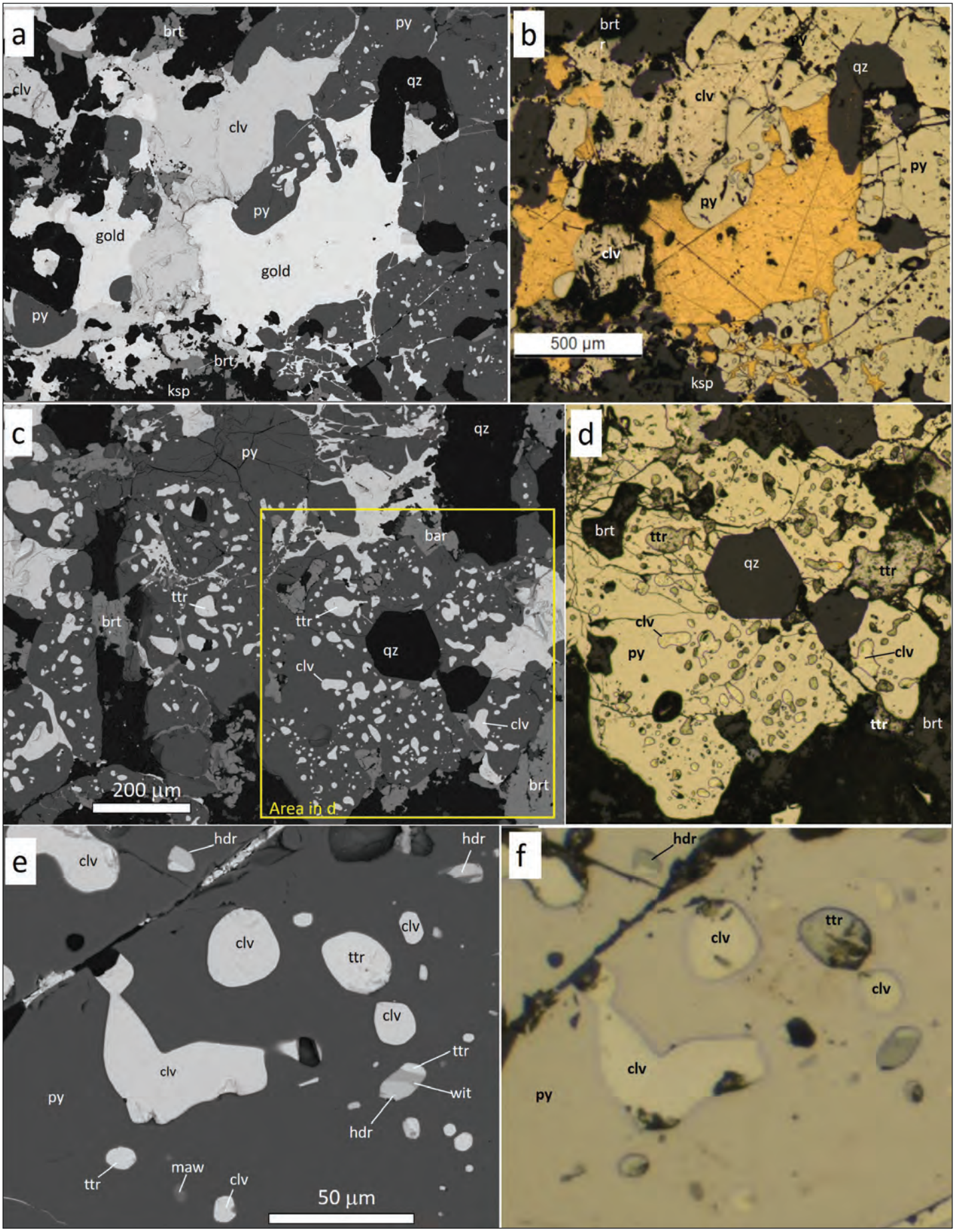

Figure 3. Paired SEM-BSE (left) and reflected light (right) photographs of sample JS-1, at increasing magnification levels. Mineral abbreviations: py, pyrite; clv, calaverite; ttr, tetradymite; wit, wittichenite; hdr, hodrušite; maw, mawsonite; qz, quartz; brt, barite.

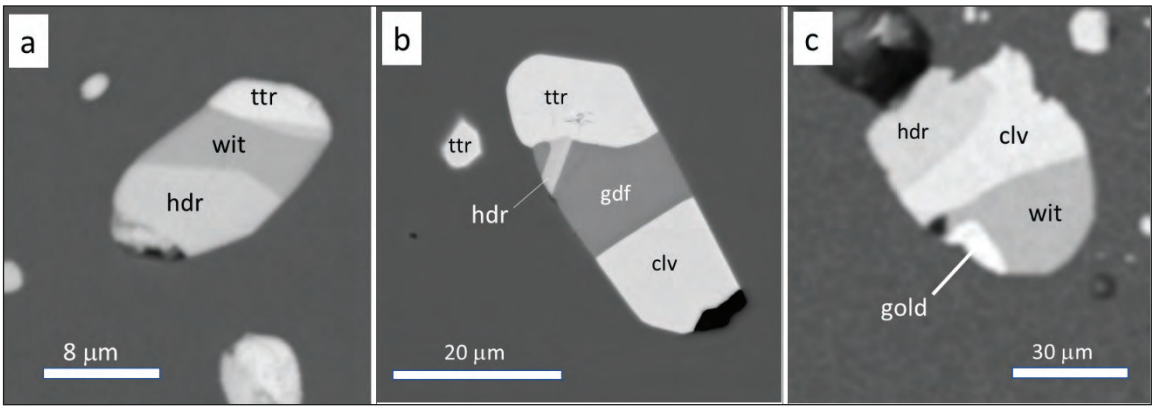

Figure 4. SEM-BSE images at high magnification, showing examples of polymineralic inclusions in pyrite. Abbreviations: ttr, tetradymite; wit, wittichenite; hdr, hodrušite; gdf, goldfieldite; clv, calaverite. Dark gray background is pyrite; black are holes.

the other ore minerals in table 1 listed in approximate order of decreasing abundance. Only one small grain of mawsonite was found (fig. 3e).

Many of the inclusions within pyrite contain two or more ore minerals in non-geometric intergrowths (fig. 4). These polymineral inclusions contain varying proportions of the same ore minerals listed in table 1, including, in some cases, native gold (fig. 4c). Although it was possible to see each mineral as solitary inclusions in pyrite, it was equally probable to see them in polymineral inclusions.

Mineral Chemistry

Selected SEM-EDS data are given in tables 2, 3 and 4 for the minerals goldfieldite, tennantite, and hodrušite. Goldfieldite (ideal formula $Cu_{10}Te_4S_{13}$) is a somewhat rare mineral that forms a partial solid solution with tennantite (ideal formula $Cu_{10}(Cu,Fe,Zn)_2As_4S_{13}$). Both tennantite and goldfieldite contain bismuth, assumed to substitute for arsenic ($Bi^{3+} \leftrightarrow As^{3+}$). For this study, a mineral was identified as goldfieldite if it had an atomic Te/As ratio >1. From 8 spot analyses, we computed an average formula for goldfieldite (normalized to 13 S atoms) of $Cu_{12.8}Te_{2.1}As_{1.3}Bi_{1.0}Fe_{0.8}S_{13}$ (table 2), while the average formula for coexisting tennantite was $Cu_{12.0}As_{2.7}Fe_{1.6}Te_{1.2}Bi_{1.0}S_{13}$ (table 3). Because many of the inclusions we analyzed had a small diameter (<5 µm in some cases), some Fe contamination from the surrounding pyrite cannot be discounted.

Table 4 gives SEM-EDS data for the rare mineral, hodrušite. Our average computed formula (normalized to 22 S atoms) based on eight spot analyses is $Cu_{8.1}Bi_{12.2}Fe_{1.9}S_{22}$, which is close to the ideal formula of $Cu_8Bi_{12}S_{22}$. Again, it is possible that some of the Fe we measured could have come from the surrounding pyrite. In the case of mawsonite, the single grain analyzed had major contamination from pyrite due to its small size (fig. 3e). However, the measured atomic Cu/Sn ratio of 6.5 is close to the ideal formula ratio of 6.0 for mawsonite.

SEM-EDS data are not shown for the other minerals listed in table 1, as they agreed with their ideal formulae in a straightforward manner. No Ag was detected in solid solution with native gold, calaverite, or tennantite–goldfieldite, and no discrete Ag minerals were found. This agrees with pXRF measurements that found no detectable silver in the GSM core box. The overall Au/Ag ratio in this part of the GSM deposit must have been very high (>100).

Table 2. SEM-EDS data for goldfieldite.

	Concentration, wt.%					
Spot	S	Fe	Cu	As	Te	Bi
5_7	22.8	2.24	44	4.32	16.9	9.7
5_8	25.4	2.94	47.3	8.99	15.3	
6_6	25.3	2.20	47.9	8.75	15.9	
6_7	22.4		46.4	4.83	14.9	11.4
7_1	22.6		45.5	4.85	15.4	11.6
8_5	22.8		45.6	4.50	15.0	12
8_9	23.1	2.63	42.8	4.35	14.0	13.1
9_1	22.3		45.5	4.56	15.1	12.5
Avg. (wt.%)	23.3	2.50	45.6	5.64	15.3	11.7
Avg. (at.%)	42.7	2.56	42.1	4.37	7.04	3.36
Atoms in formula	13	0.78	12.8	1.33	2.15	1.02
Avg. formula:	$Cu_{12.8}Te_{2.1}As_{1.3}Bi_{1.0}Fe_{0.8}S_{13}$					

Table 3. SEM-EDS data for tennantite.

	Concentration, wt.%					
Spot	S	Fe	Cu	As	Te	Bi
5_4	23.7	9.00	40.3	13.7	6.2	7.2
9_6	25.8	3.86	46.9	11.2	12.2	
9_7	22.7	4.88	43.6	11.3	4.05	13.5
9_10	25.3	3.07	48.1	10.6	12.9	
Avg. (wt.%)	24.4	5.2	44.7	11.7	8.8	10.3
Avg. (at.%)	42.0	5.17	38.9	8.65	3.79	2.83
Atoms in formula	13	1.6	12.0	2.7	1.2	0.9
Avg. formula	$Cu_{12.0}As_{2.7}Fe_{1.6}Te_{1.2}Bi_{1.0}S_{13}$					

Discussion

Comparison to pXRF Chemistry

The mineralogy observations noted above help to inform the pXRF data collected from the GSM core box by several student groups. Figure 5 shows some of the data for Au, Te, and Bi plotted in units of mmol/kg (i.e., mg/kg divided by the gram formula weight of each element). In a plot of Au vs. Te (fig. 5a), the data plot close to the ideal line corresponding to calaverite for the highest Au concentrations, but deviate at lower concentrations, indicating the presence of other Te minerals besides calaverite (tetradymite, goldfieldite, etc..). The Bi vs. Te plot (fig. 5b) is bound by the ideal 1:1 slope corresponding to tetradymite, but with higher Te concentrations, consistent with the prevalence of calaverite. Figure 5c shows that the majority of the samples with elevated Au and Bi plot near the ideal slope corresponding to the *combination* of calaverite + tetradymite. In other words, the minerals

Table 4. SEM-EDS data for hodrušite.

	Concentration, wt. %			
Spot	S	Fe	Cu	Bi
1_9	18.6	2.83	12.4	66.1
1_10	18.8	5.48	15.6	60.1
1_11	18.8	3.46	12.9	64.8
6_1	18.1	1.09	12.7	68
7_2	19.5		15	65.6
7_9	17.6	1.31	12.7	68.4
8_4	18.5		12.2	69.4
9_12	16.9		13.4	69.7
Avg. (wt.%)	18.3	2.83	13.4	66.5
Avg. (at.%)	50.6	4.34	18.5	28.2
Atoms in formula	22.0	1.89	8.07	12.3
Avg. formula	$Cu_{8.1}Bi_{12.2}Fe_{1.9}S_{22}$			

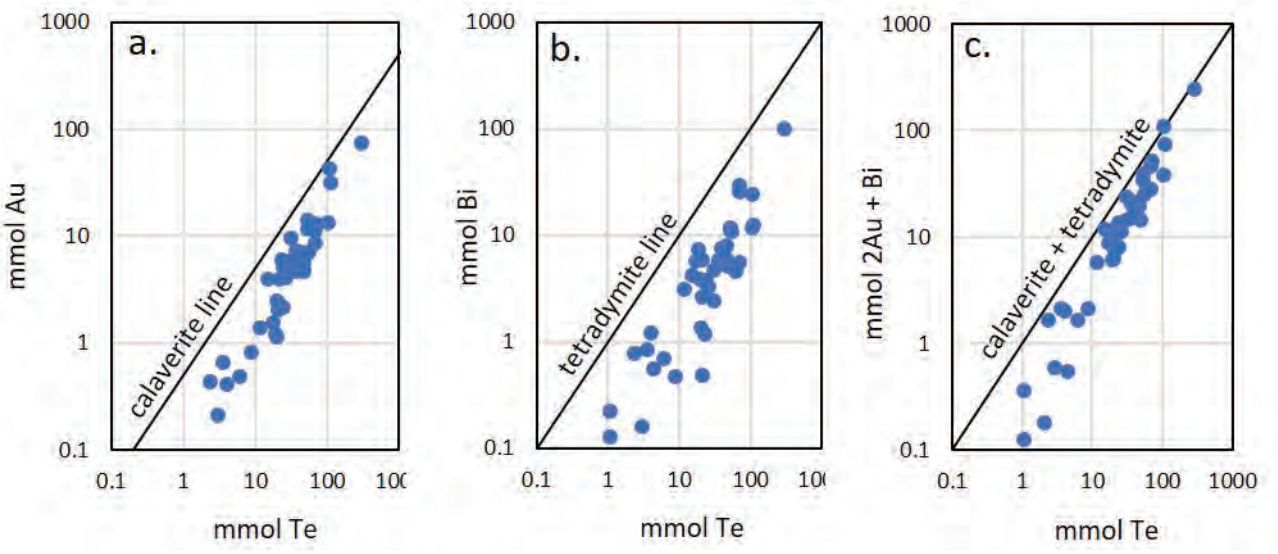

Figure 5. Comparison of the concentrations of Au, Bi, and Te obtained by pXRF measurement to the ideal compositions for calaverite, tetradymite, and calaverite + tetradymite.

calaverite and tetradymite are controlling the concentrations of gold and bismuth, respectively, in these samples.

Comparison to Previous Work

The mineralogy of the MHBP at Golden Sunlight was examined in detail by Spry and others (1997) and Spry and Thieben (2000). These authors list 51 mineral species, including most of the minerals found in this study, i.e., quartz, barite, celestite, pyrite, gold, calaverite, tetradymite, and wittichenite. These minerals fit into "Stage 1b" of the overall paragenesis for the Golden Sunlight deposit, which was the main gold-bearing event (Porter and Ripley, 1985; Spry and Thieben, 2000). However, Spry and coworkers did not report the presence of goldfieldite, mawsonite, hodrušite, or monazite. Te-bearing tennantite (with insufficient Te to be classified as goldfieldite) was found in minor amounts at the Apex deposit, a satellite ore body to the north of the main Mineral Hill breccia pipe (Gammons and others, 2022).

Hodrušite is a rare mineral, having been reported from 35 localities worldwide based on the Mindat database (accessed in October, 2023), including 4 mines in the U.S.: Bisbee (AZ), the Alice Mine (CO), the Black Metals Mine (NV), and the Outlaw Mine (NV). Mawsonite has been reported from 7 locations in the U.S., including the Mountain Con mine of Butte (MT), the Bisbee and Magma mines (AZ), the Golden Fleece and Sweet Home mines (CO), Bingham (UT), and the Silver Mine (MO). Goldfieldite is more common, having been reported from at least 15 localities in the U.S., including the Tramway Mine of Butte (MT), Bisbee (AZ), Sweet Home (CO), and several mines in the Goldfield district (NV), which is the type location for this mineral.

Speculations as to the Origin of the High-Grade Ore

The unusually high-grade Au-Te-Bi-S ore lacking Ag documented at GSM in this study begs an explanation. Although it is possible that the rich mineralization is simply an example of focused precipitation of gold, tetradymite, and calaverite from hydrothermal fluids, the dominance of calaverite and the other ore minerals as mono-mineral and polymineral inclusions in pyrite suggests another possible mechanism. A recent paper by Jian and others (2021) describes polymineral inclusions from a telluride-rich Au-Ag deposit in China. The authors speculate that the inclusions originated as small droplets of Au-Ag-Te-S melts on the pyrite surface which later, upon cooling, crystallized into the complex textures of three or more minerals observed under the microscope (see fig. 6). Other workers (e.g., Zhang and others, 2023, and

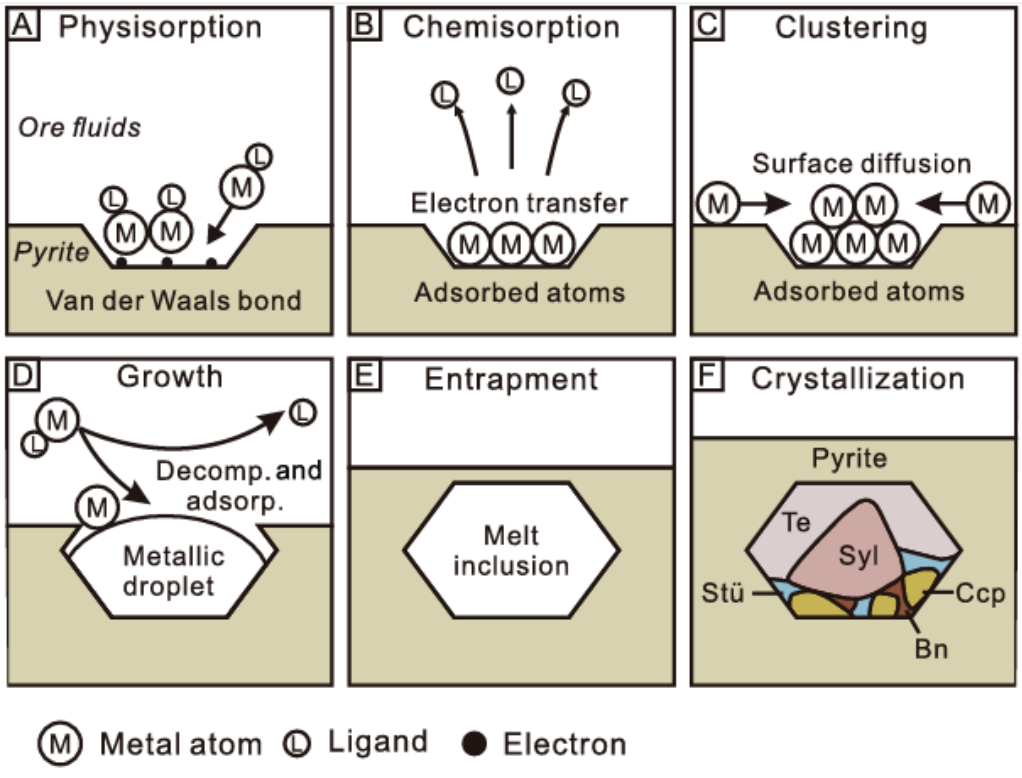

Figure 6. Reproduction of a portion of figure 7 of Jian and others (2021), showing their proposed mechanism of formation of polymineral Au-Ag-Te inclusions in pyrite. Abbreviations: M, metal; L, ligand; Te, tellurium; Syl, sylvanite; Stü, stüzite, Ccp, chalcopyrite, Bn, bornite.

references therein) have pointed out the possible role of polymetallic melts in scavenging gold from hydrothermal solutions. Recognition that melts can exist at temperatures as low as 241°C in the case of the pure Au-Bi binary system (Nathans and Lieder, 1962) led to the so-called "liquid bismuth collector model" for enrichment of gold in natural hydrothermal systems (Cockerton and Tomkins, 2012; Tooth and others, 2008, 2011). In the present case, the existence of Te, S, and Cu, in addition to Au and Bi, clouds the picture, as phase diagrams do not exist for such four- or five-component systems. Nonetheless, we believe it is plausible that Au-Bi-Te-S-Cu melt droplets overgrown by pyrite later crystallized into the polymineral inclusions that we see in figure 4. It is possible that many of the "solitary" inclusions shown in figure 3 are in fact polymineral inclusions in which the plane of the polished surface has only intersected one phase.

Conclusions

The high-grade core donated to MTU from the Golden Sunlight Mine contains an abundance of calaverite, tetradymite, and native gold, in addition to many other minerals, several of which have not previously been reported from GSM. The unique textures displayed by the ore minerals suggests the possibility that polymetallic melts could have played a role in the sequestration of gold and other elements from hydrothermal solution. More work is recommended to test this hypothesis.

Acknowledgments

We thank GSM for donating the core box, and Gary Wyss for help with the SEM work. We also thank George Brimhall and Adrian Van Rythoven for reviews of the paper.

References

Ahmad, M., Solomon, M., and Walshe, J.L., 1987, Mineralogical and geochemical studies of the Emperor gold telluride deposit, Fiji: Economic Geology, v. 82, p. 345–370, https://doi.org/10.2113/GSECONGEO.82.2.345.

Cockerton, A.B., and Tomkins, A.G., 2012, Insights into the liquid bismuth collector model through analysis of the Bi-Au Stormont skarn prospect, northwest Tasmania: Economic Geology, v. 107, p. 667–682, https://doi.org/ 10.2113/econgeo.107.4.667.

DeWitt, E., Foord, E.E., Zartman, R.E., Pearson, R.C., and Foster, F., 1996, Chronology of Late Cretaceous igneous and hydrothermal events at the Golden Sunlight gold-silver breccia pipe, southwestern Montana: U.S. Geological Survey, Bulletin 2155, 48 p.

Foster, F., and Childs, J.F., 1993, An overview of significant lode gold systems in Montana, and their regional geologic setting: Exploration and Mining Geology, v. 2, p. 217–244.

Gammons, C.H., Gnanou, H., Odt, D., and Poulson, S.R., 2020, Mineralogy and sulfur-isotope geochemistry of polymetallic, porphyry-epithermal mineralization peripheral to the Golden Sunlight gold mine, Montana: Ore Geology Reviews, v. 126, 103797, 12 p., https://doi.org/ 10.1016/j.oregeorev.2020.103797.

Gammons, C.H., Korzeb, S., and Hargrave, P., 2022, Metallic ore deposits of Montana, *in* Metesh, J.J., and Gammons, C.H., eds., Geology of Montana—Special Topics: Montana Bureau of Mines and Geology Special Publication 122, v. 2, 30 p.

Jian, W., Mao, J., Lehmann, B., Cook, N., Xie, G., Liu, P., Duan, C., Alles, J., and Niu, Z., 2021, Au-Ag-Te–rich melt inclusions in hydrothermal gold-quartz veins, Xiaoqinling lode gold district, central China: Economic Geology, v. 116, p. 1239–1248, https://doi.org/ 10.5382/econgeo.4811.

Müller, D., Kaminski, K., Uhlig, S., Graupner, T., Herzig, P.M., and Hunt, S., 2002, The transition from porphyry- to epithermal-style gold mineralization at Ladolam, Lihir Island, Papua New Guinea: A reconnaissance study: Mineralium Deposita, v. 37, p. 61–74, https://doi.org/10.1007/s00126-001-0230-y.

Porter, E.W, and Ripley, E.M, 1985, Petrologic and stable isotope study of the gold-bearing breccia pipe at the Golden Sunlight Deposit, Montana: Economic Geology, v. 80, p. 1689–1706, https://doi.org/10.2113/gsecongeo.80.6.1689.

Richards, J.P., and Kerrich, R., 1993, The Porgera gold mine, Papua New Guinea: Magmatic-hydrothermal to epithermal evolution of an alkalic-type precious metal deposit: Economic Geology, v. 88, p. 1017–1052, https://doi.org/ 10.2113/GSECONGEO.88.5.1017.

Spry, P.G., and Thieben, S.E., 2000, The distribution and recovery of gold in the Golden Sunlight gold-silver telluride deposit, Montana, U.S.A: Mineralogical Magazine, v. 64, p. 31–42.

Spry, P.G., Paredes, M.M., Foster, F., Truckle, J.S., and Chadwick, T.H., 1996, Evidence for a genetic link between gold-silver telluride and porphyry molybdenum mineralization at the Golden Sunlight Deposit, Whitehall, Montana; fluid inclusion and stable isotope studies: Economic Geology, v. 91, p. 507–526, https://doi.org/ 10.2113/GSECONGEO.91.3.507.

Spry, P.G., Foster, F., Truckle, J.S., and Chadwick T.H., 1997, The mineralogy of the Golden Sunlight gold-silver telluride deposit, Whitehall, Montana, USA: Mineralogy and Petrology, v. 59, p. 143–164.

Thompson, T.B., Trippel, A.D., and Dwelley, P.C., 1985, Mineralized veins and breccias of the Cripple Creek district, Colorado: Economic Geology, v. 80, p. 1669–1688.

Tooth, B., Brugger, J., Ciobanu, C., and Liu, W., 2008, Modeling of gold scavenging by bismuth melts coexisting with hydrothermal fluids: Geology, v. 36, p. 815–818, https://doi.org/ 10.1130/G25093A.1.

Tooth, B., Ciobanu, C.L., Green, L., O'Neill, B., and Brugger, J., 2011, Bimelt formation and gold scavenging from hydrothermal fluids: An experimental study: Geochimica et Cosmochimica Acta, v. 75, p. 5423–5443, https://doi.org/10.1016/j.gca.2011.07.020.

Zhang, M., Shen, J., Santosh, M., Li, C., Liu, H., Yu, H., Kamoto, M., Du, B., and Liu, J., 2023, Tellurium and gold enrichment aided by melts and pyrite crystallization kinetics: Insights from the Yongxin gold deposit, Northeast China: Ore Geology Reviews, 105370, https://doi.org/10.1016/j.oregeorev.2023.105370.

Mineralogy, Fluid Inclusion, and S-Isotope Investigation of the Winston Mining District, Broadwater County, Montana: A Reduced, Intrusion-Related Gold System?

Christopher H. Gammons[1] and Simon R. Poulson[2]

[1]*Montana Tech, Department of Geological Engineering, Butte, MT*

[2]*University of Nevada-Reno, Department of Geological Sciences and Engineering, Reno, NV*

cgammons@mtech.edu

Introduction

The Winston District, also known as the Beaver Creek District, lies about 20 mi (32 km) southeast of Helena on the northeast slope of the Elkhorn Mountains, near the town of Winston, Montana. Regionally, the Winston District belongs to a cluster of gold-rich deposits proximal to the northeast edge of the Boulder Batholith (fig. 1). Other deposits of note include the Diamond Hill Mine (a former Pegasus Gold Corp. underground mine), the Keating and Ohio–Keating mines of the Radersburg District, and the gold-rich skarns and breccia pipes of the Elkhorn District (Klepper and others, 1971).

Gold was first discovered in the Winston area in 1867 by George Brooks at what later became the East Pacific mine, the largest historic producer in the district (Pardee and Schrader, 1933; Earll, 1964; Klepper and others, 1971). Exploration quickly expanded, and the district was eventually home to more than 30 small- to medium-sized underground mines that operated sporadically through the early to mid-20th century (fig. 2; Earll, 1964). Between 1906 and 1957, the district produced a total of 104,000 oz of gold, 1.5 M oz of silver, over 10,000 tons of lead, and minor copper and zinc, from 149,000 short tons of ore (Earll, 1964). Between 1984 and 1995, several exploration companies conducted extensive drilling programs in an attempt to define one or more shallow, low-grade, bulk-tonnage gold deposits (Tysdal and others, 1996; Capps Geoscience, 2015). After metallurgical testing and open-pit feasibility studies, the projects were mothballed. More recently, in 2019, the Winston Gold Company drove a new decline, the Carrabba Tunnel (fig. 3A), into the side of Edna Hill to explore the western extension of the Custer and Hyantha mine workings at the 500-ft level. The objective was to intercept unoxidized veins of high enough gold grade to allow selective underground mining (Capps Geoscience, 2015). As of 2023, the Winston Gold project is on hold, awaiting financing.

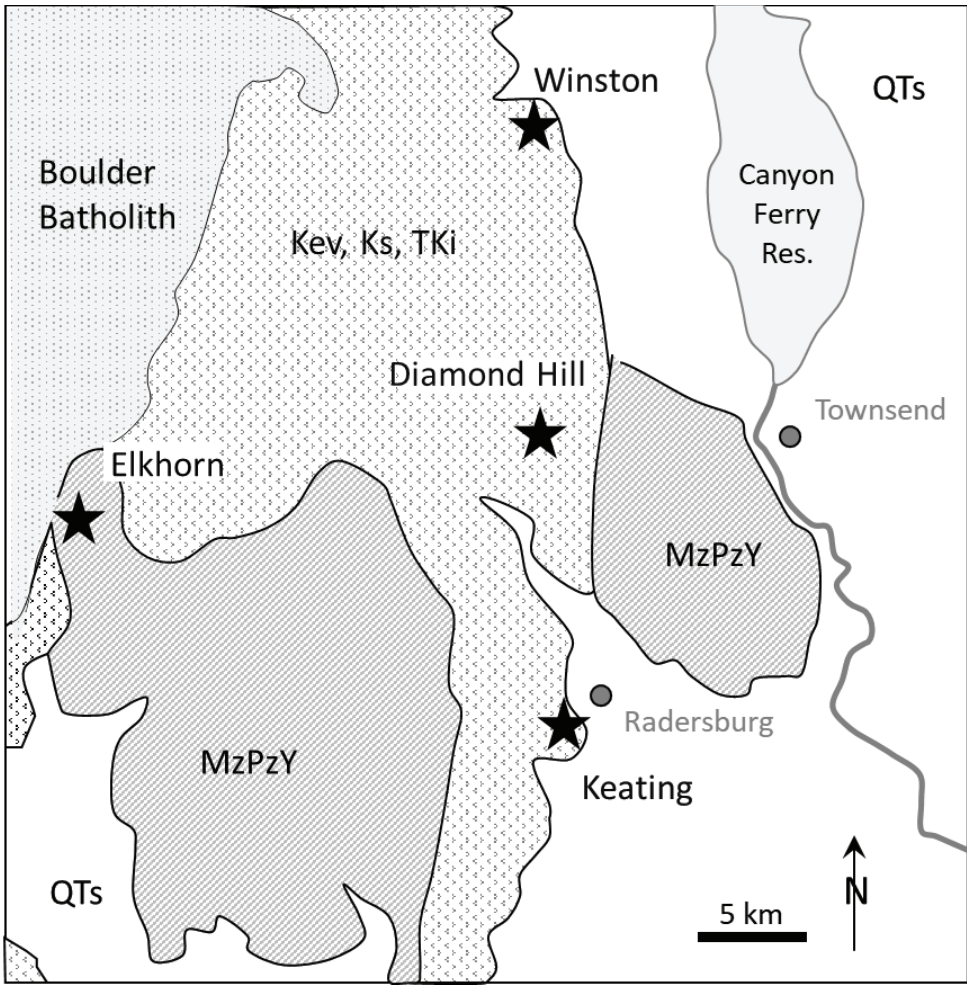

Figure 1. Simplified geologic map (after Klepper and others, 1971) of a portion of the Elkhorn Mountains showing the location of the Winston, Diamond Hill, Keating, and Elkhorn mining districts. MzPzY, Mesoproterozoic to early Cretaceous sedimentary rocks, undivided; Kev, Elkhorn Mountains Volcanics; Ks, middle to late Cretaceous sedimentary rocks; TKi, Tertiary and late Cretaceous intrusions; QTs, Tertiary to Quaternary sediments, undivided.

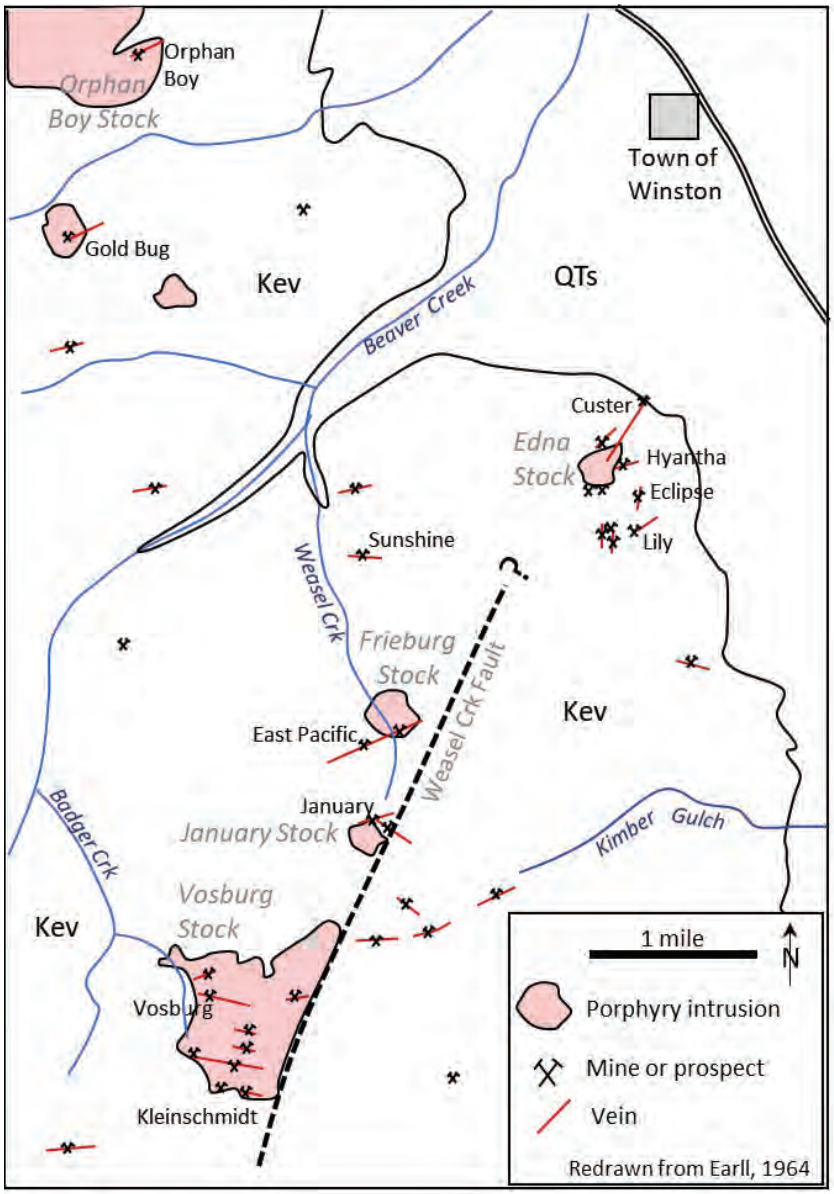

Figure 2. Simplified geology of the Winston District (redrawn from Earll, 1964), showing the locations of Cretaceous intrusions, mines, and prospects. Major veins are also shown. The approximate trace of the Weasel Creek Fault has been added (Klepper and others, 1971). Kev, Cretaceous Elkhorn Mountains volcanics; QTs, Quaternary and Tertiary sediments.

Figure 3. Photographs of the most recent mining operations, including the new Carrabba Tunnel (left) and an underground view of a narrow, steeply dipping sulfide vein (right).

Mineralization in the Winston District consists of narrow (0.1 to 2 m) fissure veins (fig. 3B) cutting the Elkhorn Mountains Volcanics and small porphyry stocks of presumed Late Cretaceous age. Several of these porphyry bodies are aligned along an inferred structure named the Weasel Creek Fault by Klepper and others (1971; fig. 2). All previous workers have noted a close spatial association between the gold-bearing veins and the intrusions, and have assumed a genetic association as well. Figure 4 shows a radial distribution of veins and faults around the Edna Stock (Capps Geoscience, 2015). Most of these veins are steeply dipping, although a set of auriferous veins with similar mineralogy parallel to layering in the shallowly dipping volcanics can be traced into the Edna Stock (Earll, 1964). Where exposed, the flat veins are cut by the steep veins (Earll, 1964). Most of the veins elsewhere in the district are steeply dipping and strike roughly east–west, although flat veins occasionally were encountered, as in the Kleinschmidt Tunnel (Klepper and others, 1971).

Methods

A set of hand samples was collected in 2020 from the Carrabba Tunnel near the intersection of the Custer and Hyantha veins at the 500 level. These samples are hereafter referred to as the "Carrabba samples." Additional samples containing quartz veins and fresh sulfides were collected in 2023 from the dumps of the East Pacific mine and the Kleinschmidt Tunnel (Vosburg Stock, see fig. 2). In addition, numerous altered and unaltered samples were collected from the January Stock (0.5 km south of East Pacific, see fig. 2) and the Edna Stock. Two other pyrite-rich samples mentioned below were collected from the Last Chance mine, a small deposit within the Diamond Hill Stock near the headwaters of Indian Creek, to the immediate south of the Winston district. Samples were sliced with a water saw and polished plugs were made to examine sulfide and gangue mineralogy by reflected light microscopy and scanning electron microscope-energy dispersive spectroscopy (SEM-EDS) at Montana Technological University (MTU). Several samples containing vein quartz were sliced

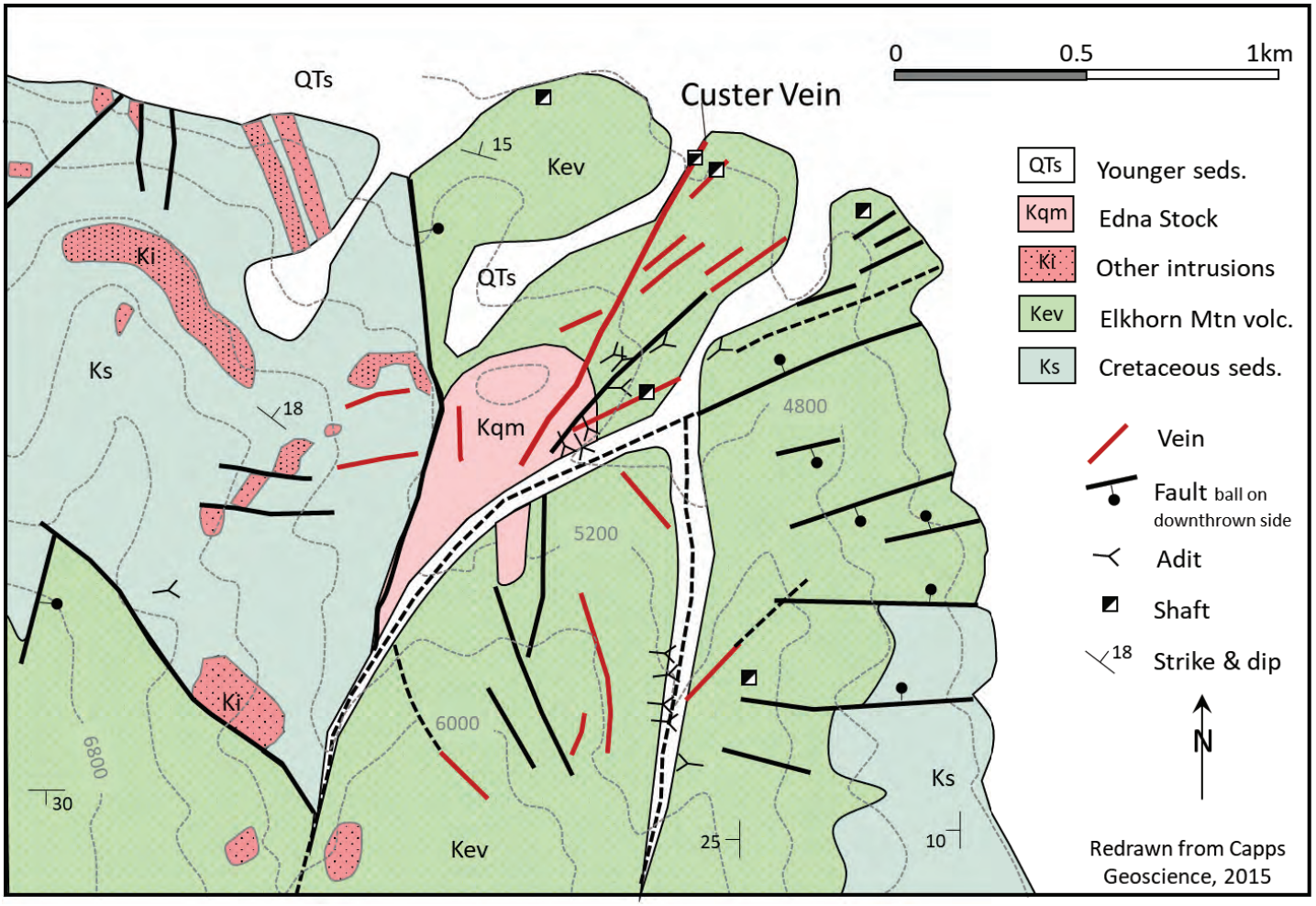

Figure 4. Geology of a portion of the Winston District (redrawn from Capps Geoscience, 2015), showing radial distribution of faults and veins around the Edna Stock (Kqm). Thin dashed lines show elevation with a contour interval of 400 ft.

to 100-µm thickness and doubly polished for fluid inclusion microthermometry using a USGS heating–freezing stage. All of this work was done at MTU. In addition, 24 samples of sulfide minerals (pyrite, galena, sphalerite, pyrrhotite, and molybdenite) were separated from the hand samples and submitted to the University Nevada-Reno for S-isotope analysis. The $\delta^{34}S$ measurements were performed on an isotope-ratio mass spectrometer (IRMS) and are reported in the usual per mil (‰) notation relative to the Vienna Canon Diablo Troilite standard. The analyses have an estimated analytical error of ±0.1‰.

Mineral Paragenesis

Carrabba Tunnel

Samples from the Custer and associated veins exposed in the Carrabba Tunnel contain abundant pyrite, arsenopyrite, sphalerite, and galena, with less common chalcopyrite, pyrrhotite (as inclusions in pyrite), and trace scheelite and molybdenite. Based on SEM-EDS analyses (n = 8), sphalerite has an average of 4.61 wt% Fe, which corresponds to a mole fraction of FeS in sphalerite (X_{FeS}) of 8.2%. This sphalerite is non-fluorescent under long-wave UV light. Traces of manganese, cadmium, copper, and indium were also seen in the EDS spectra for sphalerite. Pyrite is by far the most abundant sulfide, and can constitute up to 100% of the vein. Gold occurs with the sulfides as coarse (up to 50 µm diameter), round to irregular-shaped inclusions (fig. 5). Based on SEM-EDS analyses (n = 8), the gold is better identified as electrum, with an average fineness of 0.644 and an average mole fraction of gold (X_{Au}) = 0.51. Gangue minerals are sparse, but include quartz and Mn-bearing calcite. Scheelite was found in one of the electrum-rich samples, where it constitutes roughly 1% of the specimen (based on UV fluorescence). Under the SEM, the scheelite is seen to be intergrown with calcite in an odd texture (fig. 6). It is speculated that

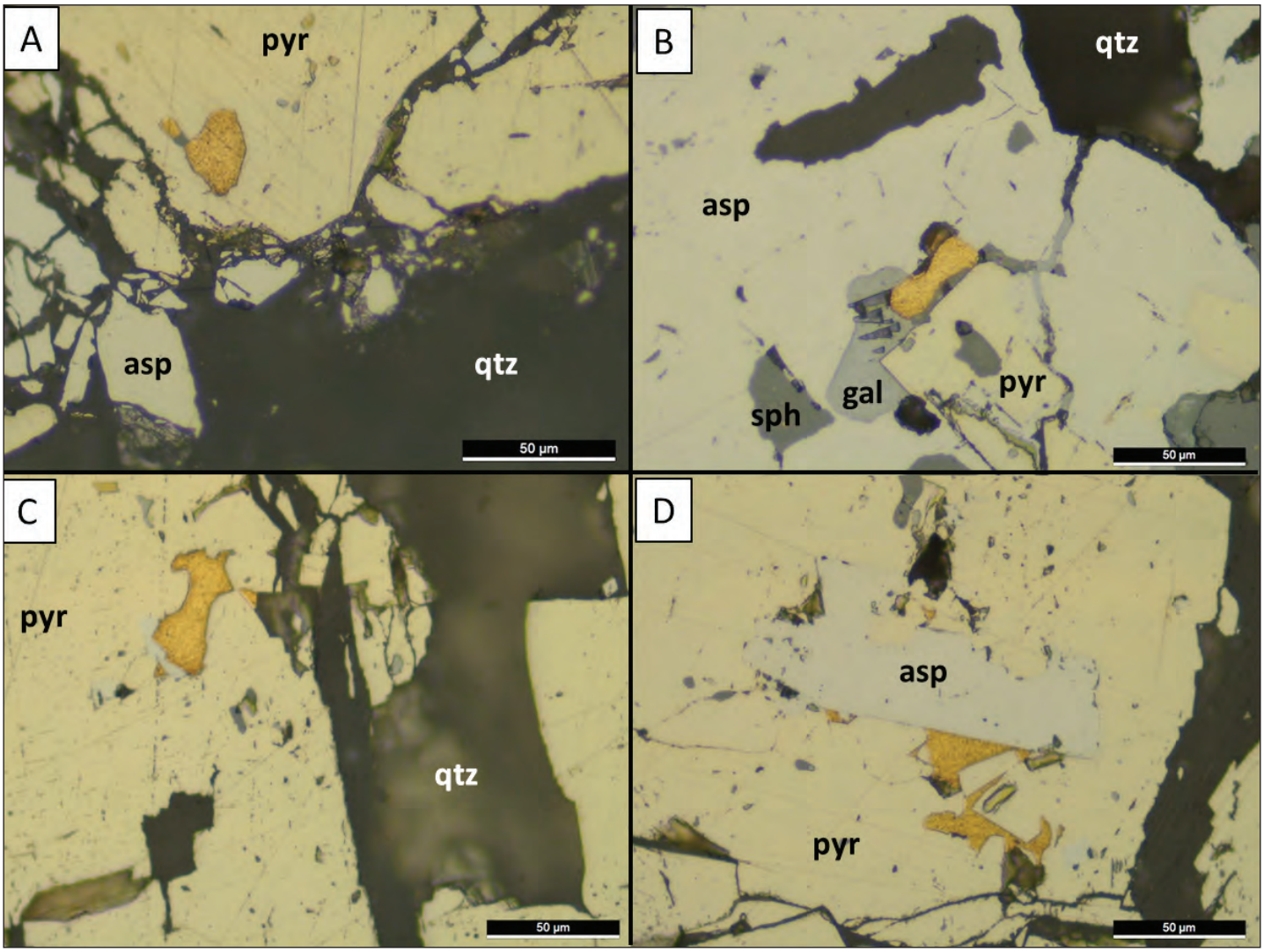

Figure 5. Photomicrographs (reflected light) of gold grains from pyrite-rich veins in the Carrabba Tunnel. Gold is the deep yellow grain in all photos. Abbreviations: pyr, pyrite; asp, arsenopyrite; sph, sphalerite; gal, galena; qtz, quartz. Scale bar is 50 µm in all photos.

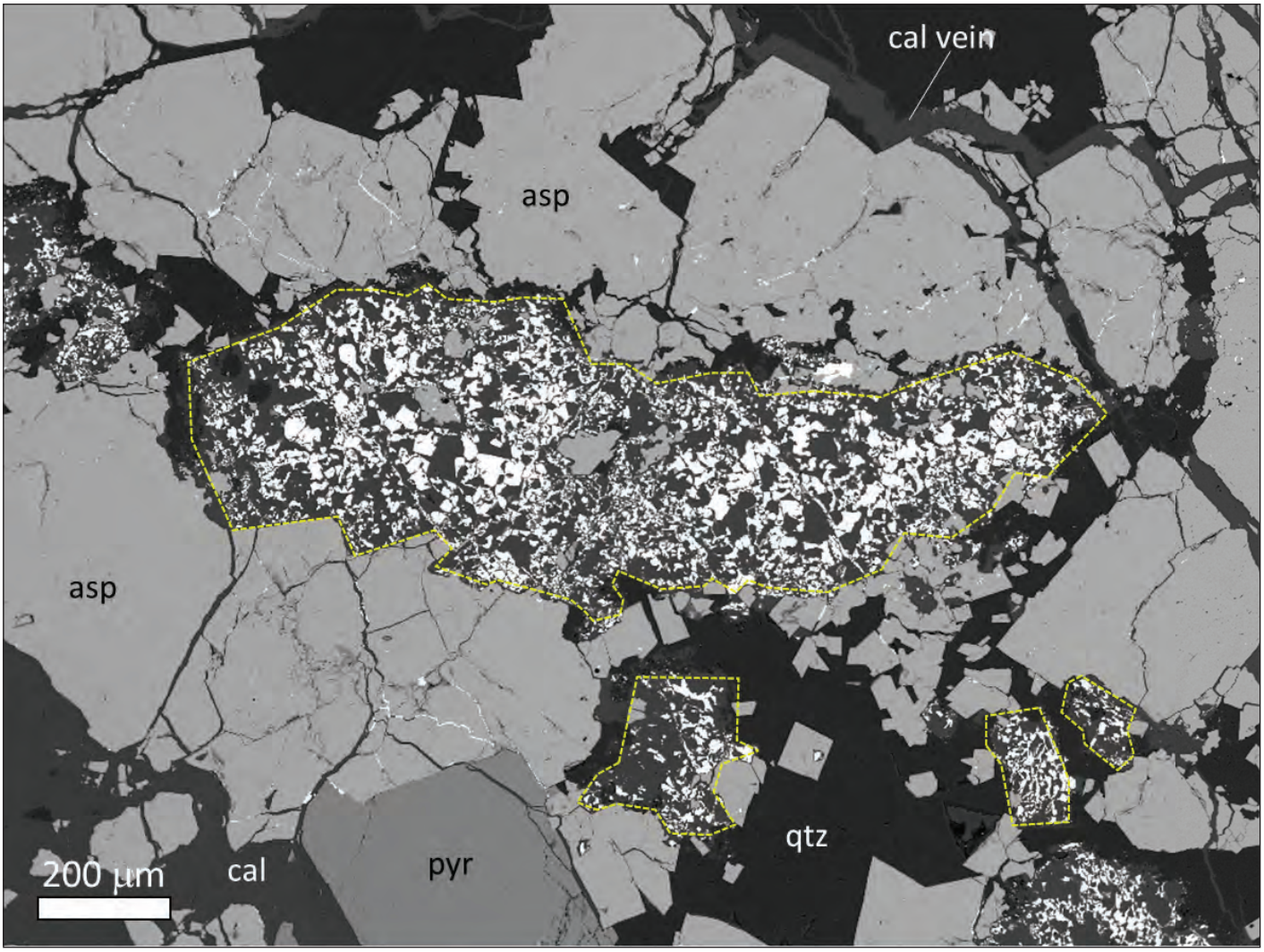

Figure 6. BSE image of scheelite–calcite intergrowths from sample W-1. The dashed yellow lines show the outlines of what may have originally been wolframite grains. Abbreviations: asp, arsenopyrite; pyr, pyrite; cal, calcite; qtz, quartz; scheelite (unlabeled) is bright white.

the original W mineral in this sample was wolframite ((Fe,Mn)WO_4), and that later fluids replaced the wolframite by a mix of scheelite + calcite. The paragenetic relationship between the common sulfides and molybdenite is not known, as the latter was only found in a single veinlet cutting altered volcanic rock, away from the main sulfide veins. Klepper and others (1971) reported that the Kleinschmidt tunnel, driven into the Vosburg (Olga) Stock, exposed a gently dipping, quartz–pyrite vein with gold and molybdenite that was cut by a steeply dipping, polymetallic sulfide vein.

Edna Stock

The granitic Edna Stock crops out at the top of a prominent hill behind and to the northwest of the portal of the Carrabba Tunnel. The stock forms blocky, Fe-oxide-stained talus and is crisscrossed by old trenches and drill roads. Where fresh, the stock contains millimieter-sized phenocrysts of black biotite (X_{annite} = 0.76), clear K-feldspar, and cloudy plagioclase (An_{20}), along with ~1 mm, round, dark gray phenocrysts of quartz, in a very hard, dark, aphanitic matrix (fig. 7). Several generations of quartz veins cut the stock, including opaque-milky and translucent-gray varieties. The latter type is younger, and is associated with sulfides. Where mineralized, the stock contains several volume % pyrite as disseminated, idiomorphic crystals (up to 4 mm) and veinlets (up to 1 cm wide) cutting the porphyritic rock. Feldspars and biotite are completely altered to clear to light green muscovite in the pyrite-bearing samples. Along with pyrite, the altered porphyry contains dispersed grains of sphalerite and galena. The sphalerite is Fe-rich (average X_{FeS} = 0.06) and has chalcopyrite disease. A single occurrence of electrum (X_{Au} = 0.54) was found in a fracture cutting pyrite.

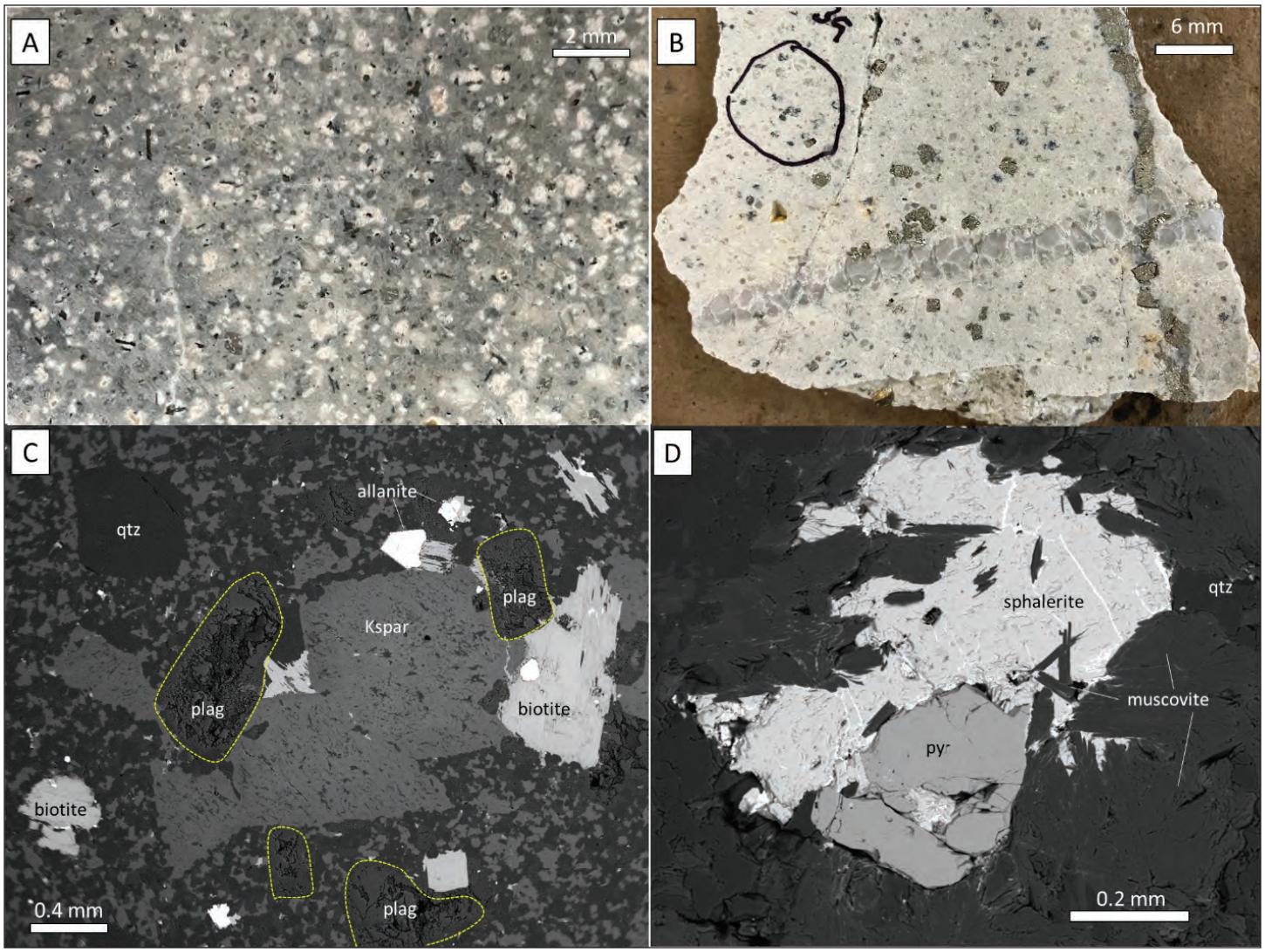

Figure 7. Photographs of the Edna Stock. (A) Unaltered Edna Stock showing phenocrysts of biotite (black), feldspars (white), and quartz (dark gray, rounded). (B) Altered Edna Stock cut by quartz and pyrite veins. Sphalerite (dark gray spots in circled area) and pyrite are disseminated through the sericite-altered matrix. (C) SEM-BSE image of the fresh stock, showing phenocrysts of K-feldspar, plagioclase (partly altered, outlined by dashed lines), quartz, and biotite in a finer matrix of quartz + Kspar. (D) SEM-BSE image of the altered stock, showing sphalerite and pyrite surrounded by muscovite + quartz.

East Pacific Mine

Compared to the veins of the Carrabba Tunnel, mineralized samples found on the dumps of the East Pacific Mine contain more quartz and a greater variety of sulfides, including sphalerite, galena, chalcopyrite, and tetrahedrite, in addition to pyrite and minor arsenopyrite. The ore minerals are coarse grained and occur as bands with cockscomb quartz and late calcite (fig. 8).Tetrahedrite is Ag-rich (average of ~ 15 wt% Ag) and has a high Sb/As ratio. The Fe-content of sphalerite is variable (X_{FeS}< 0.01 to about 0.03), but is considerably lower than at the Edna Stock and Custer Vein areas. The more Fe-rich sphalerite contains small inclusions of chalcopyrite (i.e., “chalcopyrite disease”). The Fe-poor sphalerite fluoresces orange under long-wave UV light (figs. 8B, 8D). No grains of native gold or electrum were found. Country rock at the East Pacific Mine is contact-metamorphosed andesite of the Elkhorn Mountain Volcanics. The Freiberg porphyry stock, which crops out less than 0.5 km to the northeast of the East Pacific mine workings, is on private ground and was not visited during this study.

January Stock

The January Stock was sampled where it crops out along the Weasel Creek road. This rock resembles the Edna Stock in that it is >80% aphanitic matrix, with scattered phenocrysts of plagioclase (avg. composition An_{30}) and alkali feldspar (some up to 5 mm), round quartz eyes (~1 mm), and minor clinopyroxene. Like the Edna, the January Stock weathers to a limonite-stained scree. However, the source of the Fe staining in the January Stock proved to be fine-grained, dis-

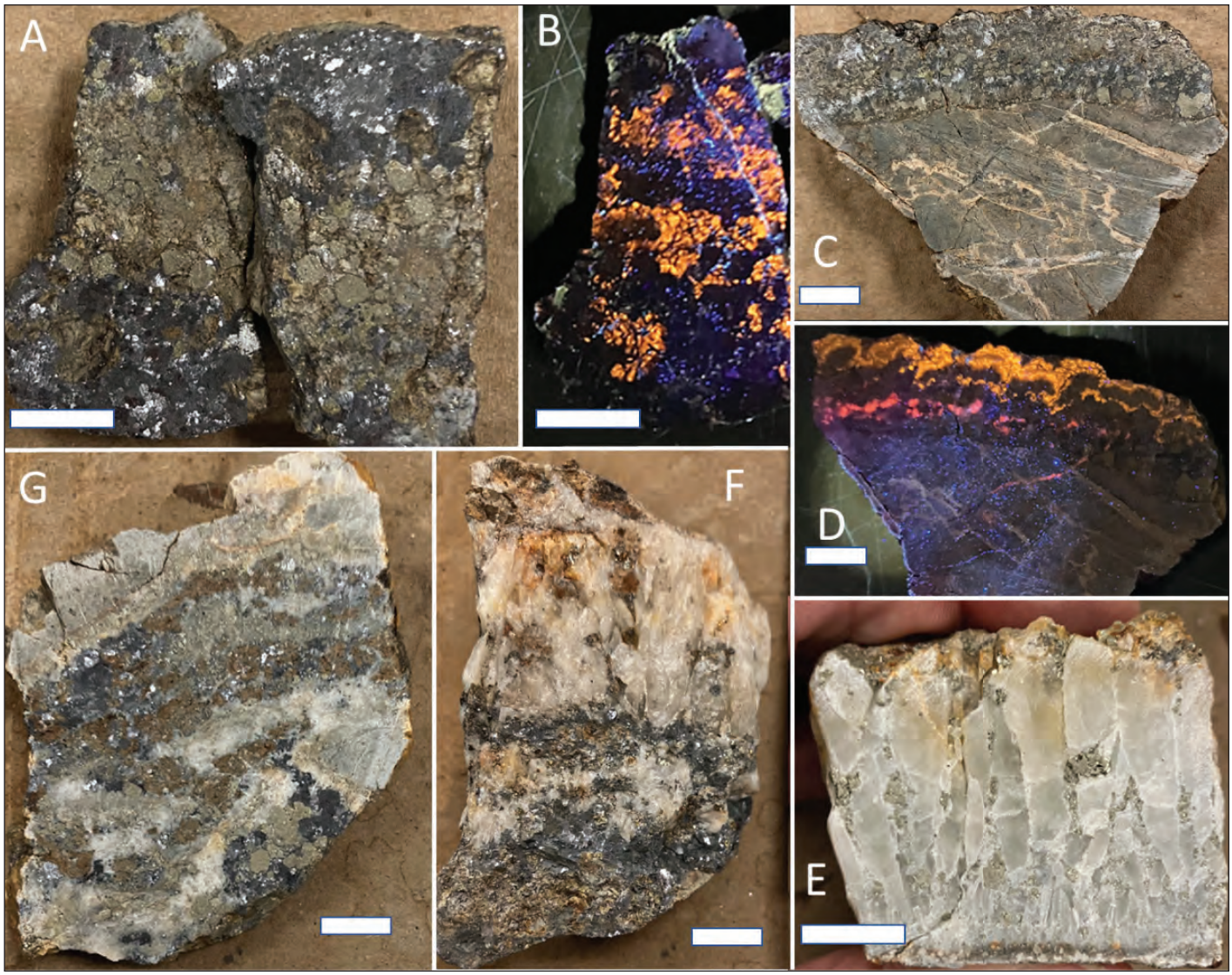

Figure 8. Photos of sawn samples from the East Pacific mine dumps. Scale bar is 1 cm. Moving clockwise: (A) massive galena, sphalerite and pyrite (EP-3); (B) long-wave UV shows fluorescent sphalerite in piece at left of image A; (C) band of sphalerite (top) cutting altered andesite (EP-1); (D) same as C, showing fluorescent orange sphalerite in outer growth band (pink is calcite); (E) coarse, comb-textured quartz with pyrite (EP-9); (F) quartz with bands of sphalerite + galena (EP-7); (G) pyrite, sphalerite (brown), and galena in a mixed quartz-carbonate gangue, with fragments of silicified andesite country rock (EP-5).

seminated pyrrhotite, as opposed to the coarse-grained pyrite of the Edna intrusion. Disseminated pyrrhotite grains constitute over 1% of the rock, and are locally intergrown with apatite. Quartz veins are comparatively scarce in the January Stock, at least where it crops out along the Weasel Creek road.

Fluid Inclusions

Three doubly polished samples of quartz were examined for fluid inclusions: (1) a sample of gray quartz intergrown with sulfides from the Custer Vein; (2) a sample of gray quartz with pyrite in a 1 cm vein cutting the Edna Stock; and (3) a sample of coarse-grained, comb-texture quartz with pyrite from the East Pacific Mine. All three samples are rich in fluid inclusions that have broadly similar characteristics, with a range in size up to 20 to 30 μm. Three different types of fluid inclusion were defined, based on the phases visible at room temperature and at the temperature of total homogenization. Type 1A are three-phase, CO_2-rich inclusions that show total homogenization to water (fig. 9); Type 1B are three-phase, CO_2-rich inclusions that show total homogenization to CO_2; Type 3 are water-rich inclusions with no evidence of CO_2 that homogenize to liquid water. Type 1A inclusions are the most common, and are thought to be primary or pseudo-secondary, judging from their abundance in the cores of zoned quartz grains. Type 1B were only found in the sample from the Edna Stock, where they coexist with Type 1A in a manner that indicates CO_2-H_2O immiscibility at the time of trapping. Type 2 inclusions are assumed to be pseudo-secondary or

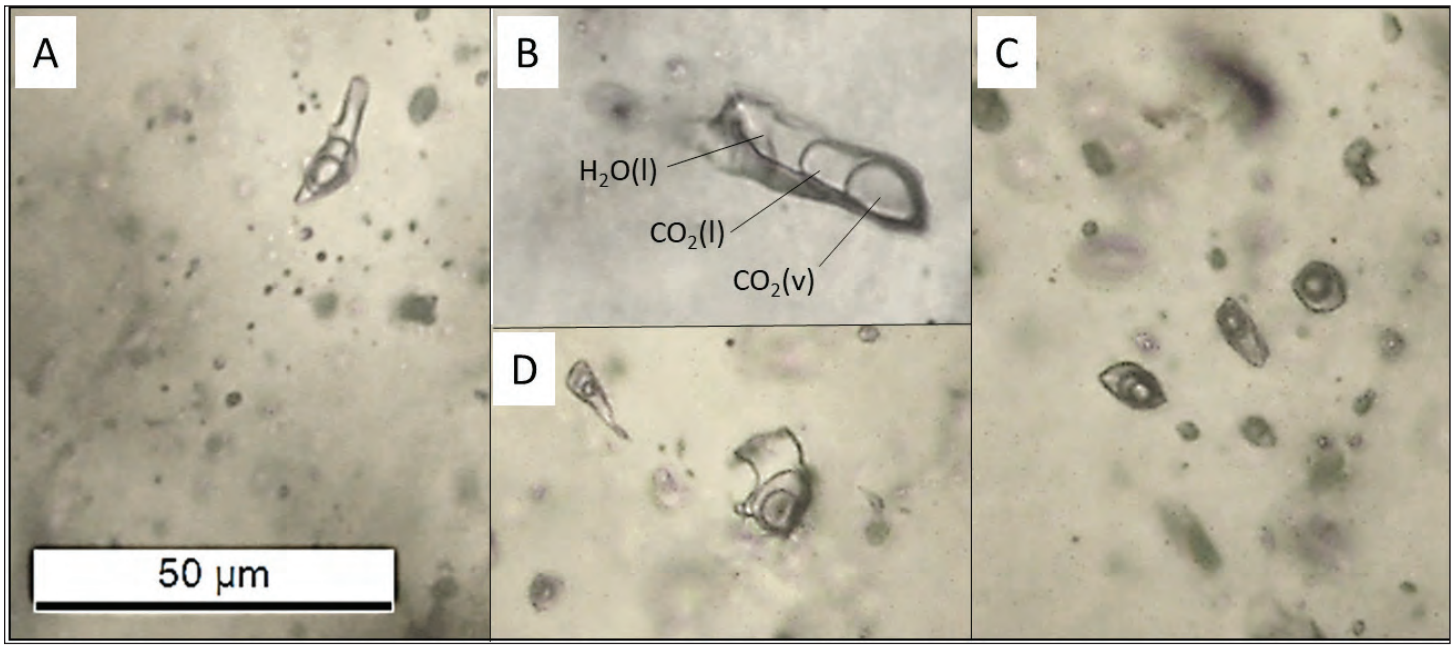

Figure 9. Photomicrographs of primary, CO_2-rich (Type 1A) fluid inclusions in quartz from the Carrabba Tunnel. (B) The inclusion is 22 µm long; (C) three Type 1A inclusions, about 8 µm in diameter; (D) inclusion in center is 15 x 25 µm.

secondary. Salinities of CO_2-rich inclusions were calculated based on the temperature of final melting of CO_2-clathrate, whereas the salinity of H_2O-rich inclusions was based on the temperature of final melting of water ice. Both types of inclusions have a similar range in salinity between 4 and 8 wt% $NaCl_{eq}$. The CO_2-rich inclusions showed varying behavior near the CO_2 critical point: some inclusions homogenized to liquid CO_2, some to vapor CO_2, and some exhibited critical behavior (the meniscus between liquid and vapor CO_2 disappeared near 31°C). Most of the larger CO_2-rich inclusions (Types 1A and 1B) decrepitated at temperatures between 250 and 300°C, before final homogenization. Water-rich inclusions showed a wider range in Th between 240 and 310°C. No daughter minerals were found in any inclusions. Histograms of fluid inclusion data from this study can be found in figure 10.

Sulfur Isotopes

The S-isotope compositions of 24 mineral separates from the Winston District are summarized in table 1 and figure 11. Samples from the Carrabba Tunnel, Edna Stock, January Stock, Kleinschmidt Tunnel, and Last Chance deposit show a range in $\delta^{34}S$ between +1.1 and +4.5‰, values that are often considered typical of an igneous, upper mantle S source. Samples from the East Pacific Mine have significantly heavier (more positive) values of $\delta^{34}S$ (+6.5 to +9.1‰). As well, the single molybdenite sample from the Carrabba Tunnel was somewhat heavier

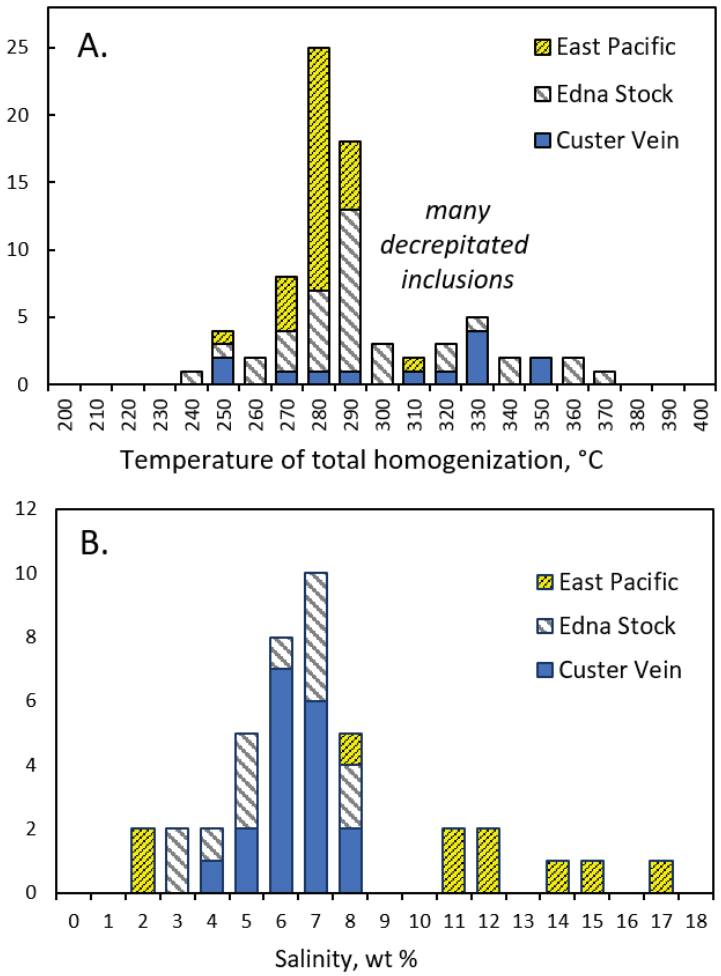

Figure 10. Histograms of fluid inclusions data: (A) total homogenization temperature; (B) salinity, wt% NaCleq. The histogram columns in panel A are underrepresented for T >300°C due to decrepitation of many CO_2-rich inclusions prior to reaching the final homogenization temperature.

Table 1. S-isotope data for sulfide minerals from the Winston District.

Sample	Mineral	$\delta^{34}S$, ‰	Sample	Mineral	$\delta^{34}S$, ‰
Carrabba-7	Pyrite	2.7	East Pacific-1	Sphalerite	8.1
Carrabba-7	Sphalerite	2.8	East Pacific-2	Sphalerite	8.0
Carrabba-7	Galena	1.1	East Pacific-2	Galena	6.0
Carrabba-4	Pyrite	4.4	East Pacific-2	Pyrite	8.1
Carrabba-6	Pyrite	4.5	East Pacific-8	Sphalerite	8.7
Carrabba-X	Molybdenite	6.3	East Pacific-8	Galena	6.5
Edna-1	Pyrite	1.8	East Pacific-9	Pyrite	8.3
Edna-2	Pyrite	3.5	East Pacific-14	Sphalerite	9.1
Kleinschmidt-1	Pyrite	3.1	East Pacific-14	Galena	7.0
Kleinschmidt-2	Pyrite	4.2	East Pacific-21	Pyrite	7.5
Kleinschmidt-3	Pyrite	2.8	Last Chance 1	Pyrite	2.7
January Stock	Pyrrhotite	2.2	Last Chance 4	Pyrite	3.4

(+6.3‰) than the other sulfide minerals in the Custer Vein area. The reasons for these differences are not known at this time.

Figure 11 includes S-isotope data from the Keating (Radersburg) gold-rich vein deposits, the Diamond Hill gold-rich skarn deposit, and the Elkhorn district (data reported previously by Gammons and Poulson, 2022; see fig. 1 for mine locations). The Elkhorn district has S-isotope compositions that are broadly similar to those of the East Pacific mine, whereas the gold-rich Keating and Diamond Hill deposits are more similar to the Carrabba Tunnel, Edna, January, and Kleinschmidt samples. The Elkhorn district was mainly a Ag-Pb-Zn producer, similar to the East Pacific mine. More data are needed to confirm a consistent difference in S-isotopes according to metallogeny (i.e., Ag-Pb-Zn vs. gold-rich) in mineral deposits along the eastern margin of the Boulder Batholith.

Isotope geothermometry was attempted for coexisting sphalerite and galena in one sample (Carrabba-7) from the Carrabba Tunnel, and three samples (EP-2, EP-8, and EP-14) from the East Pacific Mine. Different results were obtained depending on the choice of isotope fractionation factors. Using the experimentally determined equation of Czamanske and Rye (1974), temperatures of 368°C and 291 to 318°C were obtained for the Carrabba-7 and EP samples, respectively. The theoretically derived equation of Liu and others (2015) yielded somewhat higher equilibrium temperatures, i.e., 420°C for Carrabba-7 and 336

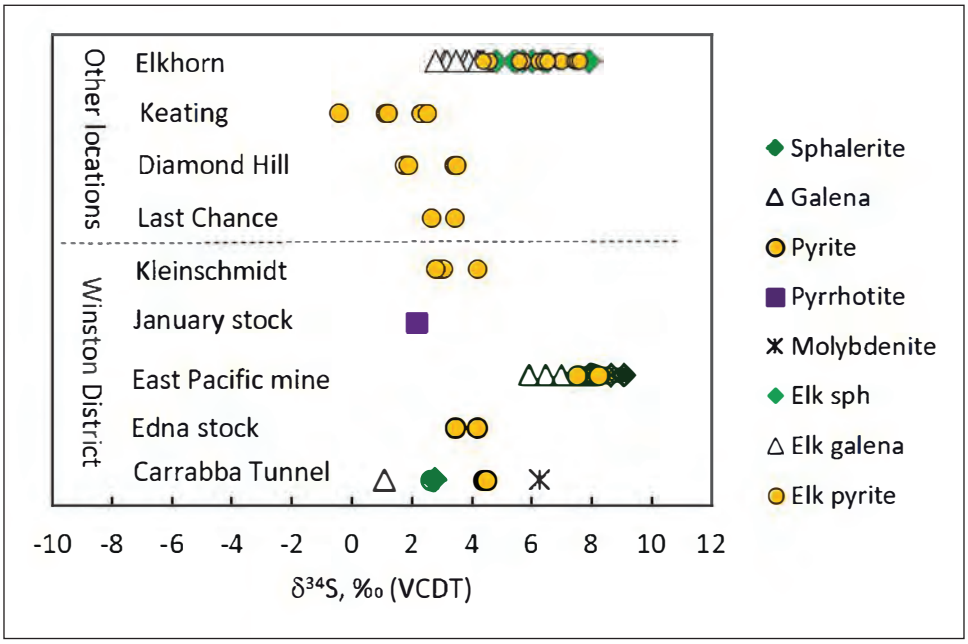

Figure 11. S-isotope results for deposits in the Winston district, compared to outlying regions. Data for the Winston district and Last Chance are from this study. Data for other nearby locations are from Gammons and Poulson (2022).

to 366°C for the East Pacific samples. Together, the S-isotope data suggest a temperature of formation of galena and sphalerite between about 290 and 420°C, which agrees fairly well with the fluid inclusion homogenization temperatures, realizing that the Th values have not been corrected for pressure of trapping.

Discussion: A "Reduced Intrusion Related Gold Systems" Model

Several lines of evidence presented in this paper suggest that Winston, as well as the nearby Diamond Hill, Keating, and Elkhorn deposits, may belong to a newly recognized category of mineralization known as "reduced, intrusion-related gold systems" (RIRGS). Examples of RIRGS deposits include Fort Knox, Alaska; Dublin Gulch, Yukon; and Kidston, Australia (Thompson and Newberry, 2000; Rowins, 2000; Hart, 2007). The characteristics of RIRGS deposits, as reviewed by Hart (2007), include: (1) a close genetic association between gold mineralization and small granitoid intrusions; (2) occurrence of gold in sheeted veins that create a bulk-mineable deposit; (3) zoned vein and/or skarn mineralization from proximal Au-As-W-Bi-Te to distal Ag-Pb-Zn; (4) a reduced sulfide mineral assemblage, including pyrrhotite; (5) formation at depths of 5 to 7 km; and (6) association with hydrothermal fluids that are low salinity (< 10 wt% NaCl) and CO_2-rich.

The close association between auriferous veins and small intrusions is well displayed at Winston (see figs. 2, 4). Also, although each individual vein is thin, the frequency of veining at certain locations is high enough that several companies evaluated the district for its bulk-mineable gold potential (Capps Geoscience, 2015). In terms of metal zonation, the veins in the Carrabba Tunnel, located near the contact of the Edna Stock and surrounding volcanic rock, are certainly enriched in gold and arsenic (as arsenopyrite), whereas the East Pacific mine, located 0.5 km from the Freiburg Stock, had mainly Ag-Pb-Zn production with subordinate, but still important, amounts of gold. The nearby Elkhorn District (fig. 1) shows a clear zonation from proximal Au-rich skarns to distal Ag-Pb-Zn carbonate replacement deposits (Brown and others, 2019). Scheelite was found in one of the Carrabba samples, where it was intergrown with pyrite and arsenopyrite. Scheelite is also an accessory mineral with gold, pyrite, pyrrhotite, and arsenopyrite at the Diamond Hill Mine. Although no telluride minerals were found in this study, several sulfide-rich samples from the Carrabba Tunnel and East Pacific mine dumps had elevated Te (several hundred to several thousand ppm) based on portable X-ray fluorescence (XRF) measurement. Bismuth concentrations are very low (<20 ppm) in all samples from the Winston district, based on XRF data. However, bismuth, in the form of bismuthinite (Bi_2S_3), tetradymite (Bi_2Te_2S), and native bismuth, has been reported in the Au-rich skarns of Elkhorn (Brown and others, 2019). Pyrrhotite is a common phase in the matrix of the January Stock at Winston, and forms small inclusions in pyrite in several Carrabba Tunnel samples. Pyrrhotite is also present in abundance in the Au-rich skarns of Elkhorn and Diamond Hill. The high Fe content of sphalerite in the Carrabba Tunnel and Edna Stock (X_{FeS} = 6 to 8.2%) is consistent with a reduced, low-fS_2 mineral assemblage. Similar high-Fe sphalerite is found at the East Pacific Mine, although low-Fe sphalerite is also present.

As shown by Steele-McInnis (2018), microthermometic measurements of CO_2-rich fluid inclusions can be used to constrain the minimum pressure of formation of hydrothermal mineral deposits. Consider the following example: one of the Type 1A fluid inclusions from the Custer Vein had Tm,clathrate = +6.6°C, Th,CO_2 = 28.8°C (with homogenization to liquid CO_2 phase), and Th,total = 321°C. Inserting these values into the excel algorithm of Steele-McInnis results in a calculated trapping pressure of 2.41 kbar. This corresponds to a depth of trapping of ~8.4 km, assuming a typical geobaric gradient of ~3.5 km/kbar. A depth this great is inconsistent with an epithermal or porphyry-epithermal origin for the Custer Vein, but is within the range of deep (>5 km) RIRGS systems. According to Baker (2002), low salinity, three-phase, CO_2(l)-rich fluid inclusions that homogenize or decrepitate at T >300°C—similar to the Type 1 fluid inclusions of this study—are typical of deep RIRGS deposits. Baker (2002) also pointed out that flat veins are widespread in some deep RIRGS deposits, such as Pogo, Alaska. The presence of flat veins at Winston, in addition to steep fissure veins, is supporting evidence of a deep (i.e., mesothermal) origin for the deposits. Flat quartz veins are also common in orogenic gold deposits that are thought to form in compressional regimes at depths corresponding to the brittle-ductile transition (Groves and others, 2018).

Although not discussed in detail in this paper, it is worth mentioning that the Miller Mountain deposit, located near the head of Confederate Gulch in the Big

Belt Mountains about 20 mi northeast of Winston, is cited as an example of an RIRGS deposit in the review papers of Lang and others (2000) and Hart (2007). The deposit was developed by Pegasus, who announced a low-grade resource of at least 11 million tons containing 310,000 oz gold (du Bray, 1995; Tysdal and others, 1996). Du Bray (1995) described the deposit as having widely disseminated gold in sheared and altered, pyrite-bearing, quartz monzodiorite. It is plausible that a significant fraction of the 600,000 oz of placer gold mined from Confederate Gulch (Lyden, 1948) came from erosion of this deposit. Lund and others (2002) dated a quartz monzodiorite pluton near the Miller Mountain deposit with U-Pb zircon methods, and obtained an age of 66.2 ± 0.9 Ma. This date is similar to the age of the quartz–porphyry dikes and associated Cu-Mo mineralization of Butte (Lund and others, 2002).

The Golden Sunlight Mine (GSM), the largest lode gold producer in Montana, is located 40 mi south–southwest of Winston. Most of the 3.5M oz of gold mined from GSM came from the Mineral Hill Breccia Pipe, an auriferous, pyrite-rich hydrothermal breccia with clasts of Belt Supergroup sedimentary rock and felsic porphyry containing molybdenite (Spry and others, 1996). Although it is tempting to include GSM in the present discussion of possible RIRGS occurrences, it should be noted that hydrothermal pyrite from GSM is isotopically light ($\delta^{34}S$ = -12 to -4‰, Porter and Ripley, 1985; Gammons and others, 2020) compared to pyrite from Winston, Elkhorn, Radersburg, and Diamond Hill (fig. 11). As well, GSM is rich in Au-Ag tellurides, has a fair amount of barite and anhydrite (indicating a relatively high oxidation state), and lacks the three-phase, CO_2-rich fluid inclusions that are abundant at Winston.

In conclusion, the Winston District contains several gold-rich vein deposits that are distinctly non-epithermal, but may instead be more closely related to reduced intrusion-related gold systems. If this idea is correct, then it could have implications for future exploration in the district.

Acknowledgments

The authors thank Ethan Coppage and Brooks Hintze of Winston Gold for access to the property and several tours of the Carrabba Tunnel with students. John Ridley and Adrian Van Rythoven are thanked for their helpful reviews of the paper.

References

Baker, T., 2002, Emplacement depth and carbon dioxide-rich fluid inclusions in intrusion-related gold deposits: Economic Geology, v. 97, p. 1111–1117, https://doi.org/10.2113/97.5.1111.

Brown, A.H., Gammons, C.H., and Poulson, S.R., 2019, New investigations of the economic geology of the historic Elkhorn mining district, Jefferson County, Montana: Montana Bureau of Mines and Geology Special Publication 120, p. 101–112.

Capps Geoscience, 2015, N143-101 Technical report on exploration at the Winston District Gold Project, Broadwater County, Montana, USA.

Czamanske, G.K., and Rye, R.O., 1974, Experimentally determined sulfur isotope fractionations between sphalerite and galena in the temperature range 600°C to 275°C: Economic Geology, v. 69, p. 17–25, https://doi.org/10.2113/gsecongeo.69.1.17.

du Bray, E.A., 1995, Geologic map showing distribution of Cretaceous intrusive rocks in the central Big Belt Mountains, Broadwater and Meagher Counties, Montana: U.S. Geological Survey Miscellaneous Field Studies Map MF-2291, scale 1:50,000.

Earll, F.N., 1964, Economic geology and geochemical study of Winston Mining District, Broadwater County, Montana: Montana Bureau of Mines and Geology Bulletin 41, 56 p., 2 plates.

Gammons, C.H., and Poulson, S.R., 2022, A review (with new data) of S-isotopes in hydrothermal mineral deposits of Montana: Montana Bureau of Mines and Geology Special Publication 123, p. 125–130, https://doi.org/ https://doi.org/10.59691/YXKU1170.

Gammons, C.H., Gnanou, H., Odt, D., and Poulson, S.R., 2020, Mineralogy and sulfur isotope geochemistry of polymetallic, porphyry-epithermal mineralization peripheral to the Golden Sunlight gold mine, Montana: Ore Geology Reviews, v. 126, 103797, https://doi.org/10.1016/j.oregeorev.2020.103797.

Groves, D.I., Santosh, M., Goldfarb, R.J., and Zhang, L., 2018, Structural geometry of orogenic gold deposits: Implications for exploration of world-class and giant deposits: Geoscience Frontiers, v. 9, p. 1163–1177, https://doi.org/10.1016/j.gsf.2018.01.006.

Hart, C.J.R., 2007, Reduced intrusion-related gold systems, *in* Goodfellow, W.D., ed., Mineral deposits of Canada: A synthesis of Major deposit types, district metallogeny, the evolution of geological provinces, and exploration methods: Geological Association of Canada, Mineral Deposits Division, Special Publication No. 5, p. 95–112.

Klepper, M.R., Ruppel, E.T., Freeman, V.L., and Weeks, R.A., 1971, Geology and mineral deposits, east flank of the Elkhorn Mountains, Broadwater County, Montana: USGS Professional Paper 665, 66 p., 4 plates, https://doi.org/10.3133/pp665.

Lang, J.R., Baker, T., Hart, C.J.R., and Mortensen, J.K., 2000, An exploration model for intrusion-related gold systems: Society of Economic Geology Newsletter, v. 40, no. 1, p. 6–15, https://doi.org/10.5382/SEGnews.2000-40.fea.

Liu, S., Li, Y., Liu, J., and Shi, Y., 2015, First-principles study of sulfur isotope fractionation in pyrite-type disulfides: American Mineralogist, v. 100, p. 203–208, https://doi.org/10.2138/am-2015-5003.

Lund, K., Aleinikoff, J.N., Kunk, M.J., Unruh, D.M., Zeihen, G.D., Hodges, W.C., du Bray, E.A., and O'Neill, J.M., 2002, SHRIMP U-Pb and $^{40}Ar/^{39}Ar$ age constraints for relating plutonism and mineralization in the Boulder Batholith region, Montana: Economic Geology, v. 97, p. 241–267, https://doi.org/10.2113/97.2.241.

Lyden, C.J., 1948, The gold placers of Montana: Montana Bureau of Mines and Geology Memoir 26, 152 p.

Pardee, J.T., and Schrader, F.C., 1933, Metalliferous deposits of the greater Helena mining region, Montana: U.S. Geological Survey Bulletin 842, plate 15, scale 1:63,360, https://doi.org/10.3133/b842.

Porter, E.W., and Ripley, E.M., 1985, Petrologic and stable isotope study of the gold-bearing breccia pipe at the Golden Sunlight deposit, Montana: Economic Geology, v. 80, p. 1689–1706, https://doi.org/10.2113/gsecongeo.80.6.1689.

Reed, G.C., 1951, Mines and mineral deposits (except fuels) of Broadwater County, Montana: U.S. Bureau of Mines Information Circular 7592, 58 p.

Rowins, S.M., 2000, Reduced porphyry copper-gold deposits: A new variation on an old theme: Geology, v. 28, p. 491–494, https://doi.org/10.1130/0091-7613(2000)28<491:RPCDAN>2.0.CO;2.

Spry, P.G., Paredes, M.M., Foster, F., Truckle, J.S., and Chadwick, T.H., 1996, Evidence for a genetic link between gold-silver telluride and porphyry molybdenum mineralization at the Golden Sunlight Deposit, Whitehall, Montana; fluid inclusion and stable isotope studies: Economic Geology, v. 91, p. 507–526, https://doi.org/ 10.2113/GSECONGEO.91.3.507.

Steele-MacInnis, 2018, Fluid inclusions in the system H_2O-NaCl-CO_2: An algorithm to determine composition, density, and isochore: Chemical Geology, v. 498, p. 31–44, https://doi.org/10.1016/j.chemgeo.2018.08.022.

Thompson, J.F.H., and Newberry, R.J., 2000, Gold deposits related to reduced granitic intrusions: Society of Economic Geologists, Reviews in Economic Geology, v. 13, p. 377–400, https://doi.org/10.5382/Rev.13.11.

Tysdal, R.G., Luddington, S., and McCafferty, A.E., 1996, Mineral and energy resource assessment of the Helena National Forest, west-central Montana: U.S. Geological Survey, Open-File Report 96-683-A, https://doi.org/10.3133/ofr96683A.

Using Indicator Minerals from Stream Sediment Samples to Detect Rare Earth Element Deposits

Michael A. Gary and Christopher H. Gammons

Montana Technological University, Department of Geological Engineering, Butte, MT

mgary@mtech.edu

Introduction

Rare earth elements (REEs) play a crucial role in various technologies ranging from electronics and renewable energy systems to advanced military and medical applications. As the global demand for these valuable elements continues to climb, the exploration and extraction of these resources become increasingly important for ensuring and sustaining global supply chains. Conventional methods for REE exploration usually rely on geological mapping surveys and geophysical techniques. While these techniques have a proven record in detecting REE deposits, they are limited by their cost and time-consuming nature, and are less useful in regions that are thickly forested with minimal outcrop. Thus, there is a need for exploration techniques that are cost-effective, efficient, and accurate for identifying REE-rich areas in remote and/or forested terrain.

Indicator minerals have been recognized in recent years as a valuable tool in REE exploration (McClenaghan, 2011; Mackay and others, 2016; Kelley and others, 2022). Erosion and weathering of mineralized host rock lead to the fluvial transportation and deposition of various ore and gangue minerals in stream sediments. The best indicator minerals are resistant to physical and chemical erosion, and are also dense (high specific gravity), allowing them to concentrate in pockets or streaks of heavy minerals (i.e., “black sand”). An indicator mineral should also be unique to the mineral deposit type that is being explored for. By analyzing the composition and abundance of indicator minerals in stream-sediment samples, geologists can potentially gain insights into the type of mineral deposits that may be present in a particular region.

This study examines the potential for using indicator minerals to explore for REE deposits in the Sheep

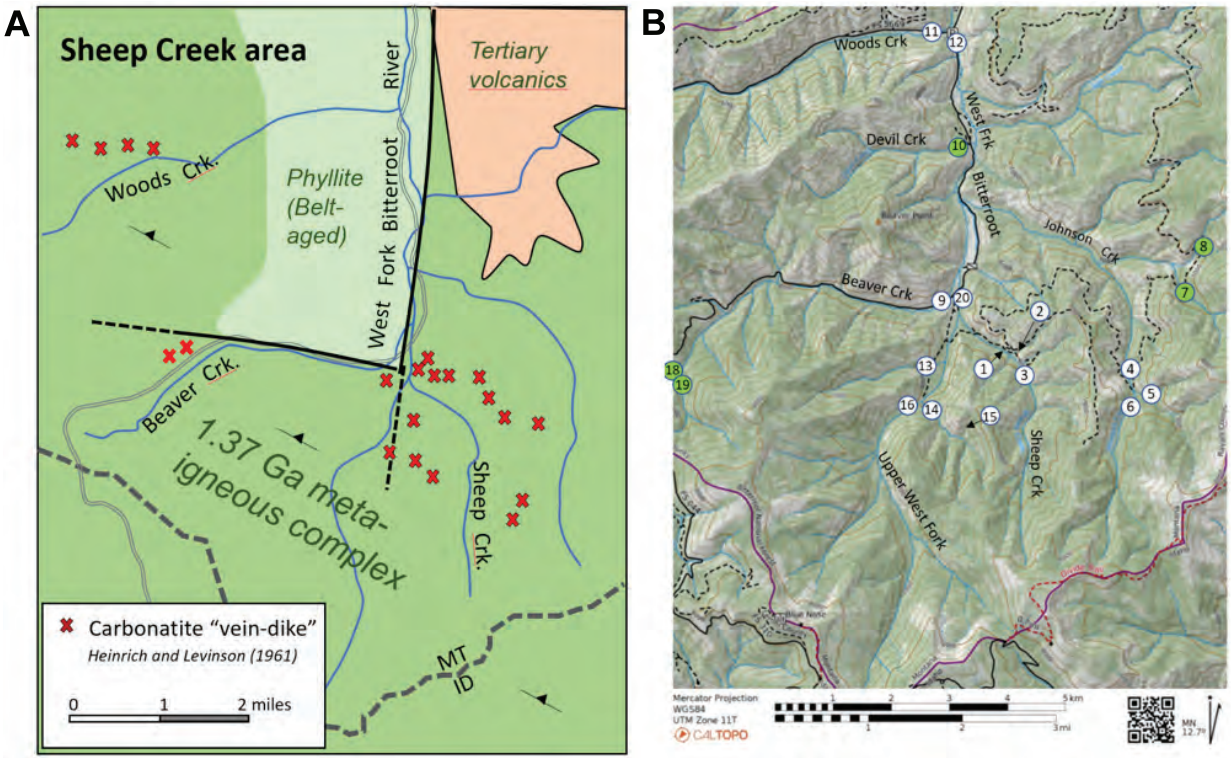

Figure 1. Maps showing the generalized geology of the study area (A) and the locations of stream-sediment samples (B). Green symbols indicate control samples collected outside of the carbonatite trend.

Creek mining district of southern Ravalli County, Montana. The Sheep Creek area is known to contain a number of REE- and Nb-rich carbonatite bodies (Heinrich and Levinson, 1961; Gammons, 2020; Risedorf, 2023). The area is rugged and heavily wooded, making conventional mapping and outcrop sampling difficult.

Methods

Figure 1A shows the geology of the study area along with the locations of known carbonatite bodies. The carbonatites crop out as steeply dipping "vein-dikes" of rusty-weathering carbonate (mix of calcite and dolomite) with biotite alteration of the surrounding country rock. Host rock includes amphibolite, meta-gabbro, and granitic augen gneiss that have been dated to 1.37–1.38 Ma (Evans and Zartman, 1990; Doughty and Chamberlain, 1996). The carbonatite bodies are small (<2 m wide), and make up a small proportion of the study area. However, they contain several minerals that fit the requirements of being "indicators" for REE-Nb mineralization, including monazite, columbite, and allanite.

Twenty stream sediments were collected at 16 locations along the upper West Fork of the Bitterroot River and tributaries (fig. 1B). Sample sites included headwater streams in the heart of the REE district, downstream samples from the East Fork, and several streams outside of the carbonatite trend as "controls." Most of the streams were small and swift-flowing, with a rocky streambed. Sediment was passed through a kitchen strainer (6.35 mm pore size) and shaken in the current with a gold pan to separate out loose organic matter before bagging. The samples were dried in an oven, weighed, and then sieved to three size fractions: coarse (>2 mm), medium (0.25 to 2 mm), and fine (<0.25 mm). The fine fractions were sent to the USGS Earth MRI laboratory in Lakewood, CO for geochemical analysis, where inductively coupled plasma atomic emission spectroscopy (ICP-OES) and wavelength dispersive X-ray fluorescence (WDXRF) were performed. The medium-sized fraction was run through a Wilfley table in the rock preparation lab of the Montana Bureau of Mines and Geology (MBMG) to obtain several subsamples of different density. The most dense subsample was processed with a hand magnet to remove magnetite, and then polished epoxy plugs (1-in round) were made prior to SEM investigation. A Niton XL5 Plus portable X-ray fluorescence (pXRF) spectrometer was used to get semi-quantitative chemical analyses for a range of major and minor elements at several steps (fig. 2).

A TESCAN Mira3 field-emission scanning electron microscope (SEM) at Montana Technological University (MTU) was used to create false color mineral maps and a table of mineral percentages and elemental abundances for each of the epoxy plugs based on automated electron dispersive spectroscopy (EDS) analysis and "Tescan Integrated Mineral Analysis" (TIMA) software. To limit cost, a relatively coarse step size of 12 to 15 μm was used for the TIMA work. Although it is possible that some fine-grained REE minerals were misidentified, or missed completely, the fact that the minimum grain size was 250 μm makes this less likely. One epoxy plug (MG-20) containing roughly 20 large monazite grains was sent to the USGS LTRACE Laboratory in Denver, CO, and Th-Pb dating was performed by Dr. Jay Thompson using laser ablation ICP mass spectroscopy (LA-ICP-MS). During the same session, coarse monazite grains from two different carbonatite locations at Sheep Creek were also dated by the Th-Pb method (Risedorf, 2023; Gammons and others, 2023).

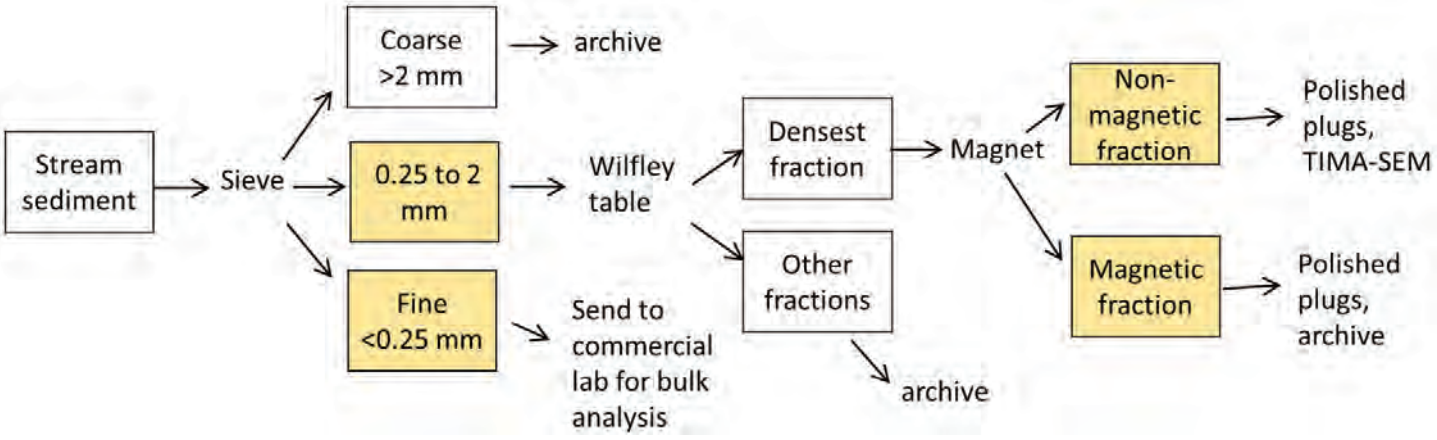

Figure 2. Flowchart for processing of stream-sediment samples. Samples analyzed by pXRF are represented by yellow boxes.

Results

SEM and Th-Pb Dating

Figure 3 shows example TIMA-SEM data for sample MG-20. This sample was collected downstream of the confluence of Sheep Creek and the East Fork, and therefore was expected to be one of the more REE-rich samples in the study. As expected, the dense, magnetic fraction was mainly magnetite, or ilmenite–magnetite intergrowths. Although magnetite is present in the carbonatite bodies, it is also a common accessory mineral in the granite/augen gneiss country rock, therefore making it useless as an indicator mineral in this study. The dense, non-magnetic fraction (fig. 2B) shows a more diverse set of minerals, the most abundant of which is ilmenite. Ilmenite is an accessory mineral in the amphibolite–metagabbro rock type (Risedorf, 2023). Several indicator minerals for carbonatites are also present, including monazite (dark green grains) and columbite (light blue grains). The monazite grains are easier to see in the cerium X-ray map of figure 3A. Other REE-rich minerals found in this study include allanite ($Ce_2(Al,Fe)_3(SiO4)_3OH$), Nb-rich baotite ($Ba_4(Nb,Ti)_8O_{16}(SiO_3)_4Cl$), hydroxyl-bastnaesite ($CeCO_3OH$), belkovite ($Ba_3(Nb,Ti)_6(Si_2O_7)_2O_{12}$), biraite ($Ce_2FeCO_3Si_2O_7$), and xenotime ($YPO_4$). In the mineral formulae above, “Ce” is a proxy for all of the light REE, whereas “Y” denotes Y plus the heavy REE. With the exception of belkovite, all of these minerals were previously documented from the Sheep Creek carbonatites by Risedorf (2023).

LA-ICP-MS dating of monazite in sample MG-20 gave a range of ages from about 180 to about 90 Ma (fig. 4B). These ages span the Jurassic–Cretaceous boundary (145.5 Ma), and overlap with the ages obtained by LA-ICP-MS analysis of monazite taken directly from two of the mineralized carbonatite bodies (fig. 5). No Precambrian monazite grains were found in MG-20, suggesting that the minerals did not erode out of the 1.37 Ma meta-igneous country rock. Additional evidence presented below suggests that the monazite grains in MG-20 came from the carbonatites.

Geochemistry Results

The USGS lab provided full REE concentration profiles for the monazite grains in sample MG-20. The results (normalized to C1 chondrite) are shown in figure 6, and are compared to “average Sheep Creek carbonatite,” which is the average of 40 bulk samples of carbonatite rock throughout the Sheep Creek district (data in Risedorf, 2023). Also shown are REE profiles for stream-sediment samples MG-13 and MG-18. MG-18 is one of the control samples, collected from a stream that is well outside the carbonatite trend (fig. 1B). The absolute REE concentrations are much higher for the monazite grains compared to the bulk rock and bulk stream-sediment samples. Importantly, the stream-sediment control sample shows a strong negative anomaly at europium. As shown by Risedorf (2023), one of the characteristics of the Sheep Creek carbonatites is the complete lack of any Eu anomaly.

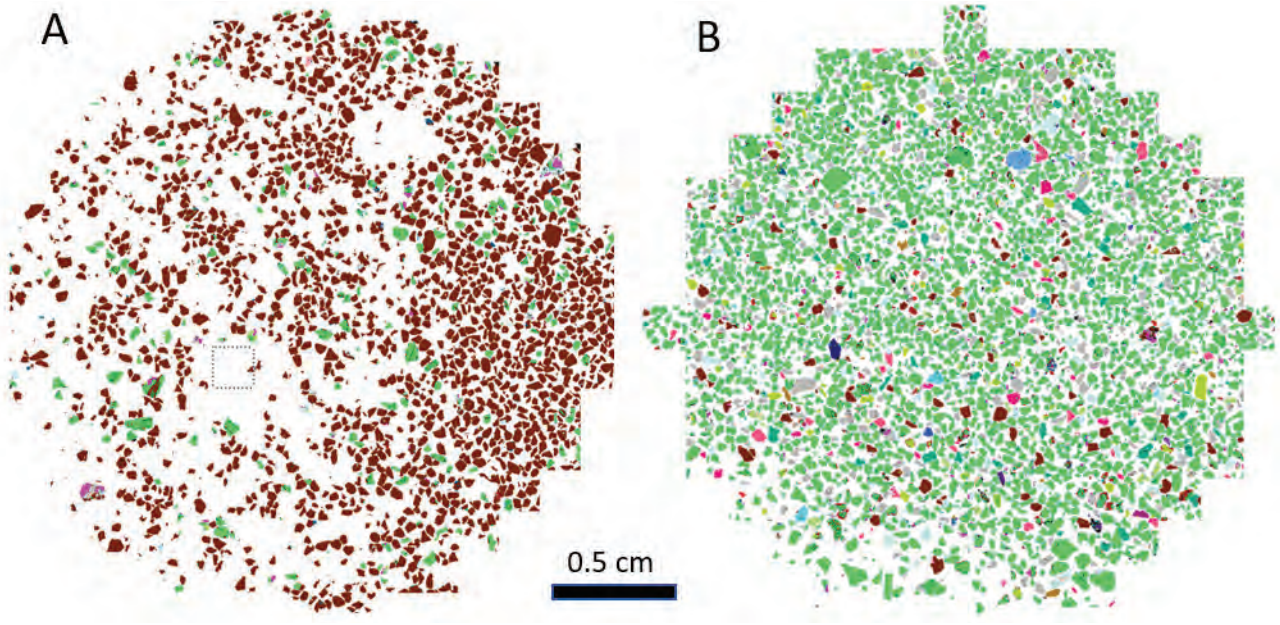

Figure 3. TIMA-false color mineral maps of sediment sample MG-20. (A) Dense, magnetic fraction; (B) dense, non-magnetic fraction. Brown phases are magnetite. Green are mostly ilmenite. The large blue grain at top-right is columbite. Further details can be found in Gary (2024).

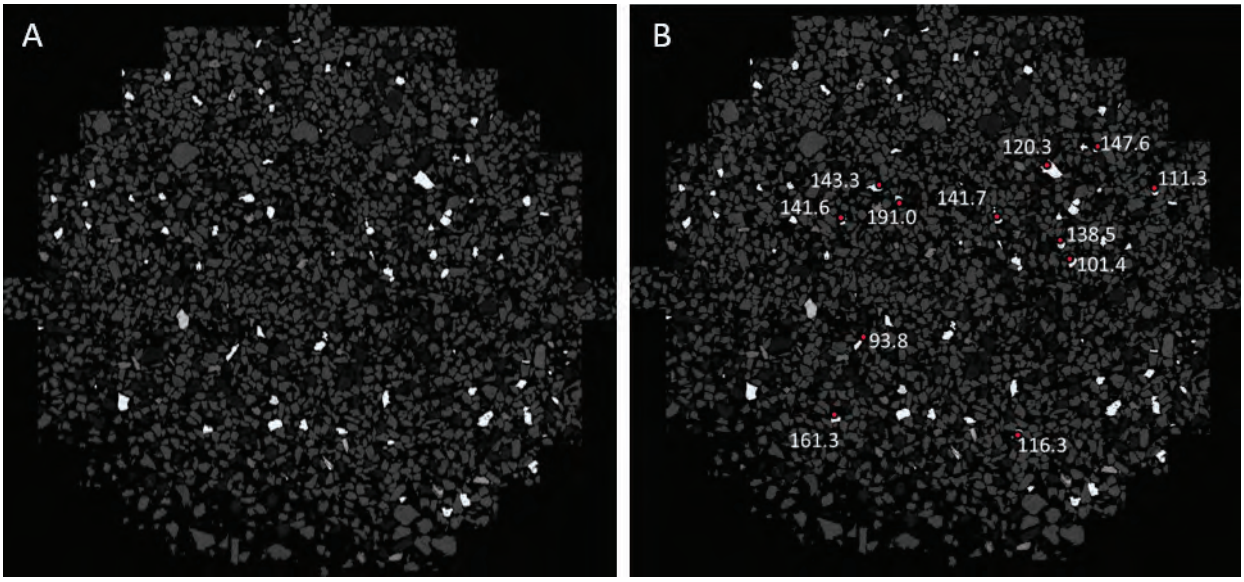

Figure 4. Cerium X-ray maps of the same sample shown in figure 3B. Bright grains are mostly monazite, but include some other REE-rich minerals. The panel at right is annotated with the ages (in Ma) of 12 of the larger monazite grains based on LA-ICP-MS Th-Pb analysis.

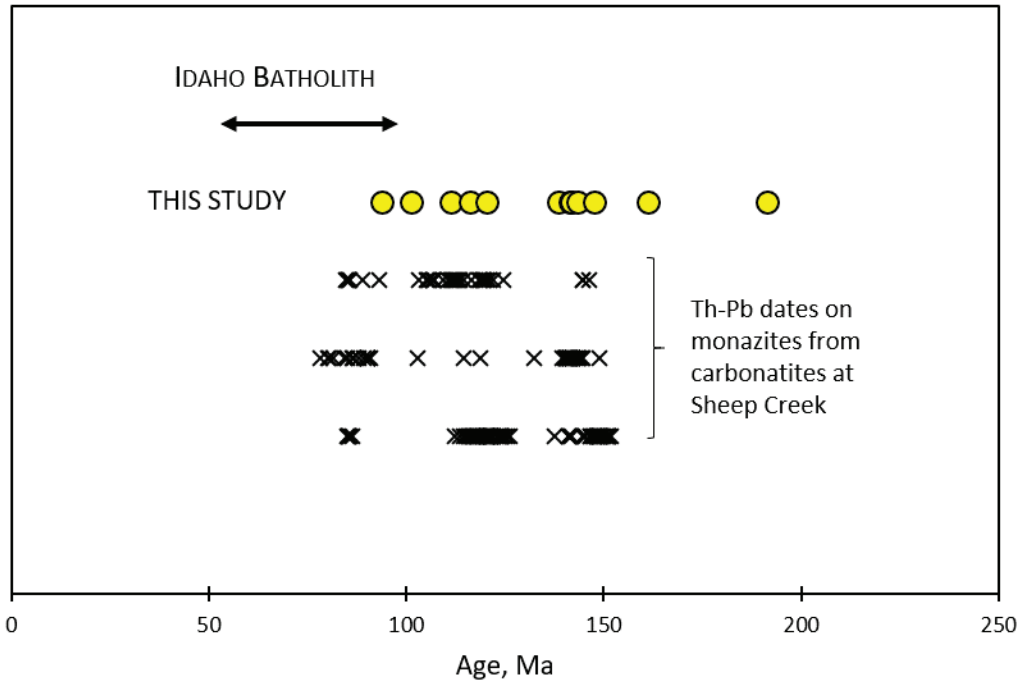

Figure 5. Monazite Th-Pb ages obtained in this study (yellow circles) compared to previously published dates for monazite from several carbonatite bodies in the Sheep Creek area (data summarized in Risedorf, 2023, and Gammons and others, 2023). Also shown is the approximate age range of intrusions in the nearby Idaho Batholith.

The monazite grains in MG-20 also show no evidence of any Eu anomaly. Therefore, it is concluded that the monazites in the stream sediment were eroded out of carbonatites, and did not originate from background (country rock) sources. Sediment sample MG-13, which is located downstream of several known carbonatite bodies, shows a weak Eu anomaly, and has higher REE concentrations than MG-18. It is likely that the REE-containing minerals in sample MG-13 came from a mixture of carbonatite sources and background sources.

Conclusions

This study has shown that specific indicator minerals such as monazite and columbite can be used to explore for REE- and Nb-rich carbonatites. Based on their ages and trace element compositions, the monazites in stream-sediment samples collected downstream of known mineralization can be traced directly to the carbonatite bodies. Stream-sediment samples collected outside the carbonatite trend have fewer indicator minerals, have lower overall REE concentrations, and exhibit a negative Eu anomaly that

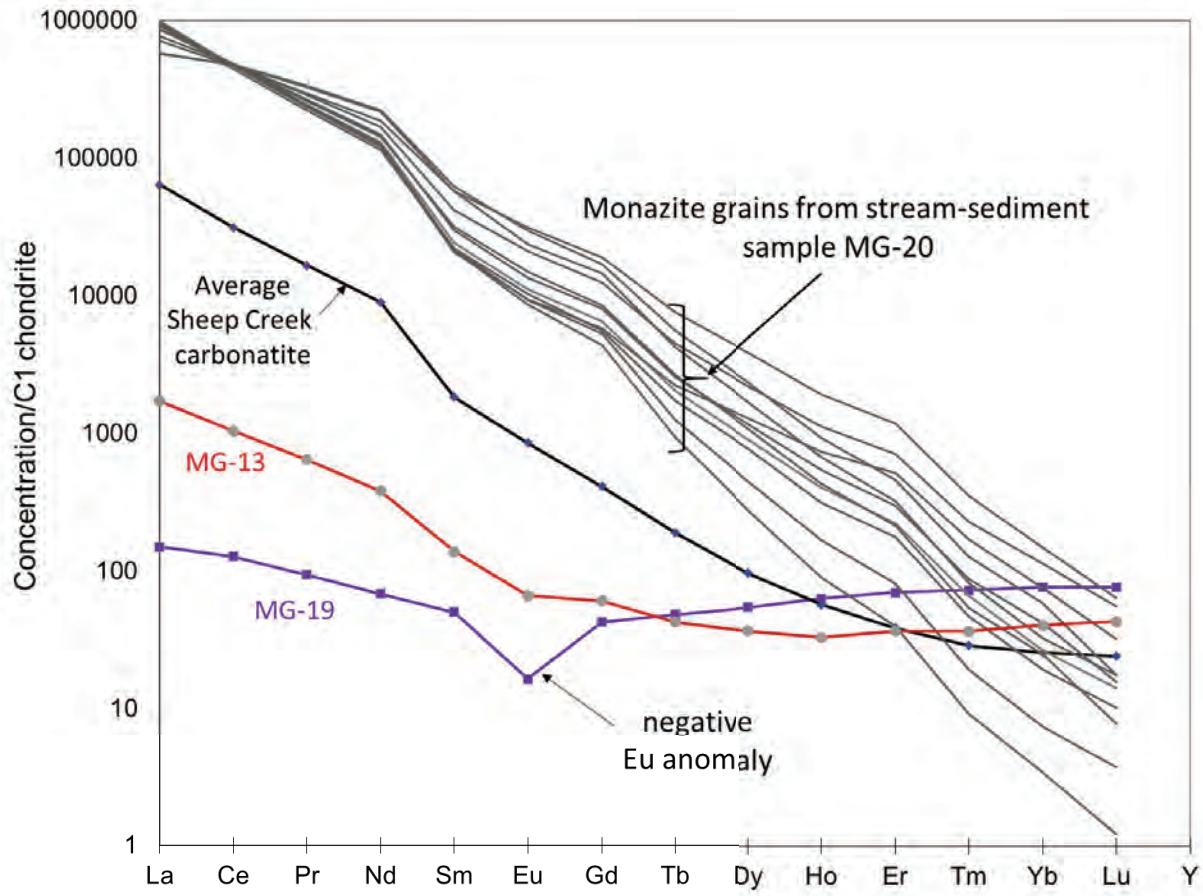

Figure 6. Chondrite-normalized (Boynton, 1984) REE profiles for monazite grains from sample MG-20 compared to average Sheep Creek carbonatite (Risedorf, 2023). Also shown are bulk chemical REE analyses for stream sediment samples MG-13 and MG-19.

can be used to differentiate a country rock vs. carbonatite source. Additional data and conclusions from this study are available in Gary (2024).

Acknowledgments

We thank Jay Thompson (USGS) for carrying out the LA-ICP-MS analyses, and Connie Thomson (MBMG) for assisting with the sample processing steps. This research was sponsored by the DEVCOM Army Research Laboratory under Cooperative Agreement W911NF-22-2-0015. The views and conclusions contained in this document are those of the authors, and should not be interpreted as representing the official policies, either expressed or implied, of the DEVCOM Army Research Laboratory or the U.S. Government. The U.S. Government is authorized to reproduce and distribute reprints for Government purposes notwithstanding any copyright notation herein. The manuscript benefited from the reviews of Adrian Van Rythoven and Ryan Davison.

References

Boynton, W.V., 1984, Geochemistry of the rare earth elements: Meteorite studies: Developments in Geochemistry, v. 2, p. 63–114, https://doi.org/10.1016/B978-0-444-42148-7.50008-3.

Doughty, P.T., and Chamberlain, K.R., 1996, Salmon River Arch revisited: New evidence for 1370 Ma rifting near the end of deposition in the Middle Proterozoic Belt basin: Canadian Journal of Earth Sciences, v. 33, p. 1037–1052, https://doi.org/10.1139/e96-079.

Evans, K.V., and Zartman, R.E., 1990, U-Th-Pb and Rb-Sr geochronology of middle Proterozoic granite and augen gneiss, Salmon River Mountains, east-central Idaho: Geological Society of America Bulletin, v. 102, p. 63–73, https://doi.org/10.1130/0016-7606(1990)102<0063:UTPARS>2.3.CO;2.

Gammons, C.H., 2020, Mineralogical investigation of the Sheep Creek carbonatite veins, Ravalli County, Montana: Montana Bureau Mines and Geology Special Publication 121, p. 81–92.

Gammons, C.H., Risedorf, S., Gary, M., Stein, H., and Thompson, J.M., 2023, Age of carbonatite-related REE-Nb mineralization in the Sheep Creek District, southern Ravalli County, Montana: Northwest Geology, v. 52, p. 83–92.

Gary, M.A., 2024, Using stream-sediment indicator minerals to explore for rare earth element deposits: Butte, Mont., Montana Technological University, M.S. thesis, available at https://digitalcommons.mtech.edu/grad_rsch/321.

Heinrich, E.W., and Levinson, A.A., 1961, Carbonatic niobium-rare earth deposits, Ravalli County, Montana: American Mineralogist, v. 46, p. 1424–1447.

Kelley, K.D., Graham, G.E., Pfaff, K., Lowers, H.A., and Koenig, A.E., 2022, Indicator mineral analyses of stream-sediment samples using automated mineralogy and mineral chemistry: Applicability to exploration in covered terranes in Eastern Alaska, USA: Ore Geology Reviews, v. 148, 105021, https://doi.org/10.1016/j.oregeorev.2022.105021.

Mackay, D.A.R., Simandl, G.J., Ma, W., Redfearn, M., and Gravel, J., 2016, Indicator mineral-based exploration for carbonatites and related specialty metal deposits—A QEMSCAN® Orientation Survey, British Columbia, Canada: Journal of Geochemical Exploration, v. 165, p. 159–173, https://doi.org/10.1016/j.gexplo.2016.03.005.

McClenaghan, M.B., 2011, Overview of common processing methods for recovery of indicator minerals from sediments and bedrock in mineral exploration: Geochemistry: Exploration, Environment, Analysis, v. 11, p. 265–278, https://doi.org/10.1144/1467-7873/10-IM-025.

Risedorf, S., 2023, New investigations of the mineralogy and geochemistry of carbonatite-related REE-Nb mineralization in the Sheep Creek area, southern Ravalli County, Montana: Butte, Mont., Montana Technological University, M.S. Thesis, available at https://digitalcommons.mtech.edu/grad_rsch/296.

Cretaceous Structural Controls and Evolution of Au-Bearing Co-Cu Deposits, Blackbird District, East-Central Idaho

Karen Lund

U.S. Geological Survey, Denver, CO

klund@usgs.gov

The Cu-Co±Au (±Ag±Ni±REE) deposits of the Blackbird district, east-central Idaho (fig. 1), were classified previously as Besshi-type VMS, as SedEx, and alternately as IOCG deposits (Slack and others, 2013), all interpreted as in an intact stratigraphic section. Alternatively, the current detailed district-wide mapping studies corroborate and expand on details from an earlier district study (Vhay, 1948), indicating that mineralized veins were introduced into thrust-stacked, variably metamorphosed sedimentary strata as a series of structurally controlled vein and alteration systems.

Modern mapping shows that mineralized intervals are hosted by Mesoproterozoic Apple Creek Formation, predominantly in the lower greenschist facies, informally named banded siltite unit and also by two higher metamorphic grade varieties of the same Formation (fig. 2). These mapped units are all S-tectonites in the footwall of the regional-scale Iron Lake thrust fault, which carried a different Mesoproterozoic stratigraphic package composed mainly of the Yellowjacket Formation. Specifically, the district lies within the lower plate, Blackbird Mountain oblique thrust ramp (fig. 3) that contains a series of structural horses (three structural-metamorphic domains) in a duplex system. The mineral deposits span the three structural-metamorphic domains. In the three domains, mineral deposits are hosted by metamorphic rocks that range from lower amphibolite facies in the structurally upper, Indian Creek domain; upper greenschist facies in the middle, Blackbird domain; to lower-middle greenschist facies in the lower and Haynes–Stellite domain (thus forming an inverted metamorphic sequence, Lund and Tysdal, 2007).

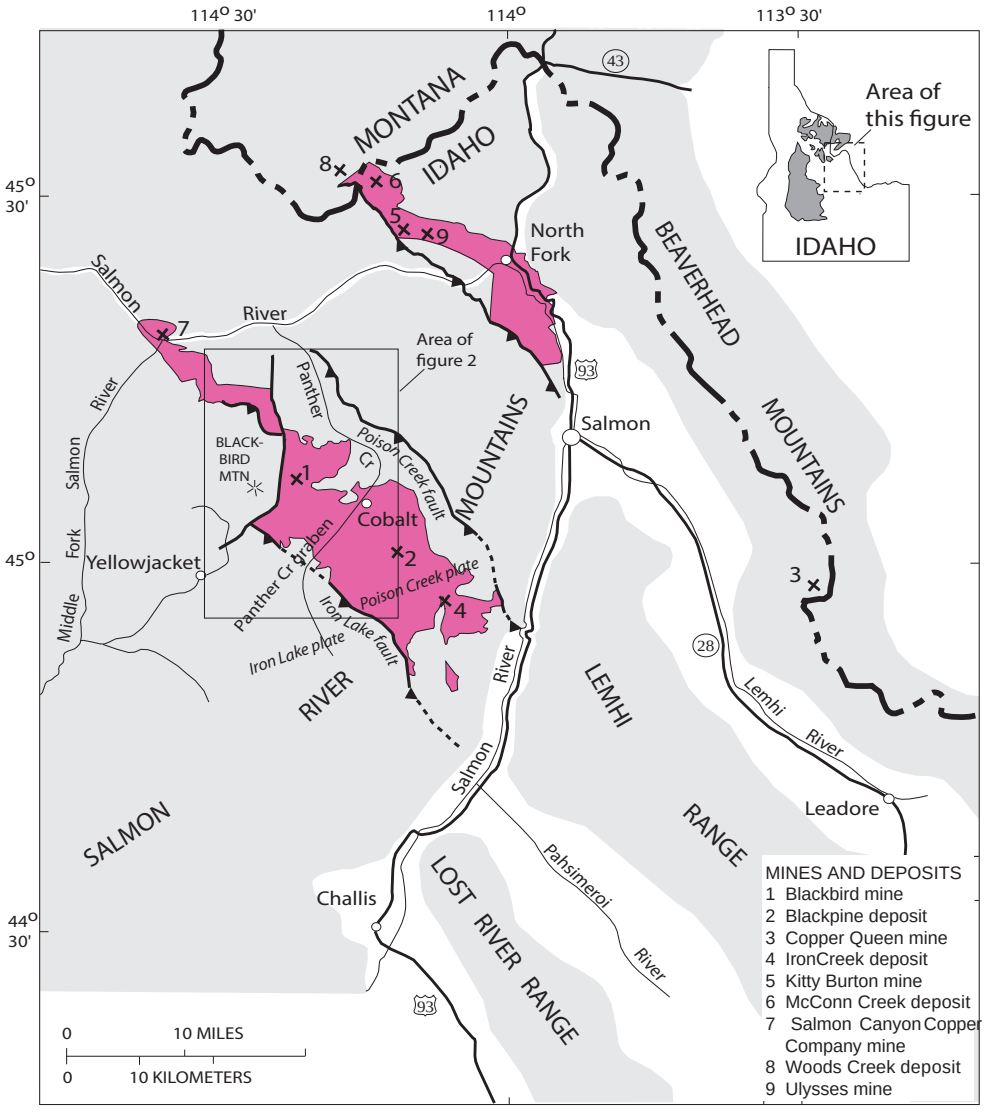

Figure 1. Index map of central Idaho, showing location of study area, major thrust faults, and distribution of Mesoproterozoic Apple Creek Formation that hosts gold–cobalt–copper deposits in the Salmon River Mountains. Inset map shows state of Idaho with area of figure 1 and location of Idaho batholith in shade pattern.

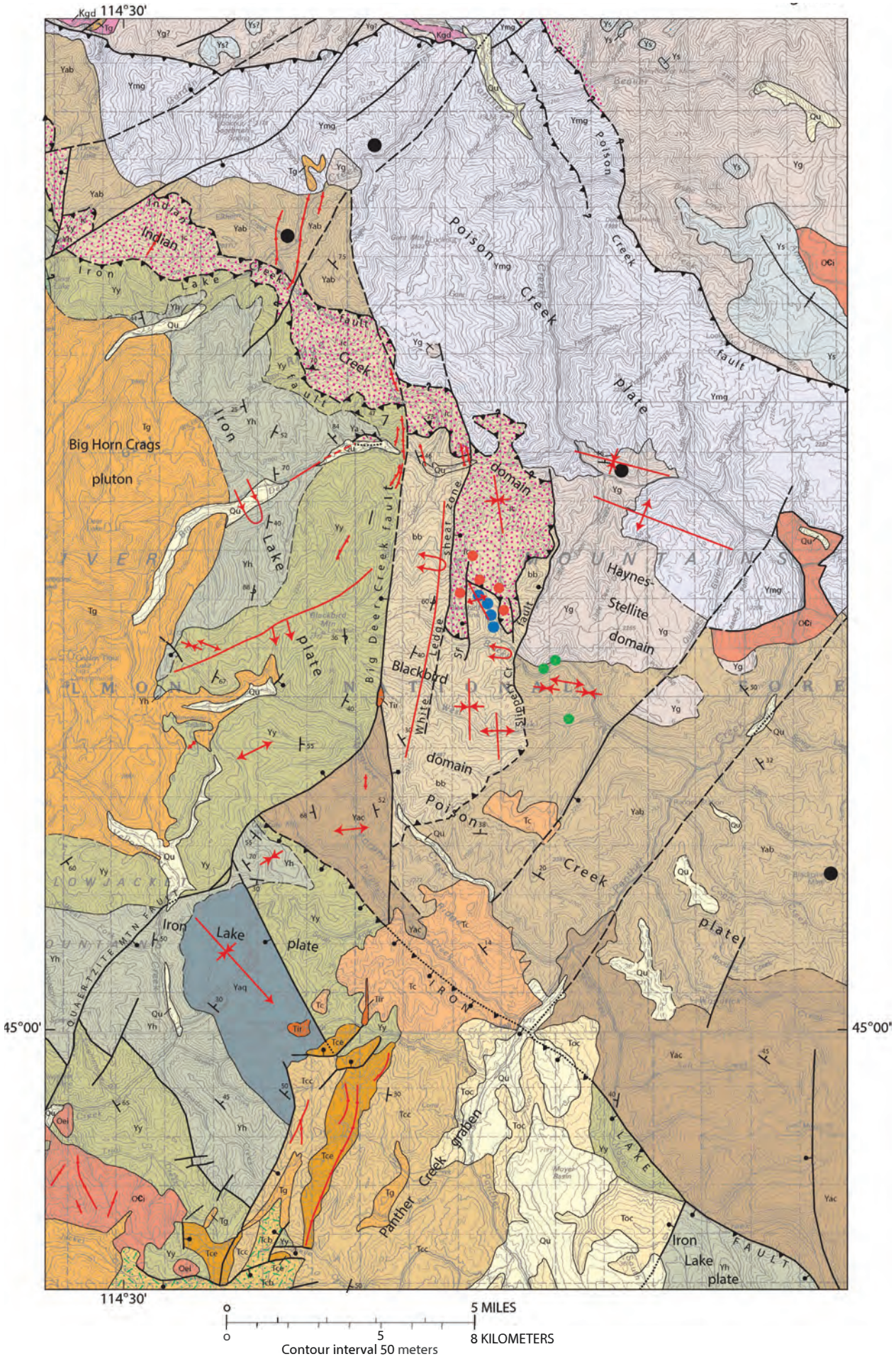
114°30'
45°00'
Big Horn Crags pluton
Indian Creek fault
Iron Lake fault
Poison Creek plate
Big Deer Creek fault
Blackbird domain
Haynes Stellite domain
White Ledge shear zone
Iron Lake plate
Panther Creek graben
Iron Lake FAULT
QUARTZITE MTN FAULT
5 MILES
0
5
8 KILOMETERS
Contour interval 50 meters

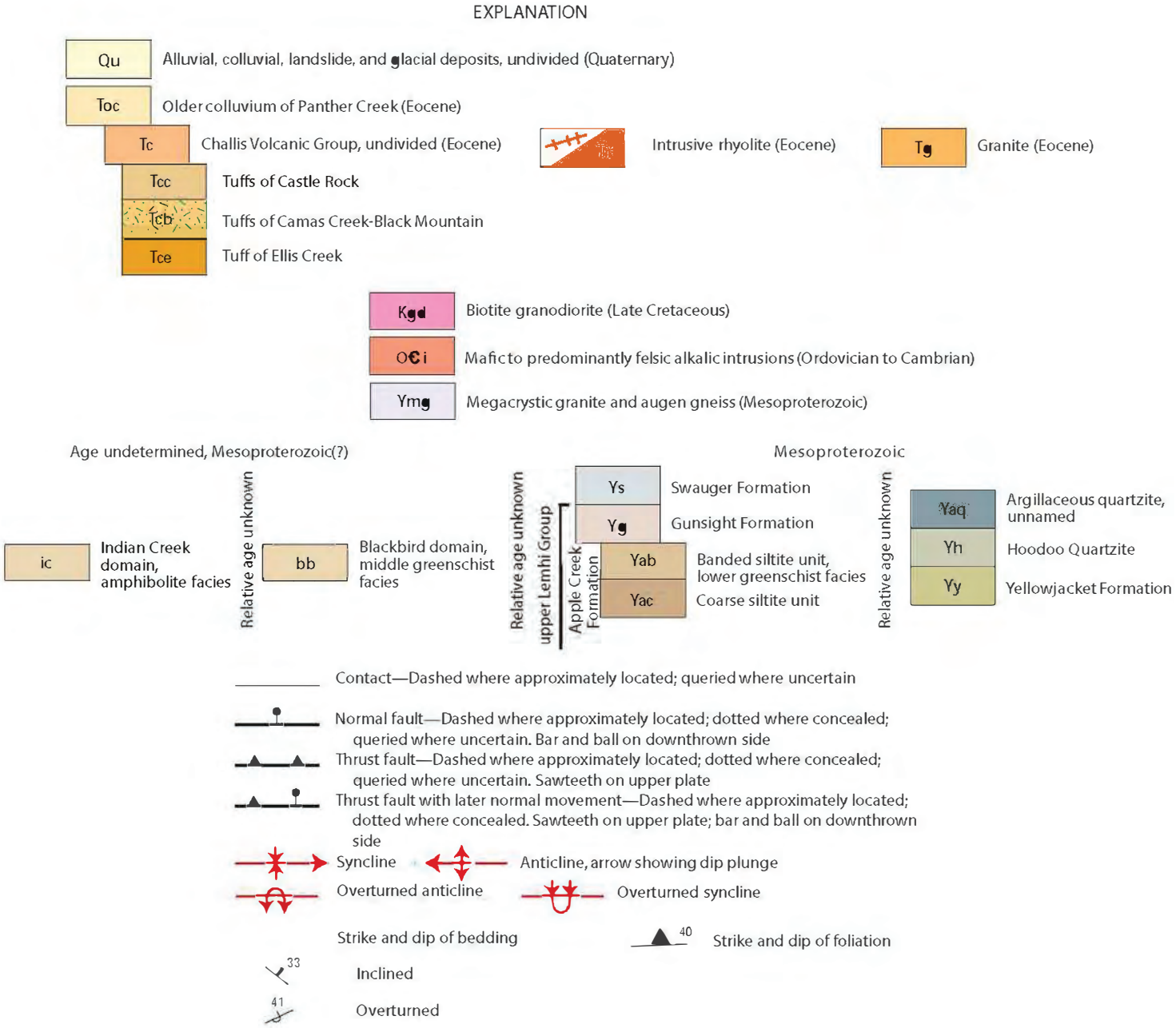

Figure 2 (previous and this page). Geologic map of the Blackbird district showing schematic location of deposits and prospects (modified from Lund and others, 2011). Red dot pattern, rocks above garnet isograd (Indian Creek domain). Location of prospects and mines shown by colored dots: red, occurrences in Indian Creek domain; blue, occurrences in Blackbird domain; green, occurrences in Haynes–Stellite domain; black, other minor occurrences.

Quartz-rich and biotite-rich ± tourmaline veins and alteration zones (some referred to as biotitite or tourmalinite) as well as minor albite and siderite veinlets maintain a consistent sequence, each with discrete sulfide mineral associations across the district. Both early and late quartz veins contain chalcopyrite and pyrite, whereas intermediate-stage biotite ± tourmaline veins host the ore mineral cobaltite. Barren early and late albite and late carbonate (generally siderite) are present as veins or as inclusions in the quartz veins. Minor REE minerals, principally monazite, allanite, and xenotime (Aleinikoff and others, 2012), are associated with both the biotite (± tourmaline) and late quartz veins (Lund and others, 2011).

The veins are present in mineralized intervals along axial planar cleavage in open folds, along intrafolial foliation in tight folds, and along shear zones. The early quartz and biotite (± tourmaline) veins were introduced during progressive folding and prolonged peak metamorphic conditions. These then underwent late-tectonic retrograde recrystallization and metamorphic mineral growth to the same extent as the country

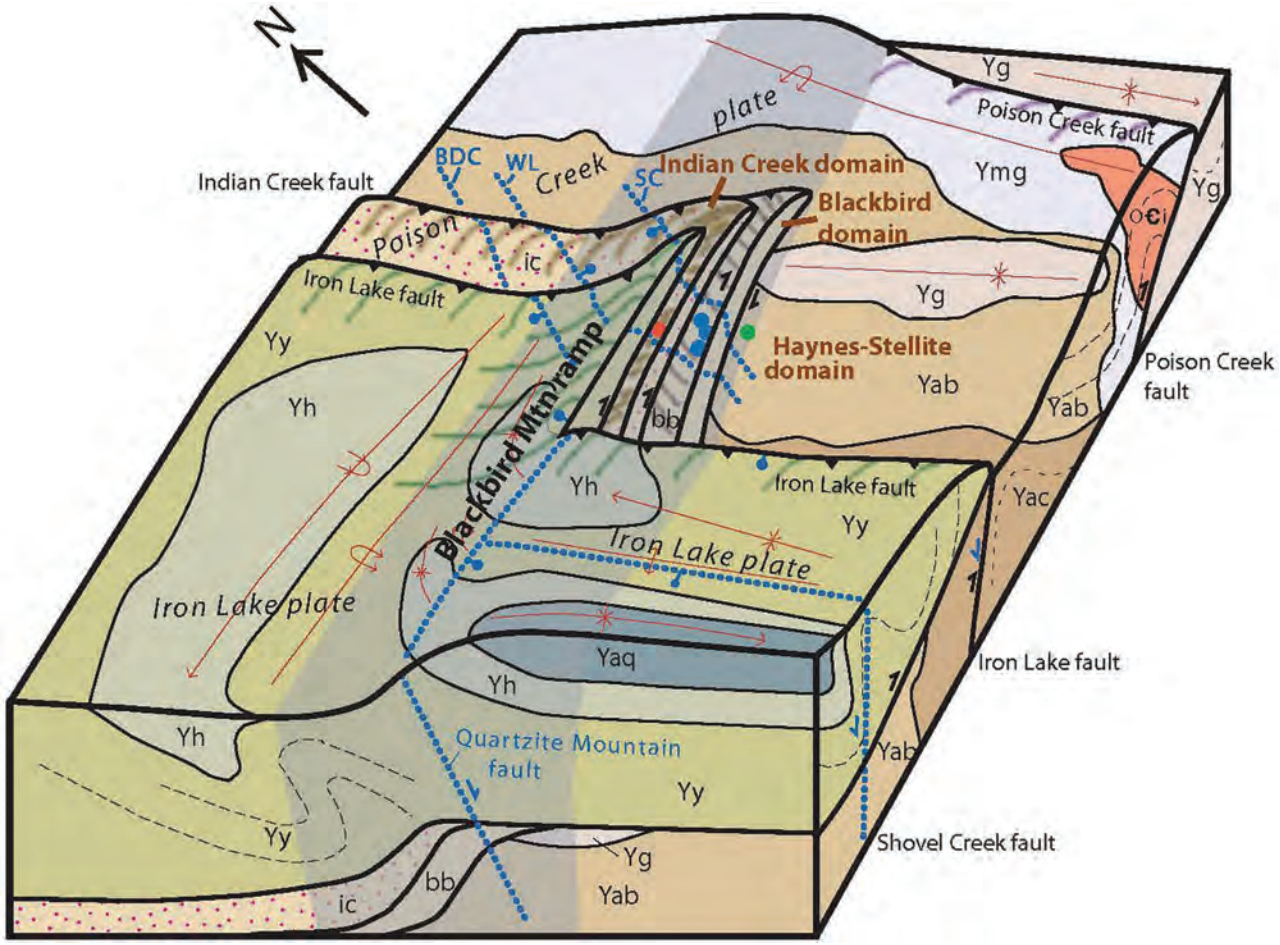

Figure 3. Schematic block diagram illustrating structural relationships in the area near the Blackbird mining district prior to normal faulting (not shown to scale, modified from Lund and others, 2011). Thrust faults in black, schematic location of future normal faults in blue. Overlay screen pattern defines area of Blackbird Mountain oblique ramp in mining district. BDC, Big Deer Creek fault; WL, White Ledge shear zone; SC, Slippery Creek fault. Fine dashed lines, structural form lines to illustrate deformation fabrics and folds. Mineral deposits located schematically: red dot, deposit in Indian Creek domain; blue dots, deposits in Blackbird domain; green dot, deposit in Haynes–Stellite domain.

rocks in each domain. The vein geometries reveal that, where deformation was least penetrative, early veins are discordant to bedding, but where folding was poly-phase and fabrics are penetrative, mineralized zones are concordant to the metamorphic compositional layering. In the most deformed domain, late quartz veins are associated with retrograde minerals and textures and are only locally deformed.

$^{40}Ar/^{39}Ar$ dating of unoriented muscovite from the selvage of a late quartz vein yields a Late Cretaceous age of about 83 Ma. This is interpreted as the time of retrograde metamorphism associated with introduction of these late quartz veins (Lund and others, 2011). Monazite grains found in cobaltite-bearing biotitite veinlets in thin section from middle and upper structural domains, where metamorphic grade is higher, are dated at 110–92 Ma. Xenotime grains found in a lithic clast of country rock in one thin section from the middle domain produced several ages of about 1,370 Ma as well as younger Mesoproterozoic ages, but xenotime and monazite grains from the surrounding vein material produced numerous ages in the range of 98–71 Ma (SHRIMP U-Pb, Aleinikoff and others, 2012). The oldest Mesoproterozoic age is the same as voluminous megacrystic granitic bodies (Aleinikoff and others, 2012) that intruded the Mesoproterozoic country rocks coeval with Mesoproterozoic basin development. Thus, the Mesoproterozoic xenotime may have formed either during diagenesis or related to the Mesoproterozoic plutonism. The Cretaceous monazite and xenotime are coeval with the general ages of deformation and metamorphism prior to emplacement of the Late Cretaceous Idaho batholith west and north of the mining district.

A Pb-isotopic study of igneous country rocks and metasedimentary country rocks determined that the Pb in Blackbird district ore minerals originated from the deposit-hosting Mesoproterozoic Apple Creek Forma-

tion. Those data further indicated that the ore metals were derived from the Mesoproterozoic host rock no earlier than the Cretaceous (Paneerselvam and others, 2012). High K, Na, Cl, and Br values in gangue and veins and isotopic values of the B found in tourmaline-rich veins are interpreted to have been derived from unspecified evaporitic sources (Landis and Hofstra, 2012). Isotopic geochemical studies suggest that composition of ore-forming fluids was most likely due to metamorphic processes (Johnson and others, 2012).

The geochronologic and isotopic data are in agreement with rock-fabric and map data at all scales to indicate that (1) the host sites for veins and the tectonic evolution of both host rocks and mineral deposits were kinematically linked to Late Cretaceous regional thrust faulting and (2) heat, fluids, and conduits for generation and circulation of fluids were part of the Late Cretaceous regional crustal thickening. Significantly, the thrust faulting also juxtaposed meta-evaporite layers in the Mesoproterozoic Yellowjacket Formation in the upper plate over Blackbird district host rocks. This likely caused chemical exchange between the juxtaposed thrust plates, resulting in leaching of essential solutes (Cl, K, B, Na) from metaevaporite rocks in the upper plate to produce brines. The brines then facilitated the scavenging of metals (Co, Cu, etc.) from the Apple Creek Formation (and possibly deeper seated rocks) in the lower plate. Resultant metalliferous brines were focused into fold hinges and fractures in the lower-plate ramp structures where metals deposition occurred. Although the potential for complex origins of metals and fluids remains, the present Cu-Co±Au (±Ag±Ni±REE) Blackbird ore deposits formed during Late Cretaceous compressional deformation.

References

Aleinikoff, J.N., Slack, J.F., Lund, K., Evans, K.V., Fanning, C.M., Mazdab, F.K., Wooden, J.L., and Pillers, R.M., 2012, Constraints on the timing of Co-Cu ± Au mineralization in the Blackbird district, Idaho, Using SHRIMP U-Pb ages of monazite and xenotime plus zircon ages of related Mesoproterozoic orthogneisses and metasedimentary rocks: Economic Geology, v. 107, p. 1143–1175, https://doi.org/10.2113/econgeo.107.6.1143.

Johnson, C.A., Bookstrom, A.A., and Slack, J.F., 2012, Sulfur, carbon, hydrogen, and oxygen isotope geochemistry of the Idaho cobalt belt: Economic Geology, v. 107, p. 1207–1221, https://doi.org/10.2113/econgeo.107.6.1207.

Landis, G.P., and Hofstra, A.H., 2012, Ore genesis constraints on the Idaho cobalt belt from fluid inclusion gas, noble gas isotope, and ion ratio analyses: Economic Geology, v. 107, p. 1189–1205, https://doi.org/10.2113/econgeo.107.6.1189.

Lund, K., and Tysdal, R.G., 2007, Stratigraphic and structural setting of sediment-hosted Blackbird gold-cobalt-copper deposits, east-central Idaho, U.S.A., *in* Link, P.K., and Lewis, R.S., eds., Proterozoic geology of western North America and Siberia: Society for Sedimentary Geology (SEPM) Special Publication 86, p. 129–147, https://doi.org/10.2110/pec.07.86.0129.

Lund, K., Tysdal, R.G., Evans, K.V., Kunk, M.J., and Pillers, R.M., 2011, Structural controls and evolution of gold-, silver-, and REE-bearing copper-cobalt ore deposits, Blackbird district, east-central Idaho: Epigenetic origins: Economic Geology, v. 106, p. 585–618, https://doi.org/10.2113/econgeo.106.4.585.

Paneerselvam, K., Macfarlane, A.W., and Salters, V.J.M., 2012, Reconnaissance lead isotope characteristics of the Blackbird deposit: Implications for the age and origin of cobalt-copper mineralization in the Idaho cobalt belt, United States: Economic Geology, v. 107, p. 1177–1188, https://doi.org/10.2133/econgeo.107.6.1177.

Slack, J.F., Johnson, C.A., Causey, J.D., Lund, K., Schulz, K.J., Gray, J.E., and Eppinger, R.G., 2013, Descriptive and geoenvironmental model for Co-Cu-Au deposits in metasedimentary rocks: U.S. Geological Survey Scientific Investigations Report 2010-5070-G, 218 p., https://doi.org/10.3133/sir20105070g.

Vhay, J.S., 1948, Cobalt-copper deposits of the Blackbird district, Lemhi County, Idaho: U.S. Geological Survey Strategic Minerals Investigation Preliminary Report 3-219, 26 p.

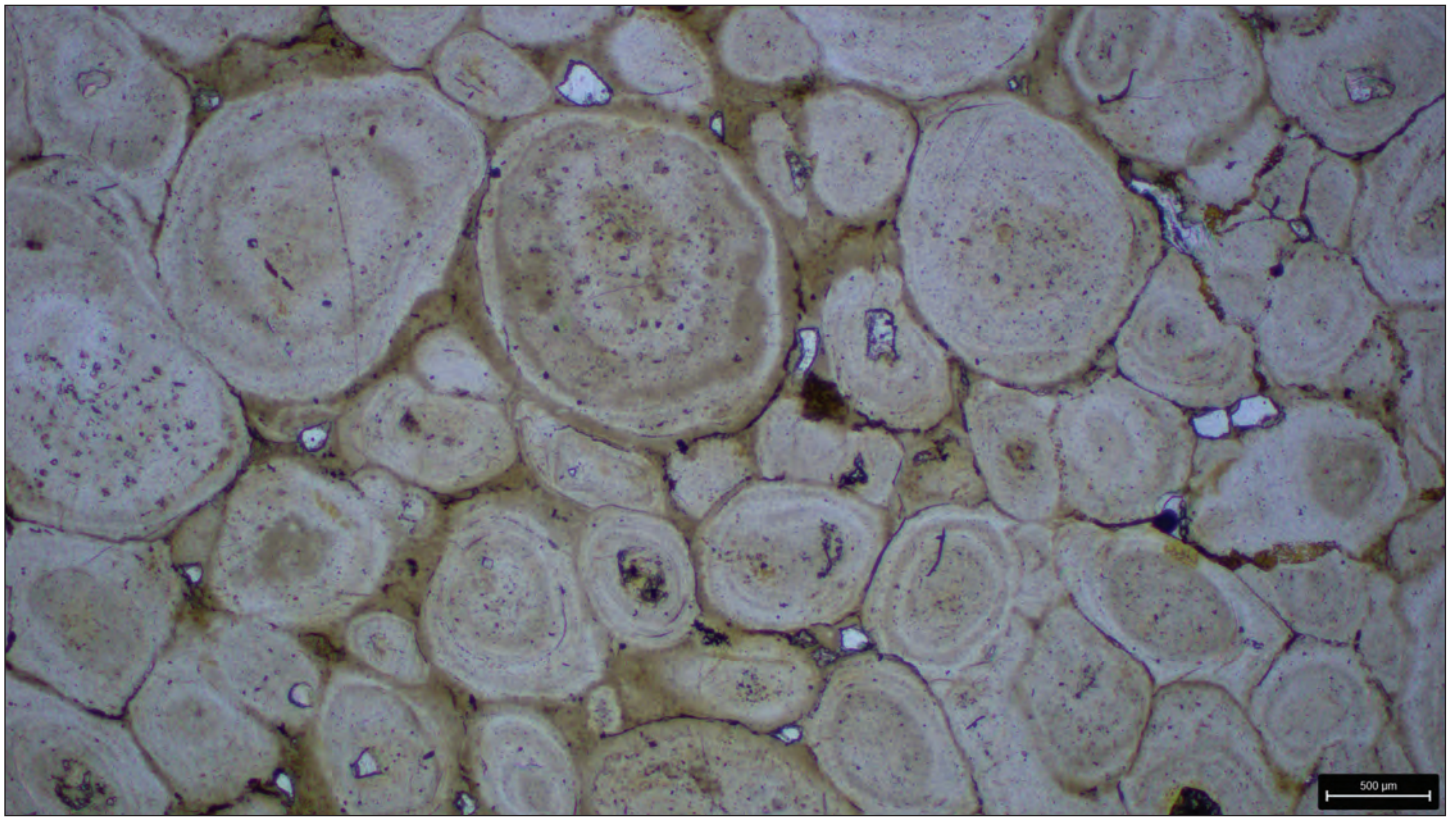

A plane-polarized transmitted light photomicrograph of weakly metamorphosed oolitic phosphorite from the Gravelly Mine, Powell County, Montana.

An Update on Hard Rock Mining in Montana

Garrett Smith

Montana Department of Environmental Quality–Mining Bureau, Helena, MT
gsmith5@mt.gov

Background and Duties

The Hard Rock Mining Section (HRMS) is the program within the Montana Department of Environmental Quality (DEQ) that regulates the mechanized exploration and development of all ore, rock, or mineral substances from hard rock sources. That definition encompasses a wide range of operations, although the resources that are excluded from the HRMS's permitting authority include bentonite, clay, coal, natural gas, oil, peat, sand and alluvial gravel, scoria, soil materials, and uranium. Other sections within the DEQ's Mining Bureau regulate mining activities for those resources. The HRMS and Field Services and Technology Section oversee mining activities conducted under small miner exclusion statements (SMES, ≤5 acres), exploration licenses, and operating permits.

The administrative duties and the permitting procedures that apply to the HRMS originate primarily from the Metal Mine Reclamation Act [MMRA; §82-4-301 et seq., Montana Code Annotated (MCA)] and the Montana Environmental Policy Act (MEPA; §75-1-101 et seq., MCA). These duties include issuing timely and complete decisions for permit applications and modifications, and ensuring permitted mineral development occurs with adequate protection of other resources. The development of environmental assessments (EAs) or environmental impact statements (EISs) is coordinated with the regulatory authorities for other permits obtained through State or Federal agencies. The HRMS reviews the annual reports or renewal statements submitted by active operations and conducts inspections at least once per calendar year to review the mining and reclamation status at each site and to offer compliance assistance. Performance bonds (i.e., financial assurances) are held by the DEQ for operating permits, exploration projects, and some SMES sites in order to perform any potential reclamation work that is not completed by the operator. The bonds are reviewed on an annual basis and recalculated at a minimum of every 5 years, following significant permit modifications, or as deemed necessary by the DEQ.

Recent Legislative Updates

Few amendments were made to the MMRA during the 2023 Montana State Legislative Session. In one example, §82-4-340, MCA was modified to remove the end date that was initially established in 2019 for the transfer of an operating permit to a successor operator. Rather than terminating on June 30, 2026, the following language in §82-4-340(2), MCA will now remain in effect:

> "For an operation with a forfeited bond where the department holds a suspended permit pursuant to 82-4-341(8), the department may transfer the permit to a successor operator provided that the successor operator:
>
> (a) complies with the requirements of this part; and
>
> (b) assumes the duty of the former operator to complete reclamation and submits:
>
> (i) any additional bond required under 82-4-338; and
>
> (ii) a $2,000 fee."

Modifications were also made to §82-4-361, MCA with regard to violation letters issued by the DEQ. Prior to the new legislation that took effect October 1, 2023, the DEQ was restricted to issue violation letters for actions of non-compliance with the MMRA or related permit conditions. The DEQ now has the expanded discretion to instead issue warning letters or administrative deficiency notices, depending on the scope and severity of non-compliance. The text of §82-4-361(1), MCA now states:

> "When the department has reason to believe that a person is in violation of this part, a rule adopted or an order issued under this part, an administrative deficiency notice, or a term or

> condition of a permit issued under this part, it shall send a letter of warning or violation to the person. The letter of warning or violation must describe the provision of the statute, rule, order, or permit alleged to be violated and the facts alleged to constitute the violation. The letter must recommend corrective actions necessary to return to compliance. Issuance of a letter of warning or violation under this subsection does not limit the authority of the department under this part to bring a judicial action for penalties or injunctive relief or to initiate an administrative enforcement action."

An administrative deficiency is further defined in §82-4-361(8), MCA as "a deficiency in reporting, recordkeeping, fee payment, or notification that the department determines is minor in nature, nonsubstantive, and unlikely to recur." To reflect the statutory modifications, updates were required for the hard rock mining rules associated with processing violations and penalties (Administrative Rules of Montana–ARM 17.24.132). The DEQ rulemaking process to address this topic was conducted through late 2023 and early 2024. Other rules were modified to condense and simplify the introductory definitions, clarify the requirements for permit applications and annual reporting, clarify procedures for bonding, and update the criteria for completed or abandoned operations. Following input from stakeholders during a public comment period and public hearing, the updated rules took effect on May 11, 2024. The hard rock mining rules (ARM 17.24.101 through 17.24.189) can be accessed on the Montana Secretary of State's website: https://rules.mt.gov/

The DEQ's implementation of MEPA for permitting actions was also modified during the 2023 legislative session. Previous language in §75-1-201(2)(a), MCA stated that an environmental review conducted under MEPA "may not include a review of actual or potential impacts beyond Montana's borders. It may not include actual or potential impacts that are regional, national, or global in nature." This was amended in 2023 to state that an environmental review "may not include an evaluation of greenhouse gas emissions or corresponding impacts to the climate in the state or beyond the state's borders." While this amendment was being developed, the prior MEPA exception was still being challenged through the First Judicial District Court (Held v. State of Montana, 2020). Plaintiffs claimed that the State's fossil fuel-based energy system and the climate change exception within MEPA violate their State constitutional rights. In August 2023, the district court judge ruled that the statutory prohibition on including greenhouse gas analyses in MEPA review is unconstitutional. That decision is being appealed to the Montana Supreme Court and final resolution has not yet been decided. While litigation is ongoing, and consistent with the First Judicial District Court's order, the DEQ has started a process to assess and improve environmental review processes, including consideration of future climate impacts.

Operating Permit Updates

The following section provides updates on select hard rock operating permits and proposed projects that are currently under development, environmental review, or have been recently approved. It does not summarize the many active SMES sites (>250) or exploration license projects (>50) that are present within the State (fig. 1), nor is it a comprehensive summary of all operating permits.

As of July 2024, there are 77 individual operating permits administered by the HRMS, with a total of 187 project sites associated with the permits (figs. 1, 2). These additional project sites may include product load-out facilities, processing sites, and/or disposal facilities that are not adjacent to the mine area. The project sites also reflect the number of multiple-site permits. These allow for more than one mining location to be covered under a single operation and reclamation plan. Multiple-site permits are more common with quarries and surficial rock picking operations that typically acquire specific types of rock from relatively small disturbance areas spread over a large region.

When tallied, the number of hard rock mine operations for rock product sites clearly outnumbers the industrial mineral and metal mines. Rock product operations often benefit from low barriers to entry for project designs and equipment needs, relatively simple operation and reclamation plans, reduced potential for environmental impacts, and permitting actions that receive little public attention or litigation. Most metal mines in Montana are currently in care and maintenance status or in the process of final reclamation and closure. Many industrial mineral mines and rock quarries have amended their permits in recent years to extend production. Rock product operations continue to expand, but they are also experiencing increased competition in many regions and are subject to the

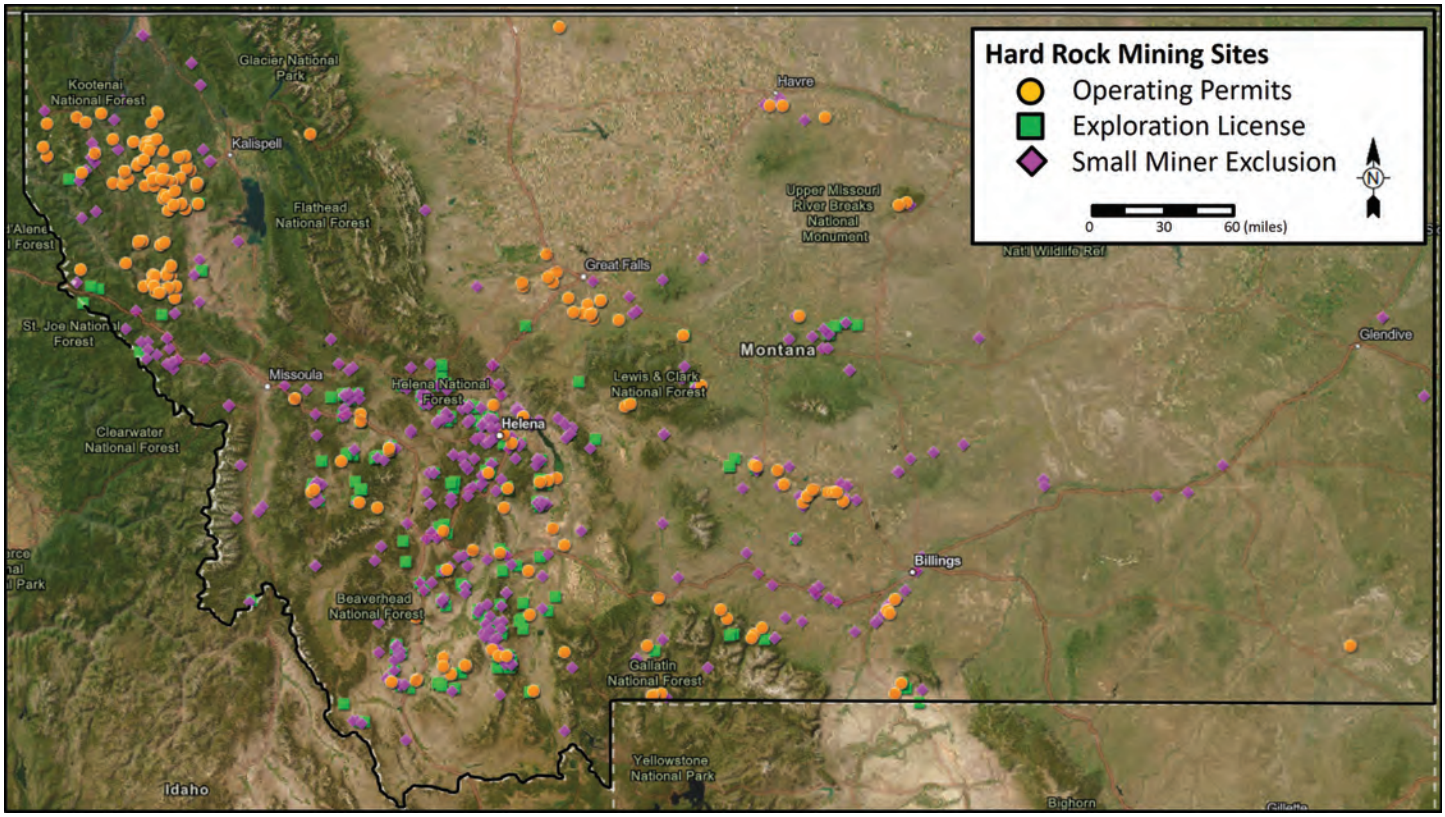

Figure 1. Locations of hard rock mine sites across Montana. The symbols represent project sites and indicate the permitting category (Operating Permit, Exploration License, or Small Miner Exclusion), but not the commodity nor activity status of each site.

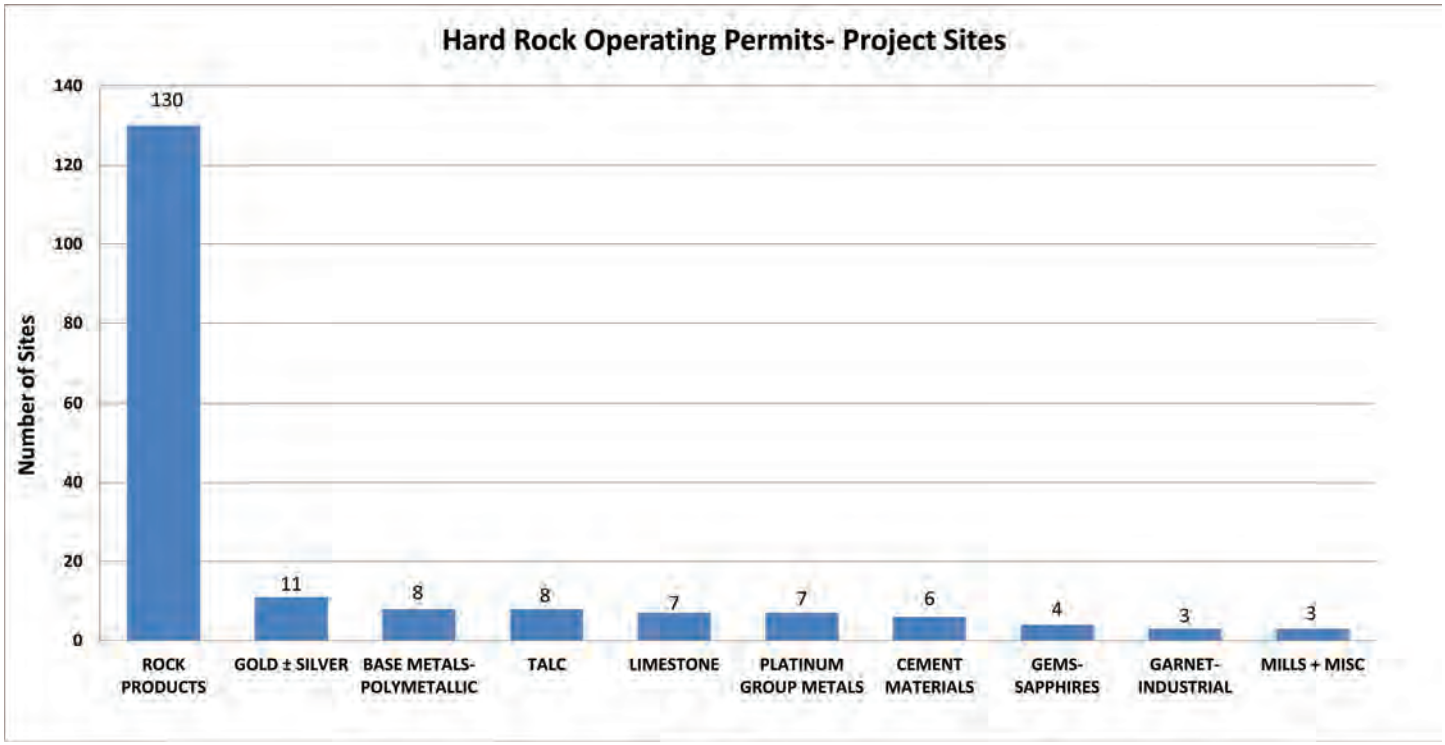

Figure 2. Distribution of Hard Rock Operating Permits by commodity. The project sites associated with a permit may include mine areas, product load-out facilities, processing sites, and/or waste disposal facilities that are not adjacent to the mine area. The project sites also reflect the multiple-site permits, which allow for more than one mining location under a single permit.

dynamics of housing and construction markets. Updates about some of the major developments at active operations and pending projects are included below.

Continental Mine Complex, Montana Resources, LLP; Butte (Cu, Mo, Ag):

Montana Resources continues to produce ore from the Continental Pit. Additionally, non-ore rock is used as construction material around the site, particularly for the embankments of the Yankee Doodle tailings storage facility (TSF). An amendment was approved in 2020 to raise the west embankment of the TSF to an elevation of 6,450 ft and expand the total storage capacity of the facility. Construction has been ongoing since amendment approval and the TSF continues to be inspected and evaluated by a third-party Engineer of Record and Independent Review Panel. The Panel consists of three experts in the field of TSF design and management.

A final EA and amendment approval were issued in 2022 for the construction of a rock disposal site in the Horseshoe Bend area, at the base of the TSF. In order to maintain water seepage flows out of this area, a series of engineered rock drains are being constructed in the foundation of the rock disposal footprint. This also requires demolition of the previous copper precipitation plant and construction of a new plant. This new facility began operating in spring 2024 and it recovers Cu from Berkeley Pit water, Horseshoe Bend seepage, and residual leach pad seepage. The Horseshoe Bend water treatment plant continues to treat a combination of sources for reuse in the concentrator and processing circuit. Pilot testing is also ongoing to evaluate the potential recovery of REEs and other critical minerals from the residual sludge produced at the treatment plant.

Groundwater at the mine is managed in accordance with Superfund (CERCLA) requirements and not the mine operating permit, but there are overlapping objectives for managing the site-wide water balance. Under the remedial action requirements for the Butte Mine Flooding Operable Unit, Montana Resources and other parties continue to implement management and treatment strategies for water in the Berkeley Pit and surrounding groundwater. The water is currently being pumped to first stage treatment prior to the mill processing circuit, which eventually discharges as tailings slurry into the TSF. Decanted water from the tailings pond is then conveyed to a “Polishing Plant” facility that treats the water to applicable surface-water-quality standards before being discharged. The water levels in the Berkeley Pit and nearby compliance points have been held at a steady elevation since 2019. As of July 2024, the total volume of the tailings pond is approximately half of the volume that was contained in 2019 (34,400 acre-ft) and the system is now maintaining a steady operational volume. More than 8.6 billion gallons of water have been treated and discharged.

Golden Sunlight Mine, Golden Sunlight Mines Inc. (Barrick Gold Corp.); Whitehall (Au, Ag):

Mining in the Mineral Hill Pit and the underground workings beneath the pit was suspended in November 2015 and April 2019, respectively. The milling and processing facility also ceased operations and stopped receiving ore for processing brought in by third parties. The third-party ore often originated from historic waste rock and tailings from across the area. The reclamation of rock disposal areas and other disturbances in the permit area has continued since mine production ceased. This is in addition to ongoing pit dewatering and other water management activities.

Following the Final EIS and Record of Decision in 2021, an amendment was approved for a tailings reprocessing project that would extend activity at the mine by approximately 12 years. The amendment allows Golden Sunlight to excavate and reprocess tailings from the previously reclaimed TSF-1 (fig. 3). This includes the construction and operation of a repulping plant to resuspend the tailings in a slurry and then process the tailings through a flotation system in the existing mill facilities. A fine gold and sulfide concentrate is produced and transported to a gold mining operation in Nevada for use in an autoclave roaster, thus lowering the sulfide concentration (and potential reactivity) of the residual tailings that are thickened and disposed as backfill in the Mineral Hill Pit. Tailings process solutions within the pit are recycled to the mill circuit and groundwater continues to be captured in the mine voids beneath the pit. The former TSF-1 footprint will be reclaimed to reflect pre-mining topography to support post-closure land uses for grazing, recreation, and wildlife habitat. The reprocessing of the tailings may also reduce the scale of long-term water treatment onsite by eliminating discharge from TSF-1, while reducing the flow and improving the water quality of water pumped from the Mineral Hill Pit.

Figure 3. Excavation of the tailings from TSF-1 at the Golden Sunlight Mine. The existing reclamation soil cap being salvaged for future use, following the removal and reprocessing of waste from the unlined facility.

Stillwater Mine, Sibanye–Stillwater Ltd.; Nye (Pt, Pd, Rh, Au, Cu, Ni, Co):

The Stillwater River experienced intense spring flooding in 2022, impacting local communities and damaging the primary access road to the Stillwater Mine, as well as compromising the bridge access to the waste rock storage facility and east side surface facilities (fig. 4). Although direct impacts to other mine facilities were minor, the lack of transportation access resulted in mine production delays and extensive repairs coordinated with nearby landowners and highway administrators. In 2023, the Benbow exploration portal and decline located to the east of the Stillwater Mine was incorporated into the mine operating permit. Groundwater encountered in the Benbow area is conveyed back to the primary mine for management and treatment. Capping of the Nye TSF is in progress while the facility is still used for water management, but all tailings are being disposed of in the Hertzler Ranch TSF, approximately 5.5 mi northeast of the mine. The East Side Waste Rock Storage Area liner project is ongoing and will provide additional lined storage capacity. Permitting for Amendment 014 is in progress with the DEQ and United States Forest Service (USFS). The proposed project would increase the crest height for the waste rock storage area and expand the capacity of the Hertzler TSF in phases.

East Boulder Mine, Sibanye–Stillwater Ltd.; McLeod (Pt, Pd, Rh, Au, Cu, Ni, Co):

The East Boulder Mine is located approximately 13 mi northwest of the Stillwater Mine. It is in a different watershed and did not encounter the full extent of flooding or production delays in 2022 that were experienced at the Stillwater Mine. An amendment was approved in 2021 for the Stage 6 expansion of the current TSF, providing storage capacity beyond 2030. A new amendment is also currently under an EIS review, which would authorize the construction of a new TSF ("Lewis Gulch") and a new waste rock storage area ("Dry Fork"). Both facilities would be constructed on liners, to manage any seepage through the waste materials. The DEQ and the United States Forest Service are on track to issue a decision in Q3 2024.

Montana Tunnels Mine, Montana Tunnels Mining, Inc.; Jefferson County (Au, Ag, Pb, Zn):

Mining activity ceased at this site in 2009 and the permit was suspended in 2018 due to failure to post additional bond following a comprehensive review. Limited reclamation tasks have been completed since that time, including grading, capping, and revegetating a small area of rock dumps and logging a hillside in anticipation of constructing a permanent diversion

Figure 4. From August 2022 site inspection, the bridge repair at the Stillwater Mine nearing completion following the June flood.

channel for Clancy Creek. Through 2021 and 2022, the DEQ issued additional violation letters and a Notice of Intent to forfeit the bond. A bond payment schedule was established in April 2022, but the operator failed to pay the required increments and filed for Chapter 11 bankruptcy by December 2022. The US Bankruptcy Court approved a reorganization plan in late 2023, but after the operator failed to post additional bond payments, the DEQ forfeited the bond in February 2024. In July 2024, The U.S. Bankruptcy Court dismissed the case, removing the operator from court protection without resolving its significant debts to creditors (DEQ, Jefferson County, and others). Under the "Successor Operator" legislation passed in 2019 (Section 82-4-340, MCA), the DEQ may hold the permit for up to 5 yr before revoking the permit and completing reclamation. The DEQ may transfer the permit to a successor operator on the condition that they submit a processing fee and any additional bond required for the permit, and comply with requirements of the MMRA to resume mining within an acceptable timeframe or complete reclamation of the mine.

Troy Mine, Hecla Mining Co.; Lincoln County (Cu, Ag)—Closure/Reclamation:

After acquiring the Troy Mine in 2015, Hecla continues to implement the reclamation plan by demolishing the mill and other surface structures, maintaining the pipeline to convey mine water to the impoundment, and by covering and vegetating other portions of the impoundment. An underground drilling program is being implemented to install drain holes and control groundwater flow within the mine, before being conveyed to the impoundment. Note that active water treatment is not required as part of the plans for closure and maintenance.

Black Butte Copper Project, Sandfire Resources America Inc./Tintina Montana Inc.; Meagher County (Cu):

The final hard rock mining permit was issued in 2020 for the Black Butte Copper Project, to the north of White Sulphur Springs. This underground mine would develop the Upper and Lower Johnny Lee deposits through cut and fill methods to extract ore and backfill the completed stopes with cemented paste tailings. The surface facilities would include a double-lined impoundment that would contain cemented paste tailings and waste rock (with no overlying pond),

process water and storm water collection ponds, a water treatment plant, groundwater infiltration galleries for treated water discharge, a paste plant, and a mill facility with crushing and flotation capabilities. The development construction for the project was approved and bonded to occur in two phases. The first phase of construction took place in 2020 and 2021, although legal challenges to the project have delayed further activity. The Fourteenth Judicial District Court ruled in 2022 that the DEQ violated the MMRA and MEPA by approving the permit application. This was appealed to the Montana Supreme Court and the final decision issued in February 2024 overturned the District Court ruling and reinstated the mining permit. Only early construction phase activities have taken place at the site. Separate litigation related to water rights has not yet been resolved by the Montana Supreme Court.

Lingshire Quarry, GCC Trident, LLC: Meagher County (Gypsum, Cement):

The final permit was issued to GCC Trident in 2023 for a new gypsum quarry near Lingshire, northwest of White Sulphur Springs. Early phase construction is ongoing and the gypsum will eventually be hauled to the cement manufacturing facility in Three Forks. The production from this site will maintain GCC's operations following the closure and ongoing reclamation of their previous gypsum mine near Geyser.

Sapphire Ranch Mine, Potentate Mining, LLC and Anaconda Bench Mine, C3, LLC; Granite County (Sapphire):

Two final permits were issued to Potentate Mining, LLC and C3, LLC for separate sapphire mining operations to the southwest of Philipsburg. Similar to placer gold mining methods, both operations consist of excavating unconsolidated alluvial materials and sequential washing and screening steps to recover sapphire (fig. 5). This area is well known for past sapphire production, with mining extending back to the 1890s.

Various companies, rock products:

In addition to many existing operations, there have been multiple operating permit applications and/or amendments recently submitted to the HRMS for rock product operations. These operations include Venture

Figure 5. Processing equipment at the Sapphire Ranch Mine, southwest of Philipsburg.

Figure 6. Rock products quarry (Four Mile site) in northwest Montana, near Marion.

Stone, LLC and Montana Frontier Sandstone, LLC between Lavina and Harlowton, and Green Diamond Resource Co., SEG Properties, LLC, and Flathead Ridge Ranch, LLC across northwest Montana. These sites produce decorative rock, building stone, riprap, and/or aggregates from a variety of sources, including Cretaceous-aged sedimentary units and intrusive igneous rocks around central and northern Montana, and the Belt Supergroup around the northwest (fig. 6).

Preliminary Results of an Investigation into the Phosphoria Formation of Southwestern Montana for Critical Mineral Potential

Adrian Van Rythoven

Montana Bureau of Mines and Geology, Butte, MT

avanrythoven@mtech.edu

Abstract

The Phosphoria Formation is a Permian (~265–274 Ma) sedimentary rock unit (former basin) that occurs in Montana, Idaho, Utah, and Wyoming. Lithology is primarily terrigenous sediments and intervals of chert intermixed with phosphorite. There are two phosphatic members of economic interest: the Retort (upper) and the Meade Peak (lower). The younger Retort Member is much more prevalent in Montana, whereas the Meade Peak is a much more significant member to the south. No current P mines are operating in Montana since the later 1980s, but many abandoned phosphorous mines (some with significant mine dumps) remain. Current mining of the Meade Peak Member occurs in southeast Idaho. In Montana, the Formation is present as subvertical to gently dipping sections in Beaverhead, Powell, Granite, Silver Bow, Deer Lodge, and Madison Counties.

In the phosphatic rocks, biogenic apatite (or carbonate-rich apatite: francolite) is the source of phosphorous. Diagenetic processes appear to have variably enriched the apatite in rare earth elements (REEs). Grades of up to ~0.27 wt.% total REE (including Y) have been determined using modern analytical methods. Contrary to conventional REE deposits hosted in carbonatite, these members are enriched in heavy REEs, with 40% to 50% of the total REE grade being Y, Tb, and heavier REEs. Shaley intervals in the phosphatic members also have potentially recoverable grades of V, Cr, Ni, and Zn. These are in addition to the known phosphorous resources in the Formation.

Considering the known economics of the Phosphoria for P, the Formation might produce significant critical mineral byproducts given the appropriate metallurgy.

Introduction

The Permian Phosphoria Formation comprises the Western Phosphate Field of the U.S. The Formation extends into southwestern Montana, eastern Idaho, western Wyoming, and northern Utah. Mining of the Formation for phosphate/phosphorous has occurred in Montana, Utah, and Wyoming since the early 1900s (Pardee, 1916). Current mining is mostly in Idaho, with one mine also in Utah. Ore from the Utah mine is processed in Wyoming. Mining in Montana ceased by the 1990s, however; dozens of large- to small-scale abandoned mine sites and a derelict processing plant remain as part of that phosphate mining legacy across five counties: Beaverhead, Granite, Silver Bow, Madison, and Powell. These mine sites typically have unreclaimed mine waste (overburden, slag, low-grade ore, etc.) piles on site.

Phosphorite beds in the Phosphoria Formation are found in the Retort Member and the underlying Meade Peak Member. Above both of these members are thick units of chert, whereas the base of the Formation has fairly abundant black shale (McKelvey and others, 1959), carbonaceous mudstone, and phosphorite at the type locality in southeastern Idaho. These rocks intertongue with and pass laterally into a dominantly sandy sequence in south-central Montana and northwestern Wyoming and into a dominantly carbonatic sequence in west-central Wyoming and northeastern Utah, although thin tongues of phosphatic and cherty rocks persist over all these areas. The carbonatic sequence in turn intertongues with and passes laterally into greenish gray and red beds in eastern Wyoming and southeastern Montana, eastern Utah, and northwestern Colorado. The plan of nomenclature developed to describe these rocks and their relationships has the following as its chief elements: (1) The Meade Peak beds are typically thicker and provide ore for the Idaho and Utah mines. Mines in Montana typically extracted ore from the Retort Member as southwestern Montana is closer to the margins of the Permian paleobasin of deposition and thus farther up the stratigraphic col-

umn. Today, the Phosphoria Formation is distributed across southwestern Montana as dissected packages of folded and inclined beds, tectonized by the Laramide Orogeny. The major phosphate mineral of interest is biochemical apatite with variable U, Sr, Na, CO_3^{2-}, and SO_4^{2-} impurities (i.e., francolite). Other major phosphorite constituent minerals are quartz, illite, carbonates, organic matter (e.g., bitumen, kerogen), and iron oxides (Gulbrandsen, 1966; Swanson, 1973).

In addition to phosphorous, the Phosphoria has previously been evaluated for vanadium and uranium (Judd and others, 1986; McKelvey and others, 1986; Sheldon, 1959). Vanadium (and lesser manganese) was extracted in 1963–2009 from ferrophosphate byproduct from fertilizer plants processing the Formation in Soda Springs, Idaho (U.S. Environmental Protection Agency, 2023). Initially, rare earth elements (REE) in the Phosphoria Formation were considered only for trace element geochemistry as paleoclimate proxies (Piper and others, 2007). Recently, investigators have noted the potential of the Formation to be an REE resource (Emsbo and others, 2015, 2016), particularly for heavy REEs (HREEs).

Methods

Rock samples (n = 29) were collected from 13 different abandoned or reclaimed mines that produced phosphate from the Phosphoria Formation in four southwestern Montana counties (Granite, Powell, Beaverhead, and Silver Bow). Slag samples (n = 6) were also collected from a former phosphate refinery furnace site in Silver Bow County (fig. 1).

Samples were collected by hand as grab samples, typically from old mine dumps (e.g., fig. 2), although

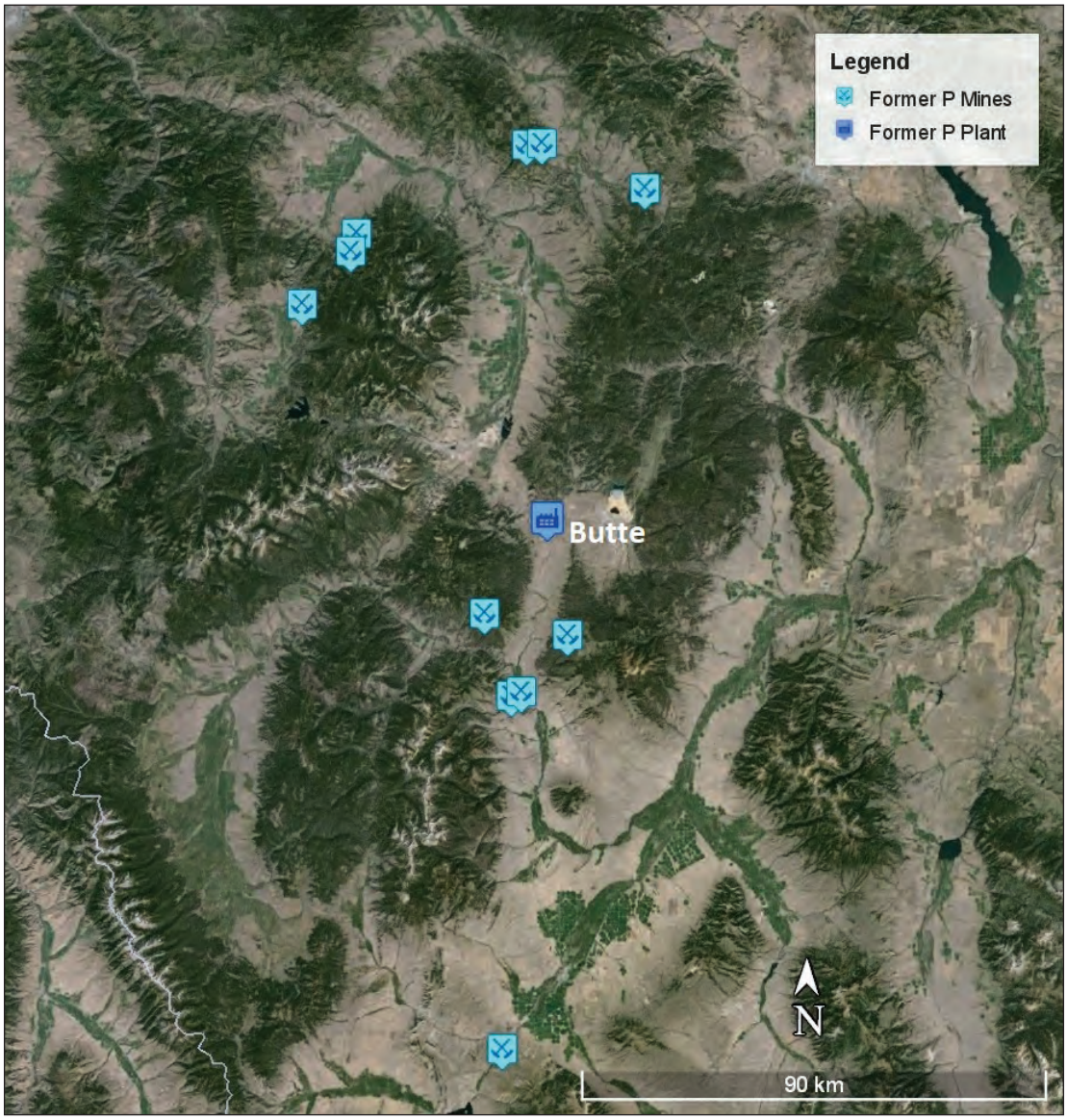

Figure 1. Map of sampled Phosphoria-related sites. Satellite imagery from Google Earth. The former elemental P furnace refinery is immediately west of the city of Butte, Montana.

Figure 2. An example of a typical waste or "low-grade" ore stockpile at the South Fork Parker Creek Mine, Silver Bow County.

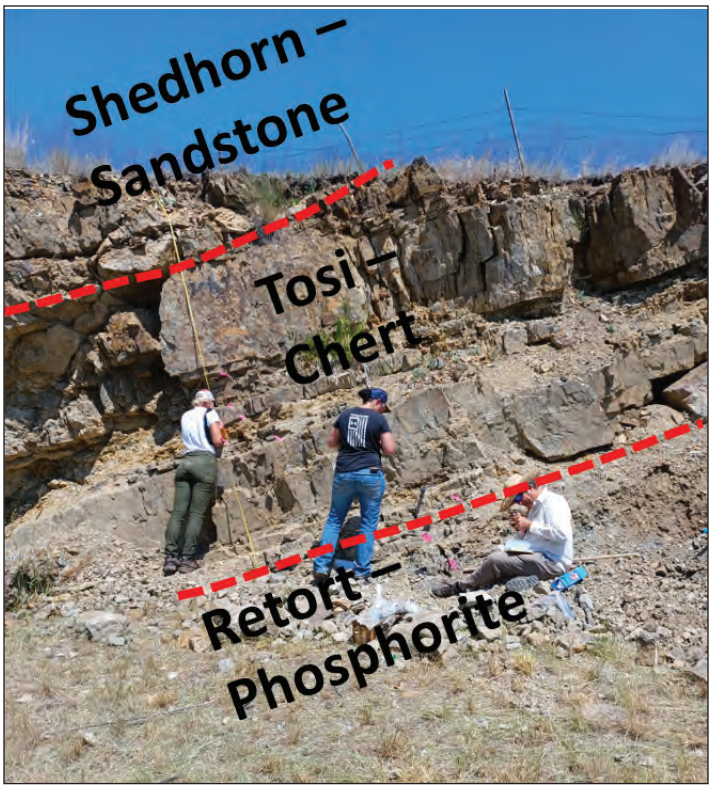

Figure 3. A rare example of preserved Phosphoria Formation Strata at the Newman Brothers Prospect Mine, Powell County. Strata are annotated.

samples from Daly's Spur and Newman Brothers Prospect were collected from mined exposures (e.g., fig. 3). All samples are likely from the Retort Member. Samples collected were split into three fractions: assay, thin section, and archive (e.g., fig. 4). Assays were conducted by ALS Global using the "Complete Characterization Package" (ALS Ltd., 2024). Details about the assay methods are given in Van Rythoven (2023).

The polished thin sections (30 µm thickness) were examined in reflected and transmitted light with a Leica DM2700 P petrographic microscope and Flexacam C3 digital camera. These were then carbon-coated and analyzed with a Tescan MIRA 3 GMU–TIMA X field emission scanning electron microscope (TIMA). Automated mineralogical analysis on the samples with the TIMA was conducted with a 10-µm point spacing, a 1,000 X-ray counts per point dwell rate, and 25 kV beam potential at 15 nA.

Post-collection data processing assigned quartz and apatite as default mineral phases. Additional phases were added iteratively from the unclassified category via manual examination of energy-dispersive spectra. Edge effects were corrected for the final step using the "auto-identify" phases function.

Figure 4. Example of typical Phosphoria phosphorite in hand sample divided for assay, thin section, and archive samples (left to right).

Results

Assays

The complete whole-rock assays with sample metadata were released as an analytical dataset (Van Rythoven, 2023). Overall Total REE grades, including Y (TREE), range 0.01–0.27 elemental wt.%. Phosphorous grades are 1.15–38.1 oxide wt.% (fig. 5). The proportion of REE grade Y with Tb and heavier (i.e., heavy REEs) is 41–57%, with an average of 51%. The distribution of individual REE grades in the samples is shown by figure 6.

V grades are 51–2,460 ppm and Cr grades are 165–2,010 ppm (fig. 7). U values are 4–138 ppm (fig. 8). Other elements of interest are Zn (30–2,770 ppm), Ni (4–394 ppm), As (<1–130 ppm), Pb (<2–1,645 ppm) and Cd (<1–431 ppm).

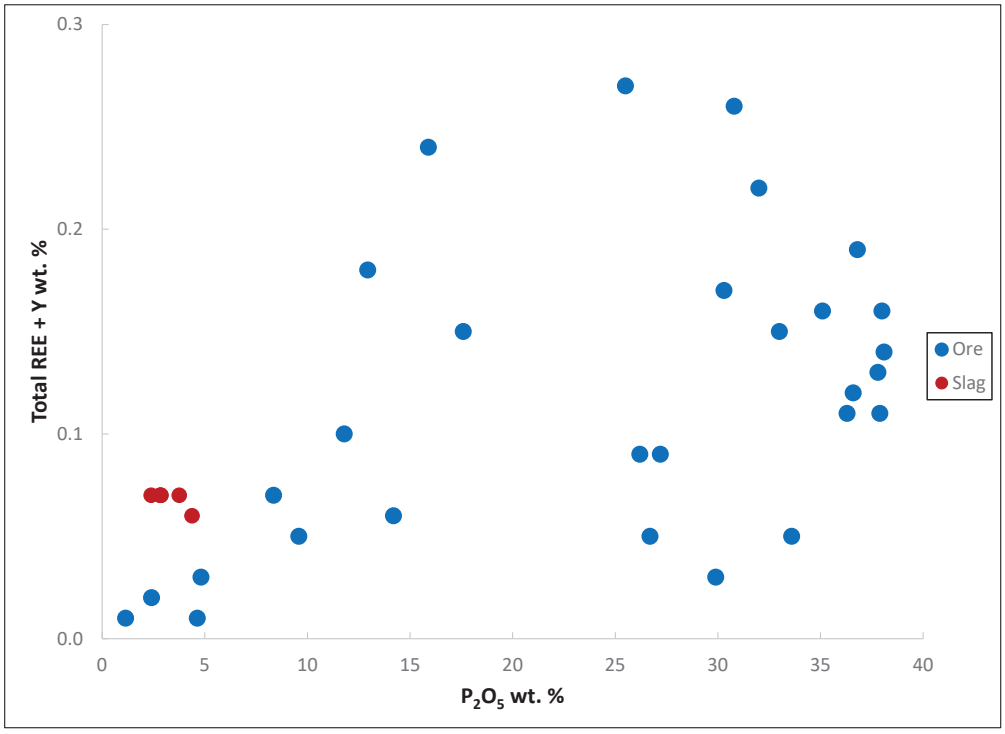

Figure 5. Plot of P_2O_5 vs. TREE for Phosphoria Formation slag and rock samples. Note that pure apatite has ~42 wt.% P_2O_5.

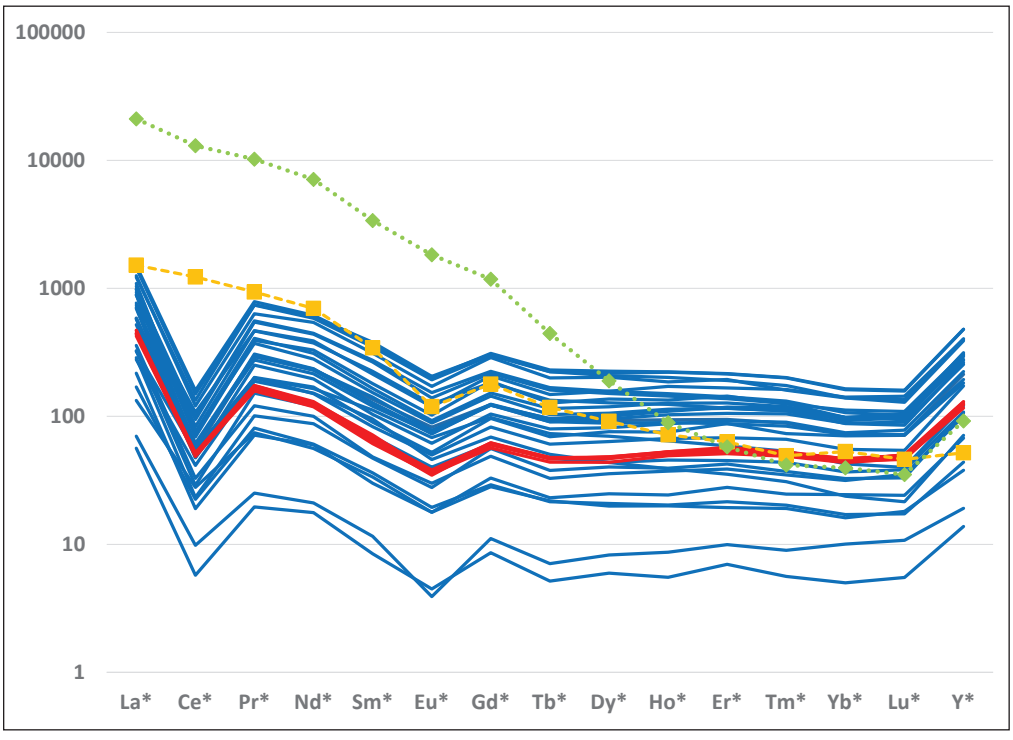

Figure 6. A chondrite-normalized REE plot of Phosphoria rock (blue) and slag (red) samples from this study. The asterisk indicates each sample lanthanide grade is divided by the grade of the same lanthanide in a chondrite standard and the result plotted on the vertical axis. Comparison estimates from resources at Bull Hill in green (Dahlberg and others, 2014) and Halleck Creek in orange (Kinnes and others, 2023), both in Wyoming, are given. Chondrite (C1) values are from Taylor and McLennan (1985).

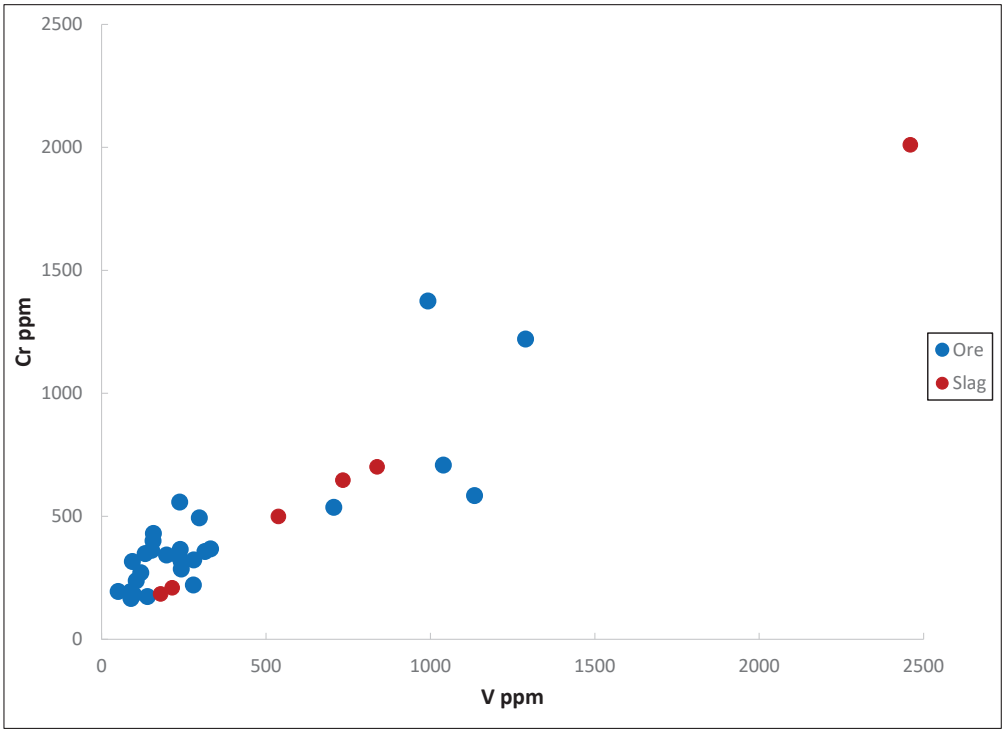

Figure 7. Plot V vs. Cr for Phosphoria Formation slag and rock samples.

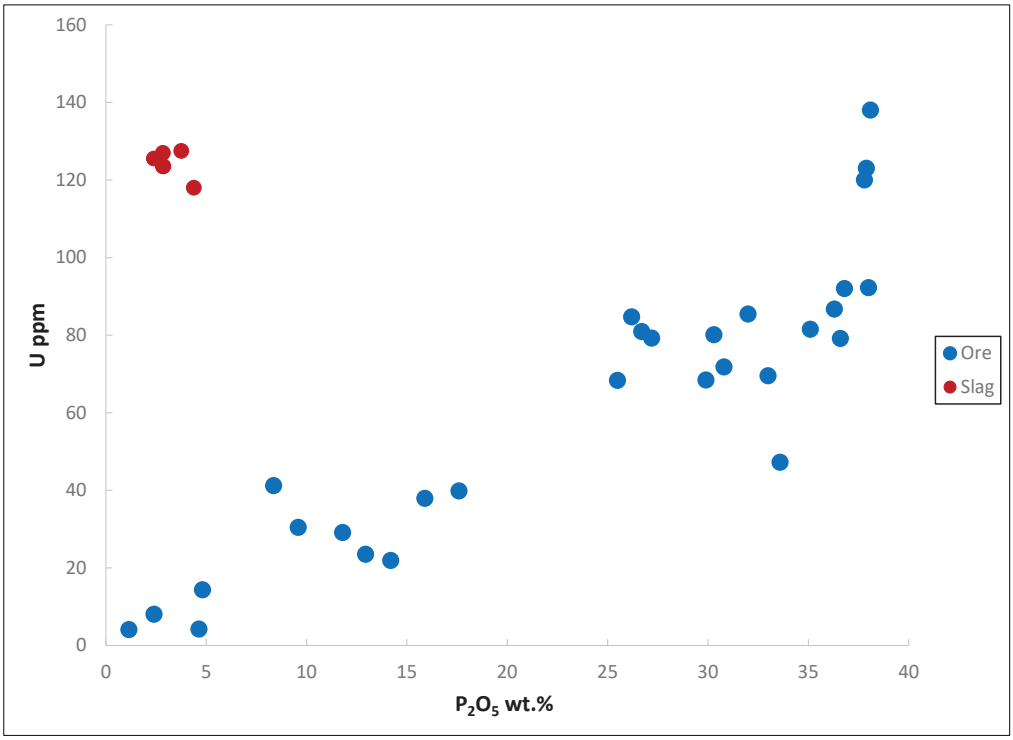

Figure 8. Plot of P_2O_5 vs. U for Phosphoria Formation slag and rock samples.

Petrography

Optical petrography confirmed a variety of textures in the phosphorites. Francolite is common as ooids and/or peloids. Interstitial mud is common and likely apatite-rich. Quartz sand grains, typically as angular silt, are the most common mineral after apatite. Carbonate, clay (illite, chlorite, smectite), feldspar, and Fe-oxide minerals are variable. Accessory barite is visible in a few samples. Intraclastic/conglomeritic textures are common (e.g., fig. 9).

Optical petrography observations were corroborated and expanded upon with TIMA analysis. The samples (aside from the slag) are predominantly apatite and quartz, sometimes as fine-grained intergrowths. Clay minerals are varied. Illite (fine-grained K-Al phyllosilicate) is common, but other undefined species are present, including one that approximates V-rich chlorite. Carbonate minerals are typically as late fracture fill (e.g., fig. 10). The slag samples have almost no apatite and abundant Ca-Mg-Fe silicates, typically as acicular crystals in vesicular glass (fig. 11).

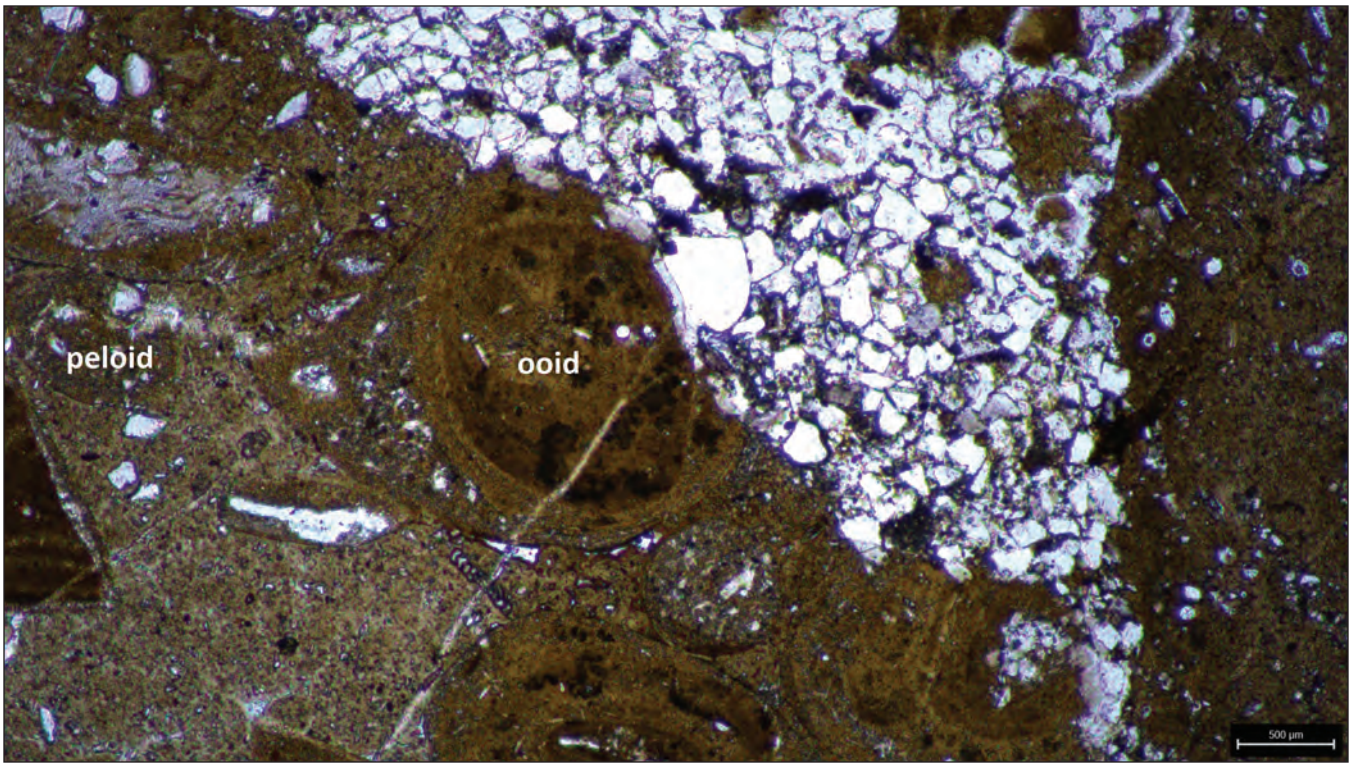

Figure 9. Plane-polarized transmitted light photomicrograph of sample ADV22PHO021: Phosphoria Formation siltstone with phosphorite clasts showing ooids and peloids (examples labeled).

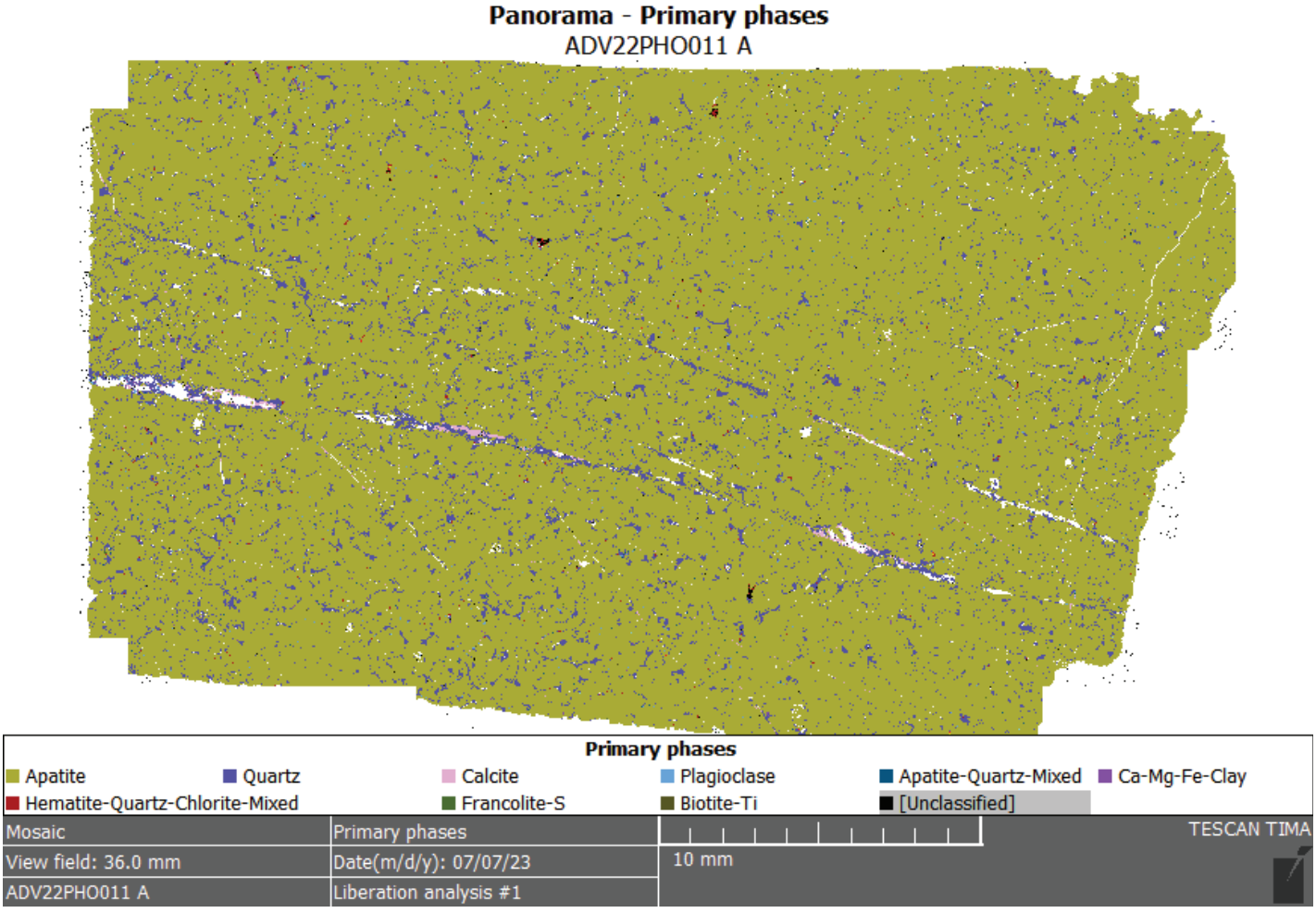

Figure 10. Pseudoimage of ADV22PHO011 created by TIMA. Phosphorite comprising apatite ooids with interstitial quartz silt, cut by late veins of quartz and calcite.

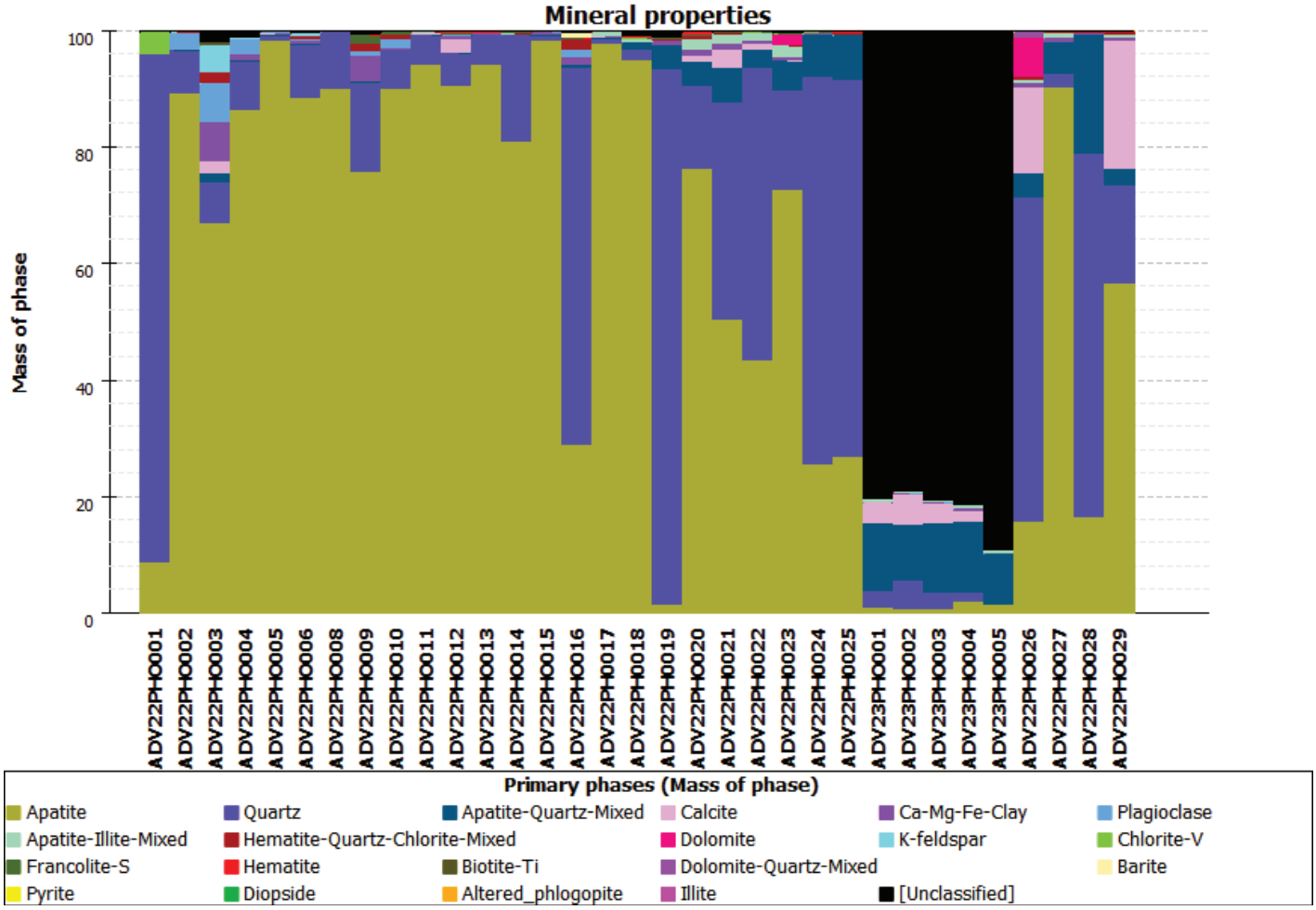

Figure 11. Histogram showing mass % of mineral phases estimated by TIMA analysis. Note the large proportion of black “unclassified” phases (Ca-Mg-Fe silicates and glass) in the slag samples (ADV23PHO001–006).

Discussion

REE content in phosphorite from the Phosphoria Formation is variable. The most significant REE content is held in apatite, but not at a consistent level, leading to high REE grades requiring high P_2O_5, but not all samples with high P possess high REE (fig. 5). This is in addition to the dilution of apatite in ore by gangue minerals, primarily quartz and carbonate. This dilution is compounded by the presence of overburden (e.g., quartzite, chert, dolostone) mixed in with phosphorite in mine waste piles.

Despite variable and absolute low grades and further dilution, REEs in the Phosphoria Formation have an economically favorable and consistent distribution, there are large tonnages in mine waste and unmined strata, and ore mineralogy is simple compared to most conventional REE deposits.

REE Distribution

To consider an REE deposit on the basis of total combined grade is akin to evaluating a polymetallic sulfide vein on combined wt.% Au, Ag, and Cu. Given the different markets and resulting pricing for these REEs, it is important to consider their individual grades. Differences in universal abundances of the REEs are normalized by use of a chondrite-normalized plot (fig. 6). Phosphoria Formation samples have an overall modest light REE (La-Gd, after Ni and others, 1995) grade, with a strong negative Ce anomaly and slight negative Eu anomaly. Heavy REE (Tb-Lu, and Y) content is fairly flat, with high Y compared to Ho. Compare this distribution with those from mineral resource estimates of Bull Hill (Dahlberg and others, 2014), a carbonatite deposit, and Halleck Creek (Kinnes and others, 2023), a peralkaline granitoid deposit, in figure 6. Halleck Creek has moderately higher light REE content, also with a negative Eu anomaly, but no Ce anomaly, and heavy REE levels that are similar to those of the Phosphoria Formation albeit with a modest heavier REE depletion. Bull Hill has a strong light REE enrichment, no Ce or Eu anomalies, and lower heavy REEs, similar in grades for the Phosphoria samples.

Although significantly lower in light REEs than conventional deposit types, the phosphorite samples contain economically prospective grades of the heavy REEs. The overall flat REE distribution and large negative Ce anomaly contribute to the more desirable heavy REEs comprising more of the overall grade than is typical for other deposits, especially those formed in carbonatite.

REE Tonnages

Conventional deposits for REEs are typically in the range of tens of megatonnes (Mt) of ore. Bull Hill and environs contain about 16.3 Mt of measured and indicated resource (Dahlberg and others, 2014). Mountain Pass has 9.5 Mt of indicated and inferred resource [SRK Consulting (U.S.), Inc., 2022]. On the high end of the scale, Halleck Creek has 1,430 Mt of indicated and inferred resource (Kinnes and others, 2023). For comparison, the remaining few mines exploiting the Phosphoria Formation process about 4 Mt of ore per year (Jasinski, 2011). The proposed Paris Hills Phosphate Project in the Idaho portion of the Formation hosts ~88 Mt of measured and indicated resource (Minnes and others, 2019).

The extent of the Formation across four states, and its structural controls as sedimentary beds (albeit tilted and folded), make for a widely distributed collection of deposits that are easily modeled. Waste piles from former mines in Montana, Idaho, and Utah (~50–100, from U.S. Geological Survey, 2024) could also be considered low-grade REE sources with a very high combined tonnage in excess of 1,500 Mt.

Ore Mineralogy

Although a few known REE mines have simple mineralogy, such as Mountain Pass (Mariano, 1989), most others have multiple ore minerals that contribute to the final ore grade: e.g., Bayan Obo (Chao and others, 1990), Bokan Mountain (Lowers and Stoeser, 2014), or Bull Hill (Van Rythoven and others, 2020). Varieties of ore minerals, especially when they are of different mineral classes (e.g., carbonate vs. oxide, vs. phosphate), present challenges to mineral processing. Some REE minerals may even be refractory and difficult to either break down and/or separate from the residue (e.g., silica gel). Silicate REE minerals such as allanite or eudialyte present such challenges, and solutions are being investigated by the metallurgical community (e.g., Davris and others, 2017; Xiao and Zhang, 2024).

In contrast, the majority of REE content in phosphorite is held in apatite/francolite under the substitutional mechanism $3Ca^{2+} \leftrightarrow 2REE^{3+}$ (Emsbo and others, 2015). Chemical processing of phosphorite ore (i.e., apatite) by sulfuric acid dissolution to produce phosphoric acid, or by smelting phosphorite in an electric furnace to produce elemental phosphorous, is well understood (see Sevim and others, 2003). Granted, metallurgical studies of these preexisting process flowsheets need to identify what steps need to be modified for optimal REE recovery. Given the intermediate grades of REEs in the slag samples (fig. 6), sulfuric acid dissolution appears to be more prospective for REE extraction, as smelting does not appear to be selective to REEs.

Other Critical Minerals

In addition to REEs in the Formation, potentially recoverable levels of V and Cr exist in some samples and are tightly correlated (fig. 7). However, the V and Cr mineralization is separate from the REE mineralization and does not always occur in phosphatic zones (fig. 12). Phyllosilicate minerals such as chlorite or illite are the common hosts for V^{3+} in these clay-rich/shaley layers (Drexler and others, 2023). Sample ADV22PHO001 has moderate V (707 ppm), but V-bearing chlorite was found in this sample by TIMA (fig. 11). However, no other samples, even those with higher V, have definite V-bearing phases. Given the close correlation between Cr and V, Cr also appears to be held in phyllosilicates. Whether this is as substitutional Cr^{3+} for Al^{3+} in the crystal lattice, or as a reduction-based sorption of Cr onto ferrous phyllosilicates (e.g., Brigatti and others, 2000) is unclear. Given the range of V and Cr grades, it is also unclear if smelting is selective for these two commodities. V in particular has been established to occur in higher-grade zones in the Meade Peak Member (McKelvey and others, 1986) with an established mechanism for its metallurgical recovery (Judd and others, 1986).

Deleterious Elements

Most REE deposits have associated Th, and sometimes U, that are elements of concern from an environmental risk perspective. These radioactive elements are commonly co-crystallized in the same minerals with the REEs (e.g., in bastnaesite, monazite, allanite, etc., see Zhu and others, 2015 for an overview). Thus, physical beneficiation of the REE ore minerals will create a mineral concentrate with higher radioactivity

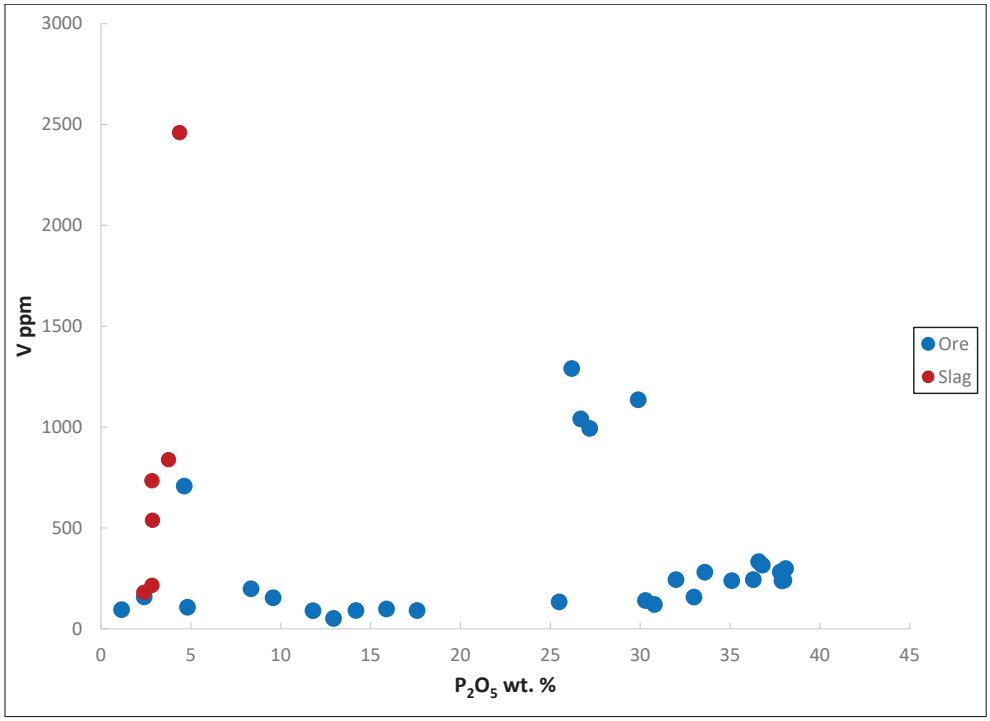

Figure 12. Plot of P_2O_5 vs. V content in samples of rock and slag.

than the ore. Further chemical processing will create chemical tails that then have even higher radioactivity on a per mass unit basis. The Bull Hill resource has about 410 ppm Th and 95 ppm U (Dahlberg and others, 2014). At Halleck Creek, Th is about 51 ppm and U is 6 ppm (Kinnes and others, 2023).

In the phosphorite samples, Th is negligible at <10 ppm; however, U is significant and ranges at 1–5 ppm per wt.% P_2O_5. Values in the slag samples are an order of magnitude higher. Unlike conventional deposits, U is not directly tied to REE content (fig. 13), but both REEs and U occur in apatite/francolite.

Heavy metals contents in the Phosphoria are low overall compared to conventional metal-sulfide deposits. Given the use of phosphorite as fertilizer ore, some jurisdictions have set limits on certain highly toxic metals in fertilizer (e.g., California Department of Food and Agriculture, 2019; European Parliament, 2019). These metals include Cd, As, and Pb. Most of the phosphorite samples are below the California

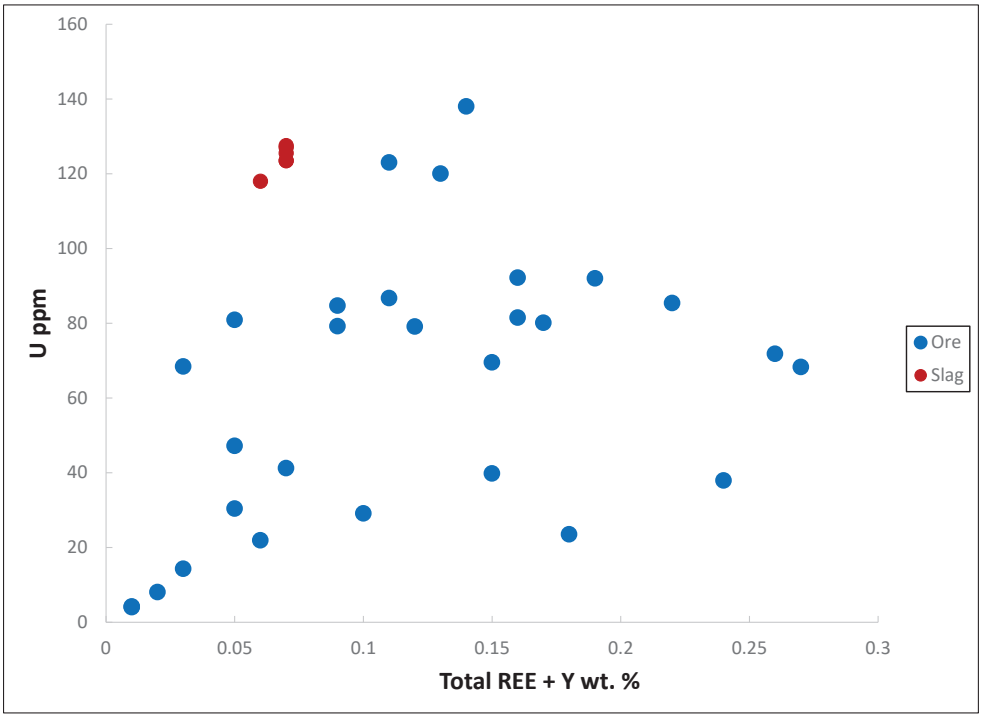

Figure 13. Plot of REE vs. U for Phosphoria Formation slag and rock samples.

thresholds of 4 ppm Cd, 2 ppm As, and 20 ppm Pb per wt.% P_2O_5. Exceptions are mostly samples that are more carbonate or siltstone rock and have <10 wt.% P_2O_5. High-P_2O_5 samples that exceed some of these limits are ADV22PHO006 and ADV22PHO012 (Van Rythoven, 2023). Note that mineral beneficiation may be able to reduce Cd, As, and/or Pb levels in phosphorite ore as these elements are not necessarily substitutional in apatite/francolite.

Conclusions

The potential for the Phosphoria Formation as a host for REE deposits is limited by low-grade, distributed deposits, and some U concerns, but supported by a heavy REE distribution, simple process mineralogy, negligible Th, and immense total tonnage. In particular, considering REEs (and other critical minerals such as Cr or V) as a byproduct to phosphate production supports the economics for such a venture.

Further sampling of the Formation, and bench-scale mineral processing texts, should be able to investigate whether economic REE production is realistic. Similarly, more sampling, combined with other analytical methods such as X-ray diffractometry, should help in determining the residency, and thus the economic viability, of V and Cr in the Formation.

Acknowledgments

Funding for this study was provided by the DEVCOM Army Research Laboratory. The author thanks A. Harley Hoiles, Amanda Rossi, Catherine McDonald, and Tiffany Ostenburg for their help with data collection. Access on marked private lands was provided by the Atlantic Richfield Company, Solvay USA Inc., David Lemmon, Thomas Seagle, and Tanya Seagle.

References

ALS Ltd., 2024, ALS Geochemistry Schedule of Services and Fees USD, p. 50.

Brigatti, M.F., Franchini, G., Lugli, C., Medici, L., Poppi, L., and Turci, E., 2000, Interaction between aqueous chromium solutions and layer silicates: Applied Geochemistry, v. 15, no. 9, p. 1307–1316, https://doi.org/10.1016/S0883-2927(99)00120-1.

California Department of Food and Agriculture, 2019, Non-Nutritive Standards, p. 1, available at https://www.cdfa.ca.gov/is/ffldrs/pdfs/HeavyMetals.pdf [Accessed September 2024].

Chao, E.T.C., Tatsumoto, M., Erickson, R.L., Minkin, J.A., Back, J.M., Buden, R.V., Okita, P.M., Zonglin, H., Qingrun, M., Yingchen, R., Weijun, S., McKee, E.H., Turrin, B., Junwen, W., Xibin, L., and Edwards, C.A., 1990, Origin and ages of mineralization of Bayan Obo, the world's largest rare earth ore deposit, Inner Mongolia, China. USGS Report 90-538, p. 11.

Dahlberg, P.S., Noble, A.C., Pickarts, J.T., Rose, W.L., and Jaacks, J.A., 2014, Bear Lodge Project Canadian NI 43-101 on the reserves and development of the Bull Hill Mine, Wyoming: October 2014, p. 514, Rare Element Resources Ltd.

Davris, P., Stopic, S., Balomenos, E., Panias, D., Paspaliaris, I., and Friedrich, B., 2017, Leaching of rare earth elements from eudialyte concentrate by suppressing silica gel formation: Minerals Engineering, v. 108, p. 115–122, https://doi.org/10.1016/j.mineng.2016.12.011.

Drexler, M., Barton, I., and Zanetta, P.-M., 2023, Vanadium in phyllosilicate ores: Occurrence, crystal chemistry, and leaching behavior: Minerals Engineering, v. 201, p. 108205, https://doi.org/10.1016/j.mineng.2023.108205.

Emsbo, P., McLaughlin, P.I., Breit, G.N., du Bray, E.A., and Koenig, A.E., 2015, Rare earth elements in sedimentary phosphate deposits: Solution to the global REE crisis? Gondwana Research, v. 27, no. 2, p. 776–785, https://doi.org/10.1016/j.gr.2014.10.008

Emsbo, P., McLaughlin, P.I., du Bray, E.A., Anderson, E.D., Vandenbroucke, T.R.A., and Zielinski, R.A., 2016, Rare earth elements in sedimentary phosphorite deposits: A global assessment, *in* Rare earth and critical elements in ore deposits: Society of Economic Geologists, v. 18, p. 101–113, https://doi.org/10.5382/Rev.18.05.

Gulbrandsen, R.A., 1966, Chemical composition of phosphorites of the Phosphoria Formation: Geochimica et Cosmochimica Acta, v. 30, no. 8, p. 769–778, https://doi.org/10.1016/0016-7037(66)90131-1.

Jasinski, S.M., 2011, Mineral commodity summary: Phosphate rock, p. 118–119, U.S. Geological Survey.

Judd, J.C., Sandberg, R.G., Huiatt, J.L., and Hodel, D.P., 1986, Recovery of vanadium, uranium, and

phosphate from idaho phosphorite ores: U.S. Bureau of Mines Report of Investigations 9025, p. 1–15.

Kinnes, D.M., Stotter, S.V., Young, K.R., Gillman, A.J., and Guilinger, J.R., 2023, Technical report of exploration and maiden resource estimates of the Halleck Creek Rare Earths Project: American Rare Earths, p. 140.

Lowers, H.A., and Stoeser, D.B., 2014, Comparison of SEM-EDS and EPMA-WDS Analysis of rare earth element containing minerals from Bokan Mountain, Alaska: Microscopy and Microanalysis, v. 20, no. 3, p. 2, https://doi.org/10.1017/S1431927614005194.

Mariano, A.N., 1989, Nature of economic mineralization in carbonatites and related rocks, *in* Bell, K., ed., Carbonatites: Genesis and evolution: Boston, Mass., Unwin Hyman Ltd., p. 149–176.

McKelvey, V.E., Williams, J.S., Sheldon, R.P., Cressman, E.R., Cheney, T.M., and Swanson, R.W., 1959, The Phosphoria, Park City and Shedhorn Formations in the Western Phosphorite Field: U.S. Geological Survey Professional Paper 313, p. 1–54, https://doi.org/10.3133/pp313A.

McKelvey, V.E., Strobell Jr., J.D., and Slaughter, A.L., 1986, The vanadiferous zone of the Phosphoria Formation in western Wyoming and southeastern Idaho: U.S. Geological Survey Professional Paper 1465, p. 27.

Minnes, E.H., DeWolfe, J., Simper, J., Hart, M.J., and Sotillo, F.J., 2019, NI 43-101 technical report on Itafos Conda and Paris Hills mineral projects: Ida., Itafos, p. 259.

Ni, Y., Hughes, J.M., and Mariano, A.N., 1995, Crystal chemistry of the monazite and xenotime structures: American Mineralogist, v. 80, p. 21–26.

Pardee, J.T., 1916, The Garrison and Philipsburg Phosphate Fields, Montana: Contributions to Economic Geology, Part I, p. 195–228.

Piper, D.Z., Perkins, R.B., and Rowe, H.D., 2007, Rare-earth elements in the Permian Phosphoria formation: Paleo proxies of ocean geochemistry: Deep-sea research Part II: Topical studies in oceanography, v. 54, no. 11–13, p. 1396–1413, https://doi.org/10.1016/J.DSR2.2007.04.012.

Regulation, EU, 2019, 2019/1009 of the European Parliament and of the Council of 5 June 2019 laying down rules on the making available on the market of EU fertilising products and amending Regulations (EC) No. 1069/2009 and (EC) No. 1107/2009 and repealing Regulation (EC) No. 2003/2003, Text with EEA Relevance, v. 114, available at https://eur-lex.europa.eu/eli/reg/2019/1009/oj [Accessed September 2024].

Sevim, F., Saraç, H., Kocakerim, M.M., and Yartaşı, A., 2003, Dissolution kinetics of phosphate ore in H_2SO_4 Solutions: Industrial and Engineering Chemistry Research, v. 42, no. 10, p. 2052–2057, https://doi.org/10.1021/ie020168o.

Sheldon, R.P., 1959, Geochemistry of uranium in phosphorites and black shales of the Phosphoria formation: U.S. Geological Survey Bulletin 1084-D, p. 83–113, https://doi.org/10.3133/b1084D.

SRK Consulting, U.S., Inc., 2022, SEC Technical report summary: Pre-feasibility study Mountain Pass Mine, San Bernardino County, California, p. 260, available at https://www.sec.gov/Archives/edgar/data/1801368/000180136822000010/d215279dex961.htm [Accessed September 2024].

Swanson, R.W., 1973, Geology and phosphate deposits of the permian rocks in central western Montana: U.S. Geological Survey Professional Paper 313-F, p. 779–833.

Taylor, S.R., and McLennan, S.M., 1985, The Continental Crust: Its composition and evolution: Blackwell Scientific Publications, Geoscience Texts.

U.S. Environmental Protection Agency, 2023, Record of Decision Amendment: Kerr-McGee Chemical Corporation Soda Springs Plant Superfund Site, Soda Springs, Ida., p. 51.

U.S. Geological Survey, 2024, Mineral resources data system: By commodity, available at https://mrdata.usgs.gov/mrds/map-commodity.html [Accessed September 2024].

Van Rythoven, A.D., 2023, Preliminary data release of whole-rock assays from Phosphoria-related entities in southwest Montana: Montana Bureau of Mines and Geology Analytical Dataset 6, https://doi.org/10.59691/GEPA6042.

Van Rythoven, A.D., Pfaff, K., and Clark, J.G., 2020, Use of QEMSCAN® to characterize oxidized REE ore from the Bear Lodge carbonatite, Wyoming, USA: Ore and Energy Resource Geology,

v. 2–3, July, no. 100005, https://doi.org/10.1016/j.oreoa.2020.100005.

Xiao, Z., and Zhang, W., 2024, Review of allanite: Properties, occurrence and mineral processing technologies: Green and Smart Mining Engineering, v. 1, no. 1, p. 40–52, https://doi.org/10.1016/j.gsme.2024.04.004.

Zhu, Z., Pranolo, Y., and Cheng, C.Y., 2015, Separation of uranium and thorium from rare earths for rare earth production—A review: Minerals Engineering, v. 77, p. 185–196, https://doi.org/10.1016/j.mineng.2015.03.012.

Controls on Fluid Flow and the Effect of Hydrothermal Alteration on Porosity in the Tuff of Sulphur Creek, Yellowstone National Park, Wyoming

Jarred Zimmerman[1,2] and Peter B. Larson[1]

[1]*Washington State University School of the Environment, Pullman, WA*

[2]*Current affiliation: Montana Bureau of Mines and Geology, Butte, MT*

jzimmerman@mtech.edu

Abstract

Thermal areas at Yellowstone are concentrated along faults, volcanic flow contacts, and local fractures; however, this observation does not fully resolve flow on the scale of a single hydrothermal system. As reactive hydrothermal fluids infiltrate a geologic unit, they modify the hydraulic properties of that unit. The eroded hydrothermal system at Seven Mile Hole provides a superb opportunity to study changes to porosity and determine controlling factors for permeability by examining veining, hydrothermal alteration patterns, and fractures. Porosity in the Tuff of Sulphur Creek was determined by comparing the density of a whole-rock sample to a powdered version. Petrologic heterogeneity, variable welding, and devitrification led to a range of porosity from 7 to 40% (mean 21 ± 11%, n = 6) in unaltered to weakly altered samples. Alkaline-chloride alteration lowered porosity, 2–30% (mean 15 ± 10%, n = 10), through the deposition of secondary minerals in pore spaces, whereas acid-sulfate alteration produced a porosity range of 4–31% (mean 23 ± 11%, n = 4), likely from the deposition of secondary minerals and the dissolution of the host unit. The steam-heated portion of the system created a porosity range of 3–33% (mean 15 ± 8%, n = 37) that appears to be a combination of secondary mineral deposition and dissolution. Permeability was determined by measuring strike and dip on 26 fractures and 44 veins, with additional strike measurements where dips were unreliable, and from map-scale features (silicified ridges, linear trend of siliceous sinter fields, elongated hydrothermal alteration) recorded through in-field and GIS methods. Dominant fracture strike populations (NNW–SSE and WNW–ESE), vein strike populations (NW–SE and NE–SW), and dominant trends of map-scale features (E–W) appear to indicate permeability is controlled by extra-caldera faults with noted displacement during the Quaternary (NNW–SSE), intra-caldera faults (NW–SE), and influence from the caldera margin that bisects the study area.

Introduction

Understanding permeability and porosity distributions in a hydrothermal system provides insight into how fluids infiltrate and alter the host rock. In epithermal systems, secondary permeability from fracturing allows for more effective infiltration of hydrothermal fluids (Norton, 1984; John and others, 2010). This study examines how fluid flow occurs at the scale of a single system within the larger Yellowstone hydrothermal system. The study area has been geologically mapped for hydrothermal alteration and separated into distinct mineral assemblages that correspond to fluid types. Primary permeability was examined through syndepositional fabrics, such as fiamme and compression banding. To account for secondary permeability, strike and dip measurements were recorded for fractures and veins in the study area. Additionally, map-scale linear trends of silicified ridges, elongated alteration zones, and a roughly linear alignment of siliceous sinter fields have been recorded through a combination of in-field and GIS-based measurements. Porosity was determined by comparing the density of a whole-rock sample to that of a powdered version. The purpose of this paper is to refine the understanding of how fluids flow through the Tuff of Sulphur Creek and examine how epithermal alteration alters the hydraulic properties of the host.

Geologic Setting

The 0.631 Ma Yellowstone caldera is located within the Basin and Range Province, which accommodates extension of North American crust. The modern stress field south of Yellowstone National Park is dominated by an E–W-directed extension and an ENE–WSW-directed extension north of the park (Parsons, 2006; Smith and others, 2009; Long, 2019). An alignment of intra-caldera volcanic vents appears

to follow normal faults north and south of the Yellowstone caldera, potentially indicating a past continuity between mountain ranges to the north and south of the caldera complex (Christiansen, 2001; Smith and others, 2009). Reactive thermal fluids at Yellowstone are concentrated by major fault zones, ring fault zones, and flow contacts that are kept open by seismicity (fig. 1; Fournier 1989; Hurwitz and Lowenstern, 2014). Broadly, the hydrothermal fluids can be separated into two end members, alkaline-chloride and acid-sulfate fluids, that can be altered by mixing with each other or diluted by meteoric waters in the shallow subsurface (Truesdell and others, 1977; Fournier, 1989; Hurwitz and Lowenstern, 2014).

Geology of Study Site

The Grand Canyon of the Yellowstone River exposes nearly 300 vertical meters of hydrothermally altered rock along a roughly 9-km stretch (Larson and others, 2009). While hydrothermal alteration is best seen in the Grand Canyon, research boreholes drilled in the 1960s provide additional insight into hydrothermal alteration, albeit not *in situ* (White and others, 1975; Dobson and others, 2003). The study area, Seven Mile Hole, is 6 km^2 between Washburn Hot Springs and the northern rim of the Grand Canyon of the Yellowstone River, spanning the caldera margin (fig. 1). The area is underlain, primarily, by the petrologically heterogeneous, variably welded, and devitrified Tuff of Sulphur Creek (TSC), which erupted 479 ± 10 ka (Gansecki and others, 1996; Christiansen, 2001; Pritchard and Larson, 2012). The modern thermal and fossil epithermal systems in Seven Mile Hole indicate the area has had prolonged thermal activity. Place names given in quotations are unofficial names used to simplify discussion. Mineral assemblages (MA)

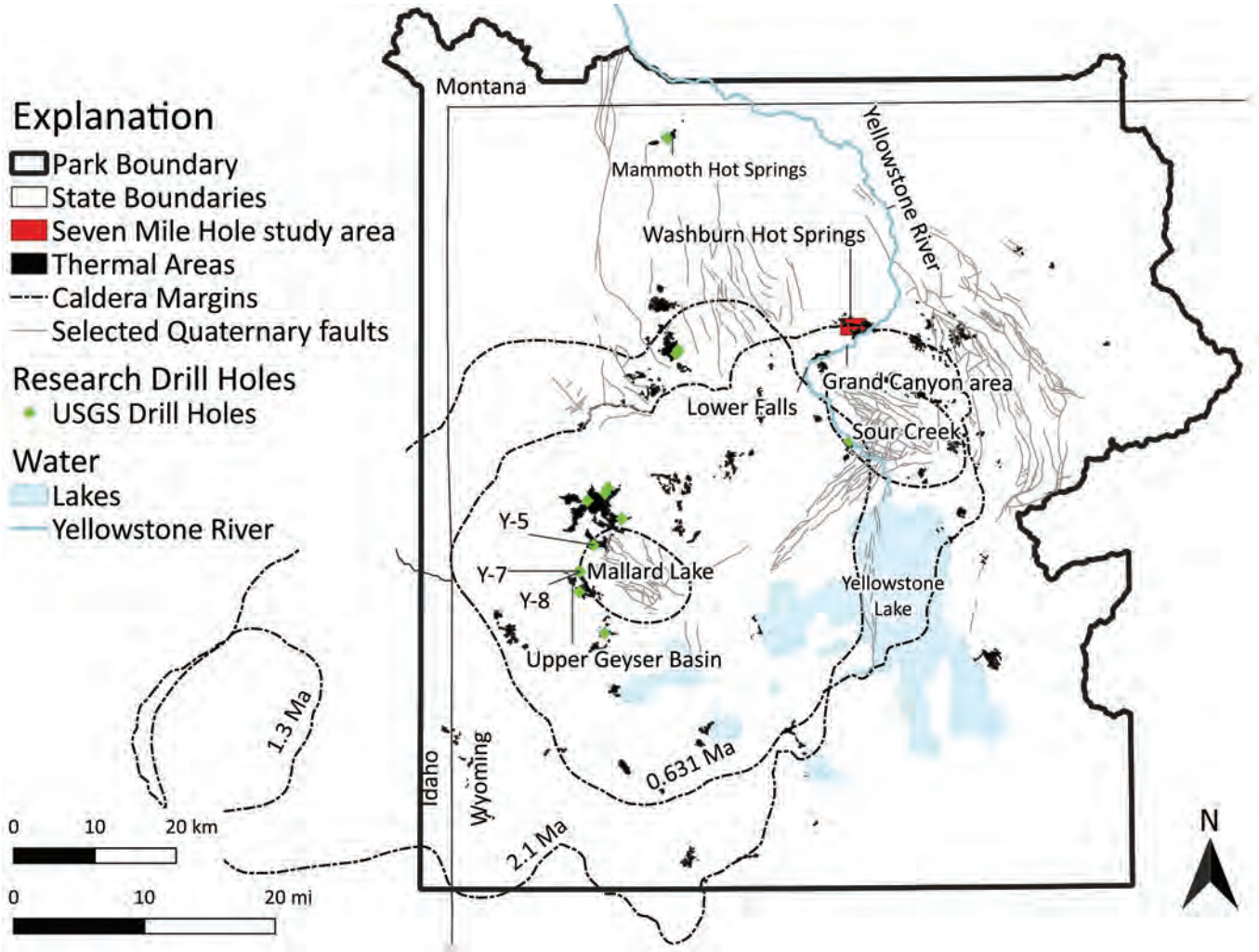

Figure 1. Map of Yellowstone National Park. Light gray lines are selected regional faults that accommodated displacement during the Quaternary period. Dashed lines define the margins of the three most recent caldera-forming eruptions, and the modern resurgent domes, Sour Creek and Mallard Lake. Irregular black regions reflect thermal areas scattered throughout the Park. The approximate location of the study area is noted by the red box south of Washburn Hot Springs. Data are from Wyoming State Geological Survey GIS database (https://www.wsgs.wyo.gov/pubs-maps/gis.aspx, accessed Feb 16, 2022), the digital geologic-GIS map of the Yellowstone National Park, and the USGS Quaternary Fault database (https://www.usgs.gov/programs/earthquake-hazards/faults, accessed April 12, 2023).

are separated based on altering fluid chemistry: alkaline-chloride (MA2, MA5, MA6), acid-sulfate (MA3, MA3A), and the shallow steam-heated zone (MA1). Siliceous sinter mounds indicate alkaline-chloride fluids discharged at the modern canyon rim elevation in the past (fig. 2). The upwelling zone at "Ridge 7741" (Pritchard and Larson, 2012) has an MA2 (illite + quartz) aureole with a distal body of MA6 (quartz

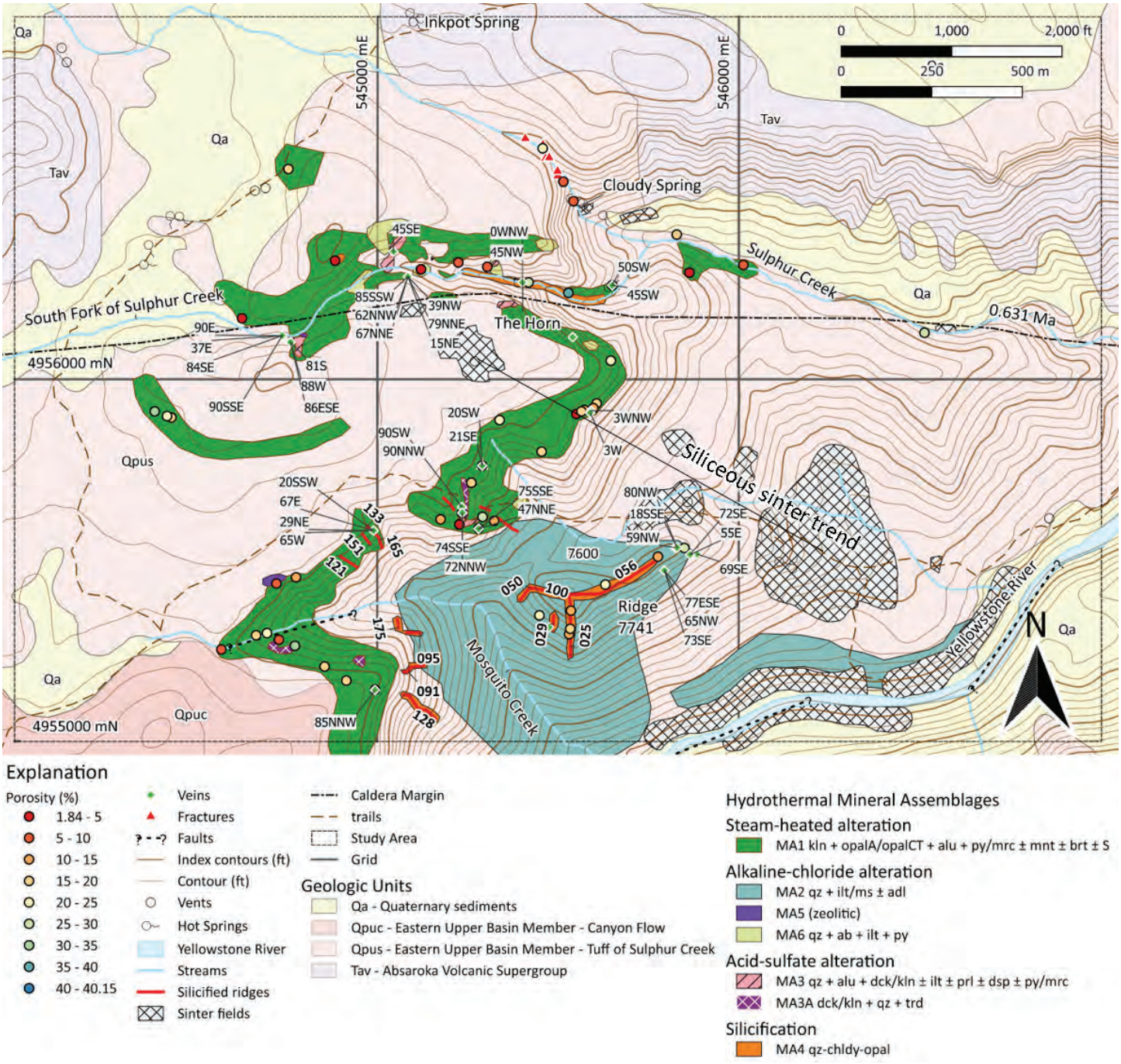

Figure 2. Geologic map and hydrothermal mineral assemblages in the study area. The boundary of the study area is noted by the dashed line with gray lines noting the Z12N UTM grid, marked every 1 km. Numbers with callouts are dip direction of veins. A line extending from the canyon rim to nearly the Yellowstone River represents the approximate trend of active and extinct siliceous sinter fields. Bolded three-digit numbers next to silicified ridges correspond to azimuth strike. Hydrothermal mineral assemblages are indicated by the color schemes, and mineral abbreviations follow IMA-CNMNC convention: kln, kaolinite; alu, alunite; py, pyrite; mrc, marcasite; mnt, montmorillonite; brt, barite; qt, quartz; ilt, illite; ms, muscovite; dck, dickite; prl, pyrophyllite; dsp, diaspore; trd, tridymite; ab, albite. The following abbreviations do not follow IMA-CNMNC convention: adl, adularia; cldy, chalcedony. The following place names are unofficial: Ridge 7741, The Horn, Cloudy Spring, and The Switchbacks. These serve to clarify locations through recognizable features. Dataset includes data presented in Manion (2010) and Phillips (2010). Geologic unit data are from the Wyoming State Geological Survey GIS database (https://www.wsgs.wyo.gov/pubs-maps/gis.aspx, accessed February 16, 2022) and the Digital geologic-GIS map of the Yellowstone National Park. The base map is a portion of the 1 x 1 degree Ashton E Wyoming topographic map (https://rockyweb.usgs.gov/vdelivery/Datasets/Staged/Elev/Shape/ accessed October 15, 2020).

+ albite + illite + pyrite), also noted in the South Fork of Sulphur Creek. MA5 is included with alkaline-chloride alteration, despite its unknown origin. MA3 (quartz + alunite + dickite/kaolinite ± illite ± pyrophyllite ± diaspore ± pyrite/marcasite) and MA3A (dickite/kaolinite + quartz + tridymite) are likely upwelling zones, noted by diaspore, pyrophyllite, and dickite (John and others, 2010). MA4, silicification, is associated with both fluid types. MA1 (kaolinite ± opaline silica ± alunite) overprints nearly all MA.

Methods and Results

Porosity Measurements

Density measurements were conducted in the Peter Hooper GeoAnalytical Lab at Washington State University following the methods described in Larson and others (1994). Rock volume measurements were conducted between one and six times, and powder volume measurements were conducted between one and four times. The difference between whole-rock powders and corresponding rock samples is a measure of the volume percentage of the rock, defined here as porosity. As hydrothermal fluids permeate a rock, pore volume may be altered through secondary mineral deposition or leaching of the host unit, which can act to increase or decrease the overall porosity of a sample. This method estimates porosity down to the size of the powder (coarser than 50 μm). Porosity is separated into 5% groups (fig. 2) and by MA (fig. 3). Unaltered porosity in the TSC ranges from 7 to 40% (mean 21 ± 11% (±1 std. dev.), n = 6). MA1 samples are scattered across the study area with porosity that ranges from 3 to 33% (mean 16 ± 8%, n = 37). MA2 is found around Ridge 7741 with porosities of 21%, 25%, and 27%. MA3 samples are from the Switchbacks, with porosities of 4%, 27%, and 30%. The sole MA3A, porosity of 31%, comes from Mosquito Creek. MA4 samples are split between Ridge 7741, where porosity ranges from 11 to 17% (mean 14 ± 2%, n = 4), and the South Fork of Sulphur Creek, porosity of 4%, 27%, and 38%. The only MA5 sample comes from Mosquito Creek and has a porosity of 8%. MA6 samples are a collection from the valley walls and streambed in the South Fork of Sulphur Creek with porosity that ranges from 2 to 30% (mean 11 ± 10%, n = 6). The least porous sample, 2%, is a silica-sulfide nodule found as float.

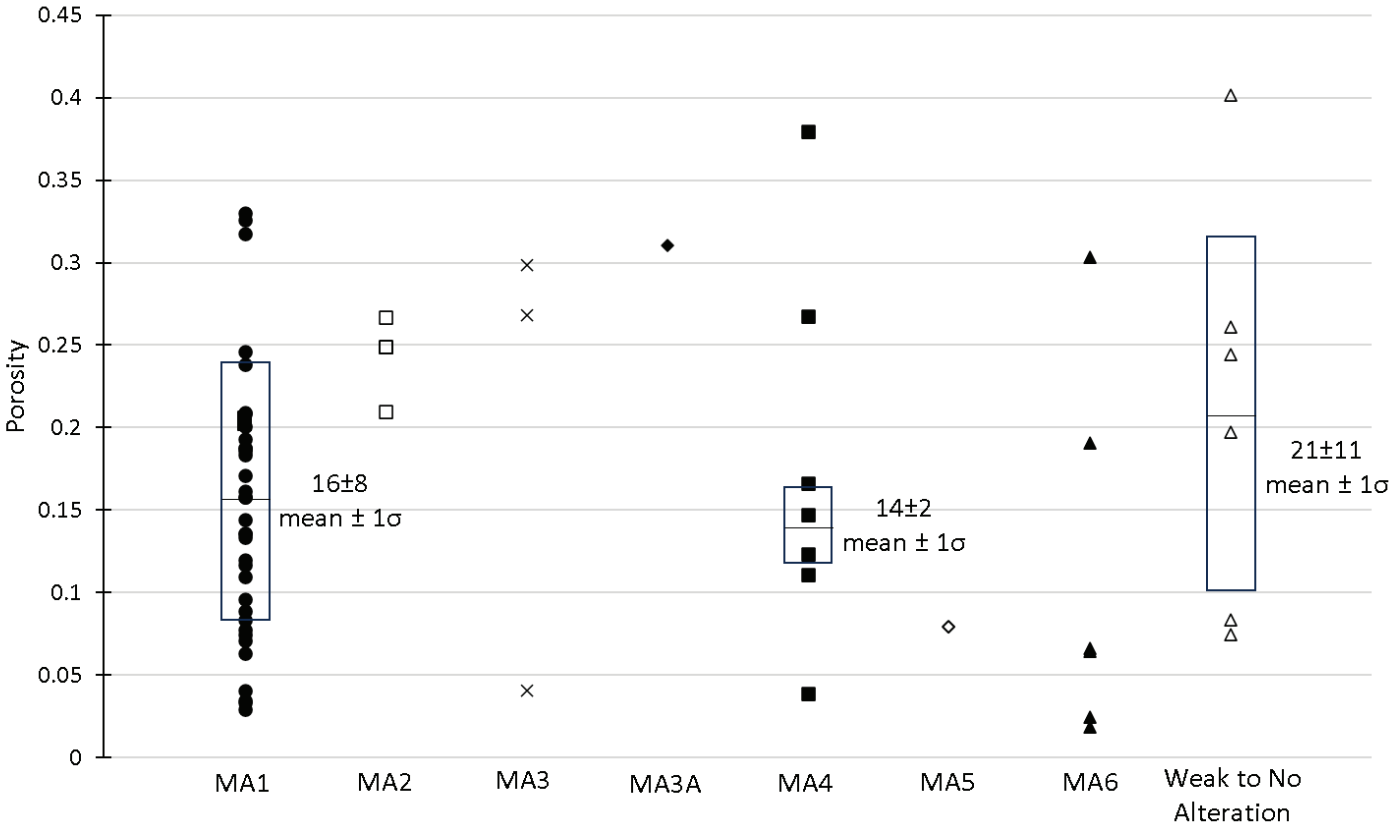

Figure 3. Porosity separated based on mineral assemblages in altered tuff and tuff with weak to no alteration. The general spread of porosity is similar between the alteration mineral assemblages. However, mean porosity values for MA1 (steam-heated alteration) and MA4 (silicification) are lower than tuff with weak to no alteration, indicating hydrothermal fluids are generally decreasing porosity in those mineral assemblages.

Trends of Primary Fabrics, Fractures, Veins, and Breccias

In Seven Mile Hole, permeability is noted through primary fabrics, fractures, veins, and map-scale trends on silicified ridges and siliceous sinter fields (fig. 4). Measured primary (i.e., syndepositional) fabrics (*n* = 8; fiamme, compression banding, one lineation of vugs) indicate those inside the caldera margin dip between 13° and 47° NE and outside of the caldera margin dip between 14° and 40° SW (fig. 4A) and have a primary strike population NW–SE (fig. 4B). Fracture surfaces can be smooth or irregular, with linear to curvilinear traces. No slickenlines were observed. Likely due to variable welding, fracture spacing is irregular. When plotted on a density contoured pole to plane stereonet (fig. 4D), the greatest fracture population is primarily N–S-striking fractures with vertical to subvertical dips, and the associated Rose diagram (fig. 4E) indicates fracture strikes are most commonly NNW–SSE and WNW–ESE, with smaller populations of NE–SW and NW–SE strikes. The density contoured pole to plane stereonet for veins (fig. 4I) indicates the data are primarily NNW–SSE striking with vertical to subvertical dips, and the associated Rose diagram (fig. 4G) indicates vein strikes have dominant NW–SE and NE–SW strike populations with a smaller population of NNW–SSE strikes. Map-scale linear trends are measured through a combination of field and map-scale measurements and are recorded in the first 180 azimuth (fig. 4C). Ridge 7741 is separated into three limbs: the eastern limb, the western limb, and the southern limb. An adjacent silicified outcrop on the western side of the southern limb trends 029. To the north and south of Mosquito Creek are silicified ridges that extend into the Grand Canyon. Trends are shown in figure 2. The elongated MA4 body in the South Fork of Sulphur Creek trends approximately 102. Siliceous sinter fields follow an approximate 135 trend. Two isolated breccia bodies, one roughly 12 m below the ridgeline of Ridge 7741 and one near "The Horn" (fig. 2), potentially indicate hydrostatic overpressuring from decreased permeability.

Discussion

Decreasing Porosity and Hydrothermal Alteration

Core recovered from research drilling in the late 1960s provides a comparison to the porosity noted in the TSC. In Y-5 (fig. 1), moderately welded, hydrothermally altered Lava Creek Tuff has a mean porosity of 15%, and non- to weakly welded core has a mean porosity of 34.1% (Dobson and others, 2003), providing an explanation for some of the spread of porosity noted in the study area. A reduction in permeability between correlated zones of Y-7 and Y-8 (fig. 1), drilled 130 m apart, is ascribed to the deposition of secondary minerals (White and others, 1975), which may explain the porosity decrease noted in MA4 at Ridge 7741, where numerous silica veinlets likely drove silicification through silica sealing. To understand the minimum volume of fluid required to reduce porosity, the following relation was used (Dobson and others, 2003).

$$\text{Fluid volume} = \frac{\text{porosity reduction} * \text{silica density}}{\text{silica concentration}}$$

Assuming the paleo-elevation and the modern elevation of the rim of the Grand Canyon of the Yellowstone River (2,500 m) are the same and a pure water hydrostatic boiling point curve, the fluid is expected to contain about 775 ppm SiO_2 (aq) (Gunnarsson and Arnórsson, 2000). Considering a 33% porosity reduction in MA4 relative to the unaltered TSC and a density for amorphous silica of 2.1 g/cm^3 (Dobson and others, 2003), a fluid volume of 903 times greater than the original pore space is required. However, this assumes all of the dissolved silica is deposited, which is unlikely (Dobson and others, 2003). Such large fluid volumes indicate porosity reduction is likely caused by the cooling of a supersaturated fluid (Dobson and others, 2003). This implication may be applicable to other assemblages with abundant silica, i.e., MA1, or with abundant phyllosilicates, i.e., MA6.

Connection to Large-Scale Structures

Veins, fractures, and map-scale linear trends indicate the primary orientation of secondary permeability in the study area. To draw meaningful connections between intra-caldera faults, regional extensional faults within the Yellowstone park boundary, and meso-scale veins and fractures measured in the TSC, we only considered faults within the park boundary with a documented displacement history in the Quaternary period (https://www.usgs.gov/programs/earthquake-hazards/faults, accessed April 12, 2023; fig. 1). Extra-caldera faults (fig. 4F) are most similar to NNW–SSE-striking vein (fig. 4G) and fracture (fig. 4E) populations, while NW–SE and NE–SW-striking populations in veins, fractures, and map-scale linear trends (fig. 4C) are

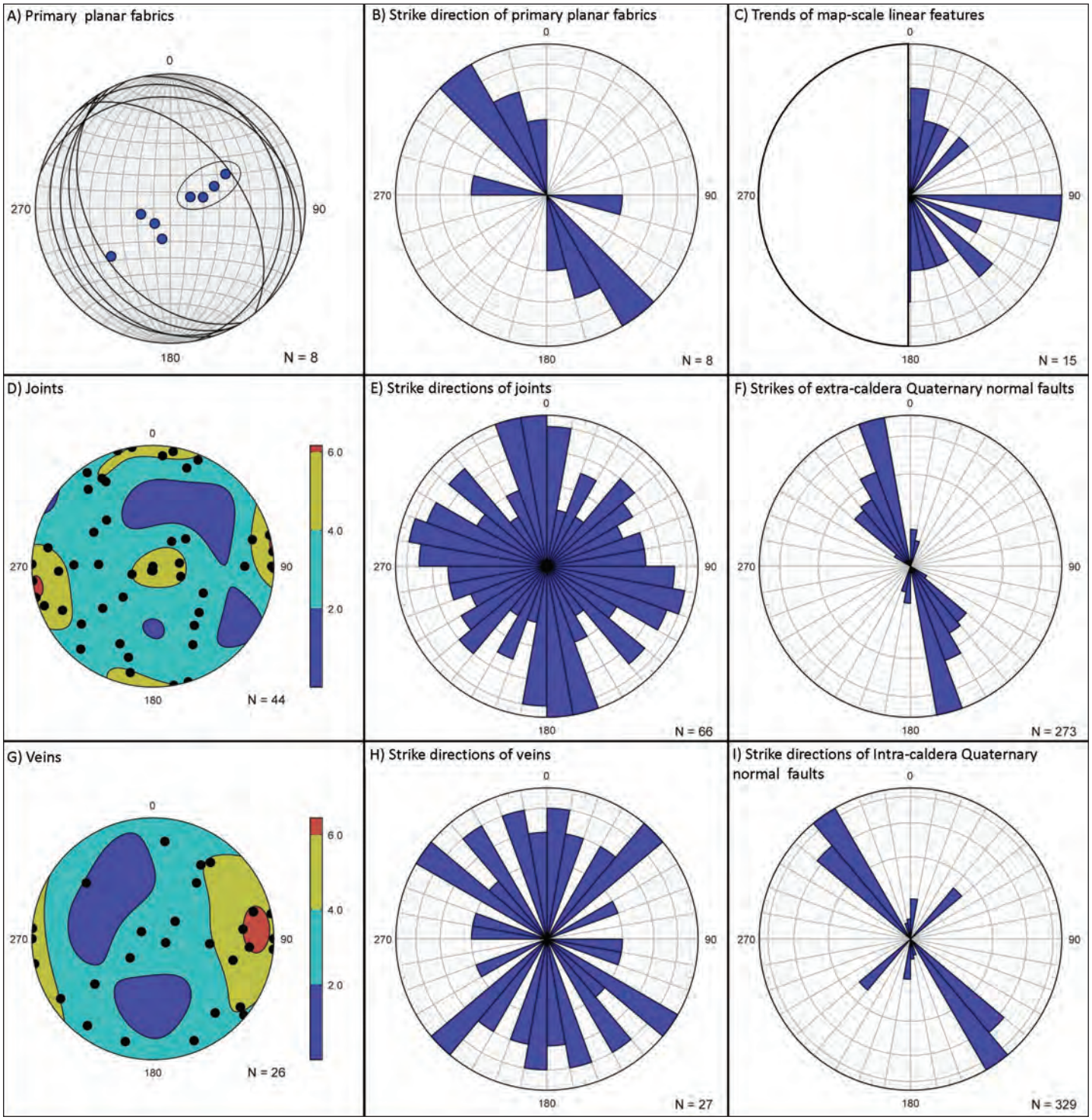

Figure 4. Stereonet and Rose diagrams of measured linear features. (A) Pole to plane stereonet of primary fabric with great circles. Orientations from outside the caldera margin are circled. (B) Rose diagram of primary fabric strikes. (C) Rose diagram of map-scale linear trends, recorded in half-azimuth. (D) Contoured pole to plane stereonet of fractures. The color scale is percent of data in a region. (E) Rose diagram of fracture strikes. (F) Rose diagram of map-scale extra-caldera fault strikes from faults within the park boundary and noted displacement during the Quaternary. (I) Contoured pole to plane stereonet of veins. The color scale is percent of data in a region. (G) Rose diagram of vein strikes. (H) Rose diagram of map-scale intra-caldera fault strikes.

more similar in orientation to the intra-caldera faults (fig. 4H). The caldera margin likely exerted control over the dominant E–W-striking population noted in linear trends and the WNW–ESE-striking population seen in fractures. Differential motion across the caldera margin may also explain the opposing dip directions noted in the primary fabric of the TSC (fig. 4A). Deviations from the dominant strike directions of veins and fractures may be due to cooling of the TSC, stresses caused by erosional unloading, and/or petrologic heterogeneity. Additionally, the discrepancy in dominant strike directions between veins (NW–SE, NE–SW) and fractures (NNW–SSE, WNW–ESE) may indicate preferred flow directions.

Development of the Hydrothermal System

Hydrothermal alteration in the TSC followed preferred flow channels, i.e., Ridge 7741. A schematic progression of hydrothermal alteration is shown in figure 5. The mean porosity of the unaltered TSC, 21% (fig. 5A), was altered by the hydrothermal fluids. Early alkaline-chloride alteration (MA2, M5, MA6, and MA4 at Ridge 7741) mainly reduced mean porosity by deposition of secondary minerals (fig. 5B). Yet, MA2 did not significantly alter mean porosity, and, with only one MA5 measurement, it is difficult to say if porosity was significantly altered. Distal MA6 lowered mean porosity to 11%. Later acid-sulfate alteration at upwelling zones produced MA3 and increased mean porosity to 28%, likely due to host unit dissolution (fig. 5C). Overprinting of MA3 by MA1 produced MA3A and increased porosity to 31% (fig. 5D), likely through continued dissolution. MA1 mean porosity is 15%, but may be lower in opaline silica blankets. Hydrothermal fluids at Seven Mile Hole alter porosity differently based on fluid chemistry and porosity may be further altered by overprinting.

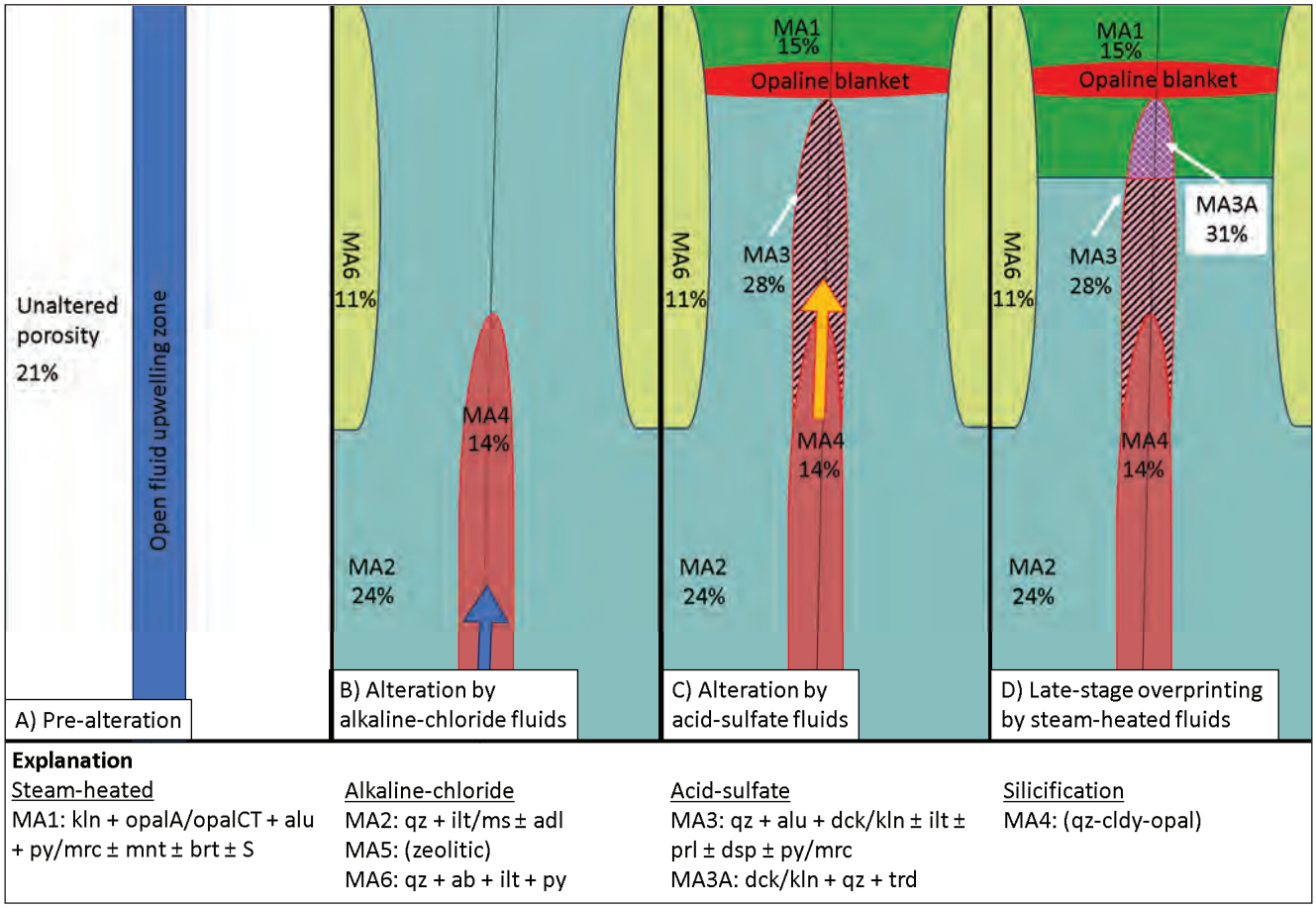

Figure 5. Schematic diagram of the progression of hydrothermal alteration with changes to mean porosity. (A) Pre-alteration. Unaltered Tuff of Sulphur Creek with an open conduit, shown in blue, and a mean porosity of 21%. (B) Alteration by alkaline-chloride fluids. Mineral assemblages (MA) associated with alkaline-chloride fluids, excluding MA5. Each color matches the color scheme used in Figure 2. The black line represents an open fracture or conduit for altering fluids (blue arrow) to follow. MA2 (light blue) alteration produces a moderate porosity increase to 24%. The pale green shoulders, MA6, are distal expressions with an 11% porosity. The red portion along the conduit is silicification, lowering porosity. (C) Alteration by acid-sulfate fluids. Influx of acid-sulfate fluids (orange arrow with red outline) produces MA3. MA3 alteration (pink with black lines) increased porosity to 28%. The appearance of MA1 (green) implies a lowering of the water table to allow the production of a steam-heated zone. The red blanket at the bottom of MA1 represents the deposition of opaline silica. (D) Late-stage overprinting by steam-heated fluids. Altering fluids stopped rising along the conduit, and the local water table continues to fall, expanding MA1 and overprinting MA3 to produce MA3A (purple with white cross-hatching).

Conclusions

Primary permeability along syndepositional fabrics drove the formation of shallowly dipping veins. Secondary permeability in the Tuff of Sulphur Creek is controlled by Basin and Range extension and intra-caldera stresses. Basin and Range extension likely controls NNW–SSE-striking structures, while intra-caldera stresses likely control NW–SE-striking structures. The caldera margin controlled roughly E–W-striking structures. The variable chemistry of hydrothermal fluids produced a range of noted porosities. The range of porosity in the unaltered to weakly altered Tuff of Sulphur Creek is likely due to petrologic variability, variable welding, and devitrification. Alteration by alkaline-chloride fluids broadly decreased the porosity of the host unit through the deposition of secondary minerals, whereas acid-sulfate fluids increased porosity through host rock dissolution. The steam-heated portion has a wide range of porosity due to a combination of deposition of secondary minerals and host rock dissolution.

References

Christiansen, R.L., 2001, The Quaternary and Pliocene Yellowstone Plateau volcanic field of Wyoming, Idaho, and Montana: U.S. Geological Survey Professional Paper 729-G, 144 p., https://doi.org/10.3133/pp729G

Dobson, P.F., Kneafsey, T.J., Hulen, J., and Simmons, A., 2003, Porosity, permeability, and fluid flow in the Yellowstone geothermal system, Wyoming: Journal of Volcanology and Geothermal Research, v. 123, p. 313–324, https://doi.org/10.1016/S0377-0273(03)00039-8.

Fournier, R.O., 1989, Geochemistry and dynamics of the Yellowstone National Park hydrothermal system: Annual Review of Earth and Planetary Sciences, v. 17, p. 13–53, https://doi.org/10.1146/annurev.ea.17.050189.000305.

Gansecki, C.A., Mahood, G.A., and McWilliams, M.O., 1996, $^{40}Ar/^{39}Ar$ geochronology of rhyolites erupted following collapse of the Yellowstone caldera, Yellowstone Plateau volcanic field: Implications for contamination: Earth and Planetary Science Letters, v. 142, p. 91–107.

Gunnarsson, I., and Arnórsson, S., 2000, Amorphous silica solubility and the thermodynamic properties of $H_4SiO°_4$ in the range of 0° to 350°C at Psat: Geochimica et Cosmochimica Acta, v. 64, p. 2295–2307, https://doi.org/10.1016/S0016-7037(99)00426-3.

Hurwitz, S., and Lowenstern, J.B., 2014, Dynamics of the Yellowstone hydrothermal system: Reviews of Geophysics, v. 51, p. 375–411, https://doi.org/10.1002/2014RG000452.

John, D.A., Vikre, P.G., du Bray, E.A., Blakely, R.J., Fey, D.L., Rockwell, B.W., Mauk, J.L., Anderson, E.D., and Graybeal, F.T., 2010, Descriptive models for epithermal gold-silver deposits: U.S. Geological Survey Special Investigations Report 2010-5070-Q, 247 p., https://doi.org/10.3133/sir20105070Q.

Larson, P.B., Cunningham, C.G., and Naeser, C.W., 1994, Hydrothermal alteration and mass exchange in the hornblende latite porphyry, Rico, Colorado: Contributions to Mineralogy and Petrology, v. 116, p. 199–215, https://doi.org/10.1007/BF00310700.

Larson, P.B., Phillips, A., John, D., Cosca, M., Pritchard, C., Andersen, A., and Manion, J., 2009, A preliminary study of older hot spring alteration in Sevenmile Hole, Grand Canyon of the Yellowstone River, Yellowstone Caldera, Wyoming: Journal of Volcanology and Geothermal Research, v. 188, p. 225–236, https://doi.org/10.1016/j.volgeores.2009.017.

Long, S.P., 2019, Geometry and magnitude of extension in the Basin and Range Province (39°N), Utah, Nevada, and California, USA: Constraints from a province-scale cross section: Geological Society of America Bulletin, v. 131, p. 99–119, https://doi.org/10.1130/B31974.1.

Manion, J.L., 2010, Epithermal alteration in Tuff of Sulphur Creek, Yellowstone National Park, Wyoming, 140 p.: Pullman, WA, Washington State University, Masters thesis.

Norton, D.L., 1984, Theory of hydrothermal systems: Annual Reviews in Earth and Planetary Sciences, v. 12, p. 155–177, https://doi.org/10.1146/annurev.ea.12.050184.001103.

Parsons, T., 2006, The basin and range province, *in* Olsen, K.H., ed., Developments in Geotectonics: San Diego, Calif., Elsevier, v. 25, p. 277–324, https://doi.org/10.1016/S0419-0254(06)80015-7.

Phillips, A.R., 2010, An oxygen isotope, fluid inclusion, and mineralogy study of the ancient hydro-

thermal alteration in the Grand Canyon of the Yellowstone River, Yellowstone National Park, Wyoming, 97 p.: Pullman, WA, Washington State University, Masters thesis.

Pritchard, C.J., and Larson, P.B., 2012, Genesis of the post-caldera eastern Upper Basin Member rhyolites, Yellowstone, WY: From volcanic stratigraphy, geochemistry, and radiogenic isotope modeling: Contributions to Mineralogy and Petrology, v. 164, p. 205–228, https://doi.org/10.1007/s00410-012-0733-9.

Smith, R.B., Jordan, M., Steinberger, B., Puskas, C.M., Farrell, J., Waite, G.P., Husen, S., Chang, W.L., and O'Connell, R., 2009, Geodynamics of the Yellowstone hotspot and mantle plume: Seismic and GPS imaging, kinematics, and mantle flow: Journal of Volcanology and Geothermal Research, v. 188, p. 26–56, https://doi.org/10.1016/j.jvolgeores.2009.08.020.

Truesdell, A.H., Nathenson, M., and Rye, R.O., 1977, The effects of subsurface boiling and dilution on the isotopic compositions of Yellowstone thermal waters: Journal of Geophysical Research, v. 82, o, 3694–3704, https://doi.org/10.1029/JB082i026p03694.

White, D.E., Fournier, R.O., and Muffler, L.J.P., 1975, Physical results of research drilling in thermal areas of Yellowstone National Park, Wyoming: U.S. Geological Survey Professional Paper 892, 70 p., https://doi.org/10.3133/pp892.

Transit difficulties *en route* to sampling the New Hope Mine (phosphate), Granite County, Montana.